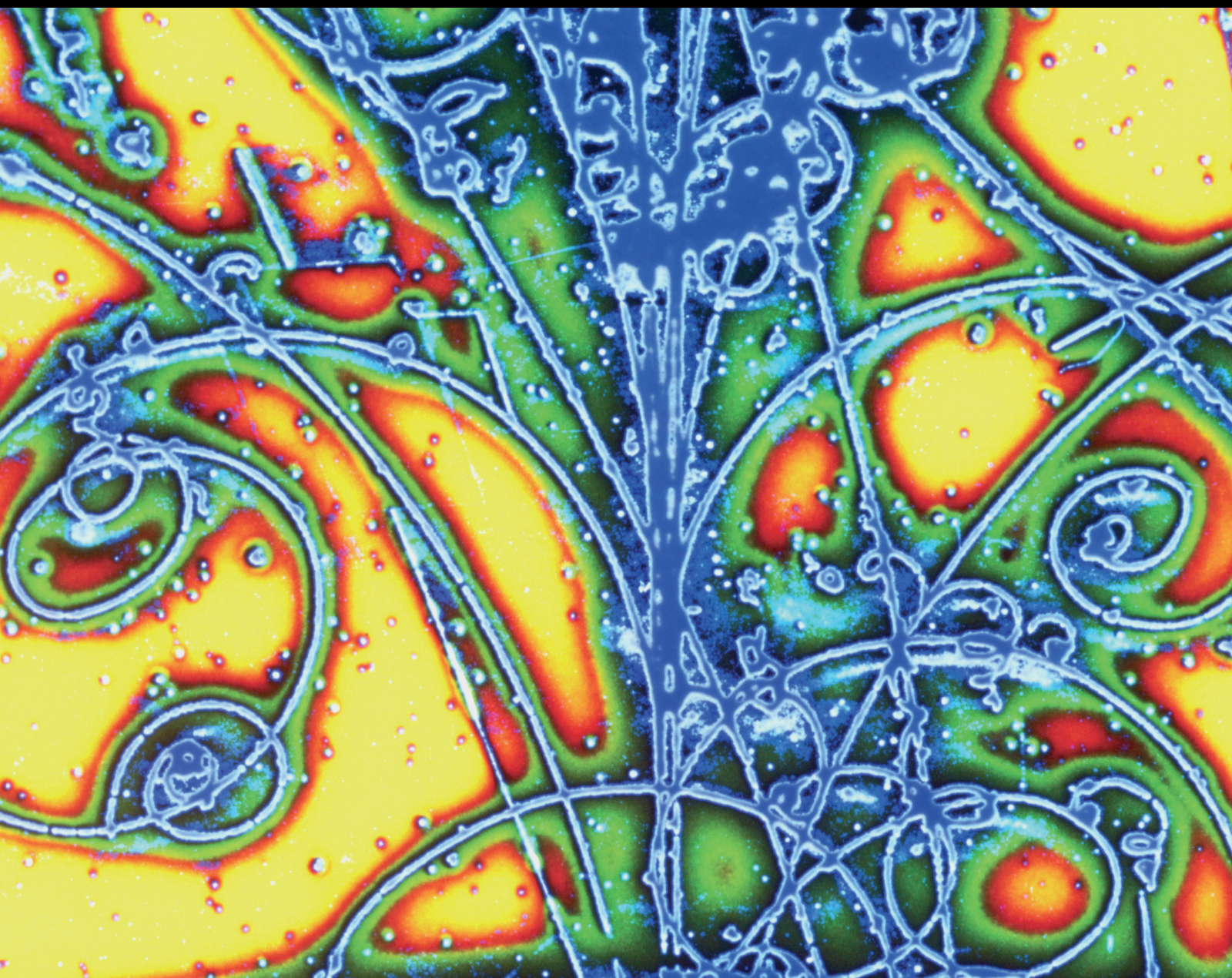


Advances in High Energy Physics

# Neutrino Physics in the Frontiers of Intensities and Very High Sensitivities 2016

Lead Guest Editor: Theodoros Kosmas

Guest Editors: Hiro Ejiri and Athanasios Hatzikoutelis





---

**Neutrino Physics in the Frontiers of Intensities  
and Very High Sensitivities 2016**

Advances in High Energy Physics

---

**Neutrino Physics in the Frontiers of Intensities  
and Very High Sensitivities 2016**

Lead Guest Editor: Theodoros Kosmas

Guest Editors: Hiro Ejiri and Athanasios Hatzikoutelis



---

Copyright © 2017 Hindawi. All rights reserved.

This is a special issue published in "Advances in High Energy Physics." All articles are open access articles distributed under the Creative Commons Attribution License, which permits unrestricted use, distribution, and reproduction in any medium, provided the original work is properly cited.

---

## Editorial Board

Luis A. Anchordoqui, USA  
T. Asselmeyer-Maluga, Germany  
Marco Battaglia, Switzerland  
Lorenzo Bianchini, Switzerland  
Burak Bilki, USA  
Adrian Buzatu, UK  
Rong-Gen Cai, China  
Anna Cimmino, Belgium  
Andrea Coccaro, Italy  
Shi-Hai Dong, Mexico  
Chao-Qiang Geng, Taiwan

Philippe Gras, France  
Xiaochun He, USA  
Filipe R. Joaquim, Portugal  
Aurelio Juste, Spain  
Ming Liu, USA  
Enrico Lunghi, USA  
Piero Nicolini, Germany  
Sergio Palomares-Ruiz, Spain  
Giovanni Pauletta, Italy  
Yvonne Peters, UK  
Anastasios Petkou, Greece

Alexey A. Petrov, USA  
Thomas Rössler, Sweden  
Juan José Sanz-Cillero, Spain  
Edward Sarkisyan-Grinbaum, USA  
Sally Seidel, USA  
George Siopsis, USA  
Luca Stanco, Italy  
Smarajit Triambak, South Africa  
Elias C. Vagenas, Kuwait  
Yau W. Wah, USA

# Contents

## **Neutrino Physics in the Frontiers of Intensities and Very High Sensitivities 2016**

Theocharis Kosmas, Hiroyasu Ejiri, and Athanasios Hatzikoutelis  
Volume 2017, Article ID 4313025, 3 pages

## **Neutrino Emission from Magnetized Microquasar Jets**

Theodoros Smponias and Odysseas Kosmas  
Volume 2017, Article ID 4962741, 7 pages

## **Impact of Nonstandard Interactions on Neutrino-Nucleon Scattering**

D. K. Papoulias and T. S. Kosmas  
Volume 2016, Article ID 1490860, 11 pages

## **Nuclear Structure Calculations for Two-Neutrino Double- $\beta$ Decay**

P. Sarriguren, O. Moreno, and E. Moya de Guerra  
Volume 2016, Article ID 6391052, 12 pages

## **New Phase Space Calculations for $\beta$ -Decay Half-Lives**

Sabin Stoica, Mihail Mirea, Ovidiu Nițescu, Jameel-Un Nabi, and Mavra Ishfaq  
Volume 2016, Article ID 8729893, 8 pages

## **Warm Dark Matter Sterile Neutrinos in Electron Capture and Beta Decay Spectra**

O. Moreno, E. Moya de Guerra, and M. Ramón Medrano  
Volume 2016, Article ID 6318102, 12 pages

## **Shell Model Studies of Competing Mechanisms to the Neutrinoless Double-Beta Decay in $^{124}\text{Sn}$ , $^{130}\text{Te}$ , and $^{136}\text{Xe}$**

Andrei Neacsu and Mihai Horoi  
Volume 2016, Article ID 1903767, 8 pages

## **Analysis of the Intermediate-State Contributions to Neutrinoless Double $\beta^-$ Decays**

Juhani Hyvärinen and Jouni Suhonen  
Volume 2016, Article ID 4714829, 13 pages

## **Lepton Pair Čerenkov Radiation Emitted by Tachyonic Neutrinos: Lorentz-Covariant Approach and IceCube Data**

Ulrich D. Jentschura and Robert Ehrlich  
Volume 2016, Article ID 4764981, 8 pages

## **Do Small-Mass Neutrinos Participate in Gauge Transformations?**

Y. S. Kim, G. Q. Maguire Jr., and M. E. Noz  
Volume 2016, Article ID 1847620, 7 pages

## **On a Search for Hidden Photon CDM by a Multicathode Counter**

A. V. Kopylov, I. V. Orekhov, and V. V. Petukhov  
Volume 2016, Article ID 2058372, 8 pages

## **Combined Effect of NSI and SFP on Solar Electron Neutrino Oscillation**

Deniz Yilmaz  
Volume 2016, Article ID 1435191, 6 pages

## **Magnetic Hexadecapole $\gamma$ Transitions and Neutrino-Nuclear Responses in Medium-Heavy Nuclei**

Lotta Jokiniemi, Jouni Suhonen, and Hiroyasu Ejiri  
Volume 2016, Article ID 8417598, 8 pages

## Editorial

# Neutrino Physics in the Frontiers of Intensities and Very High Sensitivities 2016

Theocharis Kosmas,<sup>1</sup> Hiroyasu Ejiri,<sup>2</sup> and Athanasios Hatzikoutelis<sup>3</sup>

<sup>1</sup>*Division of Theoretical Physics, University of Ioannina, 45110 Ioannina, Greece*

<sup>2</sup>*Research Center for Nuclear Physics, Osaka University, Osaka 567-0047, Japan*

<sup>3</sup>*Physics Department, University of Tennessee, Knoxville, TN, USA*

Correspondence should be addressed to Theocharis Kosmas; [hkosmas@uoi.gr](mailto:hkosmas@uoi.gr)

Received 15 May 2017; Accepted 17 May 2017; Published 30 August 2017

Copyright © 2017 Theocharis Kosmas et al. This is an open access article distributed under the Creative Commons Attribution License, which permits unrestricted use, distribution, and reproduction in any medium, provided the original work is properly cited. The publication of this article was funded by SCOAP<sup>3</sup>.

Neutrinos are the messengers of our universe about phenomena from astrophysical and Earth-bound laboratory processes alike. Despite the amazing progress in experimental, phenomenological, and theoretical neutrino physics, a remarkable number of questions associated with neutrino properties and interactions still remain unanswered. We collected articles in this volume that address topics of the current searches on these mysteries: validation that neutrinos are massive after we measure their absolute mass scale; particle-antiparticle conjugation properties of neutrinos related to the distinction (Dirac neutrinos) or no distinction (Majorana neutrinos); neutrino's moments, or at least the existence of electric dipole moment, magnetic moment, charge radius, and so forth; roles of neutrinos in astrophysics and cosmology; cosmic background neutrinos, and whether they contribute to dark matter's influence of the large-scale structure formation; high energy neutrinos associated with black-hole X-ray binary systems, active galactic nuclei, and so forth. Before delving in the particular articles we have for our readers some news and ideas on these open questions from the current research in our field of Intensity and High Sensitivity Frontier.

The finite neutrino mass may have already played a fundamental role in the appearance of little matter in our universe. Initially there were approximately equal amounts of matter and antimatter particles. A more reasonable progression should be that all matter would have been annihilated with all the antimatter. This is one of the most prominent unknown mysteries of the universe and it has inspired a great number

of extensions of the standard model. Some of these are mentioned in the articles in this special issue. For example, the mass of neutrinos implies that they may have magnetic moment. In turn, this allows for electromagnetic interactions among neutrinos and other standard model fermions as in neutrino-electron scattering. In addition to the weak interaction contribution mediated by W-boson exchange, there will be a photon exchange contribution to the interaction. Hence, the measured neutrino scattering cross sections provide an upper bound on the neutrino magnetic moment. On a grander scale, the remarkable developments of neutrino and gamma-ray astronomy have to show new telescopes and detector facilities like the ground-based observatory for gamma-ray astronomy named Cherenkov Telescope Array (CTA), the Ice-Cube neutrino observatory at the South Pole, and the KM3NeT at the Mediterranean Sea. These state-of-the-art technologies are used to detect neutrinos in a wide energy range and much higher than the energies of man-made accelerator beams. Such neutrinos are produced from very interesting galactic and extragalactic sources. Their distributions are closely related to the evolution of the various structures of our universe. The dynamical mechanisms producing astrophysical neutrinos strongly affect the neutrino emissivity and require an interdisciplinary approach.

Furthermore, one of the most interesting mysteries in neutrino physics is the number of neutrino species. Many recent experimental measurements are consistent with only three types of neutrinos coupled to the W- and Z-bosons. Therefore, if other (also called sterile) neutrino species exist

in nature, they must interact either much weaker with the W and Z or not at all. A great number of ongoing and future, high sensitivity experiments aim to determine if there exist any sterile neutrinos, how many species there are, and how strong their coupling is. We cover all of these examples of neutrino mysteries in our special issue.

In the world of High Sensitivity Frontier, extensive experimental programs and related theoretical works are going on to study the fundamental neutrino properties and weak interactions beyond Standard Electroweak Model (SM). Neutrinoless double beta decay (DBD) beyond SM is a high sensitivity unique probe for studying the Majorana nature of neutrinos ( $\nu$ ), the absolute  $\nu$ -mass scales, the mass hierarchy, the right-handed weak interactions, and others beyond SM. Nuclear matrix elements (NMEs)  $M^{0\nu}$  for  $0\nu\beta\beta$  decay are crucial for extracting neutrino properties from DBD experiments. The NMEs are connected with the light mass mechanism in that they contribute multipole states in intermediate nuclei as calculated in the pn-QRPA model. For example, the magnetic hexadecapole ( $M4$ )  $\gamma$ -decay NMEs are relevant to high multipole DBD NMEs. The cumulative sums of the NMEs define the energy region of the intermediate states. Also, experimental NMEs are compared with those of the quasi-particle model (QPM) and microscopic quasi-particle phonon model (MQPM). The fact that the experimental NMEs are reduced with respect to the QPM and MQPM NMEs suggests the existence of the nuclear and nonnuclear reduction effects on the high multipole NMEs. Our special issue includes articles on the  $M4$   $\gamma$ -decay NMEs relevant to DBD NMEs and analyses of the intermediate state contributions to these matrix elements.

The articles in our special issue discuss venues to disentangle the mixed right-handed and left-handed mechanisms ( $\lambda$  and  $\eta$ ) from the neutrino mass mechanism in the left-right symmetry. It is mostly shell model calculations that are carried out for the angular and energy distributions of the two beta rays for medium heavy nuclei. These calculations are used to identify the individual mechanisms, the mass mechanism, the  $\lambda$  dominance in competition with the mass mechanism, and the  $\eta$  dominance in competition with the mass mechanism.

The NMEs for the standard model process of the two neutrino DBDs obtained with the microscopic approach offered by the deformed self-consistent mean field are useful for the analysis of  $0\nu\beta\beta$  decay. The same nuclear Hamiltonian is entering to the two processes while the calculated NMEs are directly compared with experimental lifetimes. The phase space factors (PSFs) in the neutrino producing processes of single  $\beta^\pm$ -decay, and bound electron-capture, require accurate electron and positron wave functions obtained by modeling the solution of the Dirac equation with realistic nuclear potential. In this volume we include theoretical papers on  $2\nu\beta\beta$  decay NMEs, and on the relevant phase space.

From the world of the accelerator driven, long baseline, Intensity Frontier, there have been new scientific results and tensions that have made the 2016 a very interesting year and will be shaping the debate of neutrino physics for the next several years. The debate that caught our attention is coming

from the results presented at the biennial summer conferences Neutrino 2016 (<http://neutrino2016.iopconfs.org>) and 38th International Conference on High Energy Physics (<http://www.ichep2016.org>), the two biggest gatherings of the community.

Hosted in Japan, the T2K (Tokai to Kamioka) experiment has the world leading data set within the first three years of its run since 2010, corresponding to beam accumulation of almost  $7.5 \times 10^{20}$  protons-on-target. T2K had dazzled the neutrino world in 2012 reporting the first clear observation of e-like neutrino interactions in a  $\nu_\mu$  beam. The measurement validated the models with large values for the  $\theta_{13}$  mixing angle that are used in many of the articles in this issue. This measurement has earned for T2K the 2016 Breakthrough Prize shared with K2K, KamLAND, Daya Bay, Super-Kamiokande, and SNO (<https://breakthroughprize.org>). After its confirmation by the reactor driven neutrino experiments (Double CHOOZ, Daya Bay, RENO, etc.), the large value for  $\theta_{13}$  has opened the door to a legitimate hope of measuring the remaining, known yet unmeasured, mysteries of neutrino physics. The community is now planning to spend billions on the next generation Deep Underground Neutrino Experiment (DUNE) to search for the neutrino mass hierarchy and the CP violation in the lepton sector with its superior designed capabilities.

In the summer of 2016, T2K made yet another impression first by performing the first ever search for the CP violation in neutrino oscillations by comparing the appearance and disappearance channels in both neutrino and antineutrino beam modes. They performed this by switching the polarity of the secondary beam guiding system (horns) which changes the constitution of the tertiary beam to have more antineutrinos. Collecting another data sample with the antineutrino beam mode, again about  $7.5 \times 10^{20}$  protons-on-target within the last two years, T2K observed 4 e-like and 66  $\mu$ -like events at the far detector 295 km away. Compared to the 32 e-like and 135  $\mu$ -like neutrino interaction events observed during the initial measurement with the neutrino mode run, this observation is consistent with maximal disappearance. It is also the first ever indication that the CP violation may be maximal, which means that the value of  $\delta\text{CP}$  is probably near  $-\pi/2$  for either mass orderings. The T2K measurement excludes the CP conservation case ( $\delta\text{CP} = 0$ ) by more than  $2\sigma$  as well. Such a case of a CP conservation would imply that the observed events in both modes are consistent which is no more than 17% probable at a confidence level of 90% in this size data set.

The tension to the T2K announcement (arXiv:1701.00432) which describes the assumption is used in the analysis to constrain the T2K data, of maximal coupling with a weak preference to the second octant ( $\sin^2\theta_{23} > 0.5$ ). The tension is all on  $\theta_{23}$ . The other critical constraint, the value of  $\sin^2\theta_{13}$ , is at no danger of being challenged. The value of  $\theta_{13}$  comes from the exceptionally well defined “reactor measurement” as it has come to be known. The reactor experiments (Double CHOOZ and Daya Bay) have picked up the mantle of precision measurement experiments and have established the best ever measurements of this mixing.

The twist in the story of the 2016 summer conferences is that the NO $\nu$ A experiment, hosted in the USA, made waves by announcing (arXiv:1701.05891) a new measurement with crucial deviation from the usually accepted maximal value for  $\theta_{23}$ . All the previous calculations by NO $\nu$ A and all other experiments in the field (SK, MINOS, T2K, etc.) use  $\theta_{23} = \pi/4$ . This implies for the mass mixing of the neutrino masses that there is a symmetry of the muonic and tau ( $\tau$ ) meson components. At a level of just  $2\sigma$ , for the moment, this NO $\nu$ A precision measurement excludes maximal mixing and therefore the symmetry models of muon-tau in the neutrino sector.

NO $\nu$ A measured 78  $\mu$ -like interactions after the oscillation of a 2 GeV neutrino beam travelling underground for 810 km to a 14-kiloton surface detector. This corresponds to a data sample of just over  $6.0 \times 10^{20}$  protons-on-target after two years of world record intensity of its primary proton beam. The analysis of this observation suggests two different degenerate values for  $\sin^2\theta_{23}$  of about 0.4 or 0.6 at 68% confidence level and for both mass hierarchies. This result disfavors the maximal mixing of  $\sin^2\theta_{23} = 0.5$  at  $2\sigma$  significance. When this result is used to constrain the data of the other NO $\nu$ A observation (arXiv:1703.03328) of 33 e-like neutrino interactions in the far detector from the same beam and time period, it further disfavors the lower octant suggesting only the  $\sin^2\theta_{23} \approx 0.6$  as the more probable option for the mixing. This challenges the models of the muon and tau equal mixing in the  $\nu_3$  eigenstate of neutrino and the calculations that constrain the data from T2K and all the previous experiments.

A race for a precision measurement with much more data is warranted and the host laboratory of NO $\nu$ A has already initiated plans to increase the intensity of the NO $\nu$ A beam. Of course, it would be most interesting if NO $\nu$ A demonstrates that their reported value of the nonmaximal mixing at the high octant persists with increasing precision but the T2K never confirms it. In the meantime, with a strategic move and until the new beam intensity is established, NO $\nu$ A experiment is switching its beam to antineutrino mode in an effort to catch up and test the hierarchy and CP violations reported by T2K.

As this race is heating up, more new, precision measurements, from observations from these leading experiments, with the prolific numbers of neutrino interactions, will provide new values that will shape the theory of neutrinos. If 2016 has been interesting with the new conflicting announcements during the world conferences, the next couple of years will be really intense full of new models and calculations in publications such as our special issue.

*Theocharis Kosmas  
Hiroyasu Ejiri  
Athanasios Hatzikoutelis*

## Research Article

# Neutrino Emission from Magnetized Microquasar Jets

Theodoros Smponias<sup>1</sup> and Odysseas Kosmas<sup>2,3</sup>

<sup>1</sup>*Division of Theoretical Physics, University of Ioannina, 45110 Ioannina, Greece*

<sup>2</sup>*School of Mechanical, Aerospace and Civil Engineering, The University of Manchester, Manchester M13 9PL, UK*

<sup>3</sup>*Department of Informatics & Telecommunications, University of Peloponnese, 22100 Peloponnese, Greece*

Correspondence should be addressed to Theodoros Smponias; [t.smponias@hushmail.com](mailto:t.smponias@hushmail.com)

Received 7 November 2016; Revised 29 December 2016; Accepted 6 February 2017; Published 4 July 2017

Academic Editor: Athanasios Hatzikoutelis

Copyright © 2017 Theodoros Smponias and Odysseas Kosmas. This is an open access article distributed under the Creative Commons Attribution License, which permits unrestricted use, distribution, and reproduction in any medium, provided the original work is properly cited. The publication of this article was funded by SCOAP<sup>3</sup>.

The hadronic jets in a microquasar stellar system are modeled with the relativistic hydrocode PLUTO. We focus on neutrino emission from such jets produced by fast proton (nonthermal) collisions on thermal ones within the hadronic jet. We adopt a semianalytical approximation for the description of the secondary particles produced from p-p collisions and develop appropriate algorithms using the aforementioned injected protons as input. As a concrete example, we consider the SS-433 X-ray binary system for which several observations have been made the last decades. In contrast to the preset distribution of the fast protons along the jet employed in our previous works, in the present paper, we simulated it by using a power-law fast proton distribution along the PLUTO hydrocode. This distribution gradually sweeps aside the surrounding winds, during the jet advance through the computational grid. As a first step, in the present work, the neutrino energy spectrum is extracted from the model jet, facilitating a range of potential dynamical simulations in currently interesting microquasar jet systems.

## 1. Introduction

In binary stars commonly known as microquasars (MQs), two oppositely emitted jets of matter and radiation are produced. These systems are similar to Active Galactic Nuclei (AGN or quasars) and consist of a main sequence star (the giant companion or donor star), in coupled orbit with a compact astrophysical object (a neutron star or a black hole) [1]. A characteristic mass accretion disk develops close to the compact object from mass absorption through the inner Lagrangian Point (Roche Lobe Overflow) due to angular momentum conservation. The jets of a MQ appear quite collimated (due to the presence of a rather strong magnetic field) forming a multiwavelength and also particle emitter [2–4].

Stellar MQs are currently important astrophysical systems with growing interest in their investigations within astrophysics, particle physics, and cosmology. In the case of black hole microquasars (when the compact object is a black hole), the stellar system provides excellent testing grounds for black hole theories. Therefore, an improved understanding

of the dynamical astrophysical conditions within the jets in MQs is of significant importance [5–7].

In hadronic microquasar jets, the proton-proton interactions with the subsequent decay of the secondary particles, mostly  $\pi^\pm$  mesons, produce high-energy neutrinos. These collisions result also in the production of high-energy gamma rays, through the neutral pion ( $\pi^0$ ) decay, as discussed in previous works [7–11]. Recent simulations of high-energy p-p interactions in terrestrial laboratories provide quite accurate energy distributions of secondary products in the high-energy range (above 100 GeV) and determine parametric expressions of energy spectra for secondary particles like  $\pi^0$  and  $\pi^\pm$  mesons and neutrinos and also for gamma rays and electrons produced in inelastic p-p collisions [11, 12]. Such distributions may also be implemented when studying the hadronic MQs as neutrino and gamma ray sources [7].

Among the hadronic models proposed for the energy emission from microquasars (MQs), two are the most important. (i) In the first, relativistic protons in the jet interact with target protons from the stellar wind of the companion star. (ii) In the second, neutrinos and gamma rays are produced

from p-p interactions between relativistic (nonthermal) and cold (thermal) protons within the jets themselves [2–4, 11, 12]. In the latter case, relativistic (fast) protons within the jet are subject to different mechanisms that can make them lose energy. It is interesting to know the energy range where p-p collisions are the main (dominant) cooling process that produces the corresponding neutrinos (or gamma rays). On the other hand, the cold (slow) protons serve as targets for the relativistic protons [13, 14].

From a phenomenological point of view, microquasar neutrino and gamma ray sources need to be modeled fully relativistically [1, 7]. A suitable treatment is offered by the relativistic hydrocodes developed recently, such as the relativistic magnetohydrodynamical (RMHD) PLUTO hydrocode [15] employed in [7, 16, 17] in order to simulate the hadronic jets of the SS-433 MQ, an X-ray binary star [5, 6, 18].

The present paper is an extension of our work of [7] where we modeled simulated neutrino emission from galactic astrophysical hadronic jets originating from the vicinity of compact objects in binary stellar systems. Our dynamical simulations come out of the RMHD PLUTO code in conjunction with the in-house developed (in C, Mathematica, and IDL) codes. We now produce further results that aim to be directly comparable to the sensitivities of modern high-energy neutrino detectors, for example, the IceCube [19] and KM3NeT [20], thus clarifying the potential for observing neutrino emissions from microquasars.

## 2. Brief Description of the Main Background and Formalism

In this work, we adopt the model explaining the neutrino and gamma ray production through the p-p interactions between relativistic and cold protons occurring within the MQ jets themselves [2–4, 11, 12]. Relativistic protons in the jet are subject to various mechanisms that can lead to energy release. As is well known, in the case of hadronic MQ jets, a small portion (about 1%) of the protons (bulk flow protons) may be accelerated through first-order Fermi acceleration procedures that take place essentially at shock fronts inside the jet. In general, accelerated particles within the jet may gain energy up to the TeV scale.

For the particle (proton) acceleration rate at shocks (first-order Fermi mechanism), we have

$$t_{\text{acc}}^{-1} \simeq \eta \frac{ceB}{E_p}, \quad (1)$$

where  $B$  denotes the magnetic field and  $E_p$  denotes the proton energy ( $e$  and  $c$  are the usual parameters, i.e., the proton charge and the speed of light, resp.). The acceleration efficiency parameter  $\eta$  in our present calculations is set equal to  $\eta = 0.1$  (efficient accelerator case, mildly relativistic shocks near the jet base) [21].

From the scattering of fast protons off slow protons, high-energy pions and kaons are produced which may further

decay to very-high-energy gamma rays and neutrinos. The reaction schemes are described by equations of the form

$$pp \longrightarrow pp\pi^0 + F_0, \quad (2)$$

for the neutral-pion ( $\pi^0$ ) production channel, and

$$\begin{aligned} pp &\longrightarrow pn\pi^+ + F_1, \\ pp &\longrightarrow pn\pi^- + F_2, \end{aligned} \quad (3)$$

for the charged-pion ( $\pi^\pm$ ) production channels, where  $F_i, i = 0, 1, 2$ , comprises  $\pi^0$  and  $\pi^+\pi^-$  pairs, respectively.

Subsequently, the neutral pions  $\pi^0$  and other neutral mesons decay quickly producing high-energy gamma rays. The charged pions  $\pi^+$  ( $\pi^-$ ), needed for the purposes of our present work (and also the charged kaons), decay and lead to muons and furthermore to the production of various flavors of neutrinos as discussed below.

*2.1. Secondary Charged Particle Decay.* From inelastic p-p scatterings among nonthermal protons and thermal ones within the hadronic jet, neutrinos are mainly produced through charged-pion decay (known as prompt neutrinos). The muons included in the by-products can afterwards decay again into an electron (or a positron) and the associated two light neutrino flavors (delayed neutrino beam) according to the reactions described below.

*2.1.1. Prompt Decay Channels (Prompt Neutrinos).* The  $\pi^+$  ( $\pi^-$ ) mesons (with a mass of  $m_\pi = 139.6 \text{ MeV}/c^2$  and a half-life of  $2.6 \cdot 10^{-8} \text{ s}$ ) decay due to the weak interaction, the primary decay mode of which (with a probability of 0.999877) is a reaction leading to an antimuon (muon) and a muonic neutrino (muonic antineutrino) as

$$\begin{aligned} \pi^+ &\longrightarrow \mu^+ + \nu_\mu, \\ \pi^- &\longrightarrow \mu^- + \bar{\nu}_\mu. \end{aligned} \quad (4)$$

A less important decay mode of  $\pi^+$  ( $\pi^-$ ), with probability of occurrence just 0.000123, is its decay into a positron (electron) and an electron neutrino (electron antineutrino) as

$$\begin{aligned} \pi^+ &\longrightarrow e^+ + \nu_e, \\ \pi^- &\longrightarrow e^- + \bar{\nu}_e. \end{aligned} \quad (5)$$

In this work, we neglect the neutrino production through the latter channels.

*2.1.2. Delayed Decay Channel (Delayed Neutrinos).* The other important source of neutrinos in hadronic jets is the decay mode of the produced muons (muon leptonic decay) in reactions (4), which produces also two neutrinos described by the processes

$$\begin{aligned} \mu^+ &\longrightarrow e^+ + \nu_e + \bar{\nu}_\mu, \\ \mu^- &\longrightarrow e^- + \bar{\nu}_e + \nu_\mu. \end{aligned} \quad (6)$$

In general, the analytical formulae suggested from laboratory p-p collisions resemble the simulated distributions extracted in [11] within a few percent over a large range of the fraction of the energy of the incident proton ( $E_p$ ) transferred to the secondary particles, that is, the ratio  $x = E_i/E_p$ , with  $E_i$  being the energy of the secondary particle (e.g., pion).

From an experimental point of view, for astrophysical gamma rays and neutrinos, extremely sensitive detection systems have been developed [8, 9, 20]. These detectors sparked a renewed interest in studying stellar objects as neutrino and gamma ray sources; for example, the SS-433 system is widely known from the early 1980s as the only MQ with a verified hadronic jet content. We mention, for example, that observations of iron lines in the spectrum of the SS-433 MQ provided useful information regarding the hadronic content of its jets [21].

From a theory and phenomenology point of view, the gamma ray and neutrino production from a hadronic MQ that are of interest in the present work is based on reliably determining the distribution of the fast protons and the realistic injection functions of the produced secondary particles (pions, kaons, muons, etc.).

In previous works [7, 16, 17], the hadronic jet was modeled using the PLUTO code. The results of PLUTO were then processed in order to calculate the emissivity of various secondary particles (pions, kaons) and the produced muons, gamma rays, and so forth, on the basis of the spatial and time variation of physical parameters like the magnetic field that collimated the jet, the mass number density for every grid cell of the PLUTO code, and others.

Before proceeding to the presentation and discussion of the results, we should mention that the discrimination of prompt and delayed neutrinos from MQ jets is not possible; therefore, the results obtained in the present work refer to physical quantities pertaining to prompt neutrinos, nonetheless as they are much faster to simulate computationally.

### 3. Results and Discussion

The main results of this work refer to the mean number density of the nonthermal protons (obtained with the algorithms mentioned before and the PLUTO hydrocode), the pion injection function, and the pion energy distribution describing the pion governing (4). The evaluation of the emissivity of the prompt neutrinos relies on these calculations.

**3.1. Nonthermal Proton Density.** We begin our calculations by considering the production of nonthermal protons in the jet. The nonthermal proton population emerges from the bulk jet flow that comprises mainly thermal protons, moving mildly relativistically. Some of the slow protons are locally accelerated, at shock fronts appearing within the jet flow (first-order Fermi acceleration process), to ultrarelativistic velocities. While in our previous studies we adopted a fast (nonthermal) proton jet density  $N_p$ , equal to a tiny fraction ( $10^{-6}$ ) of the corresponding thermal proton density, in the present work, we assume a power-law distribution of the form  $N_p = N_0 E^{-\alpha}$ , with  $\alpha \approx 2$  [3]. In addition, we considered a spatial density distribution  $n_z$ , coming out of

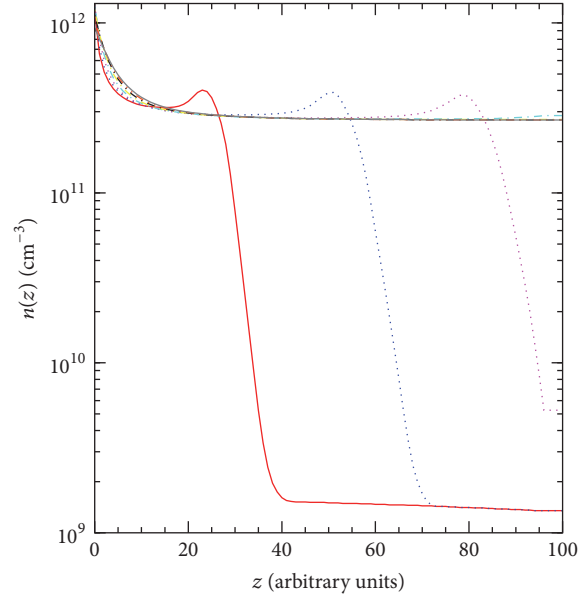


FIGURE 1: Density profile evolution for slow protons along the jet. Each snapshot represents 100 PLUTO time units in the simulation, or 33 seconds in model time. The beginning rests at the start of the simulation. The first three or four snapshots indicate dynamic jet evolution, while the rest approach a steady-state behaviour.

explicit calculations with the PLUTO hydrocode as discussed below.

For an RMHD simulation of a rather laterally restricted magnetized jet, we, first, calculated the mean matter density along the jet axis (as a function of  $z$ ), that is, the slow proton density  $n(z)$ , by evaluating the PLUTO density over a slice cut perpendicular to the jet axis. In order to cover the temporal evolution of the jet as the simulation evolves, these mean density values have been obtained for a number of 8 snapshots which are plotted in Figure 1. From this figure, we can see how the mean density profile evolves along the jet. Its peak is moving outwards while the overall maximum gradually decreases. The jet remains confined, mainly due to the presence of a toroidal magnetic field component ( $B_{\text{tor}}$ ). The surrounding wind helps shape the jet as well, especially at the early stages of the simulation, before the wind begins to be swept by the jet.

As the jet advances through the computational grid, it gradually sweeps aside the surrounding winds resulting in a near-steady state with a rather flat density profile. The magnetic jet confinement prevents the jet density from falling too much along the jet. It is worth mentioning that, for the characteristic time scales of the energy loss mechanisms, we largely follow [4, 11], incorporating mainly synchrotron and adiabatic energy loss mechanisms.

**3.2. Pion Injection Function and Pion Energy Distribution.** For every p-p interaction (one “fast,” nonthermal proton scattered off a “slow,” thermal one), we obtain a probability density of a resulting pion at every position along the possible spectrum of resulting pions; that is, we get a spectrum of

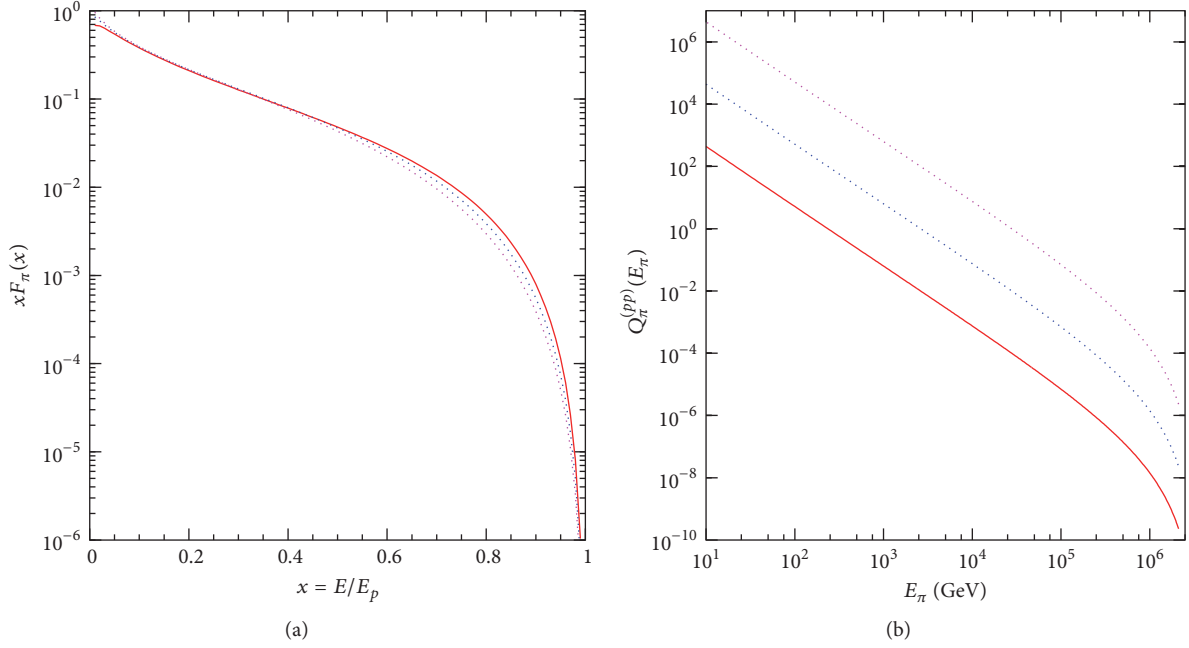


FIGURE 2: (a) Pion energy spectra, per p-p collision, obtained for three different incoming fast proton energies ( $E_p = 10^3$  GeV,  $E_p = 10^4$  GeV, and  $E_p = 10^5$  GeV), as a function of the ratio  $x = E_\pi/E_p$ . We consider charged pions ( $\pi^\pm$ ) as needed for our purposes in this work.  $E_\pi$  denotes the secondary particle (pion) energy. (b) Variation of the pion injection function,  $Q_\pi^{(pp)}(E)$ , through the pion energy spectrum, for three different jet densities  $n(z)$ , located at different points along the model jet axis.

possible energies for the resulting pion. That spectrum, per p-p collision, is represented by  $F_\pi$  and is dependent on the incoming fast proton energy (slow proton energy is negligible by comparison) and the ratio of a given position at the pion spectrum to the incoming proton energy. In [11], the function  $F_\pi$  is given by the expression

$$F_\pi^{(pp)}\left(x, \frac{E}{x}\right) = 4\alpha B_\pi x^{\alpha-1} \left(\frac{1-x^\alpha}{1+rx^\alpha(1-x^\alpha)}\right)^4 \cdot \left(\frac{1}{1-x^\alpha} + \frac{r(1-2x^\alpha)}{1+rx^\alpha(1-x^\alpha)}\right) \cdot \left(1 - \frac{m_\pi c^2}{xE_p}\right)^{1/2} \quad (7)$$

which represents the pion spectrum per proton-proton interaction.  $x = E/E_p$ ,  $B_\pi = a' + 0.25$ ,  $a' = 3.67 + 0.83L + 0.075L^2$ ,  $r = 2.6/\sqrt{a'}$ ,  $\alpha = 0.98/\sqrt{a'}$ , and  $L$  is the jet's luminosity (see [4, 11]). In Figure 2(a), the product  $xF_\pi$  is plotted as a function of the ratio  $x$ , for three different incoming fast proton energies ( $E_p = 10^3$  GeV,  $E_p = 10^4$  GeV, and  $E_p = 10^5$  GeV), which cover the energy range of interest.

With the aid of this function, we calculate the pion injection function,  $Q_\pi^{(pp)}$ , through the relation

$$Q_\pi^{(pp)}(E, z) = n(z) c \int_k^1 \frac{dx}{x} N_p\left(\frac{E}{x}, z\right) F_\pi^{(pp)}\left(x, \frac{E}{x}\right) \sigma_{PP}^{(\text{inel})}\left(\frac{E}{x}\right), \quad (8)$$

where  $k = E/E_p^{(\text{max})}$ .  $N_p$  stands for the fast proton density,  $x$  is the ratio of the pion energy to proton energy, and  $\sigma_{PP}^{(\text{inel})}$  is the proton-proton inelastic collision cross section.

The pion injection function,  $Q_\pi^{(pp)}$ , depends on the thermal proton density,  $n(z)$ . In Figure 2(b), we plot  $Q_\pi^{(pp)}$  versus the pion energy  $E_\pi$  for three different jet densities ( $n = 10^9$ ,  $n = 10^{10}$ , and  $n = 10^{11}$ ). We notice the approximate square dependence of the scale of  $Q_\pi^{(pp)}$  on the jet density, which is because  $N_p$  also depends on  $n(z)$ .

As a physical interpretation, let us consider a large number of p-p collisions. So, we add up, at every pion spectrum energy, the contributions to the probability that a pion will result at that energy. Depending on the incoming proton energy for each collision, there may be a smaller or a larger contribution to any given pion energy, as long as it is smaller than the proton's energy in the first place (pion energy cannot exceed proton energy). So, we integrate over many p-p collisions to find the pion spectrum of a collection of p-p collisions, that is, the pion injection function  $Q_\pi^{(pp)}$ .

In order to obtain the pion distribution entering neutrino emissivity, we solve the following transport equation:

$$\frac{\partial N_\pi}{\partial E} + \frac{N_\pi}{t_{\text{loss}}} = Q_\pi^{(pp)}(E, z), \quad (9)$$

where  $N_\pi(E, z)$  denotes the pion energy distribution. The numerical integration of the transport equation, for a cell of

the hydrocode, that is, a localized position in space, is given by the following expression:

$$N_{\pi}(E) = \frac{1}{|b_{\pi}(E)|} \int_E^{E^{(\max)}} dE' Q_{\pi}^{(pp)}(E') \exp[-\tau_{\pi}(E, E')], \quad (10)$$

where

$$\tau_{\pi}(E', E) = \int_{E'}^E \frac{dE'' t_{\pi}^{-1}(E'')}{|b_{\pi}(E'')|}. \quad (11)$$

We note here that the physical conditions within a cell are taken to be constant and also that the macroscopic physical parameters (density, pressure, etc.) within each cell are taken to be constant. Under these assumptions, the transport equation is only dependent on energy, which considerably simplifies its calculation. We also take the characteristic scale (mean free path) of the radiative interactions to be smaller than the cell size, leading to the containment of particle interactions within a given hydrocode cell. Furthermore, the time scale for the radiative interactions is so much smaller than the hydrocode's timestep that the radiative interactions belong to a single timestep each time.

The behaviour of the pion distribution  $N_{\pi}(E_p)$ , in the energy range of our interest, is illustrated in Figure 3. This curve refers to a typical computational cell of the PLUTO hydrocode. It could be easily extended to a number of hydrocode cells covering a span of the computational grid, therefore opening the way towards obtaining the neutrino emissivity from the whole grid.

In such a treatment, we consider a large number of interacting particles per computational cell; therefore, the probability density in the transport equation can be approximated by the number density of the particles, rendering the stochastic portion of the general transport equation inactive. Moreover, only the deterministic portion of the transport equation is employed, which simplifies it to a deterministic partial differential equation (for further details on the meaning of various symbols and functions used in this section, the reader is referred to [4, 11]).

**3.3. Neutrino Emissivity.** As mentioned before, in this work, we consider neutrinos emanating from direct pion decay (prompt neutrinos; see reaction (4)). In the semianalytical approach implemented in this work, the emissivity of prompt neutrinos is obtained with the aid of  $N_{\pi}(E_p)$  from the expression [4, 12]

$$Q_{\pi \rightarrow \nu}(E) = \int_E^{E_{\max}} dE_{\pi} t_{\pi, \text{dec}}^{-1}(E_{\pi}) N_{\pi}(E_{\pi}) \frac{\Theta(1 - r_{\pi} - x)}{E_{\pi}(1 - r_{\pi})}, \quad (12)$$

where  $x = E/E_{\pi}$  and  $t_{\pi, \text{dec}}$  is the pion decay time scale.  $\Theta(\chi)$  is the well-known theta function (for further parameter details, see [7]). The neutrino emission calculation could be performed mainly following the analysis of [3, 4, 11, 12].

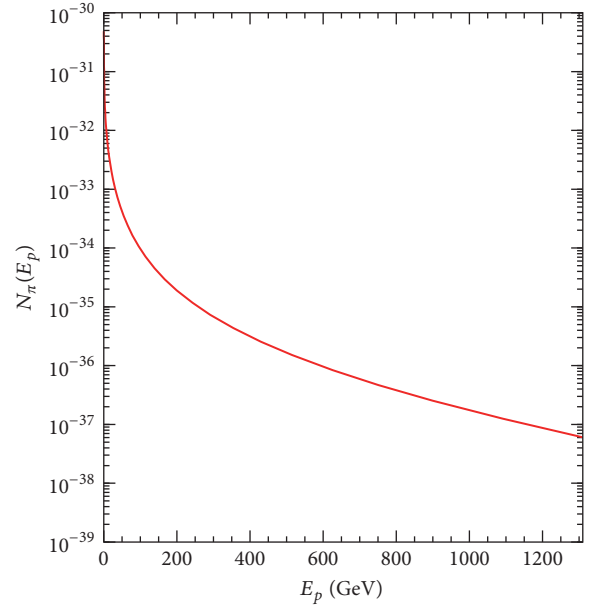


FIGURE 3: Pion energy distribution  $N_{\pi}(E_p)$  obtained through the solution of the transport equation, for a typical cell of the hydrocode. This cell is a localized position in the space of the jet.

For the readers' convenience, we should mention the following. The nonthermal proton distribution suffers synchrotron and adiabatic losses, affecting the balance in the transport between protons and pions. The total neutrino emissivity can then be calculated by adding up contributions from every volume element (3D cell) and dividing the sum by the area of a sphere with radius equal to the distance to Earth. The result is a synthetic "neutrino emission observation" of the binary system. By repeating the process for many energies, we can then obtain a synthetic spectral emission distribution, for direct comparison with observations.

As an illustration of the behaviour of neutrino emissivity  $Q_{\pi \rightarrow \nu}(E)$  versus the neutrino energy, in Figure 4, the neutrino spectra from a series of computational slices, cut perpendicular to the jet axis (at equal intervals along the model jet), are shown. The density of each slice is spatially averaged over the slice surface and that average density (see Table 1) is then employed in the neutrino emission calculation. The averaging is performed in IDL and the emission calculation in Mathematica. The results presented in Figure 4 are unnormalized, but, in order to compare to minimum detection levels of existing and future instruments, the simulation results can be normalized energetically and then calibrated for a given specific instrument (this is going to be presented elsewhere).

The integrated (across the spectrum used) energy emitted, per unit time, through neutrinos, is presumed to be a fraction of the fast (nonthermal) proton power in the jet during the eruption modeled. The latter energy is, in turn, a fraction of the total jet kinetic power, or kinetic luminosity,  $L_k$ . For  $L_k = 10^{40}$  erg/s, then  $L_{fp} = 10^{36}$  erg/s, if  $f_{fp} = 10^{-4}$ . Assuming now a neutrino fraction of  $fn = 0.5$ , we then obtain  $L_n = 0.5 \times 10^{36}$  erg/s.

TABLE 1: Number density values  $\rho_j$ ,  $j = 1, 2, \dots$ , averaged over ten slices cut as grid cross sections perpendicular to the jet axis, along the jet axis. The densities are sampled at intervals of  $2.0 \times 10^{11}$  cm, to a total grid length along the jet axis direction of  $2.0 \times 10^{12}$  cm.

	Number density (in $10^{10}$ protons/cm <sup>3</sup> )									
$\rho_j =$	$\rho_1$	$\rho_2$	$\rho_3$	$\rho_4$	$\rho_5$	$\rho_6$	$\rho_7$	$\rho_8$	$\rho_9$	$\rho_{10}$
	124.221	33.152	29.530	28.786	29.220	36.558	11.627	0.260	0.142	0.138

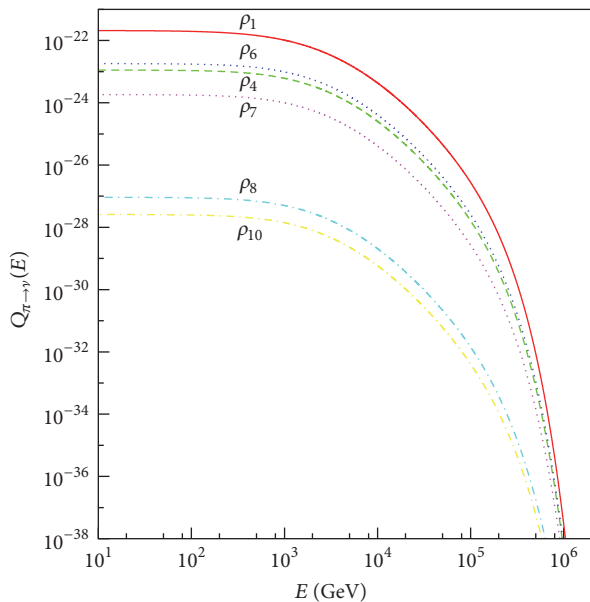


FIGURE 4: Neutrino emissivity  $Q_{\pi \to \gamma}(E)$  obtained for various values of number density  $\rho_j$  (see Table 1) by integrating numerically (12). For the sake of comparison with observations and other predictions, the value of  $Q_{\pi \to \gamma}(E)$  should be multiplied by the normalization factor  $F_{\text{norm}} = 10^{54}$  erg/GeV (see the text).

In general, to scale the neutrino intensity, a normalization factor  $F_{\text{norm}}$  is needed. In our case, that factor results from energetic arguments. This factor should multiply the neutrino emissivity of Figure 4 to obtain the neutrino intensity along the jet. As an example, assuming, as above, a fast proton energy fraction of  $10^{-4}$ , by equating the area under the  $\rho_1$  curve of Figure 4 ( $\rho_1$  corresponds to the average bulk proton density at the jet base) to the fast proton fraction of the jet kinetic luminosity  $L_k = 10^{40}$  ergs/s, we obtain  $F_{\text{norm}}$  approximately equal to  $F_{\text{norm}} = 10^{54}$  erg/GeV. The latter corresponds to a maximum neutrino intensity of about  $0.5 \times 10^{32}$ , which is compatible with the results of [4] (see, e.g., Figure 8 of this reference). We note that even though our model is quite detailed dynamically, its level of detail cannot be fully compared to observations as of today. The reason is that current and upcoming terrestrial neutrino detectors cannot resolve that much detail, due to the distance of the microquasars from Earth. Therefore, when compared to observations, the predictive power of our model is not very different from that of simpler models [3, 4].

We should point out that, in order to convert quantities from the jet reference frame to our rest frame, the calculational procedure can be, for example, that of [13] or that

of [14]. In the present work, we apply the treatment of [13]. The jet direction has been incorporated as a global effect within the jet, by imposing a fixed angle between the velocity direction of the flow and the line of sight to an observer here on Earth. Furthermore, the jet flow speed is taken to be set to  $0.26c$ , the average flow estimated for the jet. In addition, the line-of-sight direction is assumed to be constant all over the jet, at an angle of  $\theta = 78$  degrees, to the jet axis. This was done to keep the calculations within limits. In principle, each computational cell may have a different setting for the angle between its local velocity and the line of sight, as well as for the local emission calculation performed using its localized velocity value. In both cases, a much longer computational time is required.

Before closing, it is worth mentioning that the total power emitted from the jet obtained in the present work is only a first approximation to the intensity estimate. Consequently, a more detailed comparison to detectors is required. Our model is indeed able to provide, for a given direction to the observer, individual Doppler effects for each 3D computational cell and then integrate them numerically. Such detailed calculations will be included in a future publication.

#### 4. Summary and Conclusions

In the present work, we evaluated the emissivity of neutrinos originating from hadronic MQ jets, where p-p collisions occur at shock fronts, leading to cascades of secondary particles, culminating to neutrino emission. We have implemented a new model describing the mass distribution along the jet axis, using the PLUTO relativistic magnetohydrodynamic (RMHD) code (hydrocode). More specifically, the PLUTO code was executed incorporating a toroidal magnetic field component in the jet, resulting in a confined jet structure, the degree of confinement depending on the value of the field. For each cross section slice, cut along the jet (perpendicular to the jet axis), we calculated the mean values of the mass density. Then, we proceeded, in this manner, to process a number of 100 slices, covering the spatial range from the jet base to the end of the computational grid.

The main conclusion extracted from this analysis was that the hydrocode model (not based on explicit geometrical assumptions), employed for the hadronic jet, is dynamically a realistic tool. This is why we decided to utilise the PLUTO code for dynamical calculations as a basis for further investigation of the neutrino and gamma ray emissivities from the jet. For our present calculations, we used the semianalytic approach, in order to estimate the neutrino emissivity, as described in our previous work.

In studying the neutrino emissivity per grid cell, we set up a model geometry reminiscent of the semianalytical method,

but using the PLUTO hydrocode, while employing the known radiative formalism as discussed in the Introduction. This computational tool has previously provided us with a realistic modeling of radio and gamma ray emission and in this work with efficient estimation of neutrino emission events originating from microquasar jets. For the observation of such neutrino fluxes, current terrestrial detectors (e.g., IceCube at South Pole) are in operation.

## Conflicts of Interest

The authors declare that there are no conflicts of interest regarding the publication of this paper.

## References

- [1] I. F. Mirabel and L. F. Rodríguez, “Sources of relativistic jets in the galaxy,” *Annual Review of Astronomy and Astrophysics*, vol. 37, no. 1, pp. 409–443, 1999.
- [2] G. E. Romero, D. F. Torres, M. M. K. Bernadó, and I. F. Mirabel, “Hadronic gamma-ray emission from windy microquasars,” *Astronomy and Astrophysics*, vol. 410, no. 2, pp. L1–L4, 2003.
- [3] M. M. Reynoso, G. E. Romero, and H. R. Christiansen, “Production of gamma rays and neutrinos in the dark jets of the microquasar SS433,” *Monthly Notices of the Royal Astronomical Society*, vol. 387, no. 4, pp. 1745–1754, 2008.
- [4] M. M. Reynoso and G. E. Romero, “Magnetic field effects on neutrino production in microquasars,” *Astronomy and Astrophysics*, vol. 493, no. 1, pp. 1–11, 2009.
- [5] A. Ferrari, “Modeling extragalactic jets,” *Annual Review of Astronomy and Astrophysics*, vol. 36, no. 1, pp. 539–598, 1998.
- [6] S. Fabrika, “The jets and supercritical accretion disk in SS433,” *Astrophysics and Space Physics Reviews*, vol. 12, pp. 1–152, 2004.
- [7] T. Smponias and O. T. Kosmas, “High energy neutrino emission from astrophysical jets in the Galaxy,” *Advances in High Energy Physics*, vol. 2015, Article ID 921757, 7 pages, 2015.
- [8] M. Actis, G. Agnetta, F. Aharonian et al., “Design concepts for the Cherenkov Telescope Array CTA: an advanced facility for ground-based high-energy gamma-ray astronomy,” *Experimental Astronomy*, vol. 32, pp. 193–316, 2011.
- [9] A. A. Abdo and M. Ackermann, “Modulated high-energy gamma-ray emission from the microquasar Cygnus X-3,” *Science*, vol. 326, pp. 1512–1516, 2009.
- [10] T. Kosmas, H. Ejiri, and A. Hatzikoutelis, “Neutrino physics in the frontiers of intensities and very high sensitivities,” *Advances in High Energy Physics*, vol. 2015, Article ID 806067, 3 pages, 2015.
- [11] S. R. Kelner, F. A. Aharonian, and V. V. Bugayov, “Energy spectra of gamma rays, electrons, and neutrinos produced at proton-proton interactions in the very high energy regime,” *Physical Review D*, vol. 74, Article ID 034018, 2006.
- [12] P. Lipari, M. Lusignoli, and D. Meloni, “Flavor composition and energy spectrum of astrophysical neutrinos,” *Physical Review D*, vol. 75, no. 12, Article ID 123005, 2007.
- [13] D. Purmohammad and J. Samimi, “On the hadronic beam model of TeV  $\gamma$ -ray flares from blazars,” *Astronomy and Astrophysics*, vol. 371, no. 1, pp. 61–67, 2001.
- [14] D. F. Torres and A. Reimer, “Hadronic beam models for quasars and microquasars,” *Astronomy and Astrophysics*, vol. 528, article L2, 2011.
- [15] A. Mignone, G. Bodo, S. Massaglia et al., “PLUTO: a numerical code for computational astrophysics,” *Astrophysical Journal, Supplement Series*, vol. 170, no. 1, pp. 228–242, 2007.
- [16] T. Smponias and T. S. Kosmas, “Modelling the equatorial emission in a microquasar,” *Monthly Notices of the Royal Astronomical Society*, vol. 412, no. 2, pp. 1320–1330, 2011.
- [17] T. Smponias and T. S. Kosmas, “Dynamical and radiative simulations of  $\gamma$ -ray jets in microquasars,” *Monthly Notices of the Royal Astronomical Society*, vol. 438, no. 2, pp. 1014–1026, 2014.
- [18] B. Margon, “Observations of SS 433,” *Annual Review of Astronomy and Astrophysics*, vol. 22, no. 1, pp. 507–536, 1984.
- [19] M. G. Aartsen, M. Ackermann, J. Adams et al., “Search for prompt neutrino emission from gamma-ray bursts with IceCube,” *The Astrophysical Journal Letters*, vol. 805, no. 1, article L5, 2015.
- [20] S. Adrian-Martinez, M. Ageron, F. Aharonian et al., “Letter of intent for KM3NeT 2.0,” *Journal of Physics G: Nuclear and Particle Physics*, vol. 43, no. 8, Article ID 084001, 2016.
- [21] M. C. Begelman, S. P. Hatchett, C. F. McKee, C. L. Sarazin, and J. Arons, “Beam models for SS 433,” *The Astrophysical Journal*, vol. 238, pp. 722–730, 1980.

## Research Article

# Impact of Nonstandard Interactions on Neutrino-Nucleon Scattering

**D. K. Papoulias and T. S. Kosmas**

*Theoretical Physics Section, University of Ioannina, 451 10 Ioannina, Greece*

Correspondence should be addressed to D. K. Papoulias; [dimpap@cc.uoi.gr](mailto:dimpap@cc.uoi.gr)

Received 13 July 2016; Revised 30 September 2016; Accepted 15 November 2016

Academic Editor: Burak Bilki

Copyright © 2016 D. K. Papoulias and T. S. Kosmas. This is an open access article distributed under the Creative Commons Attribution License, which permits unrestricted use, distribution, and reproduction in any medium, provided the original work is properly cited. The publication of this article was funded by SCOAP<sup>3</sup>.

Nonstandard neutrino-nucleon interaction is formulated and explored within the energy range of quasi-elastic scattering. In particular, the study focuses on the neutral-current elastic (anti)neutrino scattering off nucleons described by the exotic reactions  $\nu_\alpha(\bar{\nu}_\alpha) + n \rightarrow \nu_\beta(\bar{\nu}_\beta) + n$  and  $\nu_\alpha(\bar{\nu}_\alpha) + p \rightarrow \nu_\beta(\bar{\nu}_\beta) + p$ , which provide corrections to the dominant Standard Model processes. In this context, it is shown that the required exotic nucleon form factors may have a significant impact on the relevant cross sections. Besides cross sections, the event rate is expected to be rather sensitive to the magnitude of the lepton-flavour violating parameters resulting in an excess of events. The overlap of nonstandard interactions and strange quark contributions, in the region of few GeV neutrino energies, is also examined. The formalism is applied for the case of the relevant neutrino-nucleon scattering experiments (LSND, MiniBooNE, etc.) and motivates the notion that such facilities have high potential to probe NSI.

## 1. Introduction

Neutrinos are among the most elusive particles in nature and in order to investigate their properties [1, 2] various terrestrial detectors have been built [3]. These ghostly particles fill the whole universe and reach Earth coming from the sun (solar neutrinos), from supernova explosions (supernova neutrinos), and from many other celestial objects (e.g., black hole binary stars, active galactic nuclei) [4]. The majority of them pass through Earth and through the nuclear detectors, designed for such purposes, without leaving any trace or signal [5]. This is mostly due to the fact that neutrinos interact very weakly with matter [6, 7]. For the investigation of neutrino-matter scattering, it is feasible to employ powerful accelerators operating at major laboratories such as Fermilab, J-Park, and CERN. These facilities can produce intensive neutrino beams of which a tiny fraction can be detected by novel detectors placed in the beam line (e.g., COHERENT experiment at Oak Ridge [8], TEXONO experiment in Taiwan [9],  $\nu$ GeN [10] and GEMMA [11] experiments in Russia, and CONNIE project in Brazil [12, 13]).

On the theoretical side, phenomenological models within and beyond the standard electroweak theory come out with

theoretical predictions for many aspects of neutrinos in trying to understand their properties and interactions [14] and propose appropriate neutrino probes for extracting new experimental results [15–17]. Current important areas of research concern the neutrino masses [18], neutrino oscillations [19, 20], neutrino electromagnetic properties [21–25], and so forth, their role in the evolution of astrophysical sources such as the sun or supernovae [26–28], their impact on cosmology (e.g., in answering the question of the matter-antimatter asymmetry of the universe), and others.

The neutral-current elastic (NCE) and charged-current quasi-elastic (CCQE) scattering of neutrinos with nucleons and nuclei constitute examples of fundamental electroweak interactions within the Standard Model (SM) [29], which, despite their relative simplicity, are presently not well understood. The first attempts of experimentally measuring the cross sections of the latter processes resulted in a discrepancy [30–32] with the predictions of the widely used relativistic Fermi gas (RFG) model [33–37]. There has been much effort towards quantifying this disagreement (between theory and experiment), mainly in terms of the nucleon electromagnetic form factors at intermediate energies [38, 39], while other

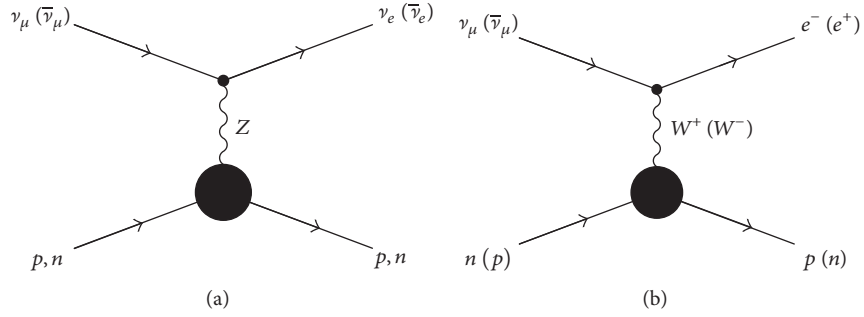


FIGURE 1: Diagrams of nonstandard neutrino-nucleon interactions for neutral-current (a) and charged-current (b) processes.

works focus on the study of the potential contribution of the strange components of the hadronic current [40–43].

Over a decade ago, an anomalous excess of events has been reported by the LSND experiment in searching for  $\nu_\mu \rightarrow \nu_e$  oscillations [44]. Recently, in the MiniBooNE neutrino-nucleon scattering experiment, an unexplained excess of electron-like events,  $\Delta N = 128.8 \pm 20.4 \pm 38.3$ , has been observed in the reconstructed neutrino energy range  $200 \leq E_\nu \leq 475$  MeV [45–49]. To interpret these data, some authors [50] argued that the RFG model is insufficient to accurately describe the neutrino-nucleon interaction in nuclei embedded in dense media [50], while other authors paid special attention to the final state interaction (FSI) effects [51–53]. Furthermore, this anomaly has triggered the intense theoretical interest and towards its explanation several models have been proposed [54, 55] including also those addressing heavy Dirac or Majorana neutrino decay [56, 57], the existence of sterile neutrinos [58], and others.

Historically, nucleons and nuclear systems have been extensively employed [59, 60] as microlaboratories for exploring open neutrino properties through charged- [61] and neutral-current interaction processes [62]. The latter involve both the vector and the axial vector components of the weak interactions [63, 64]. Thus, such probes are helpful for investigating the fundamental interactions of neutrinos with other elementary particles at low, intermediate, and high energies [65]. For the case of neutral-current coherent elastic neutrino scattering off complex nuclei, a detailed analysis focusing on possible alterations of the expected event rates due to the existence of nonstandard interactions (NSI) was performed in our previous works [66–68].

Motivated by the latter, in this paper, we explore the possibility of probing exotic neutrino processes in the relevant experiments. Thus, within the framework of NSI [69] (for a review, see [70, 71]), we consider the NCE scattering of the following neutrino-nucleon reactions:

$$\nu_\alpha (\bar{\nu}_\alpha) + n \longrightarrow \nu_\beta (\bar{\nu}_\beta) + n, \quad (1)$$

$$\nu_\alpha (\bar{\nu}_\alpha) + p \longrightarrow \nu_\beta (\bar{\nu}_\beta) + p, \quad (2)$$

where  $\alpha, \beta = \{e, \mu, \tau\}$  denote the neutrino flavour. Specifically, for the case of the MiniBooNE processes, we concentrate on the channels where  $\alpha = \mu$  and  $\beta = e$  (for NSI

scattering involving tau neutrinos, see [72, 73]). In the present study, the magnitude of the proposed novel interactions is given in terms of the adopted NSI nucleon form factors as functions of the four-momentum transfer. In our effort to explore potential NSI neutrino-nucleon interactions, as a first step, we focus only on the NSI Feynman diagrams depicted in Figure 1 where, for completeness, the corresponding diagrams involving charged-current (CC) processes are also included.

## 2. Neutral-Current Nonstandard Neutrino-Nucleon Interactions

In the present work, the assumed NSI operators are effective four-fermion operators of the form [70]

$$\mathcal{O} = (\bar{f}_1 \gamma^\mu P f_2) (\bar{f}_3 \gamma_\mu P f_4) + \text{h.c.}, \quad (3)$$

with  $f_i$ ,  $i = 1, 2, 3, 4$  being the SM fermion fields and  $P = \{L, R\}$  denoting left- and right-handed projectors. Specifically, for neutral currents, one has neutrino-induced NSI with matter of the form [69]

$$\mathcal{O}_{\alpha\beta}^{fP} = (\bar{\nu}_\alpha \gamma^\mu L \nu_\beta) (\bar{f} \gamma_\mu P f) + \text{h.c.}, \quad (4)$$

with  $f$  denoting a first-generation quark  $q = \{u, d\}$ .

**2.1. Neutrino-Nucleon Cross Sections within and beyond the SM.** The calculations of the neutrino-nucleon cross sections start by writing down the nucleon matrix elements of processes (1) and (2) in the usual  $V - A$  form, as

$$\begin{aligned} \mathcal{M} &= \frac{iG_F}{2\sqrt{2}} j_\mu \langle \mathcal{N} | J_Z^\mu | \mathcal{N} \rangle \\ &= \frac{iG_F}{2\sqrt{2}} \bar{\nu}_\alpha \gamma_\mu (1 - \gamma_5) \nu_\beta \langle \mathcal{N} | J_Z^\mu | \mathcal{N} \rangle, \end{aligned} \quad (5)$$

where  $j_\mu$  denotes the leptonic neutral current,  $G_F$  is the Fermi coupling constant, and  $|\mathcal{N}\rangle$  represents the nucleon wavefunction. In the latter expression,  $\langle \mathcal{N} | J_Z^\mu | \mathcal{N} \rangle$  is the hadronic matrix element that is (after neglecting the second-class

currents and the contribution of pseudoscalar component) expressed in terms of the known nucleon form factors as [7]

$$\begin{aligned} \langle \mathcal{N} | J_Z^\mu | \mathcal{N} \rangle = & \left\langle \mathcal{N} \left| F_1^{\text{NC};p(n)}(Q^2) \right. \right. \\ & \left. \left. + F_2^{\text{NC};p(n)}(Q^2) \frac{i\sigma^{\mu\nu} q_\nu}{2m_{\mathcal{N}}} + F_A^{\text{NC};p(n)}(Q^2) \gamma^\mu \gamma^5 \right| \mathcal{N} \right\rangle. \end{aligned} \quad (6)$$

In (6),  $F_1^{\text{NC};p(n)}(Q^2)$ ,  $F_2^{\text{NC};p(n)}(Q^2)$ , and  $F_A^{\text{NC};p(n)}(Q^2)$  stand for the Dirac, Pauli, and axial vector weak neutral-current form factors, respectively, for protons ( $p$ ) or neutrons ( $n$ ) [1].

Relying on the above nucleon matrix elements, within the relativistic Fermi gas (RFG) model, the SM differential cross section of reactions (1) and (2) for incoming (anti)neutrino energy  $E_\nu$  has been written as [29]

$$\frac{d\sigma}{dQ^2} = \frac{G_F^2 Q^2}{2\pi E_\nu^2} [A(Q^2) \pm B(Q^2)W + C(Q^2)W^2]. \quad (7)$$

In the above expression, the plus (minus) sign accounts for neutrino (antineutrino) scattering while the momentum-dependent function,  $W(Q^2)$ , reads [41]

$$W = \frac{4E_\nu}{m_{\mathcal{N}}} - \frac{Q^2}{m_{\mathcal{N}}^2}, \quad (8)$$

where the four-momentum transfer is defined in terms of the nucleon recoil energy  $T_{\mathcal{N}}$ , as

$$q^2 = q_\mu q^\mu = -Q^2 = -2m_{\mathcal{N}}T_{\mathcal{N}}. \quad (9)$$

For the nucleon mass,  $m_{\mathcal{N}}$ , we assume the value  $m_p \approx m_n = m_{\mathcal{N}} = 0.938$  GeV.

Before proceeding to the cross sections calculations, for the reader's convenience, we provide below some significant details on the aforementioned expressions  $A$ ,  $B$ , and  $C$  that depend on the form factors  $F_i^{\text{NC};p(n)}$ ,  $i = 1, 2, A$ . The functions  $A(Q^2)$ ,  $B(Q^2)$ , and  $C(Q^2)$  are defined as [42]

$$\begin{aligned} A(Q^2) = & \frac{1}{4} \left\{ \left( F_A^{\text{NC};p(n)} \right)^2 (1 + \tau) \right. \\ & - \left[ \left( F_1^{\text{NC};p(n)} \right)^2 - \tau \left( F_2^{\text{NC};p(n)} \right)^2 \right] (1 - \tau) \\ & \left. + 4\tau F_1^{\text{NC};p(n)} F_2^{\text{NC};p(n)} \right\}, \\ B(Q^2) = & -\frac{1}{4} F_A^{\text{NC};p(n)} \left( F_1^{\text{NC};p(n)} + F_2^{\text{NC};p(n)} \right), \\ C(Q^2) = & \frac{m_{\mathcal{N}}^2}{16Q^2} I \left[ \left( F_A^{\text{NC};p(n)} \right)^2 + \left( F_1^{\text{NC};p(n)} \right)^2 \right. \\ & \left. + \tau \left( F_2^{\text{NC};p(n)} \right)^2 \right], \end{aligned} \quad (10)$$

where their explicit  $Q^2$  dependence has been suppressed and  $\tau = Q^2/4m_{\mathcal{N}}^2$ .

In principle, the electromagnetic Dirac and Pauli form factors are written in terms of the well-known electric (E) and magnetic (M) form factors as follows [1]:

$$\begin{aligned} F_1^{\text{EM};p(n)} &= \frac{G_E^{p(n)}(Q^2) + \tau G_M^{p(n)}(Q^2)}{1 + \tau}, \\ F_2^{\text{EM};p(n)} &= \frac{G_M^{p(n)}(Q^2) - \tau G_E^{p(n)}(Q^2)}{1 + \tau}. \end{aligned} \quad (11)$$

In this work, the magnetic form factors are parametrised as [39]

$$\frac{G_M^{p(n)}}{\mu_{p(n)}} = \frac{1 + a_{p(n),1}^M \tau}{1 + b_{p(n),1}^M \tau + b_{p(n),2}^M \tau^2 + b_{p(n),3}^M \tau^3}, \quad (12)$$

where  $\mu_{p(n)}$  denotes the proton (neutron) magnetic moment. The proton electric form factor in a similar manner can be cast in the form [26]

$$G_E^{p(n)} = \frac{1 + a_{p(n),1}^E \tau}{1 + b_{p(n),1}^E \tau + b_{p(n),2}^E \tau^2 + b_{p(n),3}^E \tau^3}, \quad (13)$$

(for the fit parameters,  $a_{p(n),j}^{\text{M(E)}}$  and  $b_{p(n),j}^{\text{M(E)}}$ ,  $j = 1, 2, 3$ , see [39]). The electric neutron form factor,  $G_E^n$ , is expressed through the Galster-like parametrisation, as

$$G_E^n(Q^2) = \frac{\lambda_1 \tau}{1 + \lambda_2 \tau} G_D(Q^2), \quad (14)$$

with  $\lambda_1 = 1.68$  and  $\lambda_2 = 3.63$ .

**2.2. NSI Nucleon Form Factors.** As it is well known, within the SM, the weak NC Dirac and Pauli form factors are written in terms of the electromagnetic current form factors  $F_i^{\text{EM}}$ ,  $i = 1, 2$  (assuming the conserved vector current (CVC) theory) [1]. In the present work, we furthermore consider additional contributions originating from NSI that enter through the vector-type form factors  $\varepsilon_{\mu e}^{qV}(Q^2)$ . In our parametrisation, the latter are written in terms of the fundamental NSI neutrino-quark couplings  $\varepsilon_{\mu e}^{uV}$  ( $\varepsilon_{\mu e}^{dV}$ ) for  $u$  ( $d$ ) quarks discussed in [66–68], and they take the form

$$\begin{aligned} \varepsilon_{\mu e}^{pV}(Q^2) &= (2\varepsilon_{\mu e}^{uV} + \varepsilon_{\mu e}^{dV}) G_D(Q^2), \\ \varepsilon_{\mu e}^{nV}(Q^2) &= (\varepsilon_{\mu e}^{uV} + 2\varepsilon_{\mu e}^{dV}) G_D(Q^2). \end{aligned} \quad (15)$$

In the spirit of previous studies which consider the strangeness of the nucleon [41, 42], the above NSI form factors may have the same momentum dependence as those of the SM ones. Thus, the function  $G_D(Q^2)$  is assumed to be of dipole type:

$$G_D = \left( 1 + \frac{Q^2}{M_V^2} \right)^{-2}, \quad (16)$$

(for the vector mass, a commonly used value is  $M_V = 0.843$  GeV). A dipole approximation for  $G_D(Q^2)$ , apart from

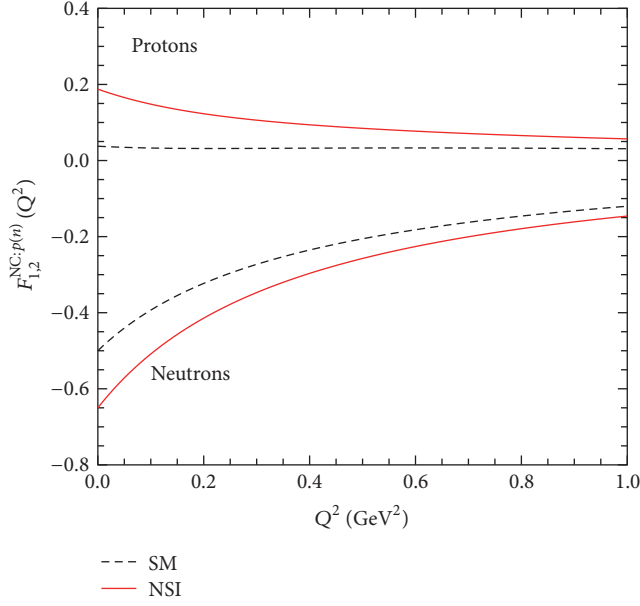


FIGURE 2: Comparison of the SM and NSI nucleon form factors employed in the present study (for details, see the text).

providing the appropriate momentum dependence, ensures also that the event rate coming out of NSI has the correct behaviour at high energies [40].

Then, the weak neutral-current nucleon form factors for protons (plus sign) and neutrons (minus sign) employed in our present calculations read

$$\begin{aligned}
 F_{1,2}^{\text{NC}:p(n)}(Q^2) &= \frac{\tau_3}{2} [F_{1,2}^{\text{EM}:p}(Q^2) - F_{1,2}^{\text{EM}:n}(Q^2)] \\
 &\quad - 2\sin^2\theta_W F_{1,2}^{\text{EM}:p(n)}(Q^2) \\
 &\quad - \frac{1}{2} F_{1,2}^{s:p(n)}(Q^2) + \tau_3 \epsilon_{\mu e}^{p(n)V}(Q^2).
 \end{aligned} \tag{17}$$

In the latter expression, the isoscalar form factors  $F_{1,2}^{s:p(n)}$  account for potential contributions to the electric charge and the magnetic moment of the nucleon due to the presence of strange quarks (in our convention, the isospin index  $\tau_3$  is +1 for proton and -1 for neutron scattering). However, throughout our calculations, on the basis of the recent results from the HAPPEX experiment [43], we take  $F_{1,2}^{s:p(n)} = 0$  (see also [52]). Note that, for low momentum transfer, the form factors discussed in [66, 67] are recovered. The effect of NSI on the form factors is illustrated graphically in Figure 2, where typical values have been adopted for the NSI parameters; that is,  $\epsilon_{\mu e}^{uV} = \epsilon_{\mu e}^{dV} = 0.05$  (apparently strange quark contributions have no impact in this case). Within the present formalism, the new nucleon form factors are rather sensitive to NSI, even for small values of the fundamental model parameters, especially for low momentum transfer.

For the case of the axial form factor  $F_A^{\text{NC}:p(n)}$ , we correspondingly employed [61]

$$F_A^{\text{NC}:p(n)}(Q^2) = \frac{1}{2} (\tau_3 g_A + g_A^s) \left(1 + \frac{Q^2}{M_A^2}\right)^{-2}. \tag{18}$$

Here, we used the static axial vector coupling,  $g_A = -1.267$  (it is determined usually through neutron beta decay). For the strange quark contribution to the nucleon spin, we adopt the static value  $2F_A^s(0) = g_A^s \pm 0.07$  with  $g_A^s = -0.15$ , while for the axial mass we take  $M_A = 1.049$  GeV (i.e., fit II of [41]). As has been recently discussed in [54], this set of values is fully compatible with the MiniBooNE data, even though a large value of  $M_A = 1.35$  GeV was reported in [47]. Furthermore, for simplicity, potential axial NSI form factors are neglected.

### 3. Results and Discussion

At first, we calculate the differential cross sections of (7) for the SM ( $\alpha = \beta$ ) weak NC elastic scattering processes (1) and (2) as well as for the NSI ones ( $\alpha \neq \beta$ ), based on (15)–(18) (neglecting potential strange quark contributions, i.e.,  $F_{1,2}^{s:p(n)} = 0$  and  $g_A^s = 0$ ). The corresponding results are demonstrated in Figure 3 for  $\nu p \rightarrow \nu p$  scattering (a) and  $\nu n \rightarrow \nu n$  scattering (b). For the sake of comparison, the bands of axial vector strange quark contributions calculated within  $g_A^s \pm 0.07$  and those of NSI contributions within the range  $\epsilon_{\mu e}^{qV} = (-0.05, 0.05)$  with  $q = \{u, d\}$  are also depicted. One sees that the resulting strange quark contributions indicate almost equal cross sections for proton and neutron scattering, while the presence of NSI leads to an enhancement of the cross sections for both  $\nu p \rightarrow \nu p$  and  $\nu n \rightarrow \nu n$  scattering channels, which becomes more important at lower energies.

From the perspective of experimental physics, it is crucial to reduce most of the background as well as beam related and systematic uncertainties. Therefore, a rather advantageous way towards determining the strange or NSI parameters is to perform measurements of the ratio of the NCE cross sections:

$$R = \frac{d\sigma_p/dQ^2}{d\sigma_n/dQ^2}. \tag{19}$$

In this context, Figure 4 illustrates a comparison of the obtained bands for the ratio  $R$  assuming neutrino-nucleon scattering in the presence of strange quarks or potential NSI. One notices that  $R$  varies between 0.75 and 1.20 when axial vector strange quark contributions are taken into account, while for the case of NSI the ratio is significantly lower; that is, it lies between 0.55 and 0.8. It is furthermore shown that, unlike the strange quark case, the SM result for  $R$  lies within the predicted NSI band.

Focusing on the relevant experiments, in order to perform reliable calculations, important effects that originate from the Pauli principle must be taken into account (Fermi motion of the initial nucleons). Specifically, for the case of nucleons bound in nuclear matter, within the Fermi gas model, it is adequate to multiply the free cross section given in (7) with a suppression factor  $S(Q^2)$ . The latter accounts for the

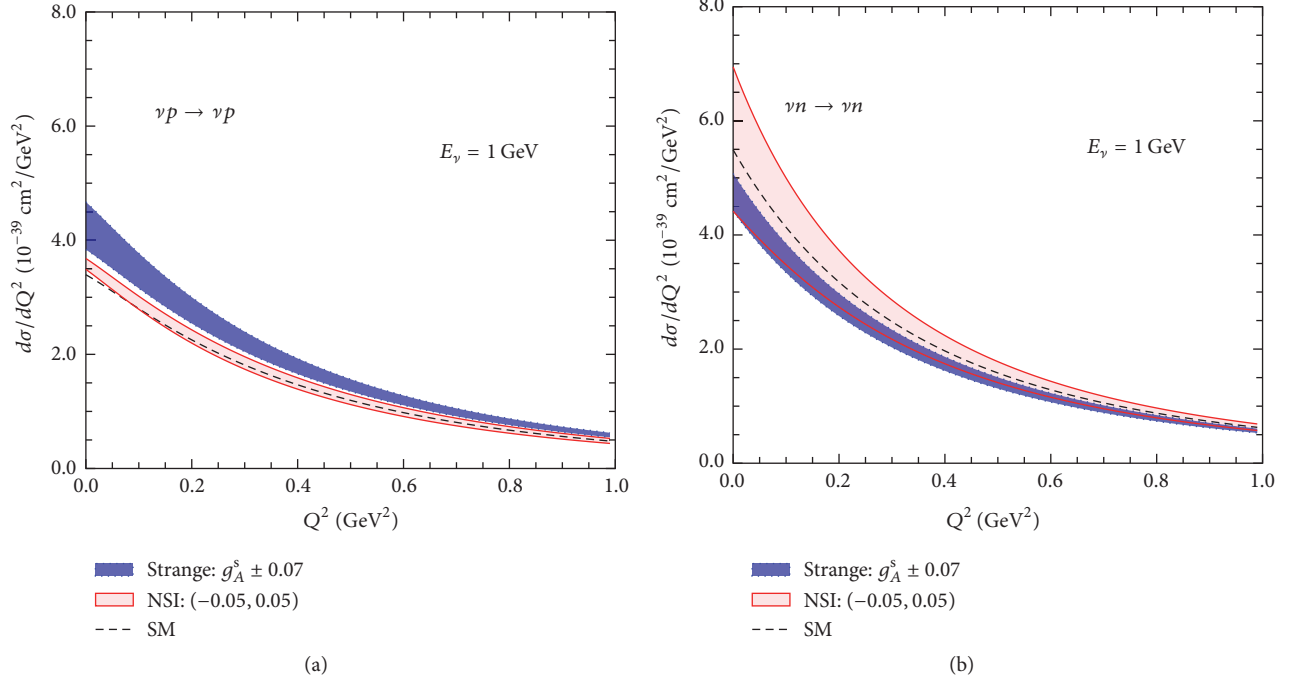


FIGURE 3: Differential cross section with respect to the momentum transfer for SM, strange quark, and NSI, for  $\nu p \rightarrow \nu p$ (a) and  $\nu n \rightarrow \nu n$  scattering (b). For details, see the text.

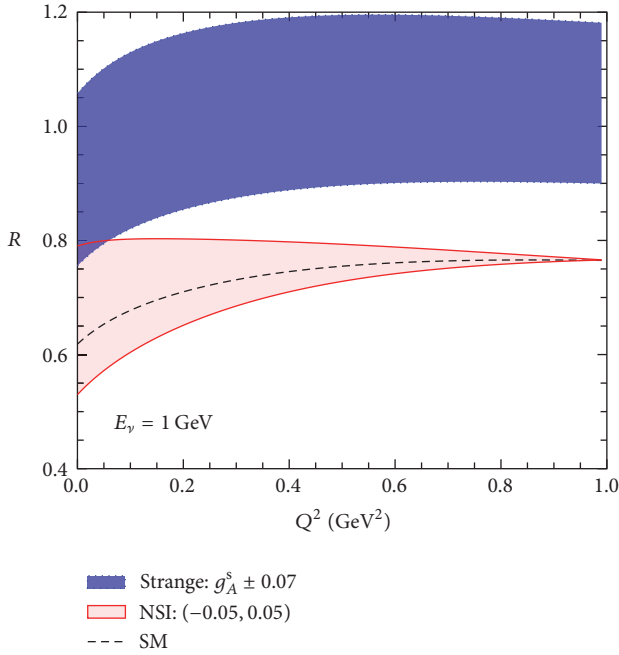


FIGURE 4: Momentum variation of the cross sections ratio for SM, strange quark, and NSI neutrino-nucleon scattering.

Pauli blocking effect on the final nucleons in a local density approximation [62] and is given by the expression [29]

$$S(Q^2) = 1 - \frac{D(Q^2)}{N}, \quad (20)$$

where  $N$  is the number of neutrons of the nuclear target. Assuming a carbon target,  $^{12}\text{C}$ ,  $D(Q^2)$  takes the form

$$D(Q^2) = \begin{cases} \frac{A}{2} \left[ 1 - \frac{3|\mathbf{q}|}{4p_F} + \frac{1}{24} \left( \frac{|\mathbf{q}|}{p_F} \right)^3 \right], & |\mathbf{q}| < 2p_F, \\ 0, & |\mathbf{q}| > 2p_F, \end{cases} \quad (21)$$

with the Fermi momentum  $p_F = 0.220 \text{ GeV}$  (for its definition, see [61, 65]) and  $|\mathbf{q}|$  being the magnitude of the three-momentum transfer. Within this framework, the total cross section may be evaluated through numerical integration of the differential cross section (7) as

$$\sigma(E_\nu) = \int_0^{Q_{\max}^2(E_\nu)} S(Q^2) \frac{d\sigma}{dQ^2} dQ^2. \quad (22)$$

For NCE scattering, the kinematics of the process provide the approximate upper limit of the momentum transfer  $Q^2$ , as

$$Q_{\max}^2(E_\nu) = \frac{4m_N E_\nu^2}{m_N + 2E_\nu}. \quad (23)$$

The obtained results are demonstrated in Figure 5 for protons and in Figure 6 for neutrons for the case of (i) free nucleon scattering, that is, on a hydrogen atom (a), and (ii) medium scattering, that is, for bound nucleons within a carbon atom (b). As expected, for both SM and NSI, the obtained integrated cross section for the  $\nu n$  process is much larger than that of the  $\nu p$  reaction. Apparently, one also notices that

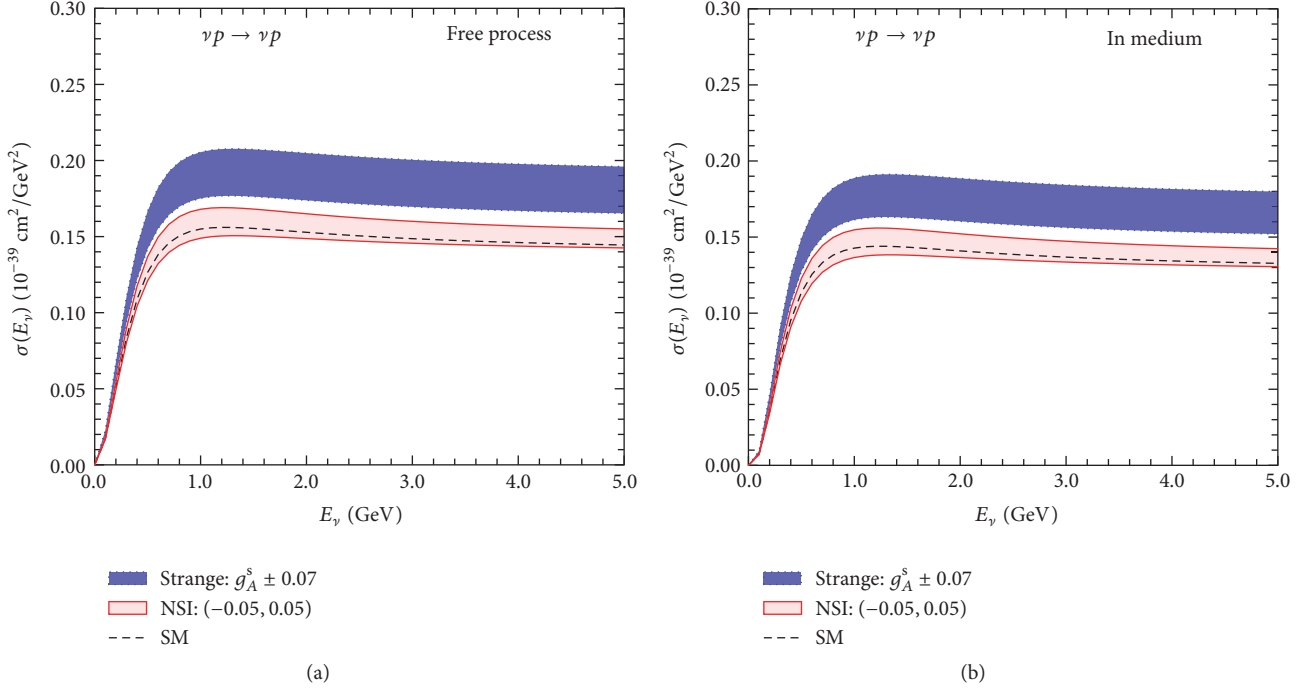


FIGURE 5: Total integrated  $\nu p \rightarrow \nu p$  scattering cross section as a function of the incoming neutrino energy due to SM, strange quark, and NSI scattering. The results refer to scattering on free protons (a) and scattering on bound protons, that is, assuming nuclear effects, at a  $^{12}\text{C}$  detector (b).

the NCE cross sections, for both  $\nu p \rightarrow \nu p$  and  $\nu n \rightarrow \nu n$  scattering channels, are enhanced when potential nonzero NSI are assumed. For the case of neutrino-proton scattering, the considered axial vector strange quark effects dominate the total cross section. On the other hand, focusing on neutrino-neutron scattering, the assumed strangeness of the nucleon leads to suppression of the total cross section. Eventually, we find that the resulting strange quark and NSI bands overlap only for  $\nu n$  processes.

At this point, we find it interesting to focus our discussion on the MiniBooNE experiment and apply the addressed NSI model. Thus, by convoluting the energy distribution of the MiniBooNE neutrino beam with the NSI cross section of (7), we evaluate the flux-integrated differential NSI neutrino-nucleon cross sections  $\langle d\sigma_{p,n}/dT_{p,n} \rangle$ , through the expression

$$\left\langle \frac{d\sigma_{p,n}}{dT_{p,n}} \right\rangle = \int s(Q^2) \frac{d\sigma}{dQ^2}(E_\nu, Q^2) \Phi_\nu(E_\nu) \cdot \delta\left(\frac{Q^2}{2m_{\mathcal{N}}} - T_{p,n}\right) dE_\nu dQ^2, \quad (24)$$

where the utilised muon neutrino flux,  $\Phi_\nu(E_\nu)$ , is normalised to unity. The results are illustrated in Figure 7, where it is clearly shown that the nuclear effects become important at low recoil energies. More specifically, for NCE scattering on free nucleons (e.g., for a hydrogen target), the cross section is significantly larger and constantly increasing for low nucleon recoil energies. On the contrary, for the case of bound nucleons within the carbon target material,  $^{12}\text{C}$ , the

behaviour of the cross section changes drastically at low recoil energies and its value minimises for energies  $\leq 100$  MeV. As for the total integrated cross sections discussed previously, our results show an overlap between the obtained strange quark and NSI bands only for the processes involving  $\nu n \rightarrow \nu n$  scattering.

We finally test the compatibility of the employed NSI scenario with recent results from the LSND and MiniBooNE experiments. To this aim, concentrating on neutrino-nucleon scattering on a mineral oil ( $\text{CH}_2$ ), the folded differential cross section reads [47]

$$\left\langle \frac{d\sigma_{\mathcal{N}}}{dT_{\mathcal{N}}} \right\rangle = \frac{1}{7} \left\langle \frac{d\sigma_p^H}{dT_p} \right\rangle + \frac{3}{7} \left\langle \frac{d\sigma_p^C}{dT_p} \right\rangle + \frac{3}{7} \left\langle \frac{d\sigma_n^C}{dT_n} \right\rangle. \quad (25)$$

Then, we evaluate the number of conventional and NSI events as a function of the nucleon recoil energy,  $T_{\mathcal{N}}$ , by assuming a  $\text{CH}_2$  detector (i.e., the detector material of the LSND and MiniBooNE experiments) through the expression

$$N_{\text{events}} = a(T_{\mathcal{N}}) \int \mathcal{N}_N N_{\text{POT}} \left\langle \frac{d\sigma_{\mathcal{N}}}{dT_{\mathcal{N}}} \right\rangle dT_{\mathcal{N}}. \quad (26)$$

In order to confront our present results with the recent MiniBooNE data, we assumed the following experimental quantities: the utilised muon neutrino flux,  $\Phi_\nu(E_\nu)$ , is normalised to the protons on target (POT) with  $N_{\text{POT}}$  denoting

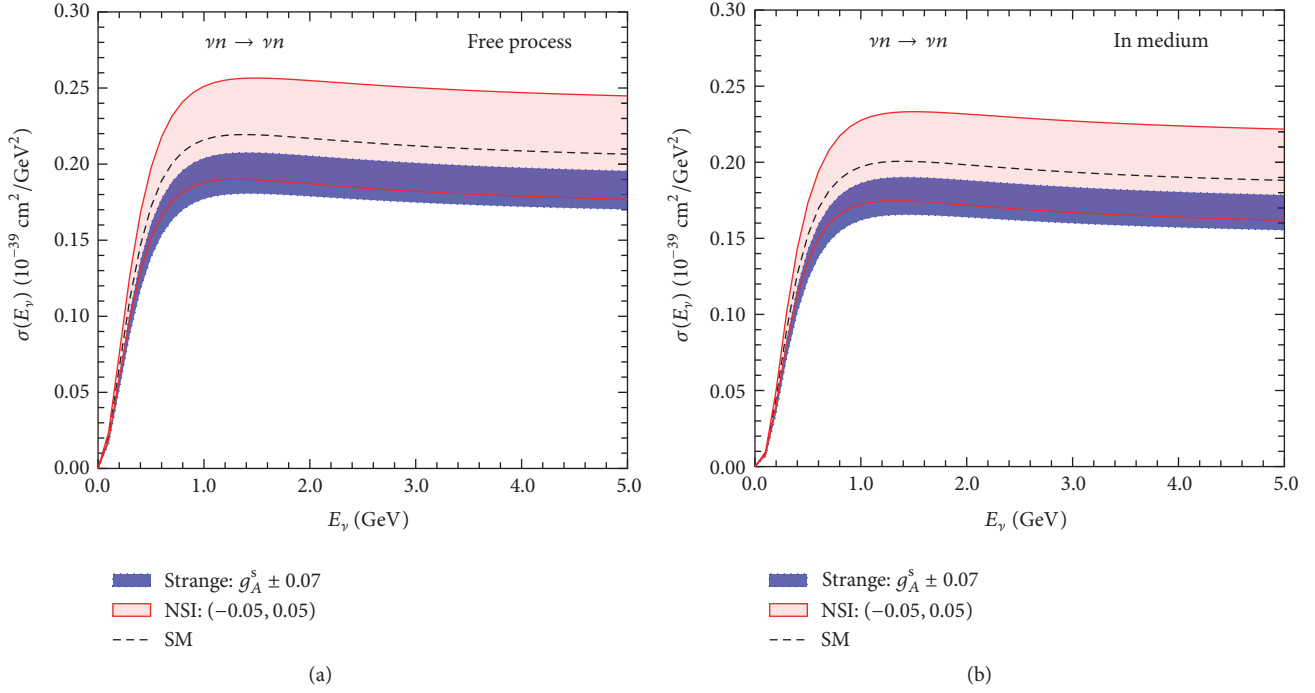
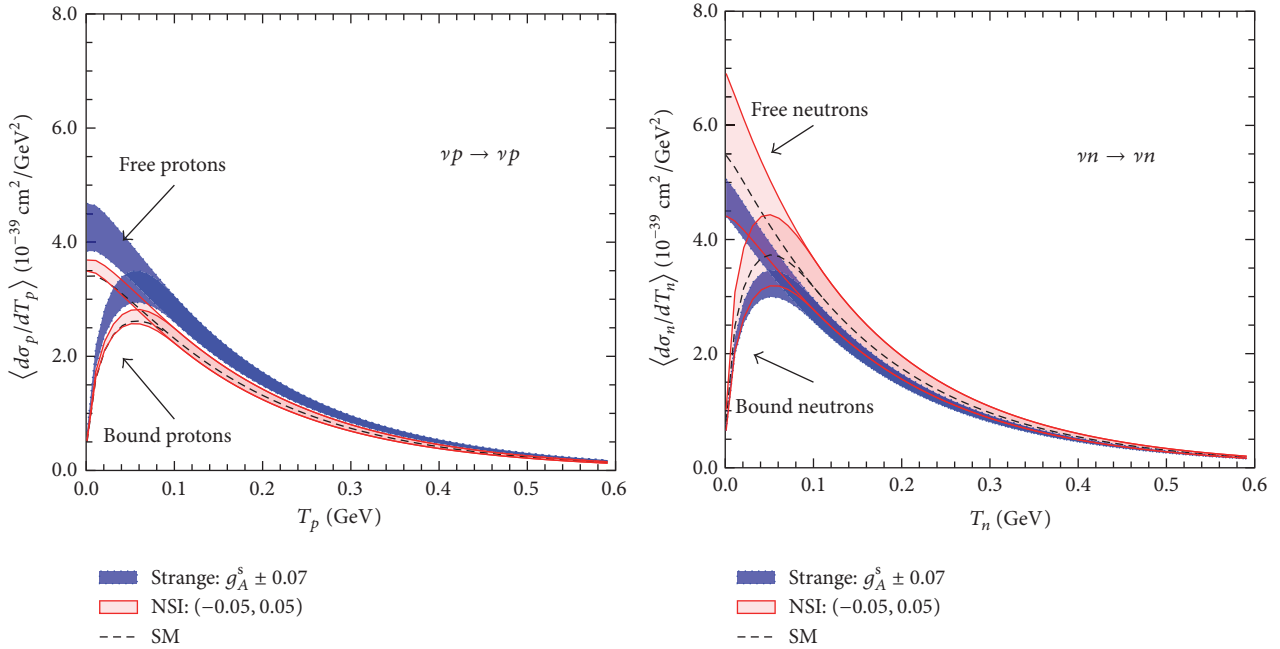

 FIGURE 6: Same as Figure 5 but for  $\gamma n \rightarrow \gamma n$  scattering.


FIGURE 7: Differential cross section as a function of the nucleon (proton or neutron) recoil energy due to SM, strange quark, and NSI. Modifications due to the employed nuclear effects are illustrated and compared with the case of scattering on free nucleons.

the number of POT in the data [46] and  $a(T_{\mathcal{N}})$  denoting the detector efficiency taken from [49]. The number of nucleon targets in the detector is evaluated as  $\mathcal{N}_N = N_A(4/3)\pi R^3 \rho_{\text{oil}}$ , where the density of mineral oil is  $\rho_{\text{oil}} = 0.845 \text{ gr/cm}^3$  at  $20^\circ\text{C}$  [48] and  $N_A$  is Avogadro's number. The fiducial volume cut of the detector is adopted from [47]. Figure 8 illustrates the number of events as a function of the nucleon kinetic

energy,  $T_{\mathcal{N}}$ , obtained within the context of the SM, as well as by assuming potential contributions to the rate arising from strange quarks or NSI (for a comparison with the MiniBooNE experimental results, see [47]). The obtained excess of events becomes significant for low recoil energies, reflecting the dipole character of the form factor  $G_D(Q^2)$  that enters the definition of the NSI nucleon form factors given in (15).

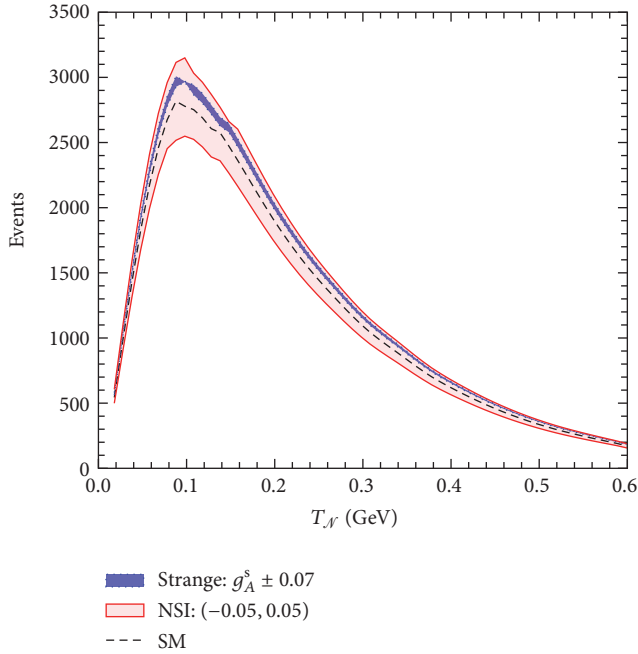


FIGURE 8: Expected number of events as a function of the nucleon recoil energy  $T_N$  assuming contributions due to the SM, strange quark, and NSI.

Motivated by our previous studies, we consider it interesting to estimate the sensitivity of MiniBooNE to nonstandard interactions, through a  $\chi^2$  fit analysis. By varying one NSI coupling at a time and by neglecting potential strange quark contributions, the minimisation of the  $\chi^2(\epsilon_{\mu e}^{uV})$  function provides constraints on the NSI parameters of the order of  $\epsilon_{\mu e}^{dV} \approx \epsilon_{\mu e}^{dV} = 0.05$ . Furthermore, in order to explore the overlap of strange quark and NSI contributions that enter the NCE scattering cross section of (7), a two-parameter combined analysis is performed. By simultaneously varying the strange quark  $g_A^s$  and NSI  $\epsilon_{\mu e}^{uV}$  (setting  $\epsilon_{\mu e}^{dV} = 0$ ) parameters, the minimisation of  $\chi^2(\epsilon_{\mu e}^{uV}, \Delta s)$  yields the contours in the parameter space  $(\epsilon_{\mu e}^{uV} - \Delta s)$  shown in Figure 9, at 68%, 90%, and 99% CL. These results indicate strongly that current neutrino-nucleon experiments are favourable facilities to provide new insights and to put severe bounds on nonstandard interaction parameters.

#### 4. Summary and Conclusions

In the present work, focusing on the NCE neutrino-nucleon scattering, potential corrections to the SM cross sections that arise from strange quark contributions and nonstandard neutrino-nucleon interactions are comprehensively investigated. In this context, the possibility of probing the relevant model parameters is explored. Furthermore, special effort has been devoted towards exploring the overlap of possible contributions due to strange quarks and NSI. The study involves reliable calculations of the differential and total neutrino-nucleon cross sections by taking into account

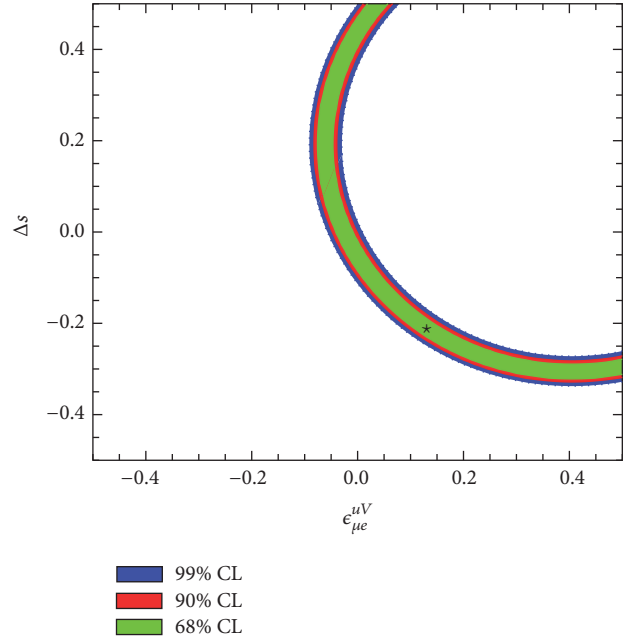


FIGURE 9: Allowed region in the  $(\epsilon_{\mu e}^{uV} - \Delta s)$  plane at MiniBooNE. The best fit point is shown by  $\star$ .

important nuclear effects such as the Pauli blocking. Within this framework, the NSI contributions originate from the respective nucleon form factors and adopt dipole momentum dependence, while the corresponding cross sections are rather sensitive to the magnitude of the NSI. The latter have a significant impact on the expected number of NCE neutrino-nucleon events and lead to an enhancement of the rate, which may be detectable by the relevant experiments (e.g., MiniBooNE), even for small values of the flavour changing parameters. It is furthermore shown that possible measurements of the ratio of the NSI cross sections for the  $\nu p$  process over the  $\nu n$  one offer a unique research path to probe NSI.

We stress, however, that the above results refer to forward NSI scattering and thus they do not reproduce accurately the reported MiniBooNE anomaly where an isotropic excess of events was found coming either from electrons or from converted photons. In addition, the NSI contribution would be small if the “standard” value of possible NSI contributions is chosen. Moreover, in this case, the recoiling protons within the mineral oil are likely to have velocity below the Cherenkov threshold and therefore cannot reproduce the Cherenkov ring. On the other hand, the presence of potential nonstandard neutrino-nucleon events may be compatible with the LSND anomaly which did not rely on Cherenkov radiation.

#### Competing Interests

The authors declare that there are no competing interests regarding the publication of this paper.

## Acknowledgments

The authors are grateful to Professor S. N. Gninenko for stimulating discussions.

## References

- [1] W. M. Alberico, S. M. Bilenky, and C. Maieron, “Strangeness in the nucleon: neutrino—nucleon and polarized electron—nucleon scattering,” *Physics Reports*, vol. 358, no. 4, pp. 227–308, 2002.
- [2] J. G. Morfín, J. Nieves, and J. T. Sobczyk, “Recent developments in neutrino/antineutrino-nucleus interactions,” *Advances in High Energy Physics*, vol. 2012, Article ID 934597, 2012.
- [3] K. Abe, Y. Hayato, T. Iida et al., “Solar neutrino results in Super-Kamiokande-III,” *Physical Review D*, vol. 83, no. 5, Article ID 052010, 19 pages, 2011.
- [4] T. Smpsonias and O. T. Kosmas, “High energy neutrino emission from astrophysical jets in the Galaxy,” *Advances in High Energy Physics*, vol. 2015, Article ID 921757, 7 pages, 2015.
- [5] K. G. Balasi, K. Langanke, and G. Martínez-Pinedo, “Neutrino-nucleus reactions and their role for supernova dynamics and nucleosynthesis,” *Progress in Particle and Nuclear Physics*, vol. 85, pp. 33–81, 2015.
- [6] J. W. F. Valle and J. C. Romao, “Neutrinos in high energy and astroparticle physics,” in *Physics Textbook*, Wiley-VCH, Weinheim, Germany, 2015.
- [7] T. S. Kosmas and E. Oset, “Charged current neutrino nucleus reaction cross-sections at intermediate-energies,” *Physical Review C*, vol. 53, no. 3, pp. 1409–1415, 1996.
- [8] D. Akimov, P. An, C. Awe et al., “The COHERENT experiment at the spallation neutron source,” <https://arxiv.org/abs/1509.08702>.
- [9] S. Kerman, V. Sharma, M. Deniz et al., “Coherency in neutrino-nucleus elastic scattering,” *Physical Review D*, vol. 93, no. 11, Article ID 113006, 2016.
- [10] V. Belov, V. Brudanin, V. Egorov et al., “The  $\nu$ GeN experiment at the Kalinin Nuclear Power Plant,” *Journal of Instrumentation*, vol. 10, no. 12, p. P12011, 2015.
- [11] A. G. Beda, V. B. Brudanin, V. G. Egorov et al., “Gemma experiment: the results of neutrino magnetic moment search,” *Physics of Particles and Nuclei Letters*, vol. 10, no. 2, pp. 139–143, 2013.
- [12] G. Fernandez Moroni, J. Estrada, E. E. Paolini, G. Cancelo, J. Tiffenberg, and J. Molina, “Charge coupled devices for detection of coherent neutrino-nucleus scattering,” *Physical Review D*, vol. 91, no. 7, Article ID 072001, 2015.
- [13] A. Aguilar-Arevalo, X. Bertou, C. Bonifazi et al., “Results of the engineering run of the Coherent Neutrino Nucleus Interaction Experiment (CONNIE),” *Journal of Instrumentation*, vol. 11, no. 7, Article ID P07024, 2016.
- [14] J. Schechter and J. W. F. Valle, “Majorana neutrinos and magnetic fields,” *Physical Review D*, vol. 24, pp. 1883–1889, 1981, Erratum: *Physical Review D*, vol. 25, article 283, 1982.
- [15] T. S. Kosmas and J. D. Vergados, “Sum rules for the inclusive  $\mu$ -e conversion exotic reaction,” *Physics Letters B*, vol. 217, no. 1-2, pp. 19–24, 1989.
- [16] T. S. Kosmas, O. G. Miranda, D. K. Papoulias, M. Tórtola, and J. W. F. Valle, “Probing neutrino magnetic moments at the Spallation Neutron Source facility,” *Physical Review D*, vol. 92, no. 1, Article ID 013011, 2015.
- [17] T. S. Kosmas, O. G. Miranda, D. K. Papoulias, M. Tórtola, and J. W. F. Valle, “Sensitivities to neutrino electromagnetic properties at the TEXONO experiment,” *Physics Letters, Section B: Nuclear, Elementary Particle and High-Energy Physics*, vol. 750, pp. 459–465, 2015.
- [18] S. M. Boucenna, S. Morisi, and J. W. F. Valle, “The low-scale approach to neutrino masses,” *Advances in High Energy Physics*, vol. 2014, Article ID 831598, 15 pages, 2014.
- [19] D. V. Forero, M. Tórtola, and J. W. F. Valle, “Global status of neutrino oscillation parameters after Neutrino-2012,” *Physical Review D*, vol. 86, no. 7, Article ID 073012, 2012.
- [20] D. Forero, M. Tórtola, and J. Valle, “Neutrino oscillations refitted,” *Physical Review D*, vol. 90, no. 9, 2014.
- [21] R. E. Shrock, “Electromagnetic properties and decays of Dirac and Majorana neutrinos in a general class of gauge theories,” *Nuclear Physics, Section B*, vol. 206, no. 3, pp. 359–379, 1982.
- [22] B. Kayser, “Majorana neutrinos and their electromagnetic properties,” *Physical Review D*, vol. 26, no. 7, pp. 1662–1670, 1982.
- [23] J. F. Nieves, “Electromagnetic properties of Majorana neutrinos,” *Physical Review D*, vol. 26, no. 11, pp. 3152–3158, 1982.
- [24] J. F. Beacom and P. Vogel, “Neutrino magnetic moments, flavor mixing, and the super-kamiokande solar data,” *Physical Review Letters*, vol. 83, no. 25-20, article 5222, 1999.
- [25] C. Broggin, C. Giunti, and A. Studenikin, “Electromagnetic properties of neutrinos,” *Advances in High Energy Physics*, vol. 2012, Article ID 459526, 47 pages, 2012.
- [26] K. G. Balasi, E. Ydrefors, and T. S. Kosmas, “Theoretical study of neutrino scattering off the stable even Mo isotopes at low and intermediate energies,” *Nuclear Physics A*, vol. 868-869, no. 1, pp. 82–98, 2011.
- [27] V. Tsakstara and T. S. Kosmas, “Low-energy neutral-current neutrino scattering on Te128,130 isotopes,” *Physical Review C - Nuclear Physics*, vol. 83, no. 5, Article ID 054612, 2011.
- [28] E. Ydrefors, K. G. Balasi, T. S. Kosmas, and J. Suhonen, “Detailed study of the neutral-current neutrino–nucleus scattering off the stable Mo isotopes,” *Nuclear Physics A*, vol. 896, pp. 1–23, 2012.
- [29] C. H. Llewellyn Smith, “Neutrino reactions at accelerator energies,” *Physics Reports*, vol. 3, no. 5, pp. 261–379, 1972.
- [30] D. Cline, A. Entenberg, W. Kozanecki et al., “Observation of elastic neutrino-proton scattering,” *Physical Review Letters*, vol. 37, pp. 252–255, 1976.
- [31] A. Entenberg, J. Horstkotte, W. Kozanecki et al., “Measurement of the elastic scattering of neutrinos and antineutrinos by protons,” *Physical Review Letters*, vol. 42, no. 18, pp. 1198–1201, 1979.
- [32] L. A. Ahrens, S. H. Aronson, P. L. Connolly et al., “Measurement of neutrino-proton and anti-neutrino-proton elastic scattering,” *Physical Review D*, vol. 35, no. 3, pp. 785–809, 1987.
- [33] R. A. Smith and E. J. Moniz, “Neutrino reactions on nuclear targets,” *Nuclear Physics B*, vol. 43, pp. 605–622, 1972, Erratum: *Nuclear Physics B*, vol. 101, pp. 547, 1975.
- [34] C. J. Horowitz, H. Kim, D. P. Murdock, and S. Pollock, “Neutrino-nucleus quasifree neutral current reactions and the nucleon strange quark content,” *Physical Review C*, vol. 48, no. 6, pp. 3078–3087, 1993.
- [35] M. B. Barbaro, A. De Pace, T. W. Donnelly, A. Molinari, and M. J. Musolf, “Probing nucleon strangeness with neutrinos: nuclear model dependences,” *Physical Review C—Nuclear Physics*, vol. 54, no. 4, pp. 1954–1969, 1996.
- [36] W. M. Alberico, M. B. Barbaro, S. M. Bilenky et al., “Inelastic neutrino and anti-neutrino scattering on nuclei and

- ‘strangeness’ of the nucleon,” *Nuclear Physics A*, vol. 623, pp. 471–497, 1997.
- [37] W. M. Alberico, M. B. Barbaro, S. M. Bilenky et al., “The ratio of p and n yields in NC neutrino (anti-neutrino) nucleus scattering and strange form-factors of the nucleon,” *Physics Letters B*, vol. 438, no. 1-2, pp. 9–13, 1998.
- [38] F. J. Ernst, R. G. Sachs, and K. C. Wali, “Electromagnetic form factors of the nucleon,” *Physical Review*, vol. 119, no. 3, pp. 1105–1114, 1960.
- [39] W. M. Alberico, S. M. Bilenky, C. Giunti, and K. M. Graczyk, “Electromagnetic form factors of the nucleon: new fit and analysis of uncertainties,” *Physical Review C*, vol. 79, no. 6, Article ID 065204, 2009.
- [40] G. T. Garvey, S. Krewald, E. Kolbe, and K. Langanke, “Strange quark contributions to neutrino induced quasielastic scattering,” *Physics Letters B*, vol. 289, no. 3-4, pp. 249–254, 1992.
- [41] G. T. Garvey, W. C. Louis, and D. H. White, “Determination of proton strange form-factors from neutrino p elastic scattering,” *Physical Review C*, vol. 48, no. 2, p. 761, 1993.
- [42] G. Garvey, E. Kolbe, K. Langanke, and S. Krewald, “Role of strange quarks in quasielastic neutrino scattering,” *Physical Review C*, vol. 48, no. 4, pp. 1919–1925, 1993.
- [43] A. Acha, K. A. Aniol, D. S. Armstrong et al., “Precision measurements of the nucleon strange form factors at  $Q^{*2} \sim 0.1\text{--}1\text{ GeV}^{*2}$ ,” *Physical Review Letters*, vol. 98, Article ID 032301, 2007.
- [44] C. Athanassopoulos, R. L. Burman, L. B. Auerbach, and S. Yellin, “Evidence for  $\bar{\nu}_\mu \rightarrow \bar{\nu}_e$  Oscillations from the LSND experiment at the los alamos meson physics facility,” *Physical Review Letters*, vol. 77, no. 15, pp. 3082–3085, 1996.
- [45] A. A. Aguilar-Arevalo, C. E. Anderson, A. O. Bazarko et al., “Unexplained excess of electronlike events from a 1-GeV neutrino beam,” *Physical Review Letters*, vol. 102, no. 10, Article ID 101802, 2009.
- [46] A. A. Aguilar-Arevalo, C. E. Anderson, A. O. Bazarko et al., “First measurement of the muon neutrino charged current quasielastic double differential cross section,” *Physical Review D*, vol. 81, no. 9, Article ID 092005, 2010.
- [47] A. A. Aguilar-Arevalo, C. Anderson, A. Bazarko et al., “Measurement of the neutrino neutral-current elastic differential cross section on mineral oil at  $E_\nu \sim 1\text{ GeV}$ ,” *Physical Review D*, vol. 82, no. 9, Article ID 092005, 2010.
- [48] A. A. Aguilar-Arevalo, B. C. Brown, L. Bugel et al., “First measurement of the muon antineutrino double-differential charged-current quasielastic cross section,” *Physical Review D*, vol. 88, no. 3, Article ID 032001, 31 pages, 2013.
- [49] A. A. Aguilar-Arevalo, B. C. Brown, L. Bugel et al., “Measurement of the antineutrino neutral-current elastic differential cross section,” *Physical Review D*, vol. 91, no. 1, Article ID 012004, 12 pages, 2015.
- [50] B. Bhattacharya, R. J. Hill, and G. Paz, “Model-independent determination of the axial mass parameter in quasielastic neutrino-nucleon scattering,” *Physical Review D—Particles, Fields, Gravitation and Cosmology*, vol. 84, no. 7, Article ID 073006, 2011.
- [51] J. Nieves, J. E. Amaro, and M. Valverde, “Inclusive quasi-elastic neutrino reactions,” *Physical Review C*, vol. 70, no. 5, Article ID 055503, 2004, Erratum: *Physical Review C*, vol. 72, Article ID 019902, 2005.
- [52] J. Nieves, M. Valverde, and M. J. Vicente Vacas, “Inclusive nucleon emission induced by quasielastic neutrino-nucleus interactions,” *Physical Review C*, vol. 73, no. 2, Article ID 025504, 2006.
- [53] T. Golan, C. Juszczak, and J. T. Sobczyk, “Effects of final-state interactions in neutrino-nucleus interactions,” *Physical Review C—Nuclear Physics*, vol. 86, no. 1, Article ID 015505, 2012.
- [54] J. Nieves, I. Ruiz Simo, and M. J. Vicente Vacas, “The nucleon axial mass and the MiniBooNE quasielastic neutrino-nucleus scattering problem,” *Physics Letters B*, vol. 707, no. 1, pp. 72–75, 2012.
- [55] J. Nieves, I. R. Simo, and M. J. V. Vacas, “Inclusive charged-current neutrino-nucleus reactions,” *Physical Review C*, vol. 83, no. 4, Article ID 045501, 2011.
- [56] S. N. Gninenko, “MiniBooNE anomaly and heavy neutrino decay,” *Physical Review Letters*, vol. 103, no. 24, Article ID 241802, 2009.
- [57] S. N. Gninenko, “Resolution of puzzles from the LSND, KAR-MEN, and MiniBooNE experiments,” *Physical Review D*, vol. 83, no. 1, Article ID 015015, 2011.
- [58] S. N. Gninenko, “New limits on radiative sterile neutrino decays from a search for single photons in neutrino interactions,” *Physics Letters B*, vol. 710, no. 1, pp. 86–90, 2012.
- [59] T. S. Kosmas and J. D. Vergados, “Nuclear densities with fractional occupation probabilities of the states,” *Nuclear Physics A*, vol. 536, no. 1, pp. 72–86, 1992.
- [60] Y. Umino, J. M. Udias, and P. J. Mulders, “Exchange current corrections to neutrino-nucleus scattering,” *Physical Review Letters*, vol. 74, no. 25, pp. 4993–4996, 1995.
- [61] T. Leitner, O. Buss, L. Alvarez-Ruso, and U. Mosel, “Electron- and neutrino-nucleus scattering from the quasielastic to the resonance region,” *Physical Review C*, vol. 79, no. 3, Article ID 034601, 2009.
- [62] T. Leitner, L. Alvarez-Ruso, and U. Mosel, “Neutral current neutrino-nucleus interactions at intermediate energies,” *Physical Review C*, vol. 74, no. 6, Article ID 065502, 2006.
- [63] P. G. Giannaka and T. S. Kosmas, “Electron capture cross sections for stellar nucleosynthesis,” *Advances in High Energy Physics*, vol. 2015, Article ID 398796, 11 pages, 2015.
- [64] P. G. Giannaka and T. S. Kosmas, “Detailed description of exclusive muon capture rates using realistic two-body forces,” *Physical Review C*, vol. 92, no. 1, Article ID 014606, 2015.
- [65] T. Leitner, L. Alvarez-Ruso, and U. Mosel, “Charged current neutrino-nucleus interactions at intermediate energies,” *Physical Review C*, vol. 73, no. 6, Article ID 065502, 2006.
- [66] D. K. Papoulias and T. S. Kosmas, “Nuclear aspects of neutral current non-standard  $\nu$ -nucleus reactions and the role of the exotic  $\mu^- \rightarrow e^-$  transitions experimental limits,” *Physics Letters, Section B: Nuclear, Elementary Particle and High-Energy Physics*, vol. 728, pp. 482–488, 2014.
- [67] D. K. Papoulias and T. S. Kosmas, “Standard and nonstandard neutrino-nucleus reactions cross sections and event rates to neutrino detection experiments,” *Advances in High Energy Physics*, vol. 2015, Article ID 763648, 17 pages, 2015.
- [68] D. K. Papoulias and T. S. Kosmas, “Neutrino transition magnetic moments within the non-standard neutrino-nucleus interactions,” *Physics Letters B*, vol. 747, pp. 454–459, 2015.
- [69] V. Barger, R. J. N. Phillips, and K. Whisnant, “Solar-neutrino solutions with matter-enhanced flavor-changing neutral-current scattering,” *Physical Review D*, vol. 44, no. 6, pp. 1629–1643, 1991.
- [70] T. Ohlsson, “Status of non-standard neutrino interactions,” *Reports on Progress in Physics*, vol. 76, no. 4, Article ID 044201, 2013.

- [71] O. G. Miranda and H. Nunokawa, “Non standard neutrino interactions: current status and future prospects,” *New Journal of Physics*, vol. 17, no. 9, Article ID 095002, 2015.
- [72] A. Rashed, M. Duraisamy, and A. Datta, “Nonstandard interactions of tau neutrino via charged Higgs and  $W'$  contribution,” *Physical Review D*, vol. 87, no. 1, Article ID 013002, 2013.
- [73] A. Rashed, P. Sharma, and A. Datta, “Tau-neutrino as a probe of nonstandard interaction,” *Nuclear Physics B*, vol. 877, no. 3, pp. 662–682, 2013.

## Research Article

# Nuclear Structure Calculations for Two-Neutrino Double- $\beta$ Decay

P. Sarriguren,<sup>1</sup> O. Moreno,<sup>2</sup> and E. Moya de Guerra<sup>2</sup>

<sup>1</sup>*Instituto de Estructura de la Materia, IEM-CSIC, Serrano 123, 28006 Madrid, Spain*

<sup>2</sup>*Departamento de Física Atómica, Molecular y Nuclear, Universidad Complutense de Madrid, 28040 Madrid, Spain*

Correspondence should be addressed to P. Sarriguren; p.sarriguren@csic.es

Received 17 June 2016; Revised 26 August 2016; Accepted 19 September 2016

Academic Editor: Theocharis Kosmas

Copyright © 2016 P. Sarriguren et al. This is an open access article distributed under the Creative Commons Attribution License, which permits unrestricted use, distribution, and reproduction in any medium, provided the original work is properly cited. The publication of this article was funded by SCOAP<sup>3</sup>.

We study the two-neutrino double- $\beta$  decay in  $^{76}\text{Ge}$ ,  $^{116}\text{Cd}$ ,  $^{128}\text{Te}$ ,  $^{130}\text{Te}$ , and  $^{150}\text{Nd}$ , as well as the two Gamow-Teller branches that connect the double- $\beta$  decay partners with the states in the intermediate nuclei. We use a theoretical microscopic approach based on a deformed self-consistent mean field with Skyrme interactions including pairing and spin-isospin residual forces, which are treated in a proton-neutron quasiparticle random-phase approximation. We compare our results for Gamow-Teller strength distributions with experimental information obtained from charge-exchange reactions. We also compare our results for the two-neutrino double- $\beta$  decay nuclear matrix elements with those extracted from the measured half-lives. Both single-state and low-lying-state dominance hypotheses are analyzed theoretically and experimentally making use of recent data from charge-exchange reactions and  $\beta$  decay of the intermediate nuclei.

## 1. Introduction

Double- $\beta$  decay is currently one of the most studied processes both theoretically and experimentally [1–5]. It is a rare weak-interaction process of second order taking place in cases where single  $\beta$  decay is energetically forbidden or strongly suppressed. It has a deep impact in neutrino physics because the neutrino properties are directly involved in the neutrinoless mode of the decay ( $0\nu\beta\beta$ ) [6–8]. This decay mode, not yet observed, violates lepton-number conservation and its existence would be an evidence of the Majorana nature of the neutrino, providing a measurement of its absolute mass scale. Obviously, to extract a reliable estimate of the neutrino mass, the nuclear structure component of the process must be determined accurately. On the other hand, the double- $\beta$  decay with emission of two neutrinos ( $2\nu\beta\beta$ ) is perfectly allowed by the Standard Model and it has been observed experimentally in several nuclei with typical half-lives of  $10^{19-21}$  years (see [9] for a review). Thus, to test the reliability of the nuclear structure calculations involved in the  $0\nu\beta\beta$  process, one checks first the ability of the nuclear models to reproduce the experimental information available about

the measured half-lives for the  $2\nu\beta\beta$  process. Although the nuclear matrix elements (NMEs) involved in both processes are not the same, they exhibit some similarities. In particular, the two processes connect the same initial and final nuclear ground states and share common intermediate  $J^\pi = 1^+$  states. Therefore, reproducing the  $2\nu\beta\beta$  NMEs is a requirement for any nuclear structure model aiming to describe the neutrinoless mode.

Different theoretical approaches have been used in the past to study the  $2\nu\beta\beta$  NMEs. Most of them belong to the categories of the interacting shell model [10–12], proton-neutron quasiparticle random-phase approximation (QRPA) [1, 2, 13–25], projected Hartree-Fock-Bogoliubov [26–28], and interacting boson model [29–31].

In this work we focus on the QRPA type of calculations. Most of these calculations were based originally on a spherical formalism, but the fact that some of the double- $\beta$  decay nuclei are deformed makes it compulsory to deal with deformed QRPA formalisms [21–25]. This is particularly the case of  $^{150}\text{Nd}$  ( $^{150}\text{Sm}$ ) that has received increasing attention in the last years because of the large phase-space factor and relatively short half-life, as well as for the large  $Q_{\beta\beta}$  energy that will

reduce the background contamination.  $^{150}\text{Nd}$  is currently considered as one of the best candidates to search for the  $0\nu\beta\beta$  decay in the planned experiments SNO+, SuperNEMO, and DCBA.

The experimental information to constrain the calculations is not limited to the  $2\nu\beta\beta$  NMEs extracted from the measured half-lives. We have also experimental information on the Gamow-Teller (GT) strength distributions of the single branches connecting the initial and final ground states with all the  $J^\pi = 1^+$  states in the intermediate nucleus. The GT strength distributions have been measured in both directions from (p, n) and (n, p) charge-exchange reactions (CER) and more recently from high-resolution reactions, such as (d,  $^2\text{He}$ ), ( $^3\text{He}$ , t), and (t,  $^3\text{He}$ ) that allow us to explore in detail the low-energy structure of the GT nuclear response in double- $\beta$  decay partners [32–41]. In some instances there is also experimental information on the  $\log(ft)$  values of the decay of the intermediate nuclei.

Nuclear structure calculations are also constrained by the experimental occupation probabilities of neutrons and protons of the relevant single-particle levels involved in the double- $\beta$  decay process. In particular, the occupation probabilities of the valence shells  $1p_{3/2}$ ,  $1p_{1/2}$ ,  $0f_{5/2}$ , and  $0g_{9/2}$  for neutrons in  $^{76}\text{Ge}$  and for protons in  $^{76}\text{Se}$  have been measured in [42] and [43], respectively. The implications of these measurements on the double- $\beta$  decay NMEs have been studied in [44–47].

In this paper we explore the possibility of describing all the experimental information available on the GT nuclear response within a formalism based on a deformed QRPA approach built on top of a deformed self-consistent Skyrme Hartree-Fock calculation [48–51]. This information includes global properties about the GT resonance, such as its location and total strength, a more detailed description of the low-lying excitations, and  $2\nu\beta\beta$  decay NMEs. The study includes the decays  $^{76}\text{Ge} \rightarrow ^{76}\text{Se}$ ,  $^{116}\text{Cd} \rightarrow ^{116}\text{Sn}$ ,  $^{128}\text{Te} \rightarrow ^{128}\text{Xe}$ ,  $^{130}\text{Te} \rightarrow ^{130}\text{Xe}$ , and  $^{150}\text{Nd} \rightarrow ^{150}\text{Sm}$ . This selection is motivated by recent high-resolution CER experiments performed for  $^{76}\text{Ge}({}^3\text{He}, t){}^{76}\text{As}$  [39],  $^{76}\text{Se}(d, {}^2\text{He}){}^{76}\text{As}$  [37],  $^{128,130}\text{Te}({}^3\text{He}, t){}^{128,130}\text{I}$  [41],  $^{116}\text{Cd}(p, n){}^{116}\text{In}$ , and  $^{116}\text{Sn}(n, p){}^{116}\text{In}$  [40], as well as for  $^{150}\text{Nd}({}^3\text{He}, t){}^{150}\text{Pm}$ , and  $^{150}\text{Sm}(t, {}^3\text{He}){}^{150}\text{Pm}$  [38]. We also discuss on these examples the validity of the single-state dominance (SSD) hypothesis [52] and the extended low-lying-state dominance (LLSD) that includes the contribution of the low-lying excited states in the intermediate nuclei to account for the double- $\beta$  decay rates.

The paper is organized as follows: In Section 2, we present a short introduction to the theoretical approach used in this work to describe the energy distribution of the GT strength. We also present the basic expressions of the  $2\nu\beta\beta$  decay. In Section 3 we present the results obtained from our approach, which are compared with the experimental data available. Section 4 contains a summary and the main conclusions.

## 2. Theoretical Approach

The description of the deformed QRPA approach used in this work is given elsewhere [22, 53–55]. Here we give only a

summary of the method. We start from a self-consistent deformed Hartree-Fock (HF) calculation with density-dependent two-body Skyrme interactions. Time reversal symmetry and axial deformation are assumed in the calculations [56]. Most of the results in this work are performed with the Skyrme force SLy4 [57], which is one of the most widely used and successful interactions. Results from other Skyrme interactions have been studied elsewhere [48–51, 58] to check the sensitivity of the GT nuclear response to the two-body effective interaction.

In our approach, we expand the single-particle wave functions in terms of an axially symmetric harmonic oscillator basis in cylindrical coordinates, using twelve major shells. This amounts to a basis size of 364, the total number of independent ( $N, n_z, \lambda, \Omega > 0$ ) deformed HO states. Pairing is included in BCS approximation by solving the corresponding BCS equations for protons and neutrons after each HF iteration. Fixed pairing gap parameters are determined from the experimental mass differences between even and odd nuclei. Besides the self-consistent HF+BCS solution, we also explore the energy curves, that is, the energy as a function of the quadrupole deformation  $\beta_2$ , which are obtained from constrained HF+BCS calculations.

The energy curves corresponding to the nuclei studied can be found in [50, 51, 58]. The profiles of the energy curves for  $^{76}\text{Ge}$  and  $^{76}\text{Se}$  exhibit two shallow local minima in the prolate and oblate sectors. These minima are separated by relatively low-energy barriers of about 1 MeV. The equilibrium deformation corresponds to  $\beta_2 = 0.14$  in  $^{76}\text{Ge}$  and  $\beta_2 = 0.17$  in  $^{76}\text{Se}$ . We get soft profiles for  $^{116}\text{Cd}$  with a minimum at  $\beta_2 = 0.25$  and an almost flat curve in  $^{116}\text{Sn}$  between  $\beta_2 = -0.15$  and  $\beta_2 = 0.25$ . We obtain almost spherical configurations in the ground states of  $^{128}\text{Te}$  and  $^{130}\text{Te}$ . The energies differ less than 300 keV between quadrupole deformations  $\beta_2 = -0.05$  and  $\beta_2 = 0.1$ . On the other hand, for  $^{128}\text{Xe}$  and  $^{130}\text{Xe}$  we get in both cases two energy minima corresponding to prolate and oblate shapes, differing by less than 1 MeV, with an energy barrier of about 2 MeV. The ground states correspond in both cases to the prolate shapes with deformations around  $\beta_2 = 0.15$ . For  $^{150}\text{Nd}$  and  $^{150}\text{Sm}$  we obtain two energy minima, oblate and prolate, but with clear prolate ground states in both cases at  $\beta_2 = 0.30$  and  $\beta_2 = 0.25$ , respectively. We obtain comparable results with other Skyrme forces. The relative energies between the various minima can change somewhat for different Skyrme forces [50, 51, 58], but the equilibrium deformations are very close to each other changing at most by a few percent.

After the HF+BCS calculation is performed, we introduce separable spin-isospin residual interactions and solve the QRPA equations in the deformed ground states to get GT strength distributions and  $2\nu\beta\beta$  decay NMEs. The residual force has both particle-hole (ph) and particle-particle (pp) components. The repulsive ph force determines to a large extent the structure of the GT resonance and its location. Its coupling constant  $\chi_{\text{ph}}^{\text{GT}}$  is usually taken to reproduce them [53–55, 59–62]. We use  $\chi_{\text{ph}}^{\text{GT}} = 3.0/A^{0.7}$  MeV. The attractive pp part is basically a proton-neutron pairing interaction. We also use a separable form [55, 60, 61] with a coupling

constant  $\kappa_{pp}^{GT}$  usually fitted to reproduce the experimental half-lives [62]. We use in most of this work a fixed value  $\kappa_{pp}^{GT} = 0.05$  MeV, although we will explore the dependence of the  $2\nu\beta\beta$  NMEs on  $\kappa_{pp}^{GT}$  in the next section. Earlier studies on  $^{150}\text{Nd}$  and  $^{150}\text{Sm}$  carried out in [24, 63] using a deformed QRPA formalism showed that the results obtained from realistic nucleon-nucleon residual interactions based on the Brueckner  $G$  matrix for the CD-Bonn force produce results in agreement with those obtained from schematic separable forces similar to those used here.

The QRPA equations are solved following the lines described in [53–55, 60, 61]. The method we use is as follows. We first introduce the proton-neutron QRPA phonon operator

$$\Gamma_{\omega_K}^+ = \sum_{\pi\nu} [X_{\pi\nu}^{\omega_K} \alpha_{\nu}^+ \alpha_{\pi}^+ + Y_{\pi\nu}^{\omega_K} \alpha_{\nu} \alpha_{\pi}], \quad (1)$$

where  $\alpha^+$  and  $\alpha$  are quasiparticle creation and annihilation operators, respectively.  $\omega_K$  labels the RPA excited state and its corresponding excitation energy, and  $X_{\pi\nu}^{\omega_K}$  and  $Y_{\pi\nu}^{\omega_K}$  are the forward and backward phonon amplitudes, respectively. The

solution of the QRPA equations is obtained by solving first a dispersion relation [55, 60, 61], which is of fourth order in the excitation energies  $\omega_K$ . The GT transition amplitudes connecting the QRPA ground state  $|0\rangle$  ( $\Gamma_{\omega_K}|0\rangle = 0$ ) to one phonon states  $|\omega_K\rangle$  ( $\Gamma_{\omega_K}^+|0\rangle = |\omega_K\rangle$ ) are given in the intrinsic frame by

$$\langle \omega_K | \sigma_K t^{\pm} | 0 \rangle = \mp M_{\pm}^{\omega_K}, \quad (2)$$

where

$$M_{-}^{\omega_K} = \sum_{\pi\nu} (\nu_{\nu} u_{\pi} X_{\pi\nu}^{\omega_K} + u_{\nu} \nu_{\pi} Y_{\pi\nu}^{\omega_K}) \langle \nu | \sigma_K | \pi \rangle, \quad (3)$$

$$M_{+}^{\omega_K} = \sum_{\pi\nu} (u_{\nu} \nu_{\pi} X_{\pi\nu}^{\omega_K} + \nu_{\nu} u_{\pi} Y_{\pi\nu}^{\omega_K}) \langle \nu | \sigma_K | \pi \rangle.$$

$\nu_{\nu,\pi}$  ( $u_{\nu,\pi}^2 = 1 - \nu_{\nu,\pi}^2$ ) are the BCS occupation amplitudes for neutrons and protons. Once the intrinsic amplitudes are calculated, the GT strength  $B(\text{GT})$  in the laboratory frame for a transition  $I_i K_i(0^+) \rightarrow I_f K_f(1^+ K)$  can be obtained as

$$B_{\omega}(\text{GT}^{\pm}) = \sum_{\omega_K} [ \langle \omega_{K=0} | \sigma_0 t^{\pm} | 0 \rangle^2 \delta(\omega_{K=0} - \omega) + 2 \langle \omega_{K=1} | \sigma_1 t^{\pm} | 0 \rangle^2 \delta(\omega_{K=1} - \omega) ]. \quad (4)$$

To obtain this expression we have used the Bohr and Motelson factorization [64, 65] to express the initial and final nuclear states in the laboratory system in terms of the intrinsic states. A quenching factor,  $q = g_A/g_{A,\text{bare}} = 0.79$ , is applied to the weak axial-vector coupling constant and included in the calculations. The physical reasons for this quenching have been studied elsewhere [10, 66, 67] and are related to the role of nonnucleonic degrees of freedom, absent in the usual theoretical models, and to the limitations of model space, many-nucleon configurations, and deep correlations missing in these calculations. The implications of this quenching on the description of single- $\beta$  and double- $\beta$  decay observables have been considered in several works [12, 30, 68–71], where both the effective value of  $g_A$  and the coupling strength of the residual interaction in the pp channel are considered free parameters of the calculation. It is found that very strong quenching values are needed to reproduce simultaneously the observations corresponding to the  $2\nu\beta\beta$  half-lives and to the single- $\beta$  decay branches. One should note however that the QRPA calculations that require a strong quenching to fit the  $2\nu\beta\beta$  NMEs were performed within a spherical formalism neglecting possible effects from deformation degrees of freedom. Because the main effect of deformation is a reduction of the NMEs, deformed QRPA calculations shall demand less quenching to fit the experiment.

Concerning the  $2\nu\beta\beta$  decay NMEs, the basic expressions for this process, within the deformed QRPA formalism used in this work, can be found in [21, 22, 72]. Deformation effects on the  $2\nu\beta\beta$  NMEs have also been studied within the

projected Hartree-Fock-Bogoliubov model [27]. Attempts to describe deformation effects on the  $0\nu\beta\beta$  decay within QRPA models can also be found in [25, 73].

The half-life of the  $2\nu\beta\beta$  decay can be written as

$$[T_{1/2}^{2\nu\beta\beta}(0_{\text{gs}}^+ \rightarrow 0_{\text{gs}}^+)]^{-1} = (g_A)^4 G^{2\nu\beta\beta} |(m_e c^2) M_{\text{GT}}^{2\nu\beta\beta}|^2, \quad (5)$$

where  $G^{2\nu\beta\beta}$  are the phase-space integrals [74, 75] and  $M_{\text{GT}}^{2\nu\beta\beta}$  the nuclear matrix elements containing the nuclear structure part involved in the  $2\nu\beta\beta$  process:

$$M_{\text{GT}}^{2\nu\beta\beta} = \sum_{K=0,\pm 1} \sum_{m_i, m_f} (-1)^K \frac{\langle \omega_{K, m_f} | \omega_{K, m_i} \rangle}{D} \langle 0_f | \sigma_{-K} t^- | \omega_{K, m_f} \rangle \langle \omega_{K, m_i} | \sigma_K t^- | 0_i \rangle. \quad (6)$$

In this equation  $|\omega_{K, m_i}\rangle(|\omega_{K, m_f}\rangle)$  are the QRPA intermediate  $1^+$  states reached from the initial (final) nucleus.  $m_i$  and  $m_f$  are labels that classify the intermediate  $1^+$  states that are reached from different initial  $|0_i\rangle$  and final  $|0_f\rangle$  ground states. The overlaps  $\langle \omega_{K, m_f} | \omega_{K, m_i} \rangle$  take into account the non-orthogonality of the intermediate states. Their expressions can be found in [21]. The energy denominator  $D$  involves the energy of the emitted leptons, which is given on average by  $(1/2)Q_{\beta\beta} + m_e$ , as well as the excitation energies of

TABLE 1: Experimental  $2\nu\beta\beta$  decay half-lives  $T_{1/2}^{2\nu\beta\beta}$  from [9], phase-space factors  $G^{2\nu\beta\beta}$  from [74], and NMEs extracted from (5) taking bare  $g_{A,\text{bare}} = 1.273$  and quenched  $g_A = 1$  factors.

	$^{76}\text{Ge}$	$^{116}\text{Cd}$	$^{128}\text{Te}$	$^{130}\text{Te}$	$^{150}\text{Nd}$
$T_{1/2}^{2\nu\beta\beta}$ ( $10^{21}$ yr)	$1.65 \pm 0.14$	$0.0287 \pm 0.0013$	$2000 \pm 300$	$0.69 \pm 0.13$	$0.0082 \pm 0.0009$
$G^{2\nu\beta\beta}$ ( $10^{-21}$ yr $^{-1}$ )	48.17	2764	0.2688	1529	36430
$M_{GT}^{2\nu\beta\beta}$ (MeV $^{-1}$ )					
$g_A = 1.273$	0.136	0.136	0.052	0.037	0.070
$g_A = 1$	0.220	0.220	0.084	0.060	0.113

the intermediate nucleus. In terms of the QRPA excitation energies the denominator can be written as

$$D_1 = \frac{1}{2} \left( \omega_{K'}^{m_f} + \omega_{K'}^{m_i} \right), \quad (7)$$

where  $\omega_K^{m_i}$  ( $\omega_K^{m_f}$ ) is the QRPA excitation energy relative to the initial (final) nucleus. It turns out that the NMEs are quite sensitive to the values of the denominator, especially for low-lying states, where the denominator takes smaller values. Thus, it is a common practice to use some experimental normalization of this denominator to improve the accuracy of the NMEs. In this work we also consider the denominator  $D_2$ , which is corrected with the experimental energy  $\bar{\omega}_{1^+}$  of the first  $1^+$  state in the intermediate nucleus relative to the mean ground-state energy of the initial and final nuclei, in such a way that the experimental energy of the first  $1^+$  state is reproduced by the calculations:

$$D_2 = \frac{1}{2} \left[ \omega_{K'}^{m_f} + \omega_{K'}^{m_i} - \left( \omega_{K'}^{1_f} + \omega_{K'}^{1_i} \right) \right] + \bar{\omega}_{1^+}. \quad (8)$$

Running  $2\nu\beta\beta$  sums will be shown later for the two choices of the denominator,  $D_1$  and  $D_2$ . When the ground state in the intermediate nucleus of the double- $\beta$  decay partners is a  $1^+$  state, the energy  $\bar{\omega}_{1^+}$  is given by

$$\bar{\omega}_{1^+} = \frac{1}{2} \left( Q_{\text{EC}} + Q_{\beta^-} \right)_{\text{exp}}, \quad (9)$$

where  $Q_{\text{EC}}$  and  $Q_{\beta^-}$  are the experimental energies of the decays of the intermediate nucleus into the parent and daughter partners, respectively. This is the case of  $^{116}\text{In}$  and  $^{128}\text{I}$ , which are both  $1^+$  ground states. In the other cases, although the ground states in the intermediate nuclei are not  $1^+$  states, the first  $1^+$  excited states appear at a very low excitation energy;  $E = 0.086$  MeV in  $^{76}\text{As}$  [39],  $E = 0.043$  MeV in  $^{130}\text{I}$  [41], and  $E = 0.11$  MeV in  $^{150}\text{Pm}$  [38]. Therefore, to a good approximation we also determine  $\bar{\omega}_{1^+}$  using (9).

The existing measurements for the  $2\nu\beta\beta$  decay half-lives ( $T_{1/2}^{2\nu\beta\beta}$ ) have been recently analyzed in [9]. Adopted values for such half-lives can be seen in Table 1. Using the phase-space factors from the evaluation [74] that involves exact Dirac wave functions including electron screening and finite nuclear size effects, we obtain the experimental NMEs shown in Table 1, for bare  $g_{A,\text{bare}} = 1.273$  and quenched  $g_A = 1$  factors. It should be clear that the theoretical NMEs defined in (6) do not depend on the  $g_A$  factors. Hence, the values

obtained for the experimental NMEs extracted from the experimental half-lives through (5) depend on the  $g_A$  value used in this equation.

### 3. Results

**3.1. Gamow-Teller Strength Distributions.** The energy distributions of the GT strength obtained from our formalism are displayed in Figures 1 and 2. Figure 1 contains the  $B(\text{GT}^-)$  strength distributions for  $^{76}\text{Ge}$ ,  $^{116}\text{Cd}$ ,  $^{128}\text{Te}$ ,  $^{130}\text{Te}$ , and  $^{150}\text{Nd}$ . The theoretical curves correspond to the calculated distributions folded with 1 MeV width Breit-Wigner functions, in such a way that the discrete spectra obtained in the calculations appear now as continuous curves. They give the GT strength per MeV and the area below the curves in a given energy interval gives us directly the GT strength contained in that energy interval. We compare our QRPA results from SLy4 obtained with the self-consistent deformations with the experimental strengths extracted from CERs [34, 38, 40]. In the cases of  $^{76}\text{Ge}$ ,  $^{128}\text{Te}$ , and  $^{130}\text{Te}$ , the data from [34] includes the total GT measured strength of the resonances and their energy location. Namely,  $B(\text{GT}) = 12.43$  at  $E = 11.13$  MeV in  $^{76}\text{Ge}$ ,  $B(\text{GT}) = 34.24$  at  $E = 13.14$  MeV in  $^{128}\text{Te}$ , and  $B(\text{GT}) = 38.46$  at  $E = 13.59$  MeV in  $^{130}\text{Te}$ . We have folded these strengths with the same functions used for the calculations to facilitate the comparison. They can be seen with dashed lines in Figure 1.

Figure 2 contains the  $B(\text{GT}^+)$  strength distributions corresponding to  $^{76}\text{Se}$ ,  $^{116}\text{Sn}$ ,  $^{128}\text{Xe}$ ,  $^{130}\text{Xe}$ , and  $^{150}\text{Sm}$ . The QRPA results folded with the same 1 MeV width Breit-Wigner functions are compared with the experimental strengths extracted from CERs [35–38, 40]. On the other hand, Figures 3 and 4 contain the accumulated GT strength in the low excitation energy. Figure 3 contains the same cases as in Figure 1 with additional high-resolution data from [39] for  $^{76}\text{Ge}$  and from [41] for  $^{128,130}\text{Te}$ . Figure 4 contains the same cases as in Figure 2, but as accumulated strengths in the low-energy range.

One should notice that the measured strength extracted from the cross sections contains two types of contributions that cannot be disentangled, namely, GT ( $\sigma t^\pm$  operator) and isovector spin monopole (IVSM) ( $r^2 \sigma t^\pm$  operator). Thus, the measured strength corresponds actually to  $B(\text{GT}+\text{IVSM})$ . Different theoretical calculations evaluating the contributions from both GT and IVSM modes are available in the literature [38, 40, 76–78]. The general conclusion tells us that in the (p, n) direction the strength distribution below

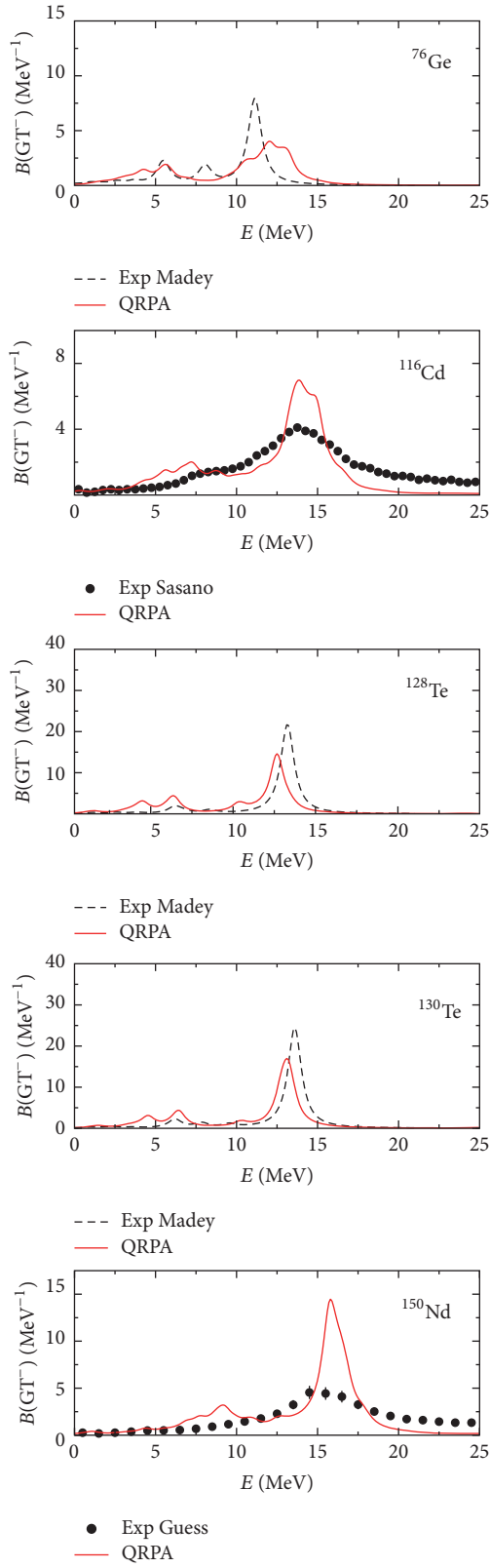


FIGURE 1: Experimental  $B(\text{GT}^-)$  from CERs [34, 38, 40] in  $^{76}\text{Ge}$ ,  $^{116}\text{Cd}$ ,  $^{128}\text{Te}$ ,  $^{130}\text{Te}$ , and  $^{150}\text{Nd}$  plotted versus the excitation energy of the daughter nuclei are compared with folded SLy4-QRPA calculations (see text).

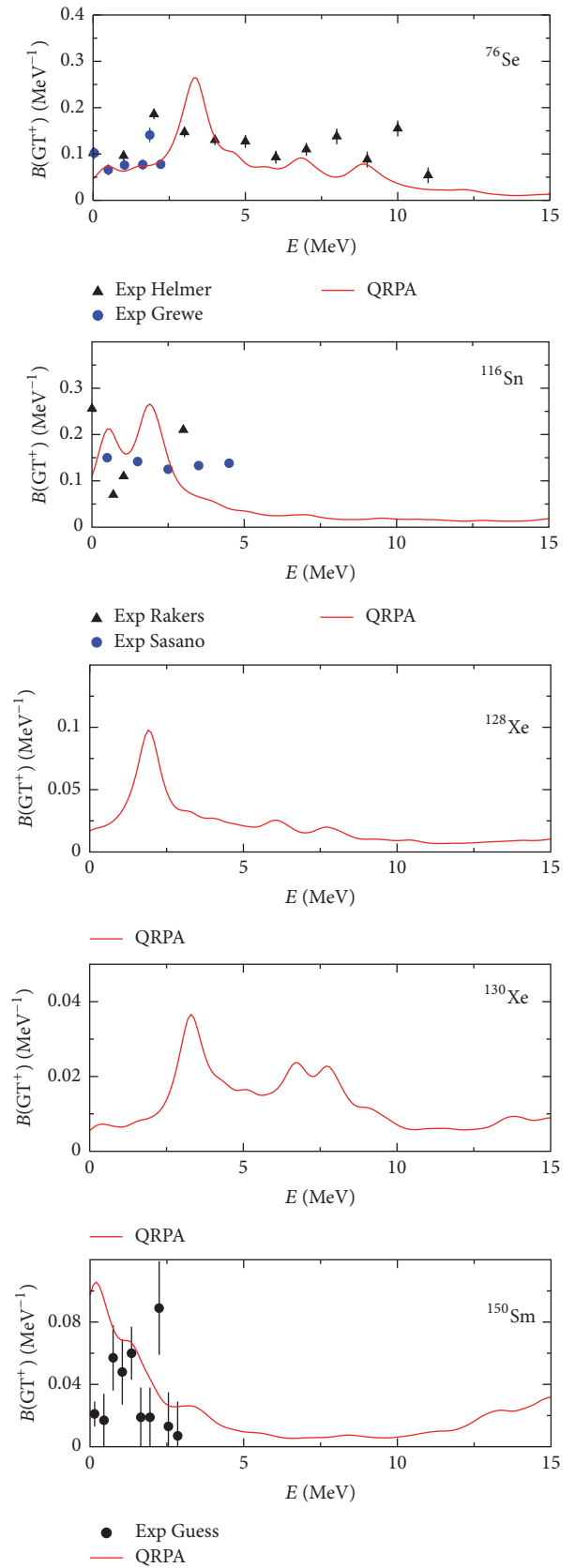


FIGURE 2: The same as in Figure 1, but for  $B(\text{GT}^+)$  in  $^{76}\text{Se}$ ,  $^{116}\text{Sn}$ ,  $^{128}\text{Xe}$ ,  $^{130}\text{Xe}$ , and  $^{150}\text{Sm}$ . Experimental data are from CERs [35–38, 40].

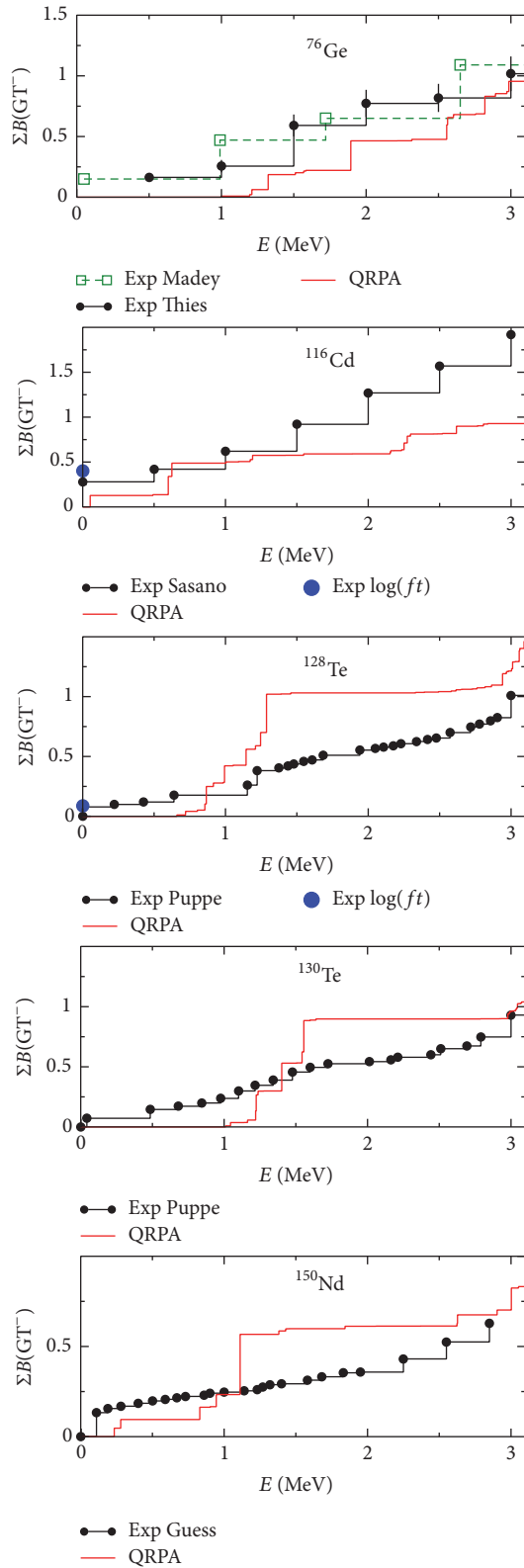


FIGURE 3: Accumulated GT strength  $B(GT^-)$  in the low-energy range. SLY4-QRPA calculations are compared with data from [34, 38–41]. Also shown in  $^{116}\text{Cd}$  and  $^{128}\text{Te}$  are the  $B(GT^-)$  values extracted from the experimental electron captures on the intermediate nuclei  $^{116}\text{I}$  and  $^{128}\text{In}$ .

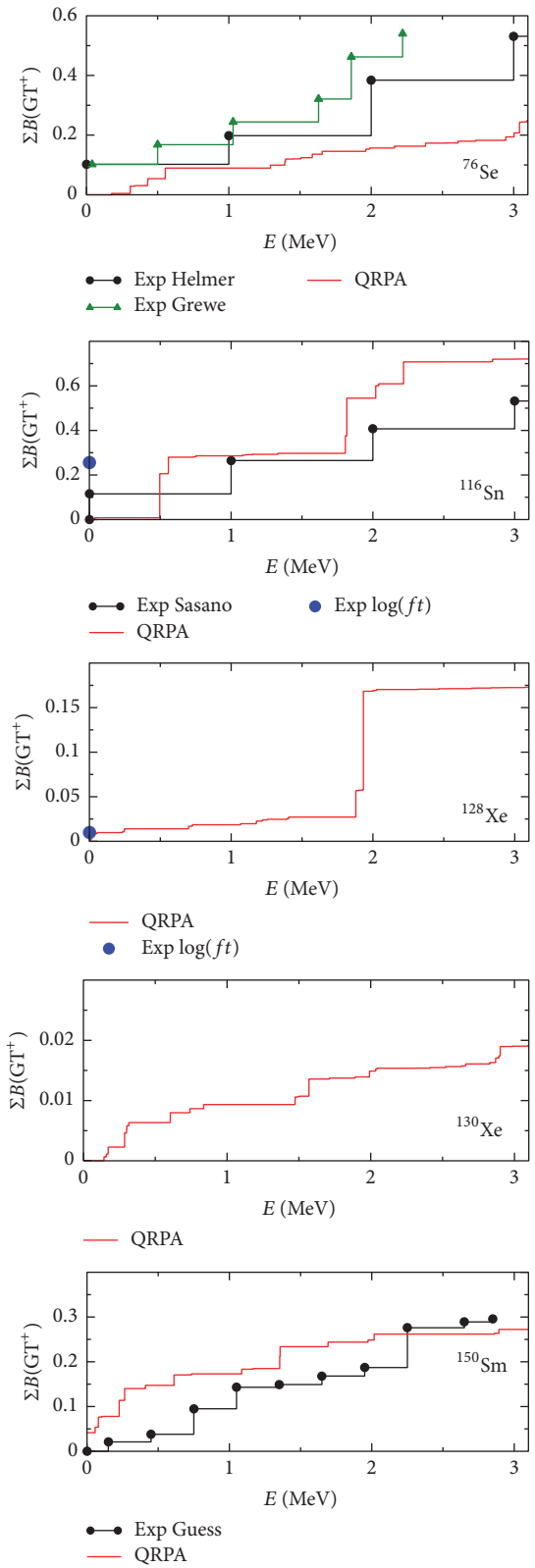


FIGURE 4: The same as in Figure 2 but plotted as accumulated strength in the low-energy range. Also shown in  $^{116}\text{Sn}$  and  $^{128}\text{Xe}$  are the  $B(GT^+)$  values extracted from the experimental  $\beta^-$  decay of the intermediate nuclei  $^{116}\text{I}$  and  $^{128}\text{In}$ .

20 MeV is mostly caused by the GT component, although nonnegligible contributions from IVSM components are found between 10 and 20 MeV. Above 20 MeV, there is no significant GT strength in the calculations. In the (n, p) direction the GT strength is expected to be strongly Pauli blocked in nuclei with more neutrons than protons and therefore the measured strength is mostly due to the IVSM resonance. Nevertheless, the strength found in low-lying isolated peaks is associated with GT transitions because the continuous tail of the IVSM resonance is very small at these energies and is not expected to exhibit any peak. In summary, the measured strength in the (p, n) direction can be safely assigned to be GT in the low-energy range below 10 MeV and with some reservations between 10 and 20 MeV. Beyond 20 MeV the strength would be practically due to IVSM. On the other hand, the measured strength in the (n, p) direction would be due to IVSM transitions, except in the low-lying excitation energy below 2-3 MeV, where the isolated peaks observed can be attributed to GT strength. This is the reason why we plot experimental data in Figure 4 only up to 3 MeV.

In general terms, we reproduce fairly well the global properties of the GT strength distributions, including the location of the  $GT^-$  resonance and the total strength measured (see Figure 1). In the (n, p) direction, the  $GT^+$  strength is strongly suppressed (compare the vertical scales in Figures 1 and 2). As expected, a strong suppression of  $GT^+$  takes place in nuclei with a large neutron excess. The experimental information on  $GT^+$  strengths is mainly limited to the low-energy region and it is fairly well reproduced by the calculations. The accumulated strengths in the low-energy range shown in Figures 3 and 4 show more clearly the degree of accuracy achieved by the calculations. Although a detailed spectroscopy is beyond the capabilities of our model and the isolated transitions are not well reproduced by our calculations, the overall agreement with the total strength contained in this reduced energy interval, as well as with the profiles of the accumulated strength distributions, is satisfactory. In general, the experimental  $B(GT^-)$  shows spectra more fragmented than the calculated ones, but the total strength up to 3 MeV is well reproduced with the only exception of  $^{116}\text{Cd}$ , where we obtain less strength than observed. The total measured  $B(GT^+)$  strength up to 3 MeV is especially well reproduced in the case of  $^{150}\text{Sm}$ , whereas it is somewhat underestimated in  $^{76}\text{Se}$  and overestimated in  $^{116}\text{Sn}$ .

We can see in Figures 3 and 4 with blue dots the  $B(GT)$  values extracted from the decays of the intermediate  $1^+$  nuclei  $^{116}\text{In}$  and  $^{128}\text{I}$ . They can be compared with experimental results extracted from CERs, as well as with the theoretical calculations. The electron capture experiment on  $^{116}\text{In}$  [79] gives  $ft = 2.84 \times 10^4$  s with a corresponding strength  $B(GT^-) = 0.402$ . The  $\beta^-$  decay yields  $B(GT^-) = 0.256$  [36]. The decay of  $^{128}\text{I}$  yields  $B(GT^-) = 0.087$  and  $B(GT^+) = 0.079$  [41]. The sensitivity of these distributions to the effective interactions and to nuclear deformation was discussed in previous works [22, 48, 49, 51, 58, 72]. Different calculations [21, 24, 68, 78, 80] based also on QRPA formalisms with different degrees of sophistication agree qualitatively in the description of the single  $\beta$  branches of double- $\beta$  decay partners.

**3.2. Double- $\beta$  Decay.** It is well known that the  $2\nu\beta\beta$  NMEs are very sensitive to the residual interactions, as well as to differences in deformation between initial and final nuclei [21, 22]. We show in Figure 5 the NMEs calculated with the self-consistent deformations as a function of the pp coupling constant of the residual force for the decays of  $^{76}\text{Ge}$ ,  $^{116}\text{Cd}$ ,  $^{128}\text{Te}$ ,  $^{130}\text{Te}$ , and  $^{150}\text{Nd}$ . The shaded bands correspond to the experimental NMEs extracted from the measured  $2\nu\beta\beta$  half-lives. For each nucleus the band is delimited by the lower and upper values obtained using bare ( $g_A = 1.273$ ) and quenched values, respectively (see Table 1). Results obtained with the energy denominator  $D_1$  are displayed with solid lines, whereas results obtained with  $D_2$  are shown with dashed lines.  $D_2$  denominators produce in all cases larger NMEs than  $D_1$ . We can see that the experimental NMEs contained in the shaded region are reproduced within some windows of the parameter  $\kappa_{pp}^{GT}$ . It is not our purpose here to get the best fit or the optimum value of  $\kappa_{pp}^{GT}$  that reproduces the experimental NMEs because this value will change by changing  $\chi_{ph}^{GT}$  or the underlying mean field structure. In this work we take  $\kappa_{pp}^{GT} = 0.05$  MeV as an approximate value that reproduces reasonably well the experimental information on both single  $\beta$  branches and  $2\nu\beta\beta$  NMEs.

Figure 6 shows the running sums for the  $2\nu\beta\beta$  NMEs calculated with  $\kappa_{pp}^{GT} = 0.05$  MeV. These are the partial contributions to the NMEs of all the  $1^+$  states in the intermediate nucleus up to a given energy. Obviously, the final values reached by the calculations at 20 MeV in Figure 6 correspond to the values in Figure 5 at  $\kappa_{pp}^{GT} = 0.05$  MeV. The final values of the running sums for other  $\kappa_{pp}^{GT}$  can be estimated by looking at the corresponding  $\kappa_{pp}^{GT}$  values in Figure 5. As in the previous figure, we also show the results obtained with denominators  $D_1$  (solid) and  $D_2$  (dashed). The main difference between them is originated at low excitation energies, where the relative effect of using shifted energies is enhanced. The effect at larger energies is negligible and we get a constant difference between  $D_1$  and  $D_2$ , which is the difference accumulated in the first few MeV. The contribution to the  $2\nu\beta\beta$  NMEs in the region between 10 and 15 MeV that can be seen in most cases is due to the GT resonances observed in Figure 1. This contribution is small because of the joint effects of large energy denominators in (6) and the mismatch between the excitation energies of the  $GT^-$  and  $GT^+$  resonances.

The running sums are very useful to discuss the extent to which the single-state dominance hypothesis applies. This hypothesis tells us that, to a large extent, the  $2\nu\beta\beta$  NMEs will be given by the transition through the ground state of the intermediate odd-odd nucleus in those cases where this ground state is a  $1^+$  state reachable by allowed GT transitions. One important consequence of the SSD hypothesis would be that the half-lives for  $2\nu\beta\beta$  decay could be extracted accurately from simple experiments, such as single  $\beta^-$  and electron capture measurements of the intermediate nuclei to the  $0^+$  ground states of the neighbor even-even nuclei. Theoretically, the SSD hypothesis would also imply an important simplification of the calculations because, to describe

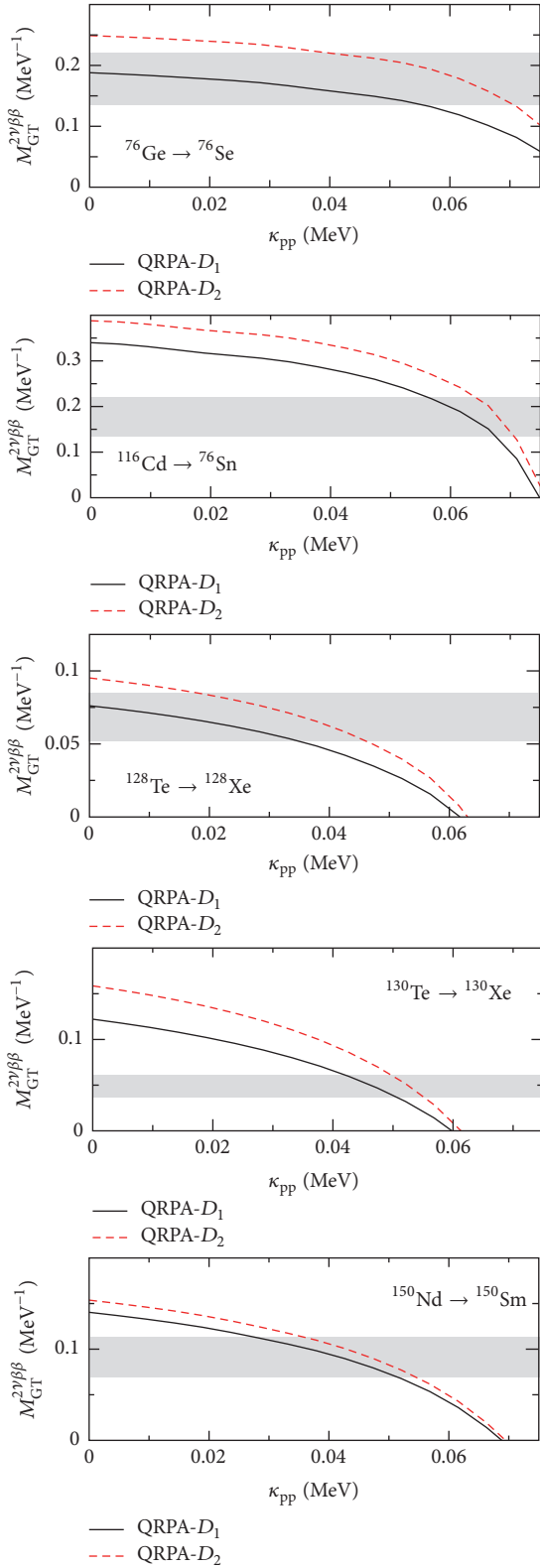


FIGURE 5: Nuclear matrix element for the  $2\nu\beta\beta$  decay of  $^{76}\text{Ge}$ ,  $^{116}\text{Cd}$ ,  $^{128}\text{Te}$ ,  $^{130}\text{Te}$ , and  $^{150}\text{Nd}$  as a function of the coupling strength  $\kappa_{pp}^{\text{GT}}$ . Solid lines correspond to calculations with the energy denominator  $D_1$ , while dashed lines correspond to  $D_2$ . The gray area corresponds to the NME experimental range obtained from the measured half-lives using bare  $g_A = 1.273$  and quenched  $g_A = 1$  factors.

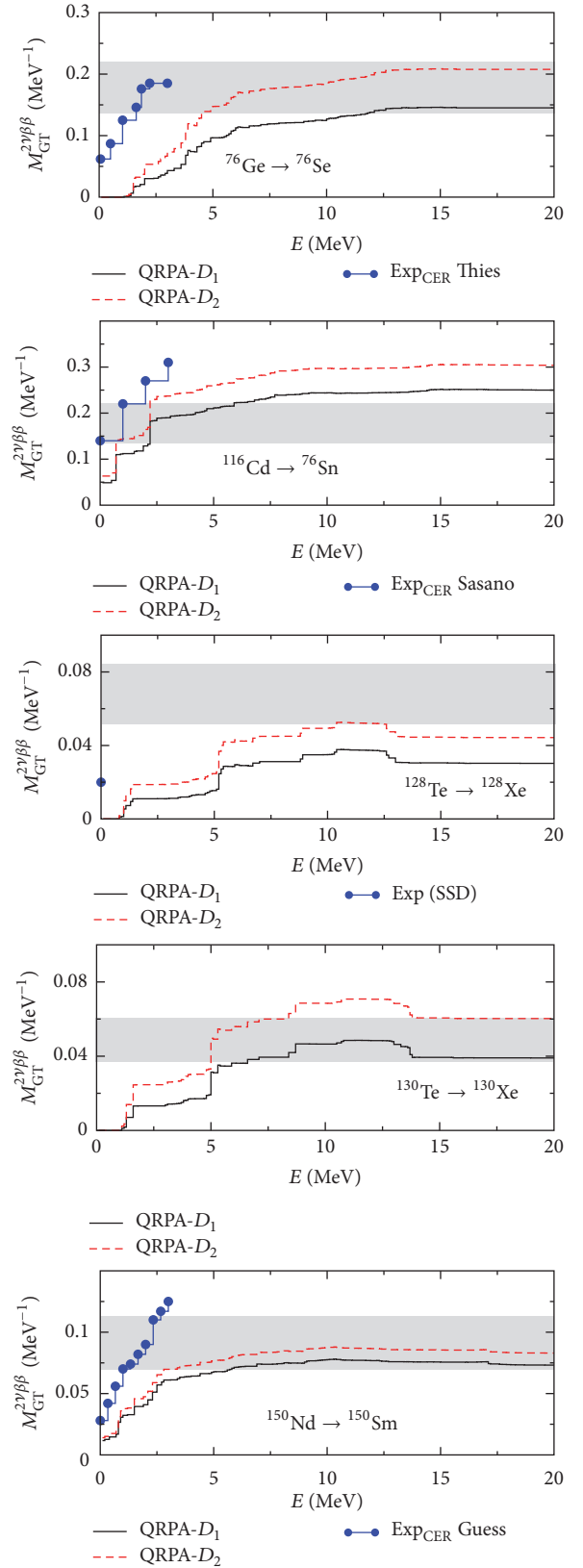


FIGURE 6: Running sums of the  $2\nu\beta\beta$  NME in  $^{76}\text{Ge}$ ,  $^{116}\text{Cd}$ ,  $^{128}\text{Te}$ ,  $^{130}\text{Te}$ , and  $^{150}\text{Nd}$  as a function of the excitation energy in the intermediate nucleus. Solid and dashed lines and shaded areas are as in Figure 5. See text.

the  $2\nu\beta\beta$  decay from ground state to ground state, only the wave function of the  $1^+$  ground state of the intermediate nucleus would be needed. Because not all of the double- $\beta$  decaying nuclei have  $1^+$  ground states in the intermediate nuclei (only  $^{116}\text{In}$  and  $^{128}\text{I}$  in the nuclei considered here), the SSD condition is extended by considering the relative contributions of the low-lying excited states in the intermediate nuclei to the total  $2\nu\beta\beta$  NMEs. This is called low-lying-single-state dominance [72] and can be studied in all  $2\nu\beta\beta$  nuclei. From the results displayed in Figure 6 we cannot establish clear evidences for SSD hypothesis from our calculations. Nevertheless, it is also worth mentioning that our NMEs calculated up to 5 MeV already account for most of the total NME calculated up to 20 MeV. This result agrees qualitatively with other results obtained in different QRPA calculations [81–84].

The SSD hypothesis can be tested experimentally in the decays of  $^{116}\text{Cd}$  and  $^{128}\text{Te}$  where the intermediate nuclei have  $1^+$  ground states. By measuring the two decay branches of  $^{116}\text{In}$  and  $^{128}\text{I}$ , the  $\log(ft)$  values of the ground state to ground state ( $1^+ \rightarrow 0^+$ ) can be extracted. From these values one can obtain the GT strength:

$$B(\text{GT}) = \frac{3A}{g_A^2 ft}, \quad (10)$$

with  $A = 6289 \text{ s}$  [85]. Finally the  $2\nu\beta\beta$  NME within SSD is evaluated as

$$\begin{aligned} M_{\text{GT}}^{2\nu\beta\beta}(\text{SSD}) &= \frac{[B(\text{GT}^-)B(\text{GT}^+)]^{1/2}}{(Q_{\beta^-} + Q_{\text{EC}})/2} \\ &= \frac{6A}{[ft_{\text{EC}}]^{1/2} [ft_{\beta^-}]^{1/2} g_A^2 (Q_{\beta^-} + Q_{\text{EC}})}. \end{aligned} \quad (11)$$

One can also determine the  $2\nu\beta\beta$  NME running sums using the experimental  $B(\text{GT})$  extracted from CERs and using the same phases for the matrix elements if one can establish a one-to-one correspondence between the intermediate states reached from parent and daughter. Then, one can construct the  $2\nu\beta\beta$  NMEs from the measured GT strengths and energies in the CERs in the parent and daughter partners:

$$M_{\text{GT}}^{2\nu\beta\beta}(\text{LLSD}) = \sum_m \frac{[B_m(\text{GT}^+)B_m(\text{GT}^-)]^{1/2}}{E_m + (Q_{\beta^-} + Q_{\text{EC}})/2}, \quad (12)$$

where  $E_m$  is the excitation energy of the  $m$ th  $1^+$  state relative to the ground state of the intermediate nucleus. Experimental  $2\nu\beta\beta$  NMEs running sums have been determined along this line using experimental  $B(\text{GT})$  from CERs in [39] for  $^{76}\text{Ge}$ , in [40] for  $^{116}\text{Cd}$ , and in [38] for  $^{150}\text{Nd}$ . In the case of  $^{128,130}\text{Te}$  they have not been determined because of the lack of data in the (n, p) direction. They can be seen in Figure 6 under the label  $\text{exp}_{\text{CER}}$ .

In the case of  $^{76}\text{Ge}$ , the  $2\nu\beta\beta$  NMEs are constructed by combining the  $\text{GT}^-$  data from  $^{76}\text{Ge}(^3\text{He}, t)^{76}\text{As}$  [39] with those for  $\text{GT}^+$  transitions from  $^{76}\text{Se}(d, ^2\text{He})^{76}\text{As}$  [37]. A

large fragmentation of the GT strength was found in the experiment, not only at high excitation energies, but also at low excitation energy, which is rather unusual. In addition, a lack of correlation between the GT excitation energies from the two different branches was also observed. Thus, for the evaluation of the  $2\nu\beta\beta$  NMEs a one-to-one connection between the  $B(\text{GT}^-)$  and  $B(\text{GT}^+)$  transitions leading to the excited state in the intermediate nucleus needs to be established. In particular, since the spectra from the two CER experiments had rather different energy resolutions, the strength was accumulated in similar bins to evaluate the  $2\nu\beta\beta$  NMEs [39]. The summed matrix element amounted to  $0.186 \text{ MeV}^{-1}$  up to an excitation energy of 2.22 MeV.

In the case of  $^{116}\text{Cd}$ ,  $^{116}\text{Cd}(p, n)^{116}\text{In}$  and  $^{116}\text{Sn}(n, p)^{116}\text{In}$  [40] CERs were used to evaluate the LLS  $2\nu\beta\beta$  NMEs. The running sum starts at  $0.14 \text{ MeV}^{-1}$  at zero excitation energy and reaches a value of  $0.31 \text{ MeV}^{-1}$  at 3 MeV excitation energy. The value at zero energy can be compared with the value obtained by using the  $ft$ -values of the decay in  $^{116}\text{In}$  mentioned above. The value constructed in this way amounts to  $\text{NME}(\text{SSD}) = 0.168 \text{ MeV}^{-1}$  [79]. In the case of  $^{128}\text{Te}$  and  $^{130}\text{Te}$  the lack of experimental information in the  $\text{GT}^+$  direction prevents us from evaluating the experimental LLS estimates. However, an estimate of  $M_{\text{GT}}^{2\nu\beta\beta}(\text{SSD}) = 0.019 \text{ MeV}^{-1}$  in  $^{128}\text{Te}$  can be obtained from the  $\log(ft)$  values of the decay in  $^{128}\text{I}$ . Finally, in the case of  $^{150}\text{Nd}$ , although the intermediate nucleus  $^{150}\text{Pm}$  is not a  $1^+$  state, assuming that the excited  $1^+$  state at 0.11 MeV excitation energy observed in  $^{150}\text{Nd}(^3\text{He}, t)^{150}\text{Pm}$  corresponds to all the GT strength measured between 50 keV and 250 keV in the reaction  $^{150}\text{Sm}(t, ^3\text{He})^{150}\text{Pm}$ , one obtains an estimate for the SSD  $M_{\text{GT}}^{2\nu\beta\beta}(\text{SSD}) = 0.028 \text{ MeV}^{-1}$  [38]. Extending the running sum by associating the corresponding GT strengths bins from the reactions in both directions and assuming a coherent addition of all the bins, one gets  $M_{\text{GT}}^{2\nu\beta\beta}(\text{SSD}) = 0.13 \text{ MeV}^{-1}$  [38] up to an excitation energy in the intermediate nucleus of 3 MeV. This experimental running sum is included in Figure 6. In all the cases, the experimental running sum is larger than the calculations and tends to be larger than the experimental values extracted from the half-lives. However, one should always keep in mind that the present experimental LLS estimates are indeed upper limits because the phases of the NMEs are considered always positive. Although the present calculations favor coherent phases in the low-energy region, the phases could change depending on the theoretical model. In particular the sensitivity of these phases to the pp residual interaction has been studied in [63].

#### 4. Summary and Conclusions

In summary, using a theoretical approach based on a deformed HF+BCS+QRPA calculation with effective Skyrme interactions, pairing correlations, and spin-isospin residual separable forces in the ph and pp channels, we have studied simultaneously the GT strength distributions of the double- $\beta$  decay partners ( $^{76}\text{Ge}$ ,  $^{76}\text{Se}$ ), ( $^{116}\text{Cd}$ ,  $^{116}\text{Sn}$ ), ( $^{128}\text{Te}$ ,  $^{128}\text{Xe}$ ), ( $^{130}\text{Te}$ ,  $^{130}\text{Xe}$ ), and ( $^{150}\text{Nd}$ ,  $^{150}\text{Sm}$ ) reaching the intermediate

nuclei  $^{76}\text{As}$ ,  $^{116}\text{In}$ ,  $^{128}\text{I}$ ,  $^{130}\text{I}$ , and  $^{150}\text{Pm}$ , respectively, as well as their  $2\nu\beta\beta$  NMEs. In this work we use reasonable choices for the two-body effective interaction, residual interactions, deformations, and quenching factors. The sensitivity of the results to the various ingredients in the theoretical model was discussed elsewhere.

Our results for the energy distributions of the GT strength have been compared with recent data from CERs, whereas the calculated  $2\nu\beta\beta$  NMEs have been compared with the experimental values extracted from the measured half-lives for these processes, as well as with the running sums extracted from CERs.

The theoretical approach used in this work has been demonstrated to be well suited to account for the rich variety of experimental information available on the nuclear GT response. The global properties of the energy distributions of the GT strength and the  $2\nu\beta\beta$  NMEs are well reproduced, with the exception of a detailed description of the low-lying GT strength distributions that could clearly be improved. The  $2\nu\beta\beta$  NMEs extracted from the experimental half-lives are also reproduced by the calculations with some overestimation (underestimation) in the case of  $^{116}\text{Cd}$  ( $^{128}\text{Te}$ ).

We have also upgraded the theoretical analysis of SSD and LLSD hypotheses and we have compared our calculations with the experimental running sums obtained by considering recent measurements from CERs and decays of the intermediate nuclei.

It will be interesting in the future to extend these calculations by including all the double- $\beta$  decay candidates and to explore systematically the potential of this method. It will be also interesting to explore the consequences of the isospin symmetry restoration, as it was investigated in [86]. In HF+BCS and QRPA neither the ground states nor the excited states are isospin eigenstates, but the expectation values of the  $T_z$  operator are conserved. This implies that in the  $B(\text{GT}^-)$  the transition operator connects states with a given expectation value of  $T_z = (N - Z)/2$  to states with expectation value of  $T_z = (N - Z)/2 - 1$ .

## Competing Interests

The authors declare that they have no competing interests.

## Acknowledgments

This work was supported by MINECO (Spain) under Research Grant no. FIS2014-51971-P. O. Moreno acknowledges support from a Marie Curie International Outgoing Fellowship within the European Union Seventh Framework Programme, under Grant Agreement PEOF-GA-2011-298364 (ELECTROWEAK).

## References

- [1] J. Suhonen and O. Civitarese, "Weak-interaction and nuclear-structure aspects of nuclear double beta decay," *Physics Report*, vol. 300, no. 3-4, pp. 123–214, 1998.
- [2] A. Faessler and F. Šimković, "Double beta decay," *Journal of Physics G: Nuclear and Particle Physics*, vol. 24, no. 12, p. 2139, 1998.
- [3] H. V. Klapdor-Kleingrothaus, *Seventy Years of Double Beta Decay*, World Scientific Publishing, Singapore, 2010.
- [4] O. Cremonesi and M. Pavan, "Challenges in double beta decay," *Advances in High Energy Physics*, vol. 2014, Article ID 951432, 40 pages, 2014.
- [5] N. Abgrall, E. Aguayo, F. T. Avignone III et al., "The Majorana Demonstrator neutrinoless double-beta decay experiment," *Advances in High Energy Physics*, vol. 2014, Article ID 365432, 18 pages, 2014.
- [6] A. Giuliani and A. Poves, "Neutrinoless double-beta decay," *Advances in High Energy Physics*, vol. 2012, Article ID 857016, 38 pages, 2012.
- [7] J. Maalampi and J. Suhonen, "Neutrinoless double  $\beta^+$ /EC decays," *Advances in High Energy Physics*, vol. 2013, Article ID 505874, 18 pages, 2013.
- [8] S. Dell'Oro, S. Marcocci, M. Viel, and F. Vissani, "Neutrinoless double beta decay: 2015 review," *Advances in High Energy Physics*, vol. 2016, Article ID 2162659, 37 pages, 2016.
- [9] A. S. Barabash, "Average and recommended half-life values for two-neutrino double beta decay," *Nuclear Physics A*, vol. 935, pp. 52–64, 2015.
- [10] E. Caurier, G. Martínez-Pinedo, F. Nowacki, A. Poves, and A. P. Zuker, "The shell model as a unified view of nuclear structure," *Reviews of Modern Physics*, vol. 77, no. 2, pp. 427–488, 2005.
- [11] J. Menéndez, A. Poves, E. Caurier, and F. Nowacki, "Disassembling the nuclear matrix elements of the neutrinoless  $\beta\beta$  decay," *Nuclear Physics A*, vol. 818, no. 3-4, pp. 139–151, 2009.
- [12] E. Caurier, F. Nowacki, and A. Poves, "Shell Model description of the  $\beta\beta$  decay of  $^{136}\text{Xe}$ ," *Physics Letters B*, vol. 711, no. 1, pp. 62–64, 2012.
- [13] P. Vogel and M. R. Zirnbauer, "Suppression of the two-neutrino double-beta decay by nuclear-structure effects," *Physical Review Letters*, vol. 57, no. 25, pp. 3148–3151, 1986.
- [14] D. Cha, " $\sigma\tau_+$  strength in nuclei," *Physical Review C*, vol. 27, no. 5, pp. 2269–2281, 1983.
- [15] T. Tomoda and A. Faessler, "Suppression of the neutrinoless  $\beta\beta$  decay?" *Physics Letters B*, vol. 199, no. 4, pp. 475–481, 1987.
- [16] K. Muto, E. Bender, and H. V. Klapdor, "Effects of ground-state correlations on  $2\nu\beta\beta$  decay rates and limitations of the QRPA approach," *Zeitschrift für Physik A Atomic Nuclei*, vol. 334, no. 2, pp. 177–186, 1989.
- [17] M. K. Cheoun, A. Bobyk, A. Faessler, F. Šimković, and G. Teneva, "Two-neutrino double-beta decay in coupled QRPA with neutron-proton pairing," *Nuclear Physics A*, vol. 564, no. 3, pp. 329–344, 1993.
- [18] A. A. Raduta, A. Faessler, and D. S. Delion, "Unified description of the  $2\nu\beta\beta$  decay in spherical and deformed nuclei," *Nuclear Physics A*, vol. 564, no. 2, pp. 185–203, 1993.
- [19] J. Suhonen and O. Civitarese, "Double-beta-decay nuclear matrix elements in the QRPA framework," *Journal of Physics G: Nuclear and Particle Physics*, vol. 39, no. 8, Article ID 085105, 2012.
- [20] A. Faessler, V. Rodin, and F. Šimković, "Nuclear matrix elements for neutrinoless double-beta decay and double-electron capture," *Journal of Physics G: Nuclear and Particle Physics*, vol. 39, no. 12, Article ID 124006, 2012.
- [21] F. Šimković, L. Pacearescu, and A. Faessler, "Two-neutrino double beta decay of  $^{76}\text{Ge}$  within deformed QRPA," *Nuclear Physics A*, vol. 733, no. 3-4, pp. 321–350, 2004.
- [22] R. Álvarez-Rodríguez, P. Sarriguren, E. M. de Guerra, L. Pacearescu, A. Faessler, and F. Šimković, "Deformed quasiparticle

- random phase approximation formalism for single- and two-neutrino double  $\beta$  decay,” *Physical Review C*, vol. 70, no. 6, Article ID 064309, 2004.
- [23] A. A. Raduta, A. Escuderos, A. Faessler, E. M. De Guerra, and P. Sarriguren, “Two neutrino double- $\beta$  decay in deformed nuclei with an angular momentum projected basis,” *Physical Review C*, vol. 69, no. 6, Article ID 064321, 2004.
- [24] M. S. Yousef, V. Rodin, A. Faessler, and F. Simkovic, “Two-neutrino double  $\beta$  decay of deformed nuclei within the quasiparticle random-phase approximation with a realistic interaction,” *Physical Review C*, vol. 79, no. 1, Article ID 014314, 2009.
- [25] M. T. Mustonen and J. Engel, “Large-scale calculations of the double- $\beta$  decay of  $^{76}\text{Ge}$ ,  $^{130}\text{Te}$ ,  $^{136}\text{Xe}$ , and  $^{150}\text{Nd}$  in the deformed self-consistent Skyrme quasiparticle random-phase approximation,” *Physical Review C*, vol. 87, no. 6, Article ID 064302, 9 pages, 2013.
- [26] R. Chandra, J. Singh, P. K. Rath, P. K. Raina, and J. G. Hirsch, “Two-neutrino double- $\beta$  decay of  $94 \leq A \leq 110$  nuclei for the  $0^+ \rightarrow 0^+$  transition,” *The European Physical Journal A*, vol. 23, no. 2, pp. 223–234, 2005.
- [27] S. Singh, R. Chandra, P. K. Rath, P. K. Raina, and J. G. Hirsch, “Nuclear deformation and the two-neutrino double- $\beta$  decay in  $^{124,126}\text{Xe}$ ,  $^{128,130}\text{Te}$ ,  $^{130,132}\text{Ba}$  and  $^{150}\text{Nd}$  isotopes,” *The European Physical Journal A*, vol. 33, no. 4, pp. 375–388, 2007.
- [28] T. R. Rodríguez and G. Martínez-Pinedo, “Energy density functional study of nuclear matrix elements for neutrinoless  $\beta\beta$  decay,” *Physical Review Letters*, vol. 105, no. 25, Article ID 252503, 2010.
- [29] J. Barea and F. Iachello, “Neutrinoless double- $\beta$  decay in the microscopic interacting boson model,” *Physical Review C*, vol. 79, no. 4, Article ID 044301, 16 pages, 2009.
- [30] J. Barea, J. Kotila, and F. Iachello, “Nuclear matrix elements for double- $\beta$  decay,” *Physical Review C*, vol. 87, no. 1, Article ID 014315, 2013.
- [31] Y. Yoshida, Y. Kanada-En’yo, and F. Kobayashi, “ $\alpha$ -Cluster excited states in  $^{32}\text{S}$ ,” *Progress of Theoretical and Experimental Physics*, vol. 2016, Article ID 043D01, 22 pages, 2016.
- [32] Y. Fujita, B. Rubio, and W. Gelletly, “Spin-isospin excitations probed by strong, weak and electro-magnetic interactions,” *Progress in Particle and Nuclear Physics*, vol. 66, no. 3, pp. 549–606, 2011.
- [33] D. Frekers, P. Puppe, J. H. Thies, and H. Ejiri, “Gamow-Teller strength extraction from  $(^3\text{He}, t)$  reactions,” *Nuclear Physics A*, vol. 916, pp. 219–240, 2013.
- [34] R. Madey, B. S. Flanders, B. D. Anderson et al., “Low-lying structures in the Gamow-Teller strength functions for the double-beta-decaying nuclei  $^{76}\text{Ge}$ ,  $^{82}\text{Se}$ ,  $^{128}\text{Te}$ , and  $^{130}\text{Te}$ ,” *Physical Review C*, vol. 40, no. 2, pp. 540–552, 1989.
- [35] R. L. Helmer, M. A. Punyasena, R. Abegg et al., “Gamow-Teller strength from the  $^{76}\text{Se}(n, p)^{76}\text{As}$  reaction: Implications for the double  $\beta$  decay of  $^{76}\text{Ge}$ ,” *Physical Review C*, vol. 55, no. 6, p. 2802, 1997.
- [36] S. Rakers, C. Bäumer, A. M. van den Berg et al., “Low-lying  $\text{GT}^+$  strength in  $\text{In}^{116}$  from a  $(d, \text{He}^2)$  reaction experiment and its implications for  $\text{Cd}^{116}$  double  $\beta$  decay,” *Physical Review C*, vol. 71, no. 5, Article ID 054313, 2005.
- [37] E.-W. Grewe, C. Bäumer, H. Dohmann et al., “The  $(d, ^2\text{He})$  reaction on  $^{76}\text{Se}$  and the double- $\beta$ -decay matrix elements for  $A = 76$ ,” *Physical Review C*, vol. 78, no. 4, Article ID 044301, 2008.
- [38] C. J. Guess, T. Adachi, H. Akimune et al., “The  $\text{Nd}^{150}(\text{He}^3, t)$  and  $\text{Sm}^{150}(t, \text{He}^3)$  reactions with applications to  $\beta\beta$  decay of  $\text{Nd}^{150}$ ,” *Physical Review C*, vol. 83, no. 6, Article ID 064318, 2011.
- [39] J. H. Thies, D. Frekers, T. Adachi et al., “The  $(^3\text{He}, t)$  reaction on  $^{76}\text{Ge}$ , and the double- $\beta$ -decay matrix element,” *Physical Review C*, vol. 86, Article ID 014304, 2012.
- [40] M. Sasano, H. Sakai, K. Yako et al., “Gamow-Teller transition strengths in the intermediate nucleus of the  $^{116}\text{Cd}$  double- $\beta$  decay by the  $^{116}\text{Cd}(p, n)^{116}\text{In}$  and  $^{116}\text{Sn}(n, p)^{116}\text{In}$  reactions at 300 MeV,” *Physical Review C*, vol. 85, no. 6, Article ID 061301, 5 pages, 2012.
- [41] P. Puppe, A. Lennarz, T. Adachi et al., “High resolution  $(^3\text{He}, t)$  experiment on the double- $\beta$  decaying nuclei  $^{128}\text{Te}$  and  $^{130}\text{Te}$ ,” *Physical Review C*, vol. 86, Article ID 044603, 2012.
- [42] J. P. Schiffer, S. J. Freeman, J. A. Clark et al., “Nuclear structure relevant to neutrinoless double  $\beta$  decay:  $^{76}\text{Ge}$  and  $^{76}\text{Se}$ ,” *Physical Review Letters*, vol. 100, no. 11, Article ID 112501, 2008.
- [43] B. P. Kay, J. P. Schiffer, S. J. Freeman et al., “Nuclear structure relevant to neutrinoless double  $\beta$  decay: the valence protons in  $^{76}\text{Ge}$  and  $^{76}\text{Se}$ ,” *Physical Review C*, vol. 79, no. 2, Article ID 021301, 4 pages, 2009.
- [44] J. Suhonen and O. Civitarese, “Effects of orbital occupancies on the neutrinoless  $\beta\beta$  matrix element of  $^{76}\text{Ge}$ ,” *Physics Letters B*, vol. 668, no. 4, pp. 277–281, 2008.
- [45] F. Šimkovic, A. Faessler, and P. Vogel, “ $0\nu\beta\beta$  nuclear matrix elements and the occupancy of individual orbits,” *Physical Review C*, vol. 79, no. 1, Article ID 015502, 2009.
- [46] J. Menéndez, A. Poves, E. Caurier, and F. Nowacki, “Occupancies of individual orbits, and the nuclear matrix element of the  $^{76}\text{Ge}$  neutrinoless  $\beta\beta$  decay,” *Physical Review C*, vol. 80, no. 4, Article ID 048501, 2009.
- [47] O. Moreno, E. Moya de Guerra, P. Sarriguren, and A. Faessler, “Theoretical mean-field and experimental occupation probabilities in the double- $\beta$  decay system  $^{76}\text{Ge}$  to  $^{76}\text{Se}$ ,” *Physical Review C*, vol. 81, no. 4, Article ID 041303, 2010.
- [48] P. Sarriguren, “Shape mixing and  $\beta$ -decay properties of neutron-deficient Kr and Sr isotopes,” *Physical Review C*, vol. 79, no. 4, Article ID 044315, 2009.
- [49] P. Sarriguren, “Deformation effects on the Gamow-Teller strength distributions in the double- $\beta$  decay partners  $^{76}\text{Ge}$  and  $^{76}\text{Se}$ ,” *Physical Review C*, vol. 86, no. 3, Article ID 034335, 2012.
- [50] P. Sarriguren, O. Moreno, and E. Moya de Guerra, “Gamow-teller strength distributions in the double-beta decay partners  $^{128,130}\text{Te}$  and  $^{128,130}\text{Xe}$ ,” *Romanian Journal of Physics*, vol. 58, pp. 1242–1250, 2013.
- [51] D. Navas-Nicolás and P. Sarriguren, “Gamow-Teller properties of the double- $\beta$ -decay partners  $^{116}\text{Cd}(\text{Sn})$  and  $^{150}\text{Nd}(\text{Sm})$ ,” *Physical Review C*, vol. 91, no. 2, Article ID 024317, 2015.
- [52] J. Abad, A. Morales, R. Nuñez-Lagos, and A. F. Pacheco, “An estimation for the half-lives of nuclear double beta emitters,” *Anales de Física A*, vol. 80, pp. 9–14, 1984.
- [53] P. Sarriguren, E. Moya de Guerra, A. Escuderos, and A. C. Carrizo, “ $\beta$  Decay and shape isomerism in  $^{74}\text{Kr}$ ,” *Nuclear Physics A*, vol. 635, no. 1-2, pp. 55–85, 1998.
- [54] P. Sarriguren, E. Moya de Guerra, and A. Escuderos, “Shapes and  $\beta$ -decay in proton rich Ge, Se, Kr and Sr isotopes,” *Nuclear Physics A*, vol. 658, no. 1, pp. 13–44, 1999.
- [55] P. Sarriguren, E. Moya de Guerra, and A. Escuderos, “Spin-isospin excitations and half-lives of medium-mass deformed nuclei,” *Nuclear Physics A*, vol. 691, no. 3-4, pp. 631–648, 2001.

- [56] D. Vautherin, "Hartree-fock calculations with skyrme's interaction. II. Axially deformed nuclei," *Physical Review C*, vol. 7, no. 1, pp. 296–316, 1973.
- [57] E. Chabanat, P. Bonche, P. Haensel, J. Meyer, and R. Schaeffer, "A Skyrme parametrization from subnuclear to neutron star densities part II. Nuclei far from stabilities," *Nuclear Physics A*, vol. 635, no. 1-2, pp. 231–256, 1998.
- [58] P. Sarriguren, E. Moya de Guerra, L. Pacearescu, A. Faessler, F. Šimkovic, and A. A. Raduta, "Gamow-Teller strength distributions in  $^{76}\text{Ge}$  and  $^{76}\text{Se}$  from deformed quasiparticle random-phase approximation," *Physical Review C*, vol. 67, no. 4, Article ID 044313, 2003.
- [59] P. Möller and J. Randrup, "New developments in the calculation of  $\beta$ -strength functions," *Nuclear Physics A*, vol. 514, no. 1, pp. 1–48, 1990.
- [60] K. Muto, E. Bender, and H. V. Klapdor, "Proton-neutron quasiparticle RPA and charge-changing transitions," *Zeitschrift für Physik A: Atomic Nuclei*, vol. 333, no. 2, pp. 125–129, 1989.
- [61] K. Muto, E. Bender, T. Oda, and H. V. Klapdor-Kleingrothaus, "Proton-neutron quasiparticle RPA with separable Gamow-Teller forces," *Zeitschrift für Physik A: Hadrons and Nuclei*, vol. 341, no. 4, pp. 407–415, 1992.
- [62] H. Homma, E. Bender, M. Hirsch, K. Muto, H. V. Klapdor-Kleingrothaus, and T. Oda, "Systematic study of nuclear  $\beta$  decay," *Physical Review C*, vol. 54, no. 6, pp. 2972–2985, 1996.
- [63] D. Fang, A. Faessler, V. Rodin, M. S. Yousef, and F. Šimkovic, "Running sums for  $2\nu\beta\beta$ -decay matrix elements within the quasiparticle random-phase approximation with account for deformation," *Physical Review C*, vol. 81, no. 3, Article ID 037303, 4 pages, 2010.
- [64] A. Bohr and B. R. Mottelson, *Nuclear Structure*, vol. 1, Benjamin, New York, NY, USA, 1969.
- [65] A. Bohr and B. R. Mottelson, *Nuclear Structure*, vol. 2, Benjamin, New York, NY, USA, 1975.
- [66] F. Osterfeld, "Nuclear spin and isospin excitations," *Reviews of Modern Physics*, vol. 64, no. 2, pp. 491–557, 1992.
- [67] G. F. Bertsch and I. Hamamoto, "Gamow-Teller strength at high excitations," *Physical Review C*, vol. 26, no. 3, pp. 1323–1326, 1982.
- [68] J. Suhonen and O. Civitarese, "Single and double beta decays in the  $A=100$ ,  $A=116$  and  $A=128$  triplets of isobars," *Nuclear Physics A*, vol. 924, pp. 1–23, 2014.
- [69] J. Suhonen and O. Civitarese, "Probing the quenching of  $g_A$  by single and double beta decays," *Physics Letters B*, vol. 725, no. 1–3, pp. 153–157, 2013.
- [70] P. Pirinen and J. Suhonen, "Systematic approach to  $\beta$  and  $2\nu\beta\beta$  decays of mass  $A = 100$ –136 nuclei," *Physical Review C*, vol. 91, no. 5, Article ID 054309, 17 pages, 2015.
- [71] A. Faessler, G. L. Fogli, E. Lisi, V. Rodin, A. M. Rotunno, and F. Šimkovic, "Overconstrained estimates of neutrinoless double beta decay within the QRPA," *Journal of Physics G: Nuclear and Particle Physics*, vol. 35, no. 7, Article ID 075104, 2008.
- [72] O. Moreno, R. Álvarez-Rodríguez, P. Sarriguren, E. Moya de Guerra, F. Šimkovic, and A. Faessler, "Single- and low-lying-states dominance in two-neutrino double-beta decay," *Journal of Physics G: Nuclear and Particle Physics*, vol. 36, no. 1, Article ID 015106, 2009.
- [73] D. L. Fang, A. Faessler, V. Rodin, and F. Šimkovic, "Neutrinoless double- $\beta$  decay of  $^{150}\text{Nd}$  accounting for deformation," *Physical Review C*, vol. 82, Article ID 051301, 2010.
- [74] J. Kotila and F. Iachello, "Phase-space factors for double- $\beta$  decay," *Physical Review C*, vol. 85, Article ID 034316, 2012.
- [75] A. Neacsu and M. Horoi, "An effective method to accurately calculate the phase space factors for  $\beta^-\beta^-$  decay," *Advances in High Energy Physics*, vol. 2016, Article ID 7486712, 8 pages, 2016.
- [76] I. Hamamoto and H. Sagawa, "Charge-exchange spin monopole modes," *Physical Review C*, vol. 62, no. 2, Article ID 024319, 2000.
- [77] D. R. Bes, O. Civitarese, and J. Suhonen, "Schematic and realistic model calculations of the isovector spin monopole excitations in  $^{116}\text{In}$ ," *Physical Review C*, vol. 86, no. 2, Article ID 024314, 2012.
- [78] O. Civitarese and J. Suhonen, "Strength of  $J^\pi = 1^+$  Gamow-Teller and isovector spin monopole transitions in double- $\beta$ -decay triplets," *Physical Review C*, vol. 89, no. 4, Article ID 044319, 2014.
- [79] C. Wrede, S. K. L. Sjuve, A. García et al., "Electron capture on  $^{116}\text{In}$  and implications for nuclear structure related to double- $\beta$  decay," *Physical Review C*, vol. 87, no. 3, Article ID 031303, 2013.
- [80] D. S. Delion and J. Suhonen, "Double- $\beta$  decay within a consistent deformed approach," *Physical Review C*, vol. 91, no. 5, Article ID 054329, 2015.
- [81] O. Civitarese and J. Suhonen, "Is the single-state dominance realized in double- $\beta$ -decay transitions?" *Physical Review C*, vol. 58, no. 3, pp. 1535–1538, 1998.
- [82] O. Civitarese and J. Suhonen, "Systematic study of the single-state dominance in  $2\nu\beta\beta$  decay transitions," *Nuclear Physics A*, vol. 653, no. 3, pp. 321–337, 1999.
- [83] P. Domin, S. Kovalenko, F. Šimkovic, and S. V. Semenov, "Neutrino accompanied  $\beta \pm \beta \pm$ ,  $\beta + \text{EC}$  and  $\text{EC}/\text{EC}$  processes within single state dominance hypothesis," *Nuclear Physics A*, vol. 753, no. 3-4, pp. 337–363, 2005.
- [84] F. Šimkovic, P. Domin, and S. V. Semenov, "The single state dominance hypothesis and the two-neutrino double beta decay of  $^{100}\text{Mo}$ ," *Journal of Physics G: Nuclear and Particle Physics*, vol. 27, no. 11, article 2233, 2001.
- [85] J. C. Hardy and I. S. Towner, "Superallowed  $0^+ \rightarrow 0^+$  nuclear  $\beta$  decays: 2014 critical survey, with precise results for  $V_{ud}$  and CKM unitarity," *Physical Review C*, vol. 91, no. 2, Article ID 025501, 2015.
- [86] F. Šimkovic, V. Rodin, A. Faessler, and P. Vogel, " $0\nu\beta\beta$  and  $2\nu\beta\beta$  nuclear matrix elements, quasiparticle random-phase approximation, and isospin symmetry restoration," *Physical Review C*, vol. 87, no. 4, Article ID 045501, 2013.

## Research Article

# New Phase Space Calculations for $\beta$ -Decay Half-Lives

Sabin Stoica,<sup>1,2</sup> Mihail Mirea,<sup>1,2</sup> Ovidiu Nițescu,<sup>2,3</sup> Jameel-Un Nabi,<sup>4</sup> and Mavra Ishfaq<sup>4</sup>

<sup>1</sup>Horia Hulubei Foundation, P.O. MG6, 077125 Magurele, Romania

<sup>2</sup>Horia Hulubei National Institute of Physics and Nuclear Engineering, P.O. Box MG6, 077125 Magurele, Romania

<sup>3</sup>Faculty of Physics, University of Bucharest, P.O. Box MG11, 077125 Magurele, Romania

<sup>4</sup>GIK Institute of Engineering Sciences and Technology, Topi 23640, Khyber Pakhtunkhwa, Pakistan

Correspondence should be addressed to Sabin Stoica; stoica@theory.nipne.ro

Received 23 June 2016; Accepted 5 October 2016

Academic Editor: Theocharis Kosmas

Copyright © 2016 Sabin Stoica et al. This is an open access article distributed under the Creative Commons Attribution License, which permits unrestricted use, distribution, and reproduction in any medium, provided the original work is properly cited. The publication of this article was funded by SCOAP<sup>3</sup>.

We revisit the computation of the phase space factors (PSF) involved in the positron decay and EC processes for a large number of nuclei of experimental interest. To obtain the electron/positron wave functions, we develop a code for solving accurately the Dirac equation with a nuclear potential derived from a realistic proton density distribution in the nucleus. The finite nuclear size (FNS) and screening effects are included through recipes which differ from those used in previous calculations. Comparing our results with previous calculations, performed with the same  $Q$ -values, we find a close agreement for positron decays, while, for the EC process, there are relevant differences. For the EC process, we also find that the screening effect has a notable influence on the computed PSF values especially for light nuclei. Further, we recomputed the same PSF values but using the most recent  $Q$ -values reported in literature. In several cases, the new  $Q$ -values differ significantly from the older ones, leading to large differences in the PSF values as compared with previous results. Our new PSF values can contribute to more reliable calculations of the beta-decay rates, used in the study of nuclei far from the stability line and stellar evolution.

## 1. Introduction

The phase space factors for beta decay and electron capture were calculated since a long time [1–3] and were considered to be evaluated with sufficient accuracy. However, in those works, the distortion of the electron wave functions (w.f.) by the Coulomb field of the nucleus was taken into account through Fermi functions which were expressed in terms of approximate radial solutions of the Dirac equation at the nuclear surface. Also, other corrections were introduced in the calculations in approximate ways. Thus, the screening effect on  $\beta$  spectrum was included by various recipes, for example, by replacing  $V(Z)$  potential with a momentum dependent screening (for low energy positrons) [3] and by modifying the electron radial w.f. [4, 5]. Also, the finite size of the nucleus (FNS) was taken into account by adding to the Fermi functions obtained in the “point-nucleus” approximation corrections that depend on  $\beta$ -particle energy and nuclear charge  $Z$  [6, 7]. Also, for the nuclear radius, older formula has

been used [3, 8]. For the EC process, the electron bound-state radial w.f. were also obtained as approximate solution of the Dirac equation evaluated at the nuclear surface. They were improved by including exchange and overlap corrections, which were obtained within a relativistic HF approach.

In this work, we revisit the computation of the PSF involved in the positron decay and electron capture (EC) processes for light and heavy nuclei of experimental interest. The Dirac equation is solved numerically with a Coulomb potential derived from a realistic proton distribution in the nucleus which includes the FNS correction. The numerical procedure follows the power series method described in [9] and is similar to that described in [10, 11]. The screening effect was introduced by using a screened Coulomb potential, obtained by multiplying the Coulomb potential by function  $\phi(x)$ , solution of the Thomas-Fermi equation obtained by the Majorana method [12]. The accuracy imposed in our numerical algorithms used to solve the Dirac equation always exceeds the convergence criteria given in those references.

Also, a more efficient procedure to identify the electron bound states without ambiguity was developed.

In order to make a comparison between the actual PSF values found in literature and ours, the same PSF are also computed with the approach described in [2, 3] and using the same  $Q$ -values. For positron decays, our results are in close agreement with the other previous results, while, for the EC process, we found significant differences. For these processes, we also find that the screening effect has a notable influence on the computed PSF values for light nuclei. Further, we recomputed the same PSF values using updated  $Q$ -values, reported recently in literature [13, 14], which, for several light nuclei, differ significantly from the older ones. As an example we cite the maximum  $\beta$ -particle energy (referred to as  $W_0$  throughout this paper) stated in Table 2 of [15]. These  $W_0$ -values differ considerably from those given in [13, 14]. One reason for this big difference could be that Wilkinson and Macefield, in order to compare their calculation with those performed earlier by Towner and Hardy [16], restricted their phase space to only pure Fermi transitions. In other words, the Gamow-Teller window was not accessed in phase space calculation of [15]. Thus, in this paper, we propose new PSF values computed with a more accurate method and using updated  $Q$ -values, for a large number of nuclei of experimental interest. Our calculations can be useful for more reliable computation of the beta-decay rates of nuclei far from the stability line, as well as for better understanding of the stellar evolution.

Our work is further motivated by similar calculations done for the double beta-decay (DBD) process. The PSF for DBD were also considered for a long time to be computed with enough accuracy and were used as such for predicting DBD lifetimes. However, recently, they were recalculated with improved methods, especially for positron and EC decay modes [17, 18], and several differences were found as compared to previous calculations where approximate electron/positron w.f. were used.

The paper is organized as follows. In Section 2, we present briefly the two approaches used to compute our PSF values. Our results are reported in Section 3. Here, we compare them with experimental data and previous results and discuss the differences. Finally, we summarize the main points and present our conclusions in Section 4.

## 2. Formalism

Following essentially the formalism from [3], we give here the necessary equations which we use to calculate the PSF.

**2.1. Phase Space Factors for  $\beta^+$  Transitions.** The probability per unit time that a nucleus with atomic mass  $A$  and charge  $Z$  decays for an allowed  $\beta$ -branch is given by

$$\lambda_0 = \frac{g^2}{2\pi^3} \int_1^{W_0} pW (W_0 - W)^2 S_0(Z, W) dW, \quad (1)$$

where  $g$  is the weak interaction coupling constant,  $p$  is the momentum of  $\beta$ -particle,  $W = \sqrt{p^2 + 1}$  is the total energy of

$\beta$ -particle, and  $W_0$  is the maximum  $\beta$ -particle energy.  $W_0 = Q - 1$ , in  $\beta^+$  decay ( $Q$  is the mass difference between initial and final states of neutral atoms). Equation (1) is written in natural units ( $\hbar = m = c = 1$ ) so that the unit of momentum is  $mc$ , the unit of energy is  $mc^2$ , and the unit of time is  $\hbar/mc^2$ . Shape factors  $S_0(Z, W)$  for allowed transitions which appear in (1) are defined as

$$S_0(Z, W) = \lambda_1(Z, W) |M_{0,1}|^2, \quad (2)$$

where  $M_{0,1}$  are the nuclear matrix elements and the Fermi functions  $\lambda_1(Z, W)$ . Thus, for calculating the  $\beta^+$  decay rates, one needs to calculate the nuclear matrix elements and the PSF that can be defined as

$$F_{\text{BP}} = \int_1^{W_0} pW (W_0 - W)^2 \lambda_1(W) dW. \quad (3)$$

For the allowed  $\beta$  decays, the Fermi functions are expressed as

$$\lambda_1(Z, W) = \frac{g_{-1}^2 + f_1^2}{2p^2}, \quad (4)$$

where  $g_{-1}(Z, W)$  and  $f_1(Z, W)$  are the large and the small radial components of the positron radial wave functions evaluated at nuclear radius  $R$  which can be obtained by solving the Dirac equation:

$$\begin{aligned} & \frac{d}{dr} \begin{pmatrix} g_\kappa(W, r) \\ f_\kappa(W, r) \end{pmatrix} \\ &= \begin{pmatrix} -\frac{\kappa}{r} & (W + V + 1) \\ -(W + V + 1) & -\frac{\kappa}{r} \end{pmatrix} \begin{pmatrix} g_\kappa(W, r) \\ f_\kappa(W, r) \end{pmatrix}, \end{aligned} \quad (5)$$

where  $V$  is the central potential for the positron and  $\kappa = (l - j)(2j + 1)$  is the relativistic quantum number. We note that (5) is also written in natural units.

An important step in the PSF calculation for  $\beta^+$  decay is the method of obtaining the positron continuum radial functions. For this, we develop a new method (code) of solving the Dirac equation, which is adapted from the method used previously for the computation of PSF for DBD process [18, 20].

We solved (5) in a nuclear potential  $V(r)$  derived from a realistic proton density distribution in the nucleus. This is done by solving the Schrodinger equation with a Woods-Saxon potential. In this case,

$$V(Z, r) = \alpha \hbar c \int \frac{\rho_e(\vec{r}')}{|\vec{r} - \vec{r}'|} d\vec{r}', \quad (6)$$

where the charge density is

$$\rho_e(\vec{r}) = \sum_i (2j_i + 1) v_i^2 |\Psi_i(\vec{r})|^2, \quad (7)$$

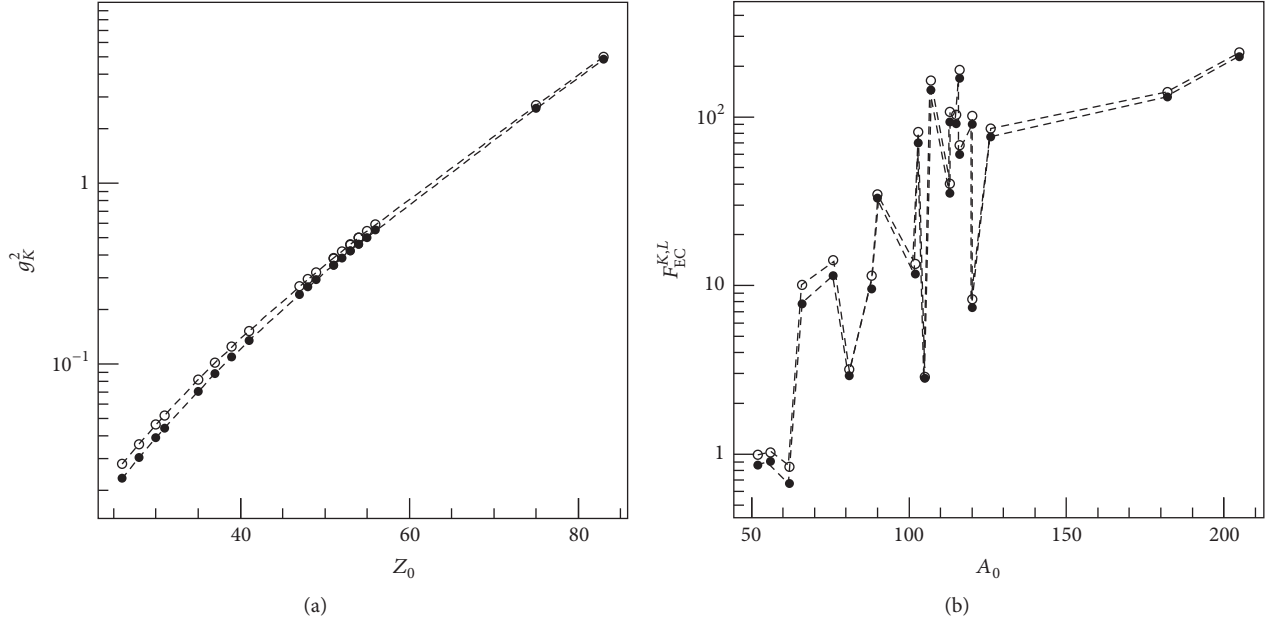


FIGURE 1: (a) Electron density on the nuclear surface of  $1s_{1/2}$  state as a function of the atomic number of the parent nucleus. The values calculated with screening are displayed with filled circles and those without screening are plotted with empty symbols. The dashed lines are given to guide the eye. (b) Calculated PSF for EC as a function of the mass number of the parent nucleus. The filled circles display the calculation with screening, while the empty ones the calculation without screening.

where  $\Psi_i$  is the proton (Woods-Saxon) w.f. of the spherical single particle state  $i$  and  $v_i$  is its occupation amplitude. Factor  $(2j_i + 1)$  reflects the spin degeneracy.

The screening effect is taken into account by multiplying the expression of  $V(r)$  with function  $\phi(r)$ , which is the solution of the Thomas-Fermi equation:  $d^2\phi/dx^2 = \phi^{3/2}/\sqrt{x}$ , with  $x = r/b$ ,  $b \approx 0.8853a_0Z^{-1/3}$  and  $a_0 =$  Bohr radius. It is calculated within the Majorana method [12]. The boundary conditions are  $\phi(0) = 1$  and  $\phi(\infty) = 0$ . As mentioned above, the screening effect is taken into account by a method developed in [12]. The possible ways in which the screening function modifies the Coulomb potential depend on the specific mechanism and its boundary conditions.

For the case of  $\beta^+$ -decay process, the potential used to obtain the electron w.f. is

$$rV_{\beta^+}(Z, r) = (rV(Z, r) + 1) \times \phi(r) - 1 \quad (8)$$

to take into account the fact that  $\beta$  decay releases a final negative ion with charge  $-1$ .  $V(Z, r)$  is positive. In our approach, we considered the solution of the Thomas-Fermi equation as a universal function, giving an effective screening. Here, product  $\alpha\hbar c = 1$ , for atomic units. The asymptotic potential between an positron and an ionized atom is  $rV_{\beta^+} = -1$ . In this case, the charge number  $Z = Z_0 - 1$  corresponds to the daughter nucleus,  $Z_0$  being the charge number of the parent nucleus. Asymptotically,  $\phi(r)$  tends to zero.

In this case, the radial solutions of the Dirac equations should be normalized in order to have the following asymptotic behavior:

$$\begin{pmatrix} g_k(\epsilon, r) \\ f_k(\epsilon, r) \end{pmatrix} \sim \frac{\hbar e^{-i\delta_k}}{pr} \cdot \begin{pmatrix} \sqrt{\frac{\epsilon + m_e c^2}{2\epsilon}} \sin\left(kr - l\frac{\pi}{2} - \eta \ln(2kr) + \delta_k\right) \\ \sqrt{\frac{\epsilon - m_e c^2}{2\epsilon}} \cos\left(kr - l\frac{\pi}{2} - \eta \ln(2kr) + \delta_k\right) \end{pmatrix}, \quad (9)$$

where  $c$  is the speed of the light,  $m_e/\epsilon$  are the electron mass/energy,  $k = p/\hbar$  is the electron wave number,  $\eta = Ze^2/\hbar v$  (with  $Z = \pm Z$  for  $\beta^\mp$  decays) is the Sommerfeld parameter,  $\delta_k$  is the phase shift, and  $V$  is the Coulomb interaction energy between the electron and the daughter nucleus.

On the other side, we also calculated the PSF for positron decays with the method described in [3].  $g_k$  and  $f_k$  functions were calculated by solving the Dirac equation for a point-nucleus unscreened Coulomb potential, for which the equation has analytical solutions. The finite nuclear size and screening effects were introduced as corrections, after the recipe described in [3]. The finite-size correction was introduced by means of an empirical deviation that depended

on atomic mass  $Z$  and energy  $W$  [6, 7]. The screening correction was given by the following replacement [4, 5]:

$$\begin{aligned} g_{-1}^2(Z, W) &\longrightarrow \frac{pW'}{p'W} g_{-1}^2(Z, W'), \\ f_{-1}^2(Z, W) &\longrightarrow \frac{pW'}{p'W} f_{-1}^2(Z, W'), \end{aligned} \quad (10)$$

where  $W' = W + V_0$ ,  $p' = \sqrt{(W')^2 - 1}$  and  $V_0$  was taken as a  $p$ -dependent screening potential. For further details of this formalism, we refer to [3]. No electromagnetic corrections were undertaken in this calculation of PSF.

**2.2. Phase Space Factors for Electron Capture (EC).** Electron capture is always an alternate decay mode for radioactive isotopes that do not have sufficient energy to decay by positron emission. This is a process which competes with positron decay. In order for electron capture leading to a vacancy in, say,  $K$ -shell, the atomic mass difference between initial and final states,  $Q$ , must be greater than the binding energy of  $K$ -shell electron in the daughter atom,  $\epsilon_K$ . The energy carried off by the neutrino is then given by

$$q_K = Q - \epsilon_K. \quad (11)$$

If the energy requirement  $Q > \epsilon_K$  is satisfied, electron capture from  $K$ -shell is more probable than that from any other shell because of the greater density at the nucleus of  $K$ -shell electrons. The total  $K$ -shell capture rate can be expressed as

$$\lambda_{\text{EC},K}^0 = \lambda_K^0 B_K, \quad (12)$$

where

$$\lambda_K^0 = \frac{g^2 |M_{0,1}|^2}{4\pi^2} q_K^2 g_K^2, \quad (13)$$

where  $g^2$  is a constant (with dimensions of  $t^{-1}$ ),  $M_{0,1}$  are specific combinations of nuclear matrix elements,  $g_K$  is the large component of the bound-state radial w.f. of the captured  $K$ -shell electron (evaluated at the nuclear surface  $R_A$ ),  $q_K$  is the neutrino energy in units of  $mc^2$ , and  $B_K$  is the ‘‘exchange’’ correction factor for the  $K$ -shell. In analogy with (12),  $L$ -shell total capture rate will be

$$\lambda_{\text{EC},L_i}^0 = \lambda_{L_i}^0 B_{L_i}, \quad (14)$$

where  $L_i$  denotes a particular  $L$ -subshell. The contribution of  $L_1$  pertaining to  $2s_{1/2}$  orbital is the most important, so we keep in our calculations only the contribution of this subshell to the calculated our PSF. The expressions for  $\lambda_{L_1}^0$  can be obtained from (13) by the replacement of  $q_K$ ,  $g_K$  by  $q_{L_1}$ ,  $g_{L_1}$ . Electron capture from  $M$ -,  $N$ -, and higher shells may be defined in a similar fashion, but they have negligible contributions in comparison with  $K$ - and  $L$ -shells.

Hence, for an allowed transition, the PSF expression of electron capture within the approximation stated above can be written as

$$F_{\text{EC}}^{K,L_1} = \frac{\pi}{2} \left( q_K^2 g_K^2 B_K + q_{L_1}^2 g_{L_1}^2 B_{L_1} \right). \quad (15)$$

For  $q_{K/L_1}$  quantities, we used the expression

$$q_{K/L_1} = W_{\text{EC}} - \epsilon_{K/L_1}, \quad (16)$$

where  $W_{\text{EC}}$  is  $Q$  value of  $\beta^+$  decay in  $m_e c^2$  units,  $\epsilon_i$  are the binding energies of  $1s_{1/2}$  and  $2s_{1/2}$  electron orbitals of the parent nucleus, and  $g_i$  are their radial densities on the nuclear surface.  $B_i \approx 1$  represent the values of the exchange correction. These are due to an imperfect overlap of the initial and final atomic states caused by the one unit charge difference [21]. In our method, we consider these exchange corrections to be unity, for the nuclei considered, the estimated error in doing that being under 1%. Relation  $W_0 = W_{\text{EC}} - 1$  holds.

$g_{K/L_1}$  are the electron bound states, solutions of the Dirac equation (5), and correspond to eigenvalues  $\epsilon_n$  ( $n$  is the radial quantum number). Quantum number  $\kappa$  is related to total angular momentum  $j_\kappa = |\kappa| - 1/2$ . These w.f. are normalized such that

$$\int_0^\infty [g_{n,\kappa}^2(r) + f_{n,\kappa}^2(r)] dr = 1. \quad (17)$$

For simplicity, we consider solutions of Dirac equations  $g_{n,\kappa}$  and  $f_{n,\kappa}$  that are divided by radial distance  $r$ . An asymptotic solution is obtained by means of the WKB approximation and by considering that potential  $V$  is negligibly small:

$$\frac{f_{n,\kappa}}{g_{n,\kappa}} = \frac{c\hbar}{\epsilon + m_e c^2} \left( \frac{g'_{n,\kappa}}{g_{n,\kappa}} + \frac{\kappa}{r} \right), \quad (18)$$

where

$$\frac{g'_{n,\kappa}}{g_{n,\kappa}} = -\frac{1}{2} \mu' \mu^{-1} - \mu, \quad (19)$$

with

$$\mu = \left[ \frac{\epsilon + m_e c^2}{\hbar^2 c^2} (V - \epsilon + m_e c^2) + \frac{\kappa^2}{r^2} \right]^{1/2}. \quad (20)$$

In our calculations, we use number nodes  $n = 0$  and  $n = 1$ , for orbitals  $1s_{1/2}$  and  $2s_{1/2}$ , respectively,  $\kappa$  being  $-1$ . Numerically, the eigenvalues of the discrete spectrum are obtained by matching two numerical solutions of the Dirac equation: the inverse solution that starts from the asymptotic conditions and the direct one that starts at  $r = 0$ .

The radial density of the bound-state electron w.f. on the nuclear surface is

$$\begin{aligned} D_{n,\kappa}^2 &= \frac{1}{(m_e c^2)^3} \left( \frac{\hbar c}{a_0} \right)^3 \left( \frac{a_0}{R_A} \right)^2 [g_{n,\kappa}^2(R_A) + f_{n,\kappa}^2(R_A)], \end{aligned} \quad (21)$$

where  $R_A = 1.2A_0^{1/3}$  is given in fm,  $a_0$  being the Bohr radius. For  $1s_{1/2}$  and  $2s_{1/2}$  electron orbitals, we use  $g_K^2 = D_{0,-1}^2$  and  $g_{L_1}^2 = D_{1,-1}^2$ , respectively.

For the EC processes, the potential used to obtain the electron w.f. reads

$$rV_{\text{EC}}(Z, r) = rV(Z, r)\phi(r), \quad (22)$$

and charge number  $Z = Z_0$  corresponds to the parent nucleus.  $V(Z, r)$  is negative.

The numerical solutions of the Dirac equation were obtained within the power series method of [9], by using similar numerical algorithm as that of [10, 11]. The method is able to provide numerical solutions of the Dirac equation for central fields. We provide a grid with values of the potential for different radial distances. The radial w.f. is expanded in an infinite power series that depends on the radial increment and the potential values. The w.f. is calculated step by step in the mesh points. The increment and the number of terms in the series expansion determine the accuracy of the solutions. In our calculations, the increment interval is  $10^{-4}$  fm and at least 100 terms are taken into account in the series expansion. These values exceed the convergence criteria of [10]. To renormalize the numerical solutions, we made use of the fact that, at very large distances, the behavior of the w.f. must approach that of the Coulomb function. Therefore, the amplitudes and the phase shifts can be extracted by comparing the numerical solution and the analytical ones. For discrete states, the asymptotic behavior of the w.f. gives a guess for the inverse solutions. The eigenvalue is obtained when the direct solutions and the inverse ones match each other. We constructed an adequate procedure to find the bound states of the electron up to an accuracy of 0.3 keV, or lower, by searching solutions up to 130 keV binding energies. In this range of energies, all the possible bound-state energies are found. We calculated the solutions starting outward from  $r = 0$  and inward from a very large value of radius  $r$ . The bound states should be obtained when both solutions are equal in an intermediate point, for the two components of the wave function. We found these energies by interpolation. We selected radial wave functions  $f_{n,\kappa}$  and  $g_{n,\kappa}$  that have the same number of nodes  $n = 0$  or 1.

For the PSF computation, all integrals in (5) were performed accurately with Gauss-Legendre quadrature in 32 points. We calculated up to 49 values of the radial functions in  $Q$  value energy interval, that were interpolated with spline functions.

We also calculated the PSF for EC process using (15) but employing essentially the formalism adopted by [2]. Here, we used the electron radial density (and density ratios) as given in Table 2 of [2]. Exchange corrections were taken as unity. Binding energies were also taken from the same reference.

### 3. Results and Discussion

We perform PSF computations for  $\beta^+$  decay and the EC process with the method described in the previous section that we call TW (this work), for a large number of nuclei of experimental interest.

For  $\beta^+$  decays, we found previous PSF results computed with approximate methods [15, 16], for sixteen nuclei of astrophysical interest. In Table 1, we display the PSF values for these nuclei calculated with our new method (TW) and, for comparison, the values taken from [15, 16]. Also, we present the PSF values computed by us using the recipe described in [3]. All calculations were done with  $W_0$  value indicated in

TABLE 1: Calculated phase space of  $\beta^+$ -decay (BP) compared with previous calculations. The value of maximum  $\beta$ -decay energy is taken from [15] for pure Fermi transitions. The last two columns show our calculated results.

Nucleus	$W_0$ [15] (MeV)	$F_{BP}$ [16]	$F_{BP}$ [15]	$F_{BP}$ [TW]	$F_{BP}$ [3]
$^{10}\text{C}$	0.8884	2.361	2.361	2.325	2.326
$^{14}\text{O}$	1.8098	43.398	43.378	42.822	42.814
$^{18}\text{Ne}$	2.383	136.83	136.83	135.19	135.08
$^{22}\text{Mg}$	3.109	427.02	426.88	422.19	421.51
$^{26}\text{Al}$	3.211	483.84	483.68	478.3	477.43
$^{26}\text{Si}$	3.817	1036.8	1035.9	1025.51	1023.059
$^{30}\text{S}$	4.439	1990.2	1987.8	1969.24	1963.9
$^{34}\text{Cl}$	4.468	2014.7	2013.4	1993.13	1987.4
$^{34}\text{Ar}$	5.021	3388.3	3383.8	3351.58	3339.85
$^{38}\text{K}$	5.028	3346.9	3344.9	3312.82	3300.54
$^{38}\text{Ca}$	5.620	5515.9	5510.3	5457.95	5449
$^{42}\text{Sc}$	5.409	4533.5	4531.7	4490.19	4462.21
$^{42}\text{Ti}$	5.964	7025.4	7024.1	6934.9	6853.74
$^{46}\text{V}$	6.032	7285.9	7284.2	7186.04	7091.9
$^{50}\text{Mn}$	6.609	10818	10810	10492.76	10262
$^{54}\text{Co}$	7.227	15956	15951	14988.470	14412.5

TABLE 2: Calculated phase space of  $\beta^+$ -decay (BP) for heavy nuclei compared with the ones we calculated using recipe of [3].

Nucleus	$W_0$ [19] (MeV)	$F_{BP}$ [TW]	$F_{BP}$ [3]
$^{52}\text{Fe}$	1.3525	8.3403	8.4132
$^{56}\text{Ni}$	1.1109	3.4439	3.5250
$^{62}\text{Zn}$	0.5974	0.2344	0.2438
$^{66}\text{Ga}$	4.153	1125.6442	1132.5483
$^{76}\text{Br}$	3.9409	835.1982	843.3343
$^{81}\text{Rb}$	1.2161	4.3222	6.8878
$^{88}\text{Y}$	2.6006	120.2644	121.8624
$^{90}\text{Nb}$	5.0893	2503.0555	2533.7049
$^{102}\text{Cd}$	1.565	11.2214	11.5267
$^{103}\text{In}$	5.0005	2100.3727	2136.0153
$^{105}\text{Ag}$	0.325	0.0102	0.1127
$^{107}\text{Sb}$	6.837	8528.5047	8931.8197
$^{113}\text{Sb}$	2.8891	168.1487	172.0209
$^{113}\text{Te}$	5.048	2124.1816	2165.2927
$^{115}\text{I}$	4.7029	1517.2376	1549.2409
$^{116}\text{I}$	6.7547	7913.1790	8272.0244
$^{116}\text{Xe}$	3.235	352.3565	361.4082
$^{120}\text{Ba}$	3.98	678.0918	705.0294
$^{120}\text{Xe}$	0.5587	0.1047	0.1108
$^{126}\text{Cs}$	3.7731	542.4653	563.8184
$^{182}\text{Re}$	1.778	16.123	17.206
$^{205}\text{Bi}$	1.6835	12.3984	13.4576

[15]. One can see that the agreement between TW results and the other results is in general under 1%, except the last two (heavy) nuclei where the differences reach  $\sim 3\%$ .

In Table 2, we display our computed PSF with the new method for few heavy nuclei, for which we did not find

TABLE 3: Calculated phase space factors  $F_{\text{EC}}$  for electron capture (assuming exchange corrections to be equal to 1). The value of maximum  $\beta$ -decay energy is taken from [15] for pure Fermi transitions. The electron densities, their ratios, and binding energies  $\epsilon$  are also provided for orbitals  $1s_{1/2}$  and  $2s_{1/2}$ , including those given in [2]. Binding energies are given in units of keV.

Nucleus	$Q_{\beta^+}$ (MeV)	$g_K^2$ [2]	$g_K^2$ [TW]	$g_{L_1}^2/g_K^2$ [2]	$g_{L_1}^2/g_K^2$ [TW]	$\epsilon_K$ [2]	$\epsilon_K$ [TW]	$\epsilon_{L_1}$ [2]	$\epsilon_{L_1}$ [TW]	$F_{\text{EC}}^{K,L_1}$ [TW]	$F_{\text{EC}}^{K,L_1}$ [2]
$^{10}\text{C}^*$	1.9104	0.00031	0.00031	0.04930	0.02867	0.18790	0.62660	0.12600	0.01176	0.00703	0.00640
$^{14}\text{O}^*$	2.83186	0.00075	0.00065	0.05640	0.04420	0.40160	1.03733	0.02440	0.03251	0.03297	0.03786
$^{18}\text{Ne}^*$	3.405	0.00151	0.00118	0.05840	0.05794	0.68540	1.48302	0.03400	0.06659	0.08713	0.11005
$^{22}\text{Mg}^*$	4.131	0.00268	0.00199	0.06660	0.06811	1.07210	2.11143	0.06330	0.15721	0.218	0.29060
$^{26}\text{Al}^*$	4.2331	0.00344	0.00251	0.06990	0.07265	1.30500	2.40715	0.08940	0.14631	0.27558	0.39270
$^{26}\text{Si}^*$	4.839	0.00435	0.00312	0.07290	0.07661	1.55960	2.74689	0.11770	0.18077	0.47240	0.65060
$^{30}\text{S}^*$	5.461	0.00664	0.00467	0.07810	0.08342	2.14550	3.49498	0.18930	0.25934	0.90680	1.27140
$^{34}\text{Cl}^*$	5.4908	0.00807	0.00563	0.08040	0.08628	2.47200	3.91749	0.22920	0.30899	1.10727	1.56600
$^{34}\text{Ar}^*$	6.043	0.00970	0.00675	0.08240	0.08862	2.82240	4.33190	0.27020	0.36199	1.61130	2.28490
$^{38}\text{K}^*$	6.05	0.01156	0.00802	0.08440	0.09079	3.20600	4.77984	0.32630	0.41921	1.92311	2.73480
$^{38}\text{Ca}^*$	6.642	0.01367	0.00947	0.08620	0.09259	3.60740	5.25087	0.37710	0.48351	2.74237	3.90650
$^{42}\text{Sc}^*$	6.4311	0.01600	0.01113	0.08790	0.09430	4.03810	5.73657	0.43780	0.54865	3.02434	4.28930
$^{42}\text{Ti}^*$	6.986	0.01870	0.01300	0.08960	0.09579	4.49280	6.25222	0.50040	0.62068	4.17496	5.92320
$^{46}\text{V}^*$	7.0543	0.02170	0.01512	0.09100	0.09699	4.96640	6.78377	0.56370	0.69826	4.95575	7.02120
$^{50}\text{Mn}^*$	7.6311	0.02870	0.02016	0.09380	0.09920	5.98920	7.92722	0.69460	0.86703	7.74617	10.9103
$^{52}\text{Fe}$	2.374	0.0328	0.0232	0.0950	0.0987	7.1120	8.5130	0.8461	0.958	0.859	1.2033
$^{54}\text{Co}^*$	8.2498	0.03730	0.02651	0.09620	0.10077	7.11200	9.14731	0.84610	1.05584	11.91799	16.6144
$^{56}\text{Ni}$	2.136	0.0423	0.0303	0.0974	0.1013	8.3328	9.7882	1.0081	1.158	0.907	1.2580
$^{62}\text{Zn}$	1.626	0.0538	0.0390	0.0995	0.1025	9.6586	11.157	1.1936	1.380	0.675	0.9261
$^{66}\text{Ga}$	5.175	0.0604	0.0410	0.1006	0.1029	10.3671	11.875	1.2977	1.498	7.80	10.613
$^{76}\text{Br}$	4.963	0.0935	0.0704	0.1035	0.1048	13.4737	15.000	1.7820	2.021	11.45	15.162
$^{81}\text{Rb}$	2.23815	0.1149	0.0883	0.1063	0.1080	15.1997	16.690	2.0651	2.263	9.069	11.744
$^{88}\text{Y}$	3.6226	0.1402	0.1091	0.1080	0.1174	17.0384	18.450	2.3725	2.438	9.528	12.114
$^{90}\text{Nb}$	6.111	0.170	0.1344	0.1098	0.1059	18.9856	20.421	2.6977	2.994	33.17	41.975
$^{102}\text{Cd}$	2.587	0.319	0.2663	0.1159	0.1102	26.7112	28.044	4.0180	4.351	11.66	14.019
$^{103}\text{In}$	6.050	0.348	0.2930	0.1168	0.1116	27.9399	29.232	4.2375	4.548	71.05	84.541
$^{105}\text{Ag}$	1.345	0.293	0.2423	0.1150	0.1086	25.5140	26.864	3.8058	4.161	2.816	3.4256
$^{107}\text{Sb}$	7.920	0.413	0.3526	0.1187	0.1096	30.4912	31.726	4.6983	5.095	146.5	172.43
$^{113}\text{Sb}$	3.913	0.413	0.3516	0.1187	0.1096	30.4912	31.726	4.6983	5.095	35.38	41.804
$^{113}\text{Te}$	6.070	0.449	0.3844	0.1196	0.1113	31.8138	33.041	4.9392	5.314	93.70	109.93
$^{115}\text{I}$	5.729	0.488	0.4121	0.1205	0.1124	33.1694	34.345	5.1881	5.542	91.54	106.40
$^{116}\text{I}$	7.780	0.488	0.4215	0.1205	0.1124	33.1694	34.345	5.1881	5.542	169.3	196.75
$^{116}\text{Xe}$	4.450	0.529	0.4609	0.1215	0.1123	34.5644	35.705	5.4528	5.822	60.15	69.410
$^{120}\text{Ba}$	5.00	0.623	0.5496	0.1234	0.1130	37.4406	38.514	5.9888	6.375	90.65	103.51
$^{120}\text{Xe}$	1.617	0.529	0.4599	0.1215	0.1123	34.5644	35.705	5.4528	5.821	7.72	8.9482
$^{126}\text{Cs}$	4.824	0.574	0.501	0.1224	0.112	35.9846	37.111	5.7143	6.128	76.88	88.697
$^{182}\text{Re}$	2.800	2.69	2.593	0.1448	0.128	71.6764	72.491	12.5267	13.26	22.86	24.152
$^{205}\text{Bi}$	2.708	4.88	4.837	0.1561	0.138	90.5259	91.373	16.2370	17.25	228.17	233.83

previous results. For comparison, we computed the same PSF values with the recipe adopted from [3].  $W_0$ -values were taken from [19] for both sets of calculations. We found a rather good agreement between the two sets of results, with differences within, generally, a few percent. There was one exception,  $^{105}\text{Ag}$ , where the difference was large ( $\sim$ a factor 10). This is a case where  $W_0$ -value is very small (0.325 MeV), and this might make our numerical routine inaccurate at such small

values. However, this discrepancy may not be so significant, as long as the calculated PSF value is small enough to have little contribution to the corresponding beta-decay rates

In Table 3, we present our results for EC for the same set of nuclei.  $Q$ -values for positron decay were taken from [15] for nuclei marked with  $*$ . For the rest of nuclei,  $Q$ -values were taken from [19]. Together with the PSF values for EC, the electron densities,  $g_{K,L_1}$ , their ratios, and binding

energies  $\epsilon$  for orbitals  $1s_{1/2}$  and  $2s_{1/2}$  are also given in Table 3. We compare the results performed with the new method (TW) with those calculated using the recipe of [2]. For these transitions, the differences between the two sets of results are significantly larger than for the positron decays, ranging from a few percent to about a mammoth 35%. We attribute these differences in the calculated PSF values mainly to electron densities,  $g_K$ , whose values, calculated with the “old” and “new” methods, differ significantly from each other. We also checked the influence of the screening effect on the PSF values. We found that while, for the positron decays, this effect is very small, for the EC transitions, there are some differences between the “screened” and “unscreened” PSF values. Figure 1 shows this effect on the electron density,  $g_K$ , and on the final PSF values. For small values of  $Z$ , the results without screening give PSF values that are 10–15% larger than those listed in Table 3. For heavier nuclei, these differences are only up to 2–3%. The screening effect in PSF calculation is more important for light nuclei and leads to a decrease in the PSF values up to 15%. Finally, in Table 4, we present PSF values for EC transitions recomputed with updated  $Q$ -values taken from [13, 14]. We propose to use these new computed values of PSF for calculation of  $\beta$ -decay rates.

#### 4. Summary and Conclusion

In summary, we constructed a new code for computing PSF values for positron decays and EC processes. In our approach, we get positron-free and electron bound w.f. by solving a Dirac equation with a Coulomb-type potential, obtained from a realistic distribution of protons in the daughter nuclei. The FNS and screening effects are addressed as well by our new recipe. Using the same  $Q$ -values, we compare our results with previous calculations where electron/positron w.f. were obtained in an approximate way. For positron decays, the agreement with older results is quite good, while, for EC processes, the differences between “new” and “old” PSF values are as big as 35%. We further found that the screening effect is important for EC processes, especially for light nuclei, having an impact up to 10–15% on the calculated PSF values. Finally, using our new method, we recomputed the PSF for all nuclei using updated  $Q$ -values. We hope that these computed PSF values will prove useful in more accurate estimations of the beta-decay rates. We are currently working on the impact of newly computed PSF values on  $\beta$ -decay half-lives and hope to report our findings in the near future.

Finally, we mention that our numerical formalism for getting exact electron/positron w.f. for free and bound states is also suited for the treatment of other charged leptons, such as muons, for example, in any central field. So, it can be also used in applications such as the calculation of muon conversion capture rates. In this respect, there are works where the exact muon w.f. are obtained by solving the Dirac equation in a Coulomb-like potential, within the context of genetic algorithms and neural network techniques [22–24]. Within this method, one can also take into account deviations from a pure central Coulomb field by using experimental finite-size charge densities for the attracting nucleons, a procedure which differs from that described in this work.

TABLE 4: Calculated phase space factors  $F_{EC}$  for electron capture, with  $Q$ -values from [13, 14].

Nucleus	$Q_{EC}$ [13, 14] (MeV)	$F_{EC}$ [TW]	$F_{EC}$ [2]	$F_{BP}$ [TW]	$F_{BP}$ [3]
<sup>10</sup> C	3.64613	0.07318	2.33265	226.780	226.834
<sup>14</sup> O	5.14131	0.21794	0.12483	1644.76	1643.41
<sup>18</sup> Ne	4.44215	0.27831	0.18733	677.970	677.912
<sup>22</sup> Mg	4.77904	0.61616	0.39020	995.887	995.685
<sup>26</sup> Al	4.00231	0.62642	0.35240	343.398	343.658
<sup>26</sup> Si	5.06645	0.51788	0.71694	1339.344	1339.30
<sup>30</sup> S	6.13834	1.14585	1.61931	3805.276	3803.16
<sup>34</sup> Cl	5.48869	1.10642	1.57889	1994.797	1995.09
<sup>34</sup> Ar	6.05858	1.61963	2.31915	3410.133	3409.96
<sup>38</sup> K	5.91093	1.83565	2.64042	2917.839	2918.62
<sup>38</sup> Ca	6.73867	2.82284	4.07367	5924.355	5929.26
<sup>42</sup> Sc	6.42269	3.01643	4.33609	4470.946	4471.87
<sup>42</sup> Ti	7.01275	4.20702	6.05196	7100.190	7130.06
<sup>46</sup> V	7.04865	4.94781	7.11022	7175.692	7209.06
<sup>50</sup> Mn	7.63042	7.74479	11.0705	10516.941	10744.5
<sup>52</sup> Fe	2.37330	0.8584	1.22082	14942.286	15765.2
<sup>54</sup> Co	8.24017	11.89015	16.8306	8.354	8.43206
<sup>56</sup> Ni	2.13175	0.9029	1.27259	3.444	3.49486
<sup>62</sup> Zn	1.61859	0.6687	0.93259	0.234	0.24131
<sup>66</sup> Ga	5.17225	7.7902	10.7797	1125.644	1131.60
<sup>76</sup> Br	4.96024	11.439	15.4388	835.295	841.531
<sup>81</sup> Rb	2.23696	2.9044	3.84415	4.321	4.41092
<sup>88</sup> Y	3.62067	9.5180	12.3759	120.264	121.864
<sup>90</sup> Nb	6.10809	33.141	42.9337	2502.372	2526.00
<sup>102</sup> Cd	2.58562	11.652	14.4027	11.221	11.5468
<sup>103</sup> In	6.01928	70.333	15.7203	2099.402	2133.61
<sup>105</sup> Ag	1.34679	2.8233	3.53114	0.01027	1.12362
<sup>107</sup> Sb	7.85483	144.059	174.745	8528.505	8918.59
<sup>113</sup> Sb	3.90909	35.311	42.9919	168.122	172.036
<sup>113</sup> Te	6.06682	93.601	113.234	2124.182	2162.53
<sup>115</sup> I	5.72192	91.3148	109.531	1509.977	1547.75
<sup>116</sup> I	7.77260	168.959	202.635	7930.046	8250.78
<sup>116</sup> Xe	4.44315	59.963	71.4659	354.467	361.241
<sup>120</sup> Ba	4.99761	90.562	106.993	685.518	703.098
<sup>120</sup> Xe	1.57992	7.3638	8.82085	0.105	0.11187
<sup>126</sup> Cs	4.79256	75.871	90.4835	542.400	555.411
<sup>182</sup> Re	2.79851	131.273	145.184	16.123	17.2282
<sup>205</sup> Bi	2.70412	227.499	247.263	12.415	13.4798

#### Competing Interests

The authors declare that they have no competing interests.

#### Acknowledgments

Sabin Stoica and Mihail Mirea would like to acknowledge the support of the ANCSI-UEFISCDI through Project

PCE-IDEI-2011-3-0318, Contract no. 58.11.2011. Jameel-Un Nabi would like to acknowledge the support of the Higher Education Commission Pakistan through the HEC Project no. 20-3099.

## References

- [1] H. Behrens and J. Jänecke, "Introduction," in *Numerical Tables for Beta-Decay and Electron Capture*, H. Schopper, Ed., vol. 4 of *Landolt-Börnstein—Group I Elementary Particles, Nuclei and Atoms*, chapter 1, pp. 1–3, Springer, Berlin, Germany, 1969.
- [2] M. J. Martin and P. H. Blichert-Toft, "Radioactive atoms: Auger-electron,  $\alpha$ -,  $\beta$ -,  $\gamma$ -, and X-ray data," *Atomic Data and Nuclear Data Tables*, vol. A8, p. 1, 1970.
- [3] N. B. Gove and M. J. Martin, "Log- $f$  tables for beta decay," *Atomic Data and Nuclear Data Tables*, vol. 10, no. 3, pp. 205–219, 1971.
- [4] M. E. Rose, "A note on the possible effect of screening in the theory of  $\beta$ -disintegration," *Physical Review*, vol. 49, no. 10, pp. 727–729, 1936.
- [5] R. H. Good Jr., "Effect of atomic electron screening on the shape of forbidden beta spectra," *Physical Review*, vol. 94, no. 4, pp. 931–933, 1954.
- [6] M. E. Rose and D. K. Holmes, "The effect of finite nuclear size in beta-decay," *Physical Review*, vol. 83, no. 1, pp. 190–191, 1951.
- [7] M. E. Rose and D. K. Holmes, "The Effect of the Finite Size of the Nucleus in Beta-Decay," ORNL-I022, 1957.
- [8] R. B. Elton, *Nuclear Sizes*, Oxford University Press, London, UK, 1961.
- [9] W. Bühring, "Computational improvements in phase shift calculations of elastic electron scattering," *Zeitschrift für Physik*, vol. 187, no. 2, pp. 180–196, 1965.
- [10] F. Salvat and R. Mayol, "Accurate numerical solution of the Schrödinger and Dirac wave equations for central fields," *Computer Physics Communications*, vol. 62, no. 1, pp. 65–79, 1991.
- [11] F. Salvat, J. M. Fernández-Varea, and W. Williamson Jr., "Accurate numerical solution of the radial Schrödinger and Dirac wave equations," *Computer Physics Communications*, vol. 90, no. 1, pp. 151–168, 1995.
- [12] S. Esposito, "Majorana solution of the Thomas-Fermi equation," *American Journal of Physics*, vol. 70, pp. 852–856, 2002.
- [13] G. Audi, M. Wang, A. H. Wapstra et al., "The Ame2012 atomic mass evaluation (I)," *Chinese Physics C*, vol. 36, no. 12, pp. 1287–1602, 2012.
- [14] M. Wang, G. Audi, A. H. Wapstra et al., "The Ame2012 atomic mass evaluation," *Chinese Physics C*, vol. 36, no. 12, pp. 1603–2014, 2012.
- [15] D. H. Wilkinson and B. E. F. Macefield, "A parametrization of the phase space factor for allowed  $\beta$ -decay," *Nuclear Physics A*, vol. 232, no. 1, pp. 58–92, 1974.
- [16] I. S. Towner and J. C. Hardy, "Superallowed  $0^+ \rightarrow 0^+$  nuclear  $\beta$ -decays," *Nuclear Physics A*, vol. 205, no. 1, pp. 33–55, 1973.
- [17] J. Kotila and F. Iachello, "Phase-space factors for double- $\beta$  decay," *Physical Review C*, vol. 85, no. 3, Article ID 034316, 2012.
- [18] M. Mirea, T. Pahomi, and S. Stoica, "Values of the phase space factors involved in double beta decay," *Romanian Reports in Physics*, vol. 67, no. 3, pp. 872–889, 2015.
- [19] G. Audi and A. H. Wapstra, "The 1995 update to the atomic mass evaluation," *Nuclear Physics, Section A*, vol. 595, no. 4, pp. 409–480, 1995.
- [20] S. Stoica and M. Mirea, "New calculations for phase space factors involved in double- $\beta$  decay," *Physical Review C*, vol. 88, no. 3, Article ID 037303, 2013.
- [21] J. N. Bahcall, "Exchange and overlap effects in electron capture and in related phenomena," *Physical Review*, vol. 132, no. 1, pp. 362–367, 1963.
- [22] R. Kitano, M. Koife, and Y. Okada, "Detailed calculation of lepton flavor violating muon-electron conversion rate for various nuclei," *Physical Review D*, vol. 66, no. 9, Article ID 096002, 2002.
- [23] I. S. Kardaras, V. N. Stavrou, I. G. Tsoulos, and T. S. Kosmas, "Exact wave functions of bound  $\mu^-$  for calculating ordinary muon capture rates," *Journal of Physics: Conference Series*, vol. 410, no. 1, Article ID 012127, 2013.
- [24] T. S. Kosmas and I. E. Lagaris, "On the muon-nucleus integrals entering the neutrinoless  $\mu^- \rightarrow e^-$  conversion rates," *Journal of Physics G: Nuclear and Particle Physics*, vol. 28, no. 12, p. 2907, 2002.

## Research Article

# Warm Dark Matter Sterile Neutrinos in Electron Capture and Beta Decay Spectra

O. Moreno,<sup>1</sup> E. Moya de Guerra,<sup>1</sup> and M. Ramón Medrano<sup>2</sup>

<sup>1</sup>*Departamento de Física Atómica, Molecular y Nuclear, Facultad de Ciencias Físicas, Universidad Complutense de Madrid, 28040 Madrid, Spain*

<sup>2</sup>*Departamento de Física Teórica I, Facultad de Ciencias Físicas, Universidad Complutense de Madrid, 28040 Madrid, Spain*

Correspondence should be addressed to O. Moreno; [osmoreno@mit.edu](mailto:osmoreno@mit.edu)

Received 1 July 2016; Revised 21 September 2016; Accepted 3 October 2016

Academic Editor: Theocharis Kosmas

Copyright © 2016 O. Moreno et al. This is an open access article distributed under the Creative Commons Attribution License, which permits unrestricted use, distribution, and reproduction in any medium, provided the original work is properly cited. The publication of this article was funded by SCOAP<sup>3</sup>.

We briefly review the motivation to search for sterile neutrinos in the keV mass scale, as dark matter candidates, and the prospects to find them in beta decay or electron capture spectra, with a global perspective. We describe the fundamentals of the neutrino flavor-mass eigenstate mismatch that opens the possibility of detecting sterile neutrinos in such ordinary nuclear processes. Results are shown and discussed for the effect of heavy neutrino emission in electron capture in Holmium 163 and in two isotopes of Lead, 202 and 205, as well as in the beta decay of Tritium. We study the deexcitation spectrum in the considered cases of electron capture and the charged lepton spectrum in the case of Tritium beta decay. For each of these cases, we define ratios of integrated transition rates over different regions of the spectrum under study and give new results that may guide and facilitate the analysis of possible future measurements, paying particular attention to forbidden transitions in Lead isotopes.

## 1. Introduction

There is an inconsistency between the amount of matter inferred from gravitational effects and the one we see on observable scales. This fact leads to considering the existence of dark matter (DM). Evidence arises from astrophysical and cosmological probes [1–4], such as the kinematics of virially bound systems, rotation curves of spiral galaxies, strong and weak lensing, cosmic microwave background (CMB) information on matter density and geometry of the Universe, mass-to-light ratios in dwarf spheroidal galaxies (dSph), and large surveys to measure Universe structures. Because of the limits inferred from Big Bang nucleosynthesis, an important fraction of DM should be nonbaryonic. Although the nature of DM is still unknown, a popular hypothesis considers that DM consists of elementary particles [3, 4]. DM is the main component of galaxies, being in average at least six times more abundant than baryonic matter (more than 81% of the matter in the Universe), but its nature is still unknown. DM self-interactions have been unobserved so far, and DM

particle candidates are bound by gravitational interactions. Very distinct predictions for small scale structures in the Universe (below 100 kpc) are obtained by DM particles with different mass scales [5]. On the large mass scale side, WIMPs (weakly interacting massive particles) are popular candidates to DM that have masses of the order of GeV or even TeV. This type of particles fall in the category of cold dark matter (CDM), which predicts, for small scales, too many galaxy satellites in the Milky Way and cusped profiles for the mass density of galaxies, contradicting present observational evidences. On the contrary, particles with mass in the keV scale, namely, warm dark matter (WDM) [6–15], are able to reproduce the number of observed satellite galaxies, as well as the cored profiles found in DM-dominated objects such as dwarf spheroidal galaxies.

Concerning the satellite problem, cosmic structures would form from the gravitational collapse of overdense regions in the DM primordial field. Free relativistic particles do not cluster, and structures at scales smaller than the particle free-streaming length  $l_{fs}$  are erased. The free-streaming

length is the distance travelled freely by a relativistic particle after decoupling from the primordial plasma due to Universe expansion (approximately the distance travelled before the transition to nonrelativistic velocities). WDM particles (keV scale) give  $l_{fs} \sim 100$  kpc, while CDM (GeV-TeV scale), which are heavier and slower than WDM, would give a  $l_{fs}$  a million times smaller and lead to the existence of a host of small scale structures [16]. On the galaxy density profiles ( $\rho$ ), CDM gives a steep cusp at the center ( $\rho \sim r^{-1}$ ) [17]. On the contrary, WDM gives a finite constant density core at the center ( $\rho \sim \rho_0$ ), in agreement with observations [18–24]. WDM quantum effects [25] could be important inside the galaxy core (below 100 pc), showing a fermionic nature for the DM particle through the manifestation of quantum nonvanishing pressure versus gravity.

Astrophysical observations from DM-dominated objects, as well as theoretical analysis, lead to a DM fermionic thermal particle with a mass around 2 keV [26]. Chandra and XMM-Newton detections in the X-ray spectra of the M31 galaxy and the Perseus cluster (both DM-dominated) seem to be consistent with sterile neutrinos of a few keV. In particular, an unidentified 3.55 keV line has been observed which seems compatible with the decay or annihilation of sterile relic neutrinos [27, 28] and that does not correspond to any known atomic emission. Although the interpretation of this line is still subject to debate, it could be considered an indication of the decay of a 7.1 keV nonthermal sterile neutrino [29, 30].

As it is well known, the Standard Model (SM) of elementary particles does not describe DM particles, nor does it provide a mass for active neutrinos ( $\nu_e, \nu_\mu, \nu_\tau$ ). In this model, neutrino eigenstates are left-handed, and they transform as doublets under the weak SU(2) gauge group. In extended SM models [31, 32], additional SU(3)  $\times$  SU(2)  $\times$  U(1) singlet right-handed neutrinos are introduced. Neutrino mass eigenstates will be linear combinations of the left and right-handed states, and mass matrix eigenvalues will split into lighter and heavier states (seesaw mechanism). The lighter mass eigenstates would be the main components of the active flavor eigenstates of the neutrinos, whereas the heavier ones would be dominant in sterile neutrino flavors [33]. Some extended SM models add three extra sterile neutrinos, one with a mass of the order of keV (see [34] and references therein). Neutrinos in the keV mass scale open the possibility to detect warm dark matter in nuclear electron capture and beta decay. Heavier sterile neutrinos cannot be produced in weak nuclear decays, and there are of course many other candidate particles for DM unconnected in principle to weak nuclear processes, such as the lightest supersymmetric particles [35, 36].

In this paper, we assume that a keV neutrino, a sound candidate for DM [37], is produced in ordinary weak nuclear processes, such as beta decay and electron capture, via neutrino mixing. Experiments searching for active neutrino masses, also look for sterile neutrinos in the keV range [38]: MARE [39–41] (that used Rhenium 187 beta decay and is not active anymore); KATRIN [42–46], PTOLEMY [47, 48], and Project8 [49] (using Tritium beta decay); and ECHO [50–52] and HOLMES [53] (using Holmium 163 electron capture). The mass of the neutrino (or antineutrino) emitted in a weak

nuclear decay has an effect on the energy spectrum of the process, as was first shown by Enrico Fermi in the early 1930s [54, 55]. For the active neutrinos, this effect shows up at the endpoint of the spectrum, whereas for the sterile neutrinos considered here it may be expected to appear at a few keV below the endpoint. Clearly, in order to leave a fingerprint the sterile neutrino mass must be within the Q window, that is, lower than the energy Q available in the decay. The energy spectrum to be analyzed corresponds to the emitted charged lepton in the case of beta decay, namely, the spontaneous conversion of a neutron into a proton or vice versa with emission of the charged lepton and an antineutrino or neutrino. In the case of electron capture only a neutrino is emitted and no charged lepton comes out, so that the spectrum to be measured corresponds to the deexcitation of the daughter atom.

A summary of current experimental studies of neutrino properties in the frontiers of intensities and sensitivities is given in [62]. Experiments are under way to determine directly the active neutrino mass from neutrinoless double beta decay [63] as well as from single beta decay [42–48] and electron capture [50–53]. The last two types of experiments also provide a way to search for WDM sterile neutrinos in the measured spectra. In electron capture experiments, the spectrum collected in a calorimeter is directly linked to the excitation energies of the daughter atoms or molecules. In a calorimeter, the active source is embedded in the detector, which collects the energy of all the particles emitted in the deexcitation processes that take place in the source, except that of the neutrinos. In beta decay, the fact that the atoms or molecules may remain excited poses a challenge on the interpretation of the electron spectrum. Electron capture experiments take advantage of the larger statistics in the spectrum regions around the capture resonances. A limitation of electron capture measurements is that in a calorimeter, where the full energy range of the spectrum is measured, pile-up can be a problem that should be prevented by limiting the activity in the experimental setup. We refer always in this paper to Earth-based experiments where both the emission and the detection of particles take place in the laboratory. Other possible scenarios, like the search for sterile neutrinos in stellar matter (stellar beta decay and electron capture rates), are beyond the scope of this paper. The phase space for these rates increases manifold in stellar environment. For a reference on stellar weak rates, see [64, 65].

## 2. Heavy Mass and Sterile Flavor in Neutrino States

Already observed neutrino oscillations (see, e.g., [66–69]) among light active neutrinos are due to the fact that the neutrino flavor eigenstates and the mass eigenstates are not the same. Each flavor eigenstate, associated with a charged lepton, can be written as a combination of mass eigenstates and vice versa [70]. For instance, the neutrino flavor eigenstate emitted after electron capture, called electron neutrino  $\nu_e$ , can be written as a combination of the three light SM mass

eigenstates and, hypothetically, of one or more extra, heavier mass eigenstates as [71–77]

$$|\nu_e\rangle = U_{e1}|\nu_1\rangle + U_{e2}|\nu_2\rangle + U_{e3}|\nu_3\rangle + \sum_h U_{eh}|\nu_h\rangle, \quad (1)$$

where the subscript  $h = \{4, 5, \dots\}$  stands for extra (heavier) mass eigenstates and the quantities  $U$  belong to the unitary neutrino mixing matrix. The masses of the three light SM mass eigenstates are so close to each other that so far no measurement has been able to discern which of them has been emitted in a given process. As a result, the three are emitted as a coherent superposition, which is at the origin of the neutrino oscillation phenomenology. The phase of each mass eigenstate changes at a different rate while travelling, giving rise to a different superposition at each location that translates into a varying (oscillatory) probability of detection of a given flavor eigenstate.

To simplify things we will consider here the linear combination of light mass eigenstates as a single, effective neutrino mass eigenstate, called “light”, with mass

$$m_l = \overline{m}_{\nu_e} = \left( U_{e1}^2 m_1^2 + U_{e2}^2 m_2^2 + U_{e3}^2 m_3^2 \right)^{1/2} \quad (2)$$

and just one extra mass eigenstate, clearly heavier than the others, called “heavy” (with mass  $m_h$ , which we shall consider in the keV range):

$$|\nu_e\rangle = \cos \zeta |\nu_l\rangle + \sin \zeta |\nu_h\rangle, \quad (3)$$

where the mixing amplitudes have been written in terms of a mixing angle  $\zeta$  between the light and the heavy neutrino mass eigenstate. The other possible combination of these two mass eigenstates would be the sterile flavor eigenstate:

$$|\nu_s\rangle = -\sin \zeta |\nu_l\rangle + \cos \zeta |\nu_h\rangle, \quad (4)$$

such that  $\langle \nu_e | \nu_s \rangle = 0$ . For the sterile neutrinos that can be relevant as WDM, cosmological constraints based on the observed average dark matter density suggest that the value of the mixing angle could approximately be  $\zeta = 0.006^\circ$  [71–74], corresponding to a flavor-mass amplitude  $U_{eh} = \sin \zeta \approx 10^{-4}$ . Other recent cosmological constraints give values of  $\sin^2(2\zeta)$  between  $2 \cdot 10^{-11}$  and  $2 \cdot 10^{-10}$  [27, 28].

Sterile neutrino states with masses close to the ones of the active neutrinos can also have an impact on the patterns measured in oscillation experiments [78]. Heavier sterile neutrinos, as in particular in the keV scale, do not modify the oscillation patterns since they are not emitted coherently with the active neutrinos due to the large mass splitting.

The differential energy spectrum of a weak process where an electronic neutrino (or antineutrino) is emitted can therefore be decomposed in a term for light neutrino emission and another term for heavy neutrino emission as follows [75–77]:

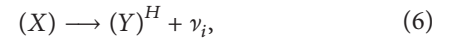
$$\frac{d\lambda}{dE} = \frac{d\lambda^l}{dE} \cos^2 \zeta + \frac{d\lambda^h}{dE} \sin^2 \zeta. \quad (5)$$

This energy spectrum can be the one of the electron emitted in beta decay or the one of the daughter atom deexcitations in

electron capture. The heavy mass eigenstate, if it exists, would be emitted independently of the other masses (noncoherently) as long as the energy resolution of the detector is better than the mass difference,  $\Delta\epsilon < (m_h - \overline{m}_e)$ . Its contribution to the measured spectrum,  $d\lambda^h/dE$ , would show up in the range where the collected energy is small enough for the heavy neutrino mass to have been produced, namely, when  $0 \leq E \leq (Q - m_h)$ , where  $Q$  is the difference between the masses of the initial and the final atoms when the reaction takes place in vacuum. At the edge of that region, at  $E = Q - m_h$ , a kink in the spectrum would be found with the size of the heavy neutrino contribution, namely, proportional to  $\sin^2 \zeta \sim \zeta^2$  (the latter approximation valid for small mixing angles, as is the case in realistic scenarios).

### 3. Theory of Electron Capture

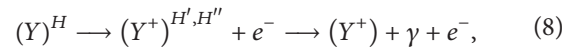
Let us consider the capture of an atomic electron by the nucleus  $X (Z, N)$  to turn into the nucleus  $Y (Z - 1, N + 1)$ . The reactions involving the corresponding atoms (represented by the symbol of the nucleus within brackets) begin with electron capture:



followed by deexcitation of the daughter atom. In (6),  $\nu_i$  is a neutrino mass eigenstate ( $\nu_l$  or  $\nu_h$ ) and the superscript  $H$  accounts for the excited state of the atom ( $Y$ ) corresponding to an electron hole in the shell  $H$ , due to the electron capture from this shell in the parent atom. The deexcitation of the daughter atom after electron capture can happen either through emission of a photon ( $X$ -ray emission):



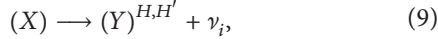
or through emission of electrons (Auger or Coster-Kronig process) and photons:



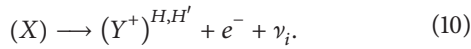
where  $H'$  and  $H''$  represent holes in the electron shells of the ion ( $Y^+$ ).

The energies carried by the emitted photons and electrons are deposited in the calorimeter that surrounds the source and that measures the full energy spectrum of these particles, provided that the corresponding deexcitation lifetimes are much smaller than the detector time response [79]. The process in (7) and (8) yields the same calorimeter spectrum; that is, the peaks appear at the same energy values corresponding to the excitation energies,  $E_H$ , of the excited daughter atom ( $Y$ ) <sup>$H$</sup> . The excitation energy is the difference between the binding energies of the captured electron shell and the additional electron in the outermost shell. The former refers to the daughter atom, whereas the latter refers to the parent:  $E_H \approx |B_H^{(Y)}| - |B_{\text{out}}^{(X)}|$ . The reason is that for the shells above the vacancy the effective charge is closer to the one in the parent atom (there is one proton less in the nucleus but also one electron less in an inner shell) and therefore its binding energies should be used [80].

An alternative capture process to the one in (6) involves the instantaneous formation of a second hole  $H'$  due to the mismatch between the spectator electron wave functions in the parent and in the daughter atom. Whereas the hole  $H$  is left by the captured electron and therefore fulfils the energy and angular momentum conditions for such process, the extra hole  $H'$  has a different origin, namely, the above mentioned incomplete overlap of electron wave functions, which may occur in many electron shells. The electron leaving the extra hole may have been “shaken up” (excited) to an unoccupied orbital in the daughter atom:

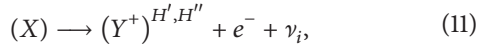


or it may have been “shaken off” to the continuum (ejected):



In a shake-up process, the deexcitation of the final atom contributes to the calorimeter energy with a peak at an energy approximately equal to the sum of the binding energies of the  $H$  and  $H'$  electrons,  $E_{H,H'} \approx |B_H^{(Y)}| + |B_{H'}^{(X)}| - |B_{\text{out}}^{(X)}|$ . Thus, satellite peaks show up located after the single-hole peak at  $E_H$ . In the case of a shake-off, the calorimeter energy is the combination of  $E_{H,H'}$  and the electron kinetic energy, the latter showing a continuous distribution as corresponds to the three-body decay of (10).

It is important to notice that some electron emission processes of the type



where none of the holes in the daughter atom correspond to the captured electron  $H$ , are quantum mechanically indistinguishable [81, 82] from the three-step process in (6) and (8), and therefore they contribute to the same one-hole peaks at  $E_H$ . The contributions to the spectrum of the two-hole excitations that are actually distinct from the one-hole excitations ((9) and (10)) have been a subject of recent studies devoted to search for the electron neutrino mass and are therefore focused on the endpoint of the spectrum (see, e.g., [80–83]). For heavy neutrino searches, a similar analysis should be performed at other regions of the energy spectrum, not just at the endpoint. In this paper, we restrict the calculations to the one-hole states.

The density of final states of the emitted neutrino in electron capture is proportional to

$$\rho = \rho_\nu(E_\nu) \propto p_\nu E_\nu = (E_\nu^2 - m_\nu^2)^{1/2} E_\nu, \quad (12)$$

where  $E_\nu$ ,  $p_\nu$ , and  $m_\nu$  are the neutrino total energy, momentum, and mass, respectively. On the other hand, the probability of capture of a bound electron follows a Breit-Wigner distribution of width  $\Gamma_x$  and peaks at the energy  $E_x$ :

$$P(E) = \frac{\Gamma_x/2\pi}{(E - E_x)^2 + \Gamma_x^2/4}. \quad (13)$$

Using Fermi’s Golden Rule, the differential reaction rate with respect to the neutrino energy yields

$$\frac{d\lambda}{dE_\nu} = K_{\text{EC}} (E_\nu^2 - m_\nu^2)^{1/2} E_\nu \sum_H W_H^{(\nu)} \cdot \frac{\Gamma_H/2\pi}{[E_\nu - (Q - E_H)]^2 + \Gamma_H^2/4}, \quad (14)$$

where  $K_{\text{EC}}$  contains, among other factors, the weak interaction coupling constant and the nuclear matrix element. The factor  $W_H^{(\nu)}$  is the squared leptonic matrix element for a given hole state  $H$ .

We write  $W_H^{(\nu)} = C_H S_H^{(\nu)}$  to have a general expression for allowed and forbidden transitions. The factor  $C_H$  is the squared amplitude of the bound-state electron radial wave function at the nuclear interior, containing also the squared overlap between the initial and the final atom orbital wave functions and the effect of electron exchange (as defined in Appendix F-2 of [56]). The cases discussed in the next sections involve allowed Gamow-Teller transitions ( $^{163}\text{Ho} (7/2^-) \rightarrow ^{163}\text{Dy} (5/2^-)$ ) and first forbidden Gamow-Teller transitions ( $^{202}\text{Pb} (0^+) \rightarrow ^{202}\text{Tl} (2^-)$  and  $^{205}\text{Pb} (5/2^-) \rightarrow ^{205}\text{Tl} (1/2^+)$ ). In the first case, the factor  $S_H^{(\nu)} = 1$  for all  $H$  states. In the second case, the factor  $S_H^{(\nu)} = 1$  for electrons captured with orbital angular momentum  $l = 1$  (and neutrinos emitted with  $l = 0$ ) and  $S_H^{(\nu)} = p_\nu^2$  for electrons captured with orbital angular momentum  $l = 0$  (and neutrinos emitted with  $l = 1$ ). The reason for this is that, due to conservation of total angular momentum, first forbidden transitions have  $L = 1$  for the leptonic pair. Hence, there is a linear momentum dependence in the leptonic matrix element corresponding to the lepton that carries the angular momentum in each specific capture. The corresponding  $p_\nu^2$  factor for the  $l = 1$  electrons is embedded in the  $C_H$  factor [56].

Equation (14) includes every possible orbital electron capture, the probability of each peaking at  $E_\nu = Q - E_H$ , as dictated by energy conservation, where  $E_H$  is the excitation energy of the final atom due to the electron hole  $H$  resulting from capture. The energy collected by a calorimeter from the atomic deexcitations is  $E_c = Q - E_\nu$ , namely, all the available energy except for the one carried away by the neutrino. The differential rate can be written in terms of the calorimeter energy as

$$\frac{d\lambda}{dE_c} = K_{\text{EC}} [(Q - E_c)^2 - m_\nu^2]^{1/2} (Q - E_c) \sum_H C_H S_H^{(\nu)} \cdot \frac{\Gamma_H/2\pi}{(E_c - E_H)^2 + \Gamma_H^2/4}. \quad (15)$$

In the next section, we shall also consider integrated rates over particular energy ranges, which can be calculated numerically from (15). A convenient compact analytical expression of the integrated rate can be obtained from (15) by replacing the Breit-Wigner distributions by Dirac deltas.

With this approximation, the integral of the differential rate can be written as

$$\lambda = K_{\text{EC}} \sum_H C_H S_H^{(\nu)} \left[ (Q - E_H)^2 - m_\nu^2 \right]^{1/2} (Q - E_H). \quad (16)$$

In this theoretical model, we have neglected two-hole peaks, deexcitations through virtual intermediate states, and interferences between deexcitation channels. The theoretical calorimeter spectrum is thus a single-hole approximation that assumes full collection of de-excitation energy by the calorimeter and no pile-up.

#### 4. Sterile Neutrino Effect in the Spectrum

Due to the smallness of the mixing angle, it is useful to consider ratios between rates that emphasize the contribution of the heavy neutrino. In [84–86], for the case of beta decay, a ratio was considered between the contributions of the heavy and the light neutrino to the differential rates, as we shall see in Section 6. For the case of electron capture, the differential decay rates contain many peaks and it is more convenient to consider integrated decay rates over specific energy ranges, as discussed in [87]. In either case (beta decay and electron capture), this amounts to consider that the detector collects events within energy ranges  $E_i \pm \Delta$  and  $E_j \pm \Delta$  in two regions of the spectrum, such that the mass of the hypothetical heavy neutrino lies in between, namely,  $E_i + \Delta < m_h < E_j - \Delta$ , with  $E_j < Q - \Delta$ . A ratio  $R$  between the number of collected events in both regions is then performed, which corresponds to the theoretical expression:

$$R = \frac{\Lambda_i}{\Lambda_j} = \frac{\kappa_i^l + \tan^2 \zeta \kappa_i^h}{\kappa_j^l}, \quad (17)$$

where  $\Lambda_i = \cos^2 \zeta \kappa_i^l + \sin^2 \zeta \kappa_i^h$  (in the region where both  $l$  and  $h$  mass eigenstates contribute) and  $\Lambda_j = \cos^2 \zeta \kappa_j^l$  (in the region where  $h$  is not energetically allowed). The integrals  $\kappa$  are defined as

$$\kappa_{i,j}^\nu = \int_{E_{i,j}-\Delta}^{E_{i,j}+\Delta} \frac{d\lambda}{dE_c} (m_\nu) dE_c. \quad (18)$$

In electron capture, the energies  $i$  and  $j$  can be selected as the energies of two peaks and the integration intervals can be chosen as the width of the capture peaks. If the peaks are approximated by delta functions, the integrals (using  $E_H = E_i$  and  $\Delta \rightarrow 0$ ) can be written as

$$\kappa_{i,r}^{\nu\text{EC}} = K_{\text{EC}} C_{i,r} S_{i,r}^{(\nu)} (Q_r - E_i)^2 \left[ 1 - \left( \frac{m_\nu}{Q_r - E_i} \right)^2 \right]^{1/2}, \quad (19)$$

where  $Q_r$  is the atomic mass difference in a given isotope  $r$ ,  $E_i$  is the energy position of a given peak  $i$  in the calorimeter spectrum,  $m_\nu$  is  $m_l \approx 0$ , the mass of a light neutrino, or  $m_h$ , the mass of a heavy neutrino, and  $S_{i,r}^{(\nu)}$  contains the neutrino momentum dependence for the peak  $i$  coming from the leptonic matrix element squared. As explained in the previous section, for allowed transitions,  $S_{i,r}^{(\nu)} = 1$ . For

first forbidden transitions, some of the capture peaks have  $S_{i,r}^{(\nu)} = p_{\nu i,r}^2$  for the  $i$  peaks corresponding to  $s_{1/2}$  shells (as well as for those corresponding to  $p_{1/2}$  shells that contribute through their admixtures with the  $l = 0$  orbital due to relativistic corrections). The other peaks have  $S_{i,r}^{(\nu)} = 1$ , where  $i$  corresponds to  $p_{3/2}$  shells (and  $d_{3/2}$  shells through their admixtures with the  $l = 1$  orbital due to relativistic corrections).

For electron capture, it is convenient to define a ratio similar to the one in (17) but where the numerator and the denominator are themselves ratios of numbers of events within the same peak but for different isotopes of the same element,  $r$  and  $s$ , so that some atomic corrections cancel out [87]

$$R' = \frac{\Lambda_{i,r}/\Lambda_{i,s}}{\Lambda_{j,r}/\Lambda_{j,s}} = \left( R_{i,j;r,s}^l \right)^{2(\gamma+1)} \left( \frac{1 + \omega_{i,r}^{2\gamma+1} \tan^2 \zeta}{1 + \omega_{i,s}^{2\gamma+1} \tan^2 \zeta} \right), \quad (20)$$

where one should notice that the factors  $C_i$  and  $C_j$  cancel out in addition to the factor  $K_{\text{EC}}$  which cancels out in both ratios ( $R$  and  $R'$ ). The factors in (20) have very simple analytical forms when one uses (19)

$$R_{i,j;r,s}^l = \frac{(Q_r - E_i)(Q_s - E_j)}{(Q_r - E_j)(Q_s - E_i)}, \quad (21)$$

$$\omega_{i;r(s)} = \left[ 1 - \left( \frac{m_h}{Q_{r(s)} - E_i} \right)^2 \right]^{1/2},$$

where  $\gamma$  depends on the angular momenta of each lepton in a given  $\Delta J^\pi$  nuclear transition. For instance, for allowed decays,  $\gamma = 0$ , whereas for first forbidden decays,  $\gamma = 1$  for  $s_{1/2}$  and  $p_{1/2}$  peaks or  $\gamma = 0$  for  $p_{3/2}$  and  $d_{3/2}$  peaks. In the expressions above, we have assumed that both peaks  $i$  and  $j$  are of the same type; namely,  $\gamma_i = \gamma_j = \gamma$ .

By measuring the ratio in (20) the mixing angle can then be obtained as

$$\zeta = \arctan \left[ \frac{\left( R_{i,j;r,s}^l \right)^{2(\gamma+1)} - R'_{\text{exp}}}{R'_{\text{exp}} \omega_{i,s}^{2\gamma+1} - \left( R_{i,j;r,s}^l \right)^{2(\gamma+1)} \omega_{i,r}^{2\gamma+1}} \right]^{1/2}, \quad (22)$$

where the theoretical values of  $R_{i,j;r,s}^l$ ,  $\omega_{i,r}$ , and  $\omega_{i,s}$  require an accurate experimental knowledge of the position of the selected peaks and, more importantly, of the atomic mass differences  $Q_r$  and  $Q_s$ . In addition, one has to consider fixed, initially unknown, values of the mass of the heavy neutrino  $m_h$  that is searched for or otherwise be content with the generation of exclusion plots in case of no effect observation.

In summary, we consider here two types of ratios that can be useful in the search for a signal of keV sterile neutrinos in electron capture: (1) the ratio between the intensity of two peaks in the electron capture spectrum of a given nucleus, as for the case of  $^{163}\text{Ho}$  discussed in Section 5. (2) The case in which two isotopes of a given element undergo electron capture where one can use the ratio defined in (20), as is the case of Lead isotopes discussed in Section 5. For the

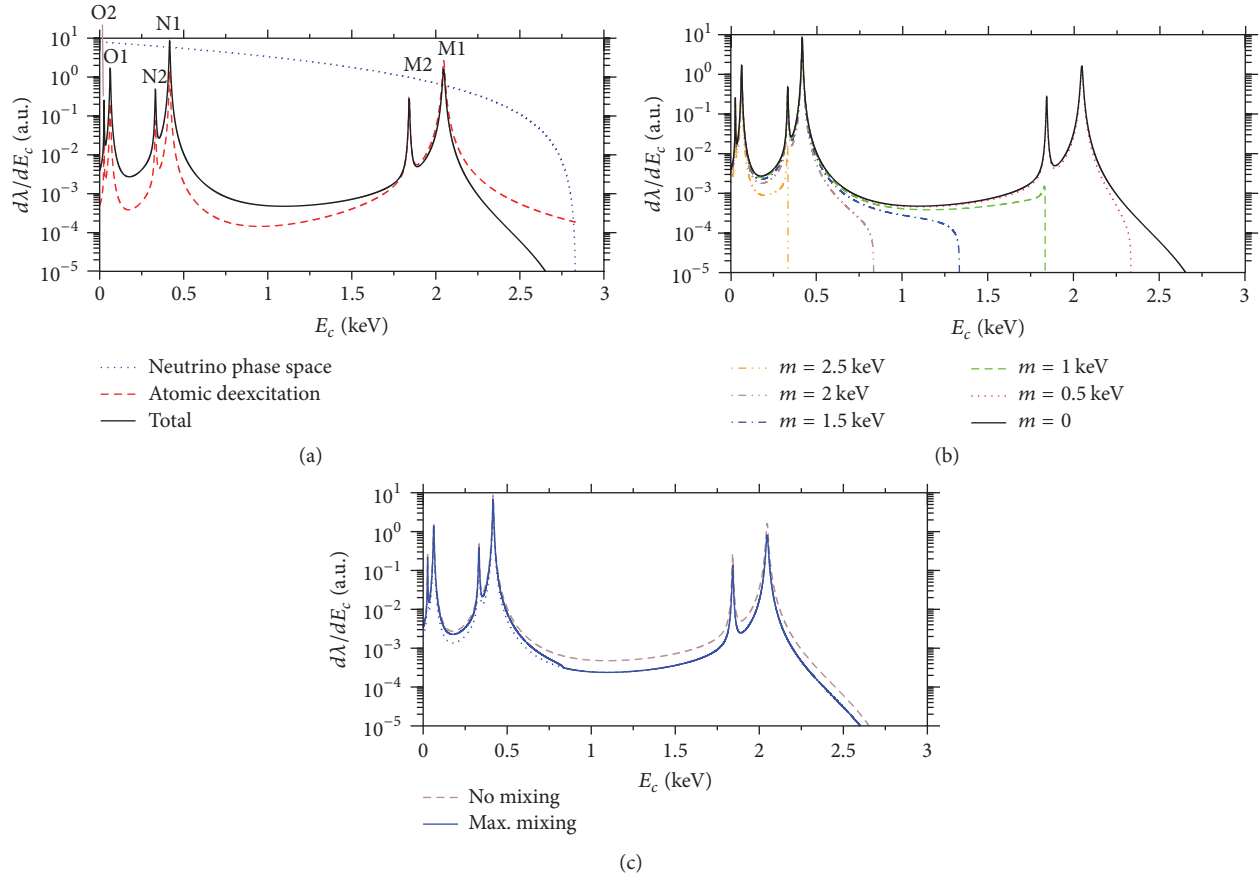


FIGURE 1: Calorimeter spectrum after electron capture in  $^{163}\text{Ho}$ . (a) Full spectrum (solid curve) and contributions: emitted neutrino phase space (dotted curve) and daughter atom deexcitation (dashed curve). (b) Full spectrum for different neutrino masses: 0, 0.5, 1, 1.5, 2, and 2.5 keV. (c) full spectrum for light ( $m_l \approx 0$  keV) - heavy ( $m_h = 2$  keV) neutrino mixing using a maximal mixing angle  $\zeta = 45^\circ$  for illustration, with (solid curve) and without (dotted curve) the heavy neutrino contribution. For comparison, the spectrum without heavy neutrino mixing (dashed curve) is also shown. We use the maximal unrealistic value  $\zeta = 45^\circ$  to make the effect visible in the scale of the figure. Realistic values of  $\zeta < 0.01^\circ$  result in a reduction of the difference between the dashed and the solid lines in (c) by more than seven orders of magnitude.

beta decay case, in Section 6 we consider the ratio between the differential rates, but the ratios between integrated rates are also useful and may be more realistic for comparison to experiments.

## 5. Results for Electron Capture Spectra

Let us first consider the capture of an atomic electron by the nucleus Holmium 163 ( $^{163}\text{Ho}$ ;  $Z = 67$ ,  $N = 96$ ) to turn into Dysprosium 163 ( $^{163}\text{Dy}$ ;  $Z = 66$ ,  $N = 97$ ), with ground state spins and parities  $J^\pi = 7/2^-$  and  $J^\pi = 5/2^-$ , respectively. It is an allowed unique Gamow-Teller transition ( $\Delta J = 1$  and no parity change, the leptons carry no orbital angular momentum,  $\Delta L = 0$ , and couple to spin  $S = 1$ ), with atomic mass difference  $Q = 2.833 \pm 0.030 \pm 0.015$  keV [88], which is being currently measured at the Electron Capture Holmium (ECHO) experiment [50–52]. Only electrons with principal quantum number  $n$  larger than 2 have a binding energy lower than the  $Q$ -value and can therefore be captured. In addition, being an allowed decay, only electrons from  $s_{1/2}$  and

$p_{1/2}$  orbitals can be captured, the latter through admixtures with the  $l = 0$  orbital due to relativistic corrections. Thus, capture from the orbitals M1, M2, N1, N2, O1, O2, and P1 (in spectroscopic notation) is possible [80, 89–91].

In Figure 1, we show the differential electron capture rate in  $^{163}\text{Ho}$  as a function of the calorimeter energy,  $E_c = Q - E_\nu$ . In Table 1, we give theoretical values of the strengths and widths of each capture peak and experimental values of the electron binding energy again for each capture peak. The strengths  $C_H$  are obtained in [56, 57] from relativistic Hartree-Fock calculations of the electron wave functions at the nuclear site, accounting for exchange and overlap contributions. In the upper plot the emitted neutrino phase space contribution and the daughter atom deexcitation contribution are plotted separately, together with the product of both, which is the full differential electron capture rate. In the middle plot we show the full differential rate for different masses of the emitted neutrino:  $m_\nu \approx 0$  (realistic) and  $m_\nu \approx 0.5, 1, 1.5, 2,$  and  $2.5$  keV (unrealistic). As can be seen in the plot, each curve ends at  $Q - m_\nu$ . Finally, the lower plot shows the spectrum resulting from the mixing of a light neutrino

TABLE 1: Atomic parameters for electron capture in Holmium from shells M1 to O2. The values of  $C_H$  [56, 57] correspond to the atomic shells in Holmium, while the orbital electron widths  $\Gamma_H$  [58] and binding energies  $B_H$  ( $<Q$ ) [59–61] correspond to the atomic shells in Dysprosium.

	M1	M2	N1	N2	O1	O2
$C_H$	0.05377	0.002605	0.01373	0.0005891	0.001708	0.0001
$\Gamma_H$ [keV]	0.013	0.006	0.006	0.005	0.005	0.002
$B_H$ [keV]	2.047	1.842	0.416	0.332	0.063	0.026

TABLE 2: Same as Table 1 (data from the same references) but for electron capture in Lead going to Thallium. The upper table summarizes the values of the relevant parameters for  $s_{1/2}$  and  $p_{1/2}$  atomic shells, while the lower table shows the values for  $p_{3/2}$  and  $d_{3/2}$  atomic shells. In the latter case,  $C_H$  includes an extra factor  $p_e^2$ .

	L1	L2	M1	M2	N1	N2	O1	O2
$C_H$	0.8781	0.06647	0.2125	0.01759	0.05849	0.004431	0.01016	0.0008052
$\Gamma_H$ [keV]	0.011	0.006	0.015	0.010	0.009	0.007	—	—
$E_H$ [keV]	15.346	14.697	3.703	3.415	0.845	0.720	0.136	0.099
	L3	M3	M4	N3	N4	O3	O4	
$C_H$ [keV <sup>2</sup> ]	18978.193	5366.014	45.383	1363.307	12.607	237.280	1.500	
$\Gamma_H$ [keV]	0.006	0.009	0.002	0.006	0.004	0.001	0.001	
$B_H$ [keV]	12.657	2.956	2.484	0.608	0.406	0.072	0.015	

mass eigenstate,  $m_l \approx 0$ , with a heavy mass eigenstate  $m_h \approx 2$  keV (solid curve) as in (5). Although the spectrum with mixing is realistic in the sense that it is the result expected if a heavy mass eigenstate exists, it is unrealistic in the degree of mixing shown in the figure, which has been maximized here for the sake of visibility of the “kink” in the scale of the figure: 50% light neutrino and 50% heavy neutrino, corresponding to a mixing angle  $\zeta = 45^\circ$ . The “kink” can be seen in this curve at  $E_c = Q - m_h = 0.833$  keV. Above this calorimeter energy, the heavy mass eigenstate cannot be produced due to energy conservation. For comparison, the spectrum for  $m_\nu \approx 0$  with no mixing with heavy states is shown in the dashed curve.

Another example of electron capture under study here is that of the Lead isotopes 202 ( $^{202}\text{Pb}$ ;  $Z = 82$ ,  $N = 120$ ) and 205 ( $^{205}\text{Pb}$ ;  $Z = 82$ ,  $N = 123$ ) going to the Thallium isotopes 202 ( $^{202}\text{Tl}$ ;  $Z = 81$ ,  $N = 121$ ) and 205 ( $^{205}\text{Tl}$ ;  $Z = 81$ ,  $N = 124$ ), respectively, where the process is in both cases a first forbidden Gamow-Teller unique transition, with  $0^+ \rightarrow 2^-$  for  $^{202}\text{Pb}$  and  $5/2^- \rightarrow 1/2^+$  for  $^{205}\text{Pb}$  ( $\Delta J = 2$  and parity change, the leptons carry  $\Delta L = 1$  and couple to  $S = 1$ ). The atomic mass differences obtained from the data in [92] are  $Q = 46 \pm 14$  keV and  $Q = 50.6 \pm 1.8$  keV, respectively. According to the explanations given in Section 3, captures from orbitals L1, L2, M1, M2, N1, N2, O1, and O2 contain an extra neutrino momentum dependence  $S^{(\nu)} = p_\nu^2$  that modifies the calorimeter spectrum and corresponds to  $\gamma = 1$ . On the other hand, captures from orbitals L3, M3, M4, N3, N4, O3, and O4, which correspond to  $\gamma = 0$ , contain an extra electron momentum dependence  $p_e^2$  which, being fixed in bound electrons, is included in the values of  $C_H$ . They are given in Table 2 together with the widths and the experimental electron binding energies in the daughter atom, Thallium.

Figure 2 shows the capture differential rate in  $^{205}\text{Pb}$  (dark curves) and in  $^{202}\text{Pb}$  (light curves). Position, width, and

strength of the capture peaks are assumed to be the same in both isotopes, but the spectra are different because of the different  $Q$ -values. Solid curves are for light neutrino emission,  $m_\nu \approx 0$ , and dashed lines are for heavy neutrino emission with  $m_\nu = 40$  keV (results are given separately for each mass, before mixing). Due to the large  $Q$ -values, electron capture in Lead isotopes allows us to explore this mass value, although it may be somewhat larger than the expected value from cosmological reasons. The analysis of the ratio in (20) can be computed, for example, using the capture peaks L3 at  $E_c = 12.657$  keV and M3 at  $E_c = 2.956$  keV, both being of the  $\gamma = 0$  type. For  $m_h = 40$  keV one would obtain  $R_{M3\ L3; 202\ 205}^1 = 1.037$ ,  $\omega_{M3;202} = 0.369$ ,  $\omega_{M3;205} = 0.543$ . These results should be introduced in (22), together with the experimental ratio  $R'_{\text{exp}}$ , to obtain the value of the mixing angle  $\zeta$ .

It is important to remark that the theoretical quantities  $R^1$  and  $\omega$  computed as described above contain several approximations. They correspond to Dirac-delta peaks, ignoring the actual shapes and widths, and thus they just refer to one single capture peak, neglecting the possible effect of the tails of nearby one-hole peaks. Moreover, the influence of two-hole peaks close to the main ones has also been neglected. Other effects that have not been taken into account but whose influence is expected to be very small are multihole (more than two) peaks, virtual intermediate states (influence of transitions through atomic shells not energetically accessible), or interference between atomic transitions resulting from addition of amplitudes instead of intensities [81, 82]. The accurate experimental determination of the ratio  $R'_{\text{exp}}$  entails its own difficulties, among them the possible existence of metastable atomic states whose delayed de-excitations fail to contribute to the collected spectrum, and the variety of chemical environments resulting in a complex mixture of  $Q$ -values.

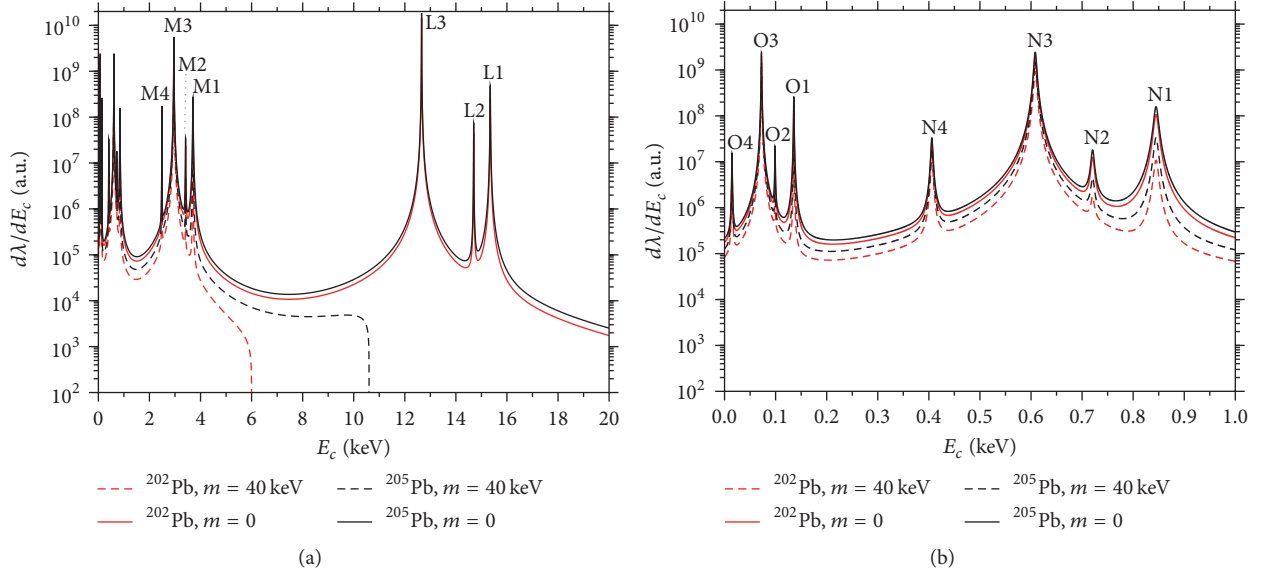
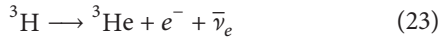


FIGURE 2: Calorimeter spectrum after electron capture in  $^{202}\text{Pb}$  (light curves) and in  $^{205}\text{Pb}$  (black curves) with emission of a light neutrino,  $m_h = 0$  (solid curves) and a heavy neutrino,  $m_h = 40\text{ keV}$  (dashed curves). (a) Full spectrum, showing L and M capture peak labels. (b) Low energy region ( $E_e = 0\text{--}1\text{ keV}$ ), showing N and O capture peak labels.

## 6. Results for Beta Decay Spectra

In addition to electron capture, we also show here the effect of heavy neutrino emission in the electron spectrum of beta decays for one of the cases of most interest, Tritium. It has been studied in depth in previous works [84–86, 93], together with another process that has also drawn considerable theoretical and experimental attention, the beta decay of Rhenium 187 [37, 39–41, 84–86]. The beta decay of Tritium ( $^3\text{H}$ ;  $Z = 1$ ,  $N = 2$ ) going to Helium 3 ( $^3\text{He}$ ;  $Z = 2$ ,  $N = 1$ ) is



and has a Q-value of 18.59 keV [92]. Both the initial and the final nuclear ground states have spin-parity  $1/2^+$ , and the transition is allowed with the electron and the antineutrino emitted in *s*-wave. The Karlsruhe Tritium Neutrino Experiment (KATRIN) [42–46] is currently studying this decay in order to determine the active neutrino mass and could also study the production of a heavy neutrino of a mass lower than 18 keV.

The differential decay rate with respect to the electron energy is given by

$$\frac{d\lambda}{dE_e} = K_\beta (E_e^2 - m_e^2)^{1/2} [(Q + m_e - E_e)^2 - m_\nu^2]^{1/2} \cdot E_e (Q + m_e - E_e), \quad (24)$$

where  $K_\beta$  contains, among others, the weak interaction coupling, the nuclear matrix element, and the Fermi function.

As an illustration of the heavy neutrino effect in the Tritium beta decay, we plot in Figure 3 the differential decay rate from (24) and (5) using a maximal mixing with an unrealistic value of the mixing angle  $\zeta = 45^\circ$ , to show the effect more

distinctly in the scale of the figure. We have used heavy mass components with  $m_h = 2\text{ keV}$  [26] (Figure 3(a)) and with  $m_h = 7\text{ keV}$  [29, 30] (Figure 3(b)). For comparison, the spectra without the heavy neutrino contribution ( $\lambda^h = 0$ ) and without mixing ( $\zeta = 0^\circ$ ) are also shown in this plot. The kink in the spectrum at  $E_e - m_e = Q - m_h$  can be observed if the experimental relative error is lower than the size of the step, the latter being very small in realistic situations.

The effect of a heavy neutrino emission can be analyzed through the ratio between the heavy and the light neutrino contributions to the spectrum:

$$\mathcal{R} \equiv \frac{d\lambda^h/dE_e}{d\lambda^l/dE_e} \tan^2 \zeta. \quad (25)$$

The full differential decay rate is also related to the ratio  $\mathcal{R}$  through

$$\frac{d\lambda}{dE_e} = \frac{d\lambda^l}{dE_e} [1 + \mathcal{R}] \cos^2 \zeta. \quad (26)$$

In Figure 4, we plot  $\mathcal{R}$ , the ratio of the heavy neutrino contribution over the light neutrino contribution to the decay rate, as a function of the momentum of the emitted electron for a heavy neutrino mass  $m_h = 2\text{ keV}$  and different mixing angles:  $\zeta = 0.01^\circ$ ,  $0.005^\circ$ , and  $0.001^\circ$ . The size of this ratio ( $<10^{-7}$ ) gives an idea of the difficulty of finding the kink in the spectrum due to the production of the heavy mass eigenstate. As can be seen in the figure, the ratio is different from zero and almost constant in the range  $0 \leq p_e < (p_e)_{\max}$ , where the maximum electron momentum is given by  $(p_e)_{\max} = [(Q - m_h)(Q - m_h + 2m_e)]^{1/2}$ . For the heavy mass used in the figure,  $(p_e)_{\max} \approx 131.3\text{ keV}$ . The ratio  $\mathcal{R}$  decreases as the mixing angle decreases, being approximately proportional to

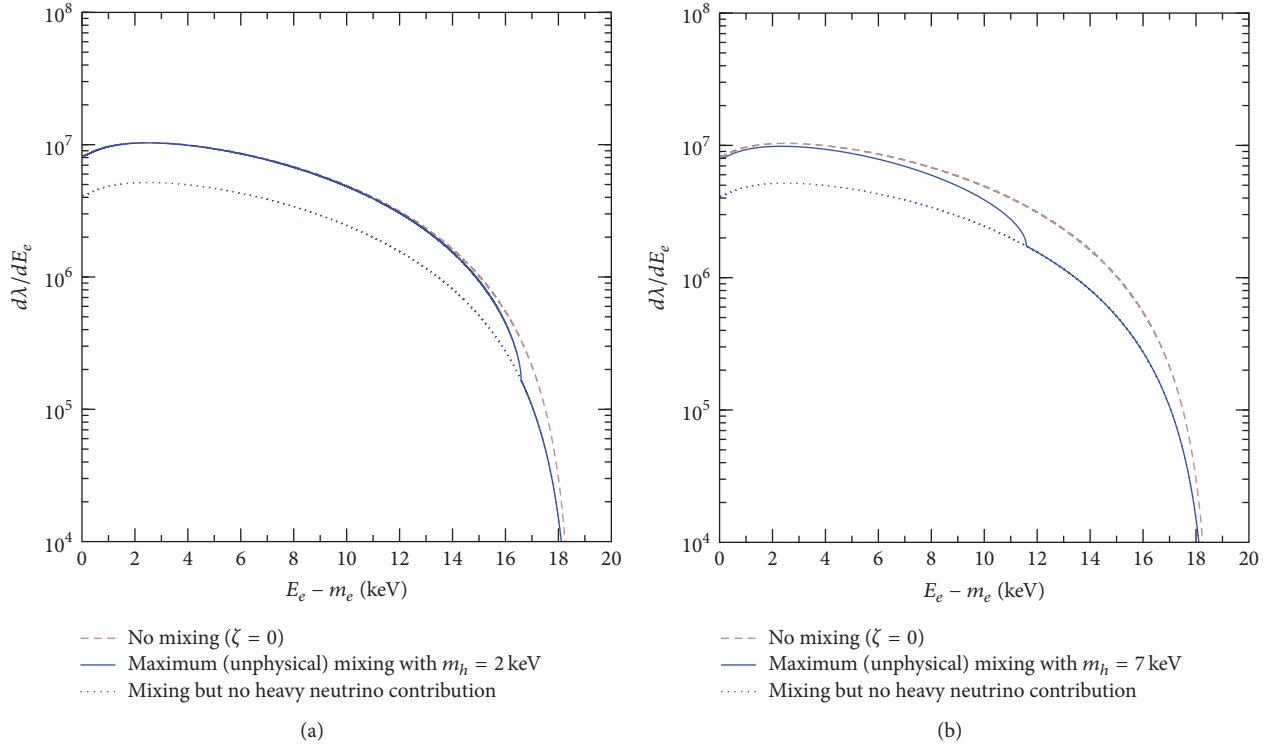


FIGURE 3: Electron spectrum of Tritium beta decay for a light-heavy neutrino mixing angle  $\zeta = 45^\circ$ , shown just for illustration, and a heavy neutrino mass (solid curve)  $m_h = 2$  keV (a) and  $m_h = 7$  keV (b). The spectrum without heavy neutrino mass contribution (dotted curve) and without mixing (dashed curve) are also shown. We use the maximal unrealistic value  $\zeta = 45^\circ$  to make the effect visible in the scale of the figure. Realistic values of  $\zeta < 0.01^\circ$  result in a reduction of the difference between the dotted and the solid lines by more than seven orders of magnitude.

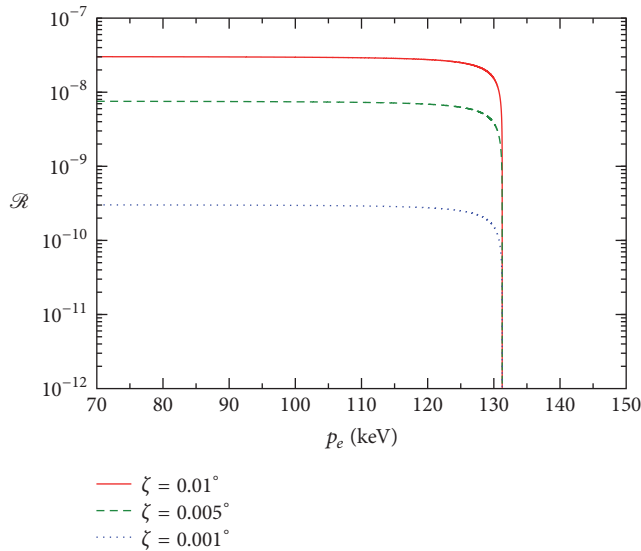


FIGURE 4: Ratio  $\mathcal{R}$ , defined in (25), for the Tritium beta decay, as a function of the electron momentum for a heavy neutrino mass  $m_h = 2$  keV and different values of the mixing angle:  $\zeta = 0.01^\circ$  (solid line),  $0.005^\circ$  (dashed line), and  $0.001^\circ$  (dotted line).

$\zeta^2$ . It also decreases for larger heavy neutrino masses  $m_h$ . A different ratio between the spectra with mixing and without

mixing ( $\mathcal{R}^*$ ) has also been considered in [84–86, 93], related with  $\mathcal{R}$  in (25) as

$$\mathcal{R}^* = -\sin^2\zeta + \mathcal{R} \cos^2\zeta = \frac{d\lambda/dE_e}{d\lambda'/dE_e} - 1. \quad (27)$$

## 7. Conclusions

Signatures of hypothetical keV sterile neutrinos, which could be warm dark matter candidates (WDM), may be found in the spectra of ordinary weak nuclear decays. The electron spectrum in beta decay is cleaner for this purpose because it is a smooth curve, while the deexcitation spectrum after electron capture shows many peaks. On the other hand, in beta decay the possible excitation of the atoms or molecules is not disentangled while in electron capture the calorimeter collects all the energy independently of the excitation of the atom and of the deexcitation path, and one has higher statistics around the capture peaks.

Figures of electron spectrum for beta decay in  $^3\text{H}$  as well as of calorimeter spectrum for electron capture in  $^{163}\text{Ho}$  and  $^{202}\text{Pb}$  and  $^{205}\text{Pb}$  are given considering various values of the heavy neutrino mass (2 keV, 7 keV, and 40 keV) that may be experimentally probed. In both weak processes, the small value of the light-heavy neutrino mixing angle requires extremely high experimental precision and the use of sources with large stability to reduce systematic errors. This is why it

is useful to consider relevant ratios between transition rates as first introduced in [84–87] to analyze the data. We consider two cases: the case of a single isotope, where one may use the ratio of accumulated number of events in different regions of the spectrum, which allows us to remove uncertainties related to the nuclear matrix element and to the values of overall constants. And in the case of two isotopes, we consider ratios of the above mentioned ratios that allow us to reduce uncertainties from atomic parameters. We give as well analytical expressions that can be used to obtain a good theoretical approximation to the experimental ratios ((19) to (21)).

Both the experimental measurement and the theoretical model must be accurate enough to detect differences in the expected versus the measured ratios of the order of the mixing angle squared,  $\zeta^2 \lesssim 10^{-8}$ . This is also the size of the kink expected in the electron spectrum of beta decay, located at the limit of the region where the production of a heavy neutrino is energetically allowed. In order to identify this kink among the statistical fluctuations of the measured spectrum, the number of collected events must be larger than the inverse of the squared ratio  $\mathcal{R}$  in (25).

Our results, particularly on the electron capture spectra of Lead isotopes that include for the first time all the possible peaks, may help in designing and analyzing future experiments to search for sterile neutrinos in the keV mass range. The use of the different types of ratios between number of events discussed here, for both electron capture and beta decay processes, may also help in planning the experiments by establishing the threshold of statistical and systematic uncertainties, required for the detection of sterile neutrinos of given mass and mixing, or to properly extract exclusion plots.

## Competing Interests

The authors declare that they have no competing interests.

## Acknowledgments

E. Moya de Guerra and O. Moreno acknowledge MINECO for partial financial support (FIS2014-51971-P) and IEM-CSIC for hospitality. O. Moreno acknowledges support from a Marie Curie International Outgoing Fellowship within the European Union Seventh Framework Programme, under Grant Agreement PEOF-GA-2011-298364 (ELECTROWEAK). M. R. M. thanks N. G. Sánchez for correspondence and conversations.

## References

- [1] F. Zwicky, “Die Rotverschiebung von extragalaktischen Nebeln,” *Helvetica Physica Acta*, vol. 6, pp. 110–127, 1933.
- [2] M. Roos, “Astrophysical and cosmological probes of dark matter,” *Journal of Modern Physics*, vol. 3, pp. 1152–1171, 2012.
- [3] S. Dodelson, *Modern Cosmology*, Academic Press, New York, NY, USA, 2003.
- [4] S. Weinberg, *Cosmology*, Oxford University Press, Oxford, UK, 2008.
- [5] J. Lesgourgues and S. Pastor, “Neutrino mass from cosmology,” *Advances in High Energy Physics*, vol. 2012, Article ID 608515, 34 pages, 2012.
- [6] D. Boyanovsky, H. J. de Vega, and N. G. Sanchez, “Constraints on dark matter particles from theory, galaxy observations, and  $N$ -body simulations,” *Physical Review D*, vol. 77, no. 4, Article ID 043518, 2008.
- [7] D. Boyanovsky, H. J. de Vega, and N. G. Sanchez, “Dark matter transfer function: free streaming, particle statistics, and memory of gravitational clustering,” *Physical Review D*, vol. 78, no. 6, Article ID 063546, 2008.
- [8] C. Destri, H. J. de Vega, and N. G. Sanchez, “Warm dark matter primordial spectra and the onset of structure formation at redshift  $z$ ,” *Physical Review D*, vol. 88, no. 8, Article ID 083512, 2013.
- [9] H. J. De Vega, P. Salucci, and N. G. Sánchez, “The mass of the dark matter particle: theory and galaxy observations,” *New Astronomy*, vol. 17, no. 7, pp. 653–666, 2012.
- [10] H. J. de Vega, P. Salucci, and N. G. Sanchez, “Observational rotation curves and density profiles versus the Thomas-Fermi galaxy structure theory,” *Monthly Notices of the Royal Astronomical Society*, vol. 442, no. 3, pp. 2717–2727, 2014.
- [11] H. J. de Vega and N. G. Sánchez, “Model-independent analysis of dark matter points to a particle mass at the keV scale,” *Monthly Notices of the Royal Astronomical Society*, vol. 404, no. 2, pp. 885–894, 2010.
- [12] H. J. de Vega and N. G. Sanchez, “Constant surface gravity and density profile of dark matter,” *International Journal of Modern Physics A*, vol. 26, no. 6, pp. 1057–1072, 2011.
- [13] H. J. de Vega and N. G. Sánchez, “Cosmological evolution of warm dark matter fluctuations. I. Efficient computational framework with Volterra integral equations,” *Physical Review D*, vol. 85, no. 4, Article ID 043516, 20 pages, 2012.
- [14] H. J. de Vega and N. G. Sanchez, “The dark matter distribution function and halo thermalization from the Eddington equation in galaxies,” *International Journal of Modern Physics A*, vol. 31, no. 13, Article ID 1650073, 2016.
- [15] N. Menci, S. Paduroiu, P. Salucci, N. Sánchez, and C. R. Watson, “lectures at the 20th Paris Cosmology Colloquium Chalonge-Héctor de Vega,” 2016, <http://chalonge.obspm.fr/>.
- [16] E. W. Kolb and M. S. Turner, *The Early Universe*, Addison Wesley, Boston, Mass, USA, 1990.
- [17] J. F. Navarro, C. S. Frenk, and S. D. M. White, “A universal density profile from hierarchical clustering,” *Astrophysical Journal Letters*, vol. 490, no. 2, pp. 493–508, 1997.
- [18] W. J. G. de Blok, “The core-cusp problem,” *Advances in Astronomy*, vol. 2010, Article ID 789293, 14 pages, 2010.
- [19] G. Gilmore, M. I. Wilkinson, R. F. G. Wyse et al., “The observed properties of dark matter on small spatial scales,” *Astrophysical Journal*, vol. 663, no. 2, pp. 948–959, 2007.
- [20] P. Salucci and Ch. Frigerio Martins, “The mass distribution in Spiral galaxies,” *EAS Publications Series*, vol. 36, pp. 133–140, 2009.
- [21] J. van Eymeren, C. Trachternach, B. S. Koribalski, and R.-J. Dettmar, “Non-circular motions and the cusp-core discrepancy in dwarf galaxies,” *Astronomy & Astrophysics*, vol. 505, no. 1, pp. 1–20, 2009.
- [22] M. Walker and J. Peñarrubia, “A method for measuring (slopes of) the mass profiles of dwarf spheroidal galaxies,” *The Astrophysical Journal*, vol. 742, no. 1, p. 20, 2011.

- [23] R. F. G. Wyse and G. Gilmore, “Observed properties of dark matter on small spatial scales,” in *Proceedings of the Proceedings of the International Astronomical Union Symposium (IUA '07)*, vol. 3, no. 244, pp. 44–52, Cardiff, UK, June 2007.
- [24] A. Burkert, “The structure of dark matter halos in dwarf galaxies,” *Astrophysical Journal*, vol. 447, no. 1, pp. L25–L28, 1995.
- [25] C. Destri, H. J. de Vega, and N. G. Sánchez, “Quantum WDM fermions and gravitation determine the observed galaxy structures,” *Astroparticle Physics*, vol. 46, pp. 14–22, 2013.
- [26] N. Menci, N. G. Sanchez, M. Castellano, and A. Grazian, “Constraining the warm dark matter particle mass through ultra-deep UV luminosity functions at  $Z = 2$ ,” *The Astrophysical Journal*, vol. 818, no. 1, article 90, 2016.
- [27] E. Bulbul, M. Markevitch, A. Foster, R. K. Smith, M. Loewenstein, and S. W. Randall, “Detection of an unidentified emission line in the stacked X-ray spectrum of galaxy clusters,” *Astrophysical Journal*, vol. 789, article 13, 2014.
- [28] A. Boyarsky, O. Ruchayskiy, D. Iakubovskiy, and J. Franse, “Unidentified line in X-ray spectra of the Andromeda galaxy and Perseus galaxy cluster,” *Physical Review Letters*, vol. 113, no. 25, Article ID 251301, 2014.
- [29] K. N. Abazajian, “Resonantly produced 7 keV sterile neutrino dark matter models and the properties of Milky Way satellites,” *Physical Review Letters*, vol. 112, no. 16, Article ID 161303, 5 pages, 2014.
- [30] N. Menci, A. Grazian, M. Castellano, and N. G. Sánchez, “Shock connectivity in the 2010 August and 2012 July solar energetic particle events inferred from observations and ENLIL modeling,” *Astrophysical Journal Letters*, vol. 825, no. 1, article 1, 2016.
- [31] A. D. Dolgov, “Neutrinos in cosmology,” *Physics Report*, vol. 370, no. 4-5, pp. 333–535, 2002.
- [32] A. Kusenko, “Sterile neutrinos: the dark side of the light fermions,” *Physics Reports*, vol. 481, no. 1-2, pp. 1–28, 2009.
- [33] B. Pontecorvo, “Neutrino experiments and the problem of conservation of leptonic charge,” *Soviet Physics-JETP*, vol. 26, no. 5, pp. 984–988, 1968.
- [34] A. Merle, “keV neutrino model building,” *International Journal of Modern Physics D*, vol. 22, no. 10, Article ID 1330020, 2013.
- [35] J. D. Vergados and T. S. Kosmas, “Searching for cold dark matter. A case of coexistence of supersymmetry and nuclear physics,” *Physics of Atomic Nuclei*, vol. 61, p. 1066, 1998.
- [36] E. Holmlund, M. Kortelainen, T. S. Kosmas, J. Suhonen, and J. Toivanen, “Microscopic calculation of the LSP detection rates for the  $^{71}\text{Ga}$ ,  $^{73}\text{Ge}$  and  $^{127}\text{I}$  dark-matter detectors,” *Physics Letters B*, vol. 584, no. 1-2, pp. 31–39, 2004.
- [37] R. Adhikari, M. Agostini, N. Anh Ky et al., “A white paper on keV sterile neutrino dark matter,” <https://arxiv.org/abs/1602.04816>.
- [38] G. Drexlin, V. Hannen, S. Mertens, and C. Weinheimer, “Current direct neutrino mass experiments,” *Advances in High Energy Physics*, vol. 2013, Article ID 293986, 39 pages, 2013.
- [39] MARE collaboration, <http://mare.dfm.uninsubria.it/frontend/exec.php>.
- [40] A. Nucciotti, “Neutrino mass calorimetric searches in the MARE experiment,” <https://arxiv.org/abs/1012.2290>.
- [41] A. Nucciotti, “On behalf of the MARE collaboration, lecture at the Workshop Chalonge Meudon,” 2011, <http://chalonge.obspm.fr/>.
- [42] KATRIN Collaboration, <http://www.katrin.kit.edu>.
- [43] C. Weinheimer, “Direct determination of neutrino mass from tritium beta spectrum,” <https://arxiv.org/abs/0912.1619>.
- [44] C. Weinheimer, lecture at the 20th Paris Cosmology Chalonge-Héctor de Vega Colloquium, 2016, <http://chalonge.obspm.fr/>.
- [45] G. Drexlin lecture at the 19th Paris Cosmology Colloquium 2015.
- [46] A. Huber, lecture at the Chalonge-de Vega Meudon Workshop, 2016, <http://chalonge.obspm.fr/>.
- [47] C. Tully, lecture at the 19th Paris Cosmology Colloquium 2015.
- [48] S. Betts, W. R. Blanchard, R. H. Carnevale et al., “Development of a relic neutrino detection experiment at PTOLEMY: princeton tritium observatory for light, early-universe, massive-neutrino yield,” <https://arxiv.org/abs/1307.4738>.
- [49] D. M. Asner, R. F. Bradley, L. de Viveiros et al., “Single-electron detection and spectroscopy via relativistic cyclotron radiation,” *Physical Review Letters*, vol. 114, no. 16, Article ID 162501, 2015.
- [50] P. C.-O. Ranitzsch, J.-P. Porst, S. Kempf et al., “Development of metallic magnetic calorimeters for high precision measurements of calorimetric  $^{187}\text{Re}$  and  $^{163}\text{Ho}$  spectra,” *Journal of Low Temperature Physics*, vol. 167, no. 5-6, pp. 1004–1014, 2012.
- [51] C. Hassel, “Lecture at the International School of Astrophysics Daniel Chalonge—Héctor de Vega,” 2015.
- [52] L. Gastaldo, K. Blaum, A. Doerr et al., “The electron capture  $^{163}\text{Ho}$  experiment ECHO,” *Journal of Low Temperature Physics*, vol. 176, no. 5, pp. 876–884, 2014.
- [53] B. Alpert, M. Balata, D. Bennett et al., “The electron capture decay of  $^{163}\text{Ho}$  to measure the electron neutrino mass with sub-eV sensitivity,” *The European Physical Journal C*, vol. 75, article 112, 2015.
- [54] E. Fermi, “Radioattività prodotta da bombardamento di neutroni,” *Il Nuovo Cimento*, vol. 11, no. 7, pp. 429–441, 1934.
- [55] E. Fermi, “Versuch einer theorie der  $\beta$ -strahlen. I,” *Zeitschrift für Physik*, vol. 88, no. 3, pp. 161–177, 1934.
- [56] R. B. Firestone and V. S. Shirley, Eds., *Table of Isotopes*, John Wiley & Sons, New York, NY, USA, 8th edition, 1999.
- [57] W. Bambynek, H. Behrens, M. H. Chen et al., “Orbital electron capture by the nucleus,” *Reviews of Modern Physics*, vol. 49, no. 1, pp. 77–221, 1977.
- [58] J. L. Campbell and T. Papp, “Widths of the atomic K-N7 levels,” *Atomic Data and Nuclear Data Tables*, vol. 77, no. 1, pp. 1–56, 2001.
- [59] J. A. Bearden and A. F. Burr, “Reevaluation of X-ray atomic energy levels,” *Reviews of Modern Physics*, vol. 39, no. 1, pp. 125–142, 1967.
- [60] M. Cardona and L. Ley, Eds., *Photoemission in Solids I: General Principles*, Springer, Berlin, Germany, 1978.
- [61] J. C. Fuggle and N. Martensson, “Core-level binding energies in metals,” *Journal of Electron Spectroscopy and Related Phenomena*, vol. 21, no. 3, pp. 275–281, 1980.
- [62] T. Kosmas, H. Ejiri, and A. Hatzikoutelis, “Neutrino physics in the frontiers of intensities and very high sensitivities,” *Advances in High Energy Physics*, vol. 2015, Article ID 806067, 3 pages, 2015.
- [63] A. Giuliani and A. Poves, “Neutrinoless double-beta decay,” *Advances in High Energy Physics*, vol. 2012, Article ID 857016, 38 pages, 2012.
- [64] J.-U. Nabi and H. V. Klapdor-Kleingrothaus, “Weak interaction rates of sd-shell nuclei in stellar environments calculated in the proton-neutron quasiparticle random-phase approximation,” *Atomic Data and Nuclear Data Tables*, vol. 71, no. 2, pp. 149–345, 1999.

- [65] J.-U. Nabi and H. V. Klapdor-Kleingrothaus, “Microscopic calculations of stellar weak interaction rates and energy losses for fp- and fp<sub>g</sub>-shell nuclei,” *Atomic Data and Nuclear Data Tables*, vol. 88, no. 2, pp. 237–476, 2004.
- [66] Y. Fukuda, T. Hayakawa, E. Ichihara et al., “Evidence for oscillation of atmospheric neutrinos,” *Physical Review Letters*, vol. 81, no. 8, pp. 1562–1567, 1998.
- [67] Q. R. Ahmad and SNO Collaboration, “Measurement of the rate of  $\nu_e + d \rightarrow p + p + e^-$  interactions produced by  $^8\text{B}$  solar neutrinos at the Sudbury Neutrino Observatory,” *Physical Review Letters*, vol. 87, no. 7, Article ID 071301, 6 pages, 2001.
- [68] Q. R. Ahmad, R. C. Allen, T. C. Andersen et al., “Direct evidence for neutrino flavor transformation from neutral-current interactions in the sudbury neutrino observatory,” *Physical Review Letters*, vol. 89, no. 1, Article ID 011301, 2002.
- [69] G. J. Feldman, J. Hartnell, and T. Kobayashi, “Long-baseline neutrino oscillation experiments,” *Advances in High Energy Physics*, vol. 2013, Article ID 475749, 30 pages, 2013.
- [70] S. T. Petcov, “The nature of massive neutrinos,” *Advances in High Energy Physics*, vol. 2013, Article ID 852987, 20 pages, 2013.
- [71] A. D. Dolgov, “Neutrinos in cosmology,” *Physics Report*, vol. 370, no. 4-5, pp. 333–535, 2002.
- [72] A. Kusenko, “Sterile neutrinos: the dark side of the light fermions,” *Physics Reports*, vol. 48, no. 1-2, pp. 1–28, 2009.
- [73] F. Munyaneza and P. L. Biermann, “Degenerate sterile neutrino dark matter in the cores of galaxies,” *Astronomy & Astrophysics*, vol. 458, no. 2, pp. L9–L12, 2006.
- [74] D. Boyanovsky and C. M. Ho, “Sterile neutrino production via active-sterile oscillations: the quantum Zeno effect,” *Journal of High Energy Physics*, vol. 2007, no. 7, p. 30, 2007.
- [75] R. Shrock, “New tests for and bounds on neutrino masses and lepton mixing,” *Physics Letters B*, vol. 96, no. 1-2, pp. 159–164, 1980.
- [76] R. E. Shrock, “General theory of weak processes involving neutrinos. I. Leptonic pseudoscalar-meson decays, with associated tests for, and bounds on, neutrino masses and lepton mixing,” *Physical Review D*, vol. 24, no. 5, pp. 1232–1274, 1981.
- [77] R. E. Shrock, “Implications of neutrino masses and mixing for weak processes,” in *Proceedings of the Weak Interactions as Probes of Unification*, vol. 72 of *AIP Conference Proceedings*, p. 368, Blacksburg, Va, USA, 1981.
- [78] J. M. Conrad, C. M. Ignarra, G. Karagiorgi, M. H. Shaevitz, and J. Spitz, “Sterile neutrino fits to short-baseline neutrino oscillation measurements,” *Advances in High Energy Physics*, vol. 2013, Article ID 163897, 2013.
- [79] A. Nucciotti, “The use of low temperature detectors for direct measurements of the mass of the electron neutrino,” *Advances in High Energy Physics*, vol. 2016, Article ID 9153024, 41 pages, 2016.
- [80] R. G. H. Robertson, “Examination of the calorimetric spectrum to determine the neutrino mass in low-energy electron capture decay,” *Physical Review C*, vol. 91, no. 3, Article ID 035504, 2015.
- [81] A. De Rújula, “Two old ways to measure the electron-neutrino mass,” <https://arxiv.org/abs/1305.4857>.
- [82] A. De Rújula, “An upper bound on the exceptional characteristics for Lusztig’s character formula,” <https://arxiv.org/abs/0811.1674v2>.
- [83] A. Faessler and F. Šimkovic, “Can electron capture tell us the mass of the neutrino?” *Physica Scripta*, vol. 91, no. 4, Article ID 043007, 2016.
- [84] H. J. de Vega, O. Moreno, E. Moya de Guerra, M. Ramón Medrano, and N. G. Sánchez, “Role of sterile neutrino warm dark matter in rhenium and tritium beta decays,” *Nuclear Physics B*, vol. 866, no. 2, pp. 177–195, 2013.
- [85] E. M. de Guerra, O. Moreno, P. Sarriguren, and M. Ramón Medrano, “Topics on nuclear structure with electroweak probes,” *Journal of Physics: Conference Series*, vol. 366, Article ID 012011, 2012.
- [86] J. M. Boillos, O. Moreno, and E. Moya de, “Active and sterile neutrino mass effects on beta decay spectra,” in *Proceedings of the La Rabida International Scientific Meeting on Nuclear Physics: Basic Concepts in Nuclear Physics: Theory, Experiments, and Applications*, vol. 1541 of *AIP Conference Proceedings*, p. 167, La Rábida, Spain, September 2012.
- [87] P. E. Filianin, K. Blaum, S. A. Eliseev et al., “On the keV sterile neutrino search in electron capture,” *Journal of Physics G: Nuclear and Particle Physics*, vol. 41, no. 9, Article ID 095004, 2014.
- [88] S. Eliseev, K. Blaum, M. Block et al., “Direct measurement of the mass difference of  $^{163}\text{Ho}$  and  $^{163}\text{Dy}$  solves the Q-value puzzle for the neutrino mass determination,” *Physical Review Letters*, vol. 115, no. 6, Article ID 062501, 2015.
- [89] A. De Rújula, “A new way to measure neutrino masses,” *Nuclear Physics, Section B*, vol. 188, no. 3, pp. 414–458, 1981.
- [90] M. Lusignoli and M. Vignati, “Relic antineutrino capture on  $^{163}\text{Ho}$  decaying nuclei,” *Physics Letters B*, vol. 697, no. 1, pp. 11–14, 2011.
- [91] A. Faessler, L. Gastaldo, and F. Šimkovic, “Electron capture in  $^{163}\text{Ho}$ , overlap plus exchange corrections and neutrino mass,” *Journal of Physics G: Nuclear and Particle Physics*, vol. 42, no. 1, Article ID 015108, 2015.
- [92] G. Audi, F. G. Kondev, M. Wang et al., “The Nubase2012 evaluation of nuclear properties,” *Chinese Physics C*, vol. 36, no. 12, pp. 1157–1286, 2012.
- [93] S. Mertens, “Sensitivity of next-generation tritium beta-decay experiments for keV-scale sterile neutrinos,” *JCAP*, vol. 1502, no. 2, p. 20, 2015.

## Research Article

# Shell Model Studies of Competing Mechanisms to the Neutrinoless Double-Beta Decay in $^{124}\text{Sn}$ , $^{130}\text{Te}$ , and $^{136}\text{Xe}$

Andrei Neacsu and Mihai Horoi

Department of Physics, Central Michigan University, Mount Pleasant, MI 48859, USA

Correspondence should be addressed to Andrei Neacsu; [neacsu@cmich.edu](mailto:neacsu@cmich.edu)

Received 29 June 2016; Accepted 8 September 2016

Academic Editor: Theocharis Kosmas

Copyright © 2016 A. Neacsu and M. Horoi. This is an open access article distributed under the Creative Commons Attribution License, which permits unrestricted use, distribution, and reproduction in any medium, provided the original work is properly cited. The publication of this article was funded by SCOAP<sup>3</sup>.

Neutrinoless double-beta decay is a predicted beyond Standard Model process that could clarify some of the not yet known neutrino properties, such as the mass scale, the mass hierarchy, and its nature as a Dirac or Majorana fermion. Should this transition be observed, there are still challenges in understanding the underlying contributing mechanisms. We perform a detailed shell model investigation of several beyond Standard Model mechanisms that consider the existence of right-handed currents. Our analysis presents different venues that can be used to identify the dominant mechanisms for nuclei of experimental interest in the mass  $A \sim 130$  region ( $^{124}\text{Sn}$ ,  $^{130}\text{Te}$ , and  $^{136}\text{Xe}$ ). It requires accurate knowledge of nine nuclear matrix elements that we calculate in addition to the associated energy-dependent phase space factors.

## 1. Introduction

Should the neutrinoless double-beta decay ( $0\nu\beta\beta$ ) be experimentally observed, the lepton number conservation is violated by two units and the back-box theorems [1–4] predict the neutrino to be a Majorana particle. In addition to the nature of the neutrino (whether a Dirac or a Majorana fermion), there are other unknown properties of the neutrino that could be investigated via  $0\nu\beta\beta$ , such as the mass scale, the absolute mass, or the underlying neutrino mass mechanism. There are several beyond Standard Model mechanisms that could compete and contribute to this process [5, 6]. Reliable calculations of the nuclear matrix elements (NME) are necessary to perform an appropriate analysis that could help evaluate the contribution of each mechanism.

The most commonly investigated neutrinoless  $0\nu\beta\beta$  mechanism is the so-called mass mechanism involving the exchange of light left-handed neutrinos, for which the NME were calculated using many nuclear structure methods. Calculations that consider the contributions of heavy, mostly sterile, right-handed neutrinos have become recently available, while left-handed heavy neutrinos have been shown to have a negligible effect [7, 8] and their contribution is generally dismissed. A comparison of the recent mass mechanism

results obtained with the most common methods can be seen in Figure 6 of [9], where one can notice the differences that still exist among these nuclear structure methods. Figure 7 of [9] shows the heavy neutrino results for several nuclear structure methods, and the differences are even larger than those in the light neutrino case because of the uncertainties related to the short-range correlation (SRC) effects. There are efforts to reduce these uncertainties by the development of an effective transition operator that treats the SRC consistently [10].

Because shell model calculations were successful in predicting two-neutrino double-beta decay half-lives [11] before experimental measurements and as shell model calculations of different groups largely agree with each other without the need to adjust model parameters, we calculate our nuclear matrix elements using shell model techniques and Hamiltonians that reasonably describe the experimental spectroscopic observables.

Experiments such as SuperNEMO [12, 13] could track the outgoing electrons and help distinguish between the mass mechanism ( $\nu$ ) and so-called  $\lambda$  and  $\eta$  mechanisms [14, 15]. This would also provide complementary data at low energies for testing the existence of right-handed contributions predicted by left-right symmetric models [15–19], currently

investigated at high energies in colliders and accelerators such as LHC [20]. To distinguish the possible contribution of the heavy right-handed neutrino using shell model nuclear matrix elements, measurements of lifetimes for at least two different isotopes are necessary, ideally that of an  $A \sim 80$  isotope and another lifetime of an  $A \sim 130$  isotope, as discussed in Section V of [21]. It is expected that if the neutrinoless double-beta decay is confirmed in any of the experiments, more resources and upgrades could be dedicated to boost the statistics and to reveal more information on the neutrino properties.

Following our recent study for  $^{82}\text{Se}$  in [21], which is the baseline isotope of SuperNEMO, we extend our analysis of  $\lambda$  and  $\eta$  mechanisms to other nuclei of immediate experimental interest:  $^{124}\text{Sn}$ ,  $^{130}\text{Te}$ , and  $^{136}\text{Xe}$ . These isotopes are under investigation by the TIN.TIN [22] ( $^{124}\text{Sn}$ ), CUORE [23, 24], SNO+ [25] ( $^{130}\text{Te}$ ), NEXT [26], EXO [27], and KamLAND-Zen [28] ( $^{136}\text{Xe}$ ) experiments. For the mass region  $A \sim 130$ , we perform calculations in  $jj55$  model space consisting of  $0g_{7/2}$ ,  $1d_{5/2}$ ,  $1d_{3/2}$ ,  $2s_{1/2}$  and  $0h_{11/2}$  valence orbitals using the SVD shell model Hamiltonian [29] that was fine-tuned with experimental data from Sn isotopes. Our tests of this Hamiltonian include energy levels,  $B(E2)\uparrow$  transitions, occupation probabilities, Gamow-Teller strengths, and NME decomposition for configurations of protons/neutrons pairs coupled to some spin ( $I$ ) and some parity (positive or negative), called  $I$ -pair decomposition. These tests and validations of the SVD Hamiltonian can be found in [9] for  $^{124}\text{Sn}$  and in [30] for  $^{130}\text{Te}$  and  $^{136}\text{Xe}$ . Calculations of NME in larger model spaces (e.g.,  $jj77$  model space that includes  $0g_{9/2}$  and  $0h_{9/2}$  orbitals missing in  $jj55$  models space) were successfully performed for  $^{136}\text{Xe}$  [31], but for  $^{124}\text{Sn}$  and  $^{130}\text{Te}$  they are much more difficult and would require special truncations.

In this work, assuming the detection of several tens of  $0\nu\beta\beta$  decay events, we present a possibility to identify right-handed contributions from  $\lambda$  and  $\eta$  mechanisms by analyzing the two-electron angular and energy distributions that could be measured.

We organize this paper as follows: Section 2 shows a brief description of the neutrinoless double-beta decay formalism considering a low-energy Hamiltonian that takes into account contributions from right-handed currents. Section 3 presents an analysis of the half-lives and of the two-electron angular and energy distributions results for  $^{124}\text{Sn}$ ,  $^{130}\text{Te}$ , and  $^{136}\text{Xe}$ . Finally, we dedicate Section 4 to conclusions.

## 2. Brief Formalism of $0\nu\beta\beta$

The existence of right-handed currents and their contributions to the neutrinoless double-beta decay rate has been considered for a long time [14, 32], but most frequent calculations treat only the light left-handed neutrino-exchange mechanism (commonly referred to as “the mass mechanism”). One model that considers the right-handed currents contributions and includes heavy particles that are not part of the Standard Model is the left-right symmetric model [17, 18].

Within the framework of the left-right symmetric model, the neutrinoless double-beta decay half-life expression is

$$\begin{aligned} [T_{1/2}^{0\nu}]^{-1} = G_{01}^{0\nu} g_A^4 & \left| M^{0\nu} \eta_\nu + M^{0N} (\eta_{N_R}^L + \eta_{N_R}^R) + \eta_\lambda X_\lambda \right. \\ & \left. + \eta_\eta X_\eta + \dots \right|^2, \end{aligned} \quad (1)$$

where  $\eta_\nu$ ,  $\eta_{N_R}^L$ ,  $\eta_{N_R}^R$ ,  $\eta_\lambda$ , and  $\eta_\eta$  are neutrino physics parameters defined in [15] (see also Appendix A of [21]),  $M^{0\nu}$  and  $M^{0N}$  are the light and heavy neutrino-exchange nuclear matrix elements [5, 6], and  $X_\lambda$  and  $X_\eta$  are combinations of NME and phase space factors, which are calculated in this paper.  $G_{01}^{0\nu}$  is a phase space factor [33] that one can calculate [34] with good precision for most cases [35–37]. The “...” sign represents other possible contributions, such as those of R-parity violating SUSY particle exchange [5, 6], Kaluza-Klein modes [6, 38, 39], violation of Lorentz invariance, and equivalence principle [40–42], which we neglected here.  $\eta_{N_R}^L$  term also exists in the seesaw type I mechanisms but its contribution is negligible if the heavy mass eigenstates are larger than 1 GeV [8]. We consider a seesaw type I dominance [43] and we will neglect this contribution here.

For an easier read, we perform the following change of notation:  $\langle \nu \rangle = |\eta_\nu|$ ,  $\langle \lambda \rangle = |\eta_\lambda|$ , and  $\langle \eta \rangle = |\eta_\eta|$ .

In this paper, we provide an analysis of the two-electron relative energy and angular distributions for  $^{124}\text{Sn}$ ,  $^{130}\text{Te}$ , and  $^{136}\text{Xe}$  using shell model NME that we calculate. The purpose of this analysis is to identify the relative contributions of  $\eta_\lambda$  and  $\eta_\eta$  terms in (1). A similar analysis for  $^{82}\text{Se}$  was done using QRPA NME in [12] and with shell model NME in [21]. As in [21], we start from the classic paper of Doi et al. [14], describing the neutrinoless double-beta decay process using a low-energy effective Hamiltonian that includes the effects of the right-handed currents. By simplifying some notations and ignoring the contribution from  $\eta_{N_R}^R$  term, which has the same energy and angular distribution as  $\eta_\nu$  term, the half-life expression [14] is written as

$$\begin{aligned} [T_{1/2}^{0\nu}]^{-1} = & \left| M_{\text{GT}}^{0\nu} \right|^2 \left\{ C_{\nu^2} + C_{\nu\lambda} \cos \phi_1 + C_{\nu\eta} \cos \phi_2 + C_{\lambda^2} \right. \\ & \left. + C_{\eta^2} + C_{\lambda\eta} \cos (\phi_1 - \phi_2) \right\}, \end{aligned} \quad (2)$$

where  $\phi_1$  and  $\phi_2$  are the relative CP-violating phases (Eq. A7 of [21]) and  $M_{\text{GT}}^{0\nu}$  is the Gamow-Teller contribution of the light neutrino-exchange NME.  $C_\alpha$  are contributions from different mechanisms:  $C_{\nu^2}$  are from the left-handed leptonic currents,  $C_{\lambda^2}$  are from the right-handed leptonic and right-handed hadronic currents, and  $C_{\eta^2}$  are from the right-handed leptonic and left-handed hadronic currents.  $C_{\nu\lambda}$ ,  $C_{\nu\eta}$ , and  $C_{\lambda\eta}$  contain the interference between these terms. These are defined as

$$\begin{aligned} C_{\nu^2} &= C_1 \langle \nu \rangle^2, \\ C_{\nu\lambda} &= C_2 \langle \nu \rangle \langle \lambda \rangle, \\ C_{\nu\eta} &= C_3 \langle \eta \rangle \langle \nu \rangle, \\ C_{\lambda^2} &= C_4 \langle \lambda \rangle^2, \end{aligned}$$

$$\begin{aligned}
C_{\eta^2} &= C_5 \langle \eta \rangle^2, \\
C_{\lambda\eta} &= C_6 \langle \eta \rangle \langle \lambda \rangle,
\end{aligned} \tag{3}$$

where  $C_{1-6}$  are combinations of nuclear matrix elements and phase space factors (PSF). Their expressions can be found in Appendix B, Eqs. (B1) of [21].  $M_{\text{GT}}^{0\nu}$  and the other nuclear matrix elements that appear in the expressions of the  $C_i$  factors are presented in Eq. (B4) of [21].

We write the differential decay rate for  $0^+ \rightarrow 0^+ 0\nu\beta\beta$  transition as

$$\frac{d^2 W_{0^+ \rightarrow 0^+}^{0\nu}}{d\epsilon_1 d \cos \theta_{12}} = \frac{a_{0\nu} \omega_{0\nu}(\epsilon_1)}{2 (m_e R)^2} [A(\epsilon_1) + B(\epsilon_1) \cos \theta_{12}]. \tag{4}$$

Here,  $\epsilon_1$  is the energy of one electron in units of  $m_e c^2$ ,  $R$  is the nuclear radius ( $R = r_0 A^{1/3}$ , with  $r_0 = 1.2$  fm),  $\theta_{12}$  is the angle between the outgoing electrons, and the expressions for the constant  $a_{0\nu}$  and the function  $\omega_{0\nu}$  are given in Appendix C, Eqs. (C2) and (C3) of [34], respectively. The functions  $A(\epsilon)$  and  $B(\epsilon)$  are defined as combinations of factors that include PSF and NME:

$$\begin{aligned}
A(\epsilon_1) &= |N_1(\epsilon_1)|^2 + |N_2(\epsilon_1)|^2 + |N_3(\epsilon_1)|^2 \\
&\quad + |N_4(\epsilon_1)|^2,
\end{aligned} \tag{5a}$$

$$B(\epsilon_1) = -2 \text{Re} [N_1^*(\epsilon_1) N_2(\epsilon_1) + N_3^*(\epsilon_1) N_4(\epsilon_1)]. \tag{5b}$$

The detailed expressions of  $N_{1-4}(\epsilon_1)$  components are presented in Eqs. (B7) of [21].

We can express the half-life as follows:

$$\begin{aligned}
[T_{1/2}^{0\nu}]^{-1} &= \frac{1}{\ln 2} \int dW_{0^+ \rightarrow 0^+}^{0\nu} \\
&= \frac{a_{0\nu}}{\ln 2 (m_e R)^2} \cdot \int_1^{T+1} A(\epsilon_1) \omega_{0\nu}(\epsilon_1) d\epsilon_1,
\end{aligned} \tag{6}$$

with the normalized kinetic energy  $T$  defined as

$$T = \frac{Q_{\beta\beta}}{m_e c^2}, \tag{7}$$

where  $Q_{\beta\beta}$  is the Q-value of the decay.

The integration of (4) over  $\epsilon_1$  provides the angular distribution of the electrons that we write as

$$\begin{aligned}
\frac{dW_{0^+ \rightarrow 0^+}^{0\nu}}{d\Omega} &= \frac{a_{0\nu}}{4\pi (m_e R)^2} \left[ \int_1^{T+1} A(\epsilon_1) \omega_{0\nu}(\epsilon_1) d\epsilon_1 \right. \\
&\quad \left. + \frac{d\Omega}{2\pi} \int_1^{T+1} B(\epsilon_1) \omega_{0\nu}(\epsilon_1) d\epsilon_1 \right],
\end{aligned} \tag{8}$$

where  $d\Omega = 2\pi d \cos \theta_{12}$ .

Integrating (4) over  $\cos \theta_{12}$  provides the single-electron spectrum. As in [21], we express the decay rate as a function of the difference in the energy of the two outgoing electrons:  $\Delta t = (\epsilon_1 - \epsilon_2) m_e c^2$ , where  $\epsilon_2 = T + 2 - \epsilon_1$  is the kinetic energy of

TABLE 1: The nine NME of  $^{124}\text{Sn}$ ,  $^{130}\text{Te}$ , and  $^{136}\text{Xe}$ .

	$M_{\text{GT}}$	$M_F$	$M_{\text{GT}\omega}$	$M_{F\omega}$	$M_{\text{GT}q}$	$M_{Fq}$	$M_T$	$M_R$	$M_P$
$^{124}\text{Sn}$	1.85	-0.47	2.05	-0.46	1.79	-0.27	0.01	2.66	-2.06
$^{130}\text{Te}$	1.66	-0.44	1.86	-0.43	1.59	-0.25	-0.01	2.56	-1.73
$^{136}\text{Xe}$	1.50	-0.40	1.68	-0.39	1.44	-0.23	-0.01	2.34	-1.62

the second electron. We can write the energy of one electron as

$$\epsilon_1 = \frac{T + 2 + \Delta t / m_e c^2}{2}. \tag{9}$$

Changing the variable, the energy distribution as a function of  $\Delta t$  is

$$\frac{2dW_{0^+ \rightarrow 0^+}^{0\nu}}{d(\Delta t)} = \frac{2a_{0\nu}}{(m_e R)^2} \frac{\omega_{0\nu}(\Delta t)}{m_e c^2} A(\Delta t). \tag{10}$$

### 3. Results

The formalism used in this paper is taken from [21], where it was used to analyze the two-electron angular and energy distributions for  $^{82}\text{Se}$ , the baseline isotope of the SuperNEMO experiment [12, 13]. It was adapted from [14, 33] with some changes for simplicity and consistency and updated with modern notations. Here we use it to analyze in detail  $0\nu\beta\beta$  decay two-electron angular and energy distributions for  $^{124}\text{Sn}$ ,  $^{130}\text{Te}$ , and  $^{136}\text{Xe}$ . The nine NME required are calculated in this paper using the SVD shell model Hamiltonian [29] in  $jj55$  model space which was thoroughly tested and validated for  $^{124}\text{Sn}$  in [9] and for  $^{130}\text{Te}$  and  $^{136}\text{Xe}$  in [30]. For an easier comparison to other results, we use  $g_A$  value of 1.254; we include short-range correlations with CD-Bonn parametrization, finite nucleon size effects, and higher-order corrections of the nucleon current [44]. Should one change to the newer recommended  $g_A$  value of 1.27 [45], the NME results would change by only 0.5% [46] and the effective PSF (multiplied by  $g_A^4$ ) would change by 5%. This is negligible when compared to the uncertainties in the NME.  $g_A$  quenching is not considered here and an extended justification for this decision is given in [21].

In Table 1, we present the nine dimensionless NME for  $^{124}\text{Sn}$ ,  $^{130}\text{Te}$ , and  $^{136}\text{Xe}$  calculated in this work using an optimal closure energy  $\langle E \rangle = 3.5$  MeV which was obtained using a recently proposed method [47]. By using an optimal closure energy obtained for this Hamiltonian, we get  $0\nu\beta\beta$  NME results in agreement with beyond closure approaches [48]. The definition of these NME and the details regarding their calculations are given in Appendix B of [21].

The integrated PSF of the outgoing electrons, denoted by  $G_1 - G_9$ , which enter  $C_\alpha$  terms of (2), depend on the Q-value of the transition, the mass, and the charge of the final nucleus. We calculate these integrated PSF using a new effective method [34] which was in agreement with the latest results and was tested for 11 nuclei. Their complete expressions can also be found in Appendix C of [21]. The largest difference between our PSF and those of [35], among our three isotopes

TABLE 2: The nine PSF expressed in  $[\text{yr}^{-1}]$ .

	$G_1 \cdot 10^{14}$	$G_2 \cdot 10^{14}$	$G_3 \cdot 10^{14}$	$G_4 \cdot 10^{15}$	$G_5 \cdot 10^{13}$	$G_6 \cdot 10^{12}$	$G_7 \cdot 10^{10}$	$G_8 \cdot 10^{11}$	$G_9 \cdot 10^{11}$
$^{124}\text{Sn}$	1.977	4.184	1.248	3.909	6.685	3.648	2.749	2.585	0.731
$^{130}\text{Te}$	3.122	8.026	2.092	6.267	10.18	5.335	4.340	4.261	1.106
$^{136}\text{Xe}$	3.188	7.798	2.114	6.372	10.79	5.464	4.458	4.522	1.099

TABLE 3:  $C_i$  factors ( $i = 1, \dots, 6$ ) corresponding to (3) expressed in  $[\text{yr}^{-1}]$ .

	$C_1 \cdot 10^{14}$	$C_2 \cdot 10^{14}$	$C_3 \cdot 10^{11}$	$C_4 \cdot 10^{13}$	$C_5 \cdot 10^9$	$C_6 \cdot 10^{13}$
$^{124}\text{Sn}$	2.67	-1.43	0.69	0.54	1.34	-0.71
$^{130}\text{Te}$	4.25	-2.41	1.08	1.64	2.26	-2.34
$^{136}\text{Xe}$	4.36	-2.44	1.30	1.04	2.24	-1.34

TABLE 4: The neutrino parameter values chosen for  $0\nu\beta\beta$  mechanisms described in the text.

	$\langle\nu\rangle$	$\langle\lambda\rangle$	$\langle\eta\rangle$
Mass mechanism ( $\nu$ )	$2 \cdot 10^{-7}$	0	0
Lambda mechanism ( $\lambda$ )	$2 \cdot 10^{-7}$	$2 \cdot 10^{-7}$	0
Eta mechanism ( $\eta$ )	$2 \cdot 10^{-7}$	0	$2 \cdot 10^{-9}$

of interest, is of about 16% for  $G_8$  of  $^{136}\text{Xe}$ . Should one use the older formalism of [14], differences of about 88% are expected in the case of  $G_8$  for  $^{136}\text{Xe}$ . One should keep in mind that the expressions for the two-electron angular and energy distributions ( $A$  and  $B$  terms in (5a) and (5b)) contain energy-dependent (unintegrated) PSF and not the integrated PSF that are found in tables throughout the literature. Eqs. (B7) of [21] provide the details of their expressions. The values for the nine integrated PSF are presented in Table 2. The results shown include  $g_A^4 = 1.254$  constant, such that  $G_1 = G_{01}^{0\nu} g_A^4$  in (1) and  $G_{[1,9]} = G_{[01,09]} g_A^4$  of [35].

$C_i$  factors ( $i = 1, \dots, 6$ ) of (3), representing combinations of NME and PSF, are presented in Table 3. As one can clearly see,  $C_5$  term that appears in  $\eta$  mechanism is the largest. This is because of the large magnitude of  $G_7$ ,  $G_8$ , and  $G_9$  PSF displayed in Table 2.

To test the possibility of disentangling the right-handed contributions in the framework of the left-right symmetric model, we consider three theoretical cases: the case of the mass mechanism denoted with  $\nu$  and presented with the black color in the figures, the case of  $\lambda$  mechanism dominance in competition with  $\nu$  denoted with  $\lambda$  and displayed with the blue color, and the case of  $\eta$  mechanism dominance in competition with  $\nu$  denoted with  $\eta$  and displayed with the red color. This color choice is consistent throughout all the figures.

Considering the latest experimental limits [15, 35] from  $^{76}\text{Ge}$   $0\nu\beta\beta$  half-life, we select a value for the mass mechanism parameter  $\nu$  which corresponds to a light neutrino mass of about 1 meV, while the values for  $\lambda$  and  $\eta$  effective parameters are chosen to barely dominate over the mass mechanism. Should their values be reduced four times, their contributions would not be distinguishable from the mass mechanism.

TABLE 5: Calculated half-lives ( $T_{1/2}$ ) intervals for each mechanism expressed in years. The range of the interval corresponds to the uncertainty in the CP phases  $\phi_1$  and  $\phi_2$  in (2).

	$\nu$	$\lambda$	$\eta$
$^{124}\text{Sn}$	$2.73 \cdot 10^{26}$	$[7.41, 10.44] \cdot 10^{25}$	$[2.47, 4.69] \cdot 10^{25}$
$^{130}\text{Te}$	$2.12 \cdot 10^{26}$	$[5.07, 6.94] \cdot 10^{25}$	$[1.85, 3.34] \cdot 10^{25}$
$^{136}\text{Xe}$	$2.53 \cdot 10^{26}$	$[6.23, 8.60] \cdot 10^{25}$	$[2.20, 4.00] \cdot 10^{25}$

Table 4 shows the values of these parameters used in the analysis.

We consider four combinations for the CP phases  $\phi_1$  and  $\phi_2$  (each one being 0 or  $\pi$ ) which can influence the half-lives and the two-electron distributions. The maximum difference arising from the interference of these phases produces the uncertainties that are displayed as bands in the figures, changing the amplitudes and the shapes. The color convention for Figures 2–9 assigns red bands with a wavy pattern (lighter grey in black and white print) to  $\eta$  mechanism and blue bands without a pattern (darker grey in black and white print) to  $\lambda$  mechanism. As the mass mechanism does not depend on  $\phi_1$  and  $\phi_2$ , there is no interference, and it is represented by a single thick black line. Because the mass mechanism is the most studied case in the literature, one may consider it as the reference case.

The calculated half-lives of  $^{124}\text{Sn}$ ,  $^{130}\text{Te}$  and  $^{136}\text{Xe}$  are presented in Table 5. Their values can be obtained either from (2) or from (6). The maximum differences from the interference phases produce the intervals. For an easier comparison of the half-lives and the uncertainties, we also plot them in Figure 1. One can notice that the inclusion of  $\lambda$  or  $\eta$  contributions reduces the half-lives.

The shapes of the two-electron angular distributions of (8) could be used to distinguish between the mass mechanism and  $\lambda$  or  $\eta$  mechanisms. However, many recorded events (tens or more) are needed for a reliable evaluation, and even then one can face difficulties due to the unknown CP phases.  $^{124}\text{Sn}$  angular distribution is presented in Figure 2. One can see that  $\lambda$  (blue bands) and  $\eta$  (red bands) exhibit similar shapes, differing in amplitude and opposite to that of the mass mechanism (black line). In the case of  $^{130}\text{Te}$ , the same is to be expected, but  $\lambda$  and  $\eta$  bands overlap due to the unknown

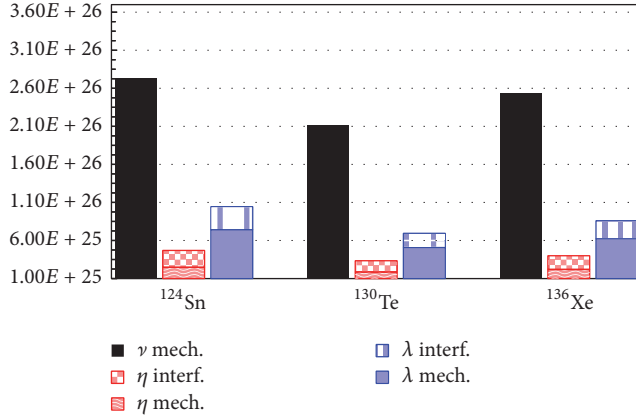


FIGURE 1: The calculated lifetimes and their uncertainties (the hatched bars) from the interference of the unknown CP phases. From left to right, the three vertical bars for each nucleus correspond to the mass mechanism,  $\eta$  mechanism, and  $\lambda$  mechanism, respectively.

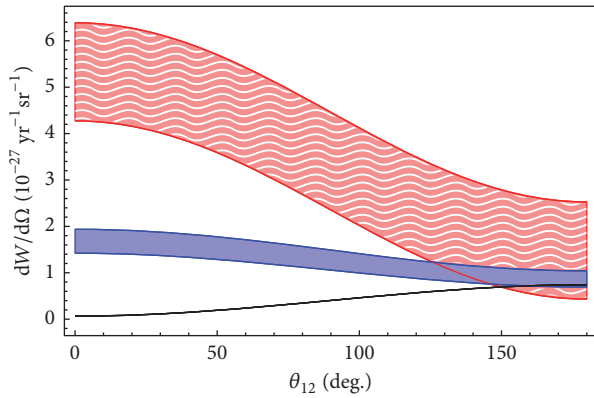


FIGURE 2: Electrons angular distribution for  $^{124}\text{Sn}$ . The red band corresponds to  $\eta$  mechanism and the blue band corresponds to  $\lambda$  mechanism. The width of the bands represents the uncertainties arising from the unknown CP phases  $\phi_1$  and  $\phi_2$ .

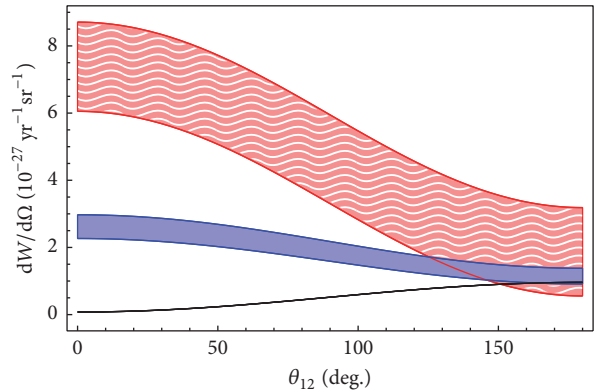


FIGURE 3: Same as Figure 2 for  $^{130}\text{Te}$ .

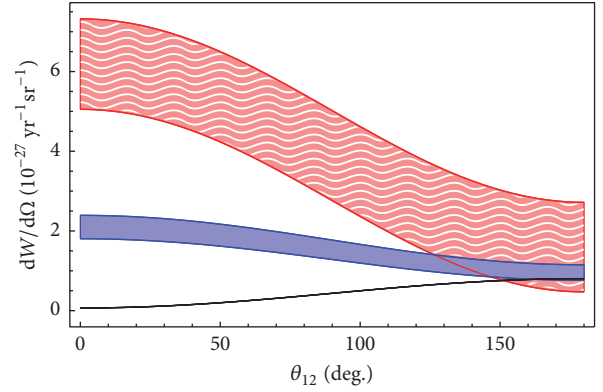


FIGURE 4: Same as Figure 2 for  $^{136}\text{Xe}$ .

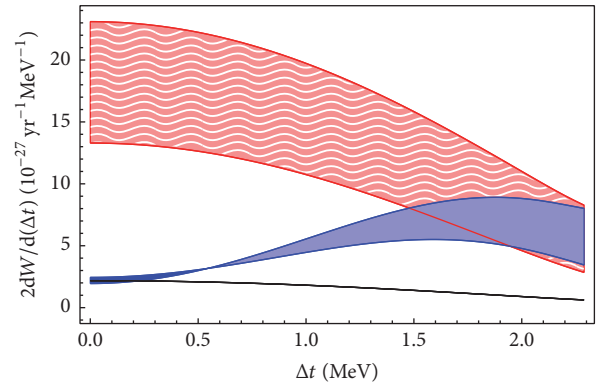


FIGURE 5: Electrons energy distribution for  $^{124}\text{Sn}$ . The red band corresponds to  $\eta$  mechanism and the blue band corresponds to  $\lambda$  mechanism. The width of the bands represents the uncertainties arising from the unknown CP phases  $\phi_1$  and  $\phi_2$ .

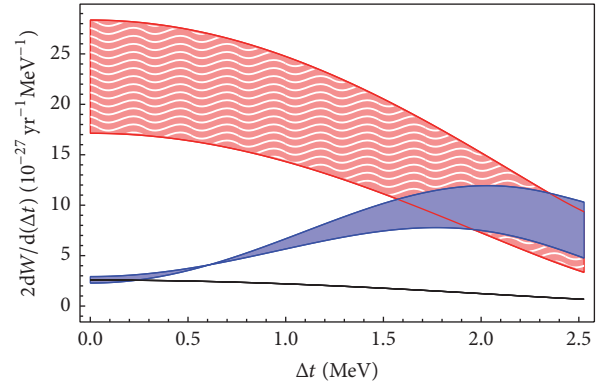
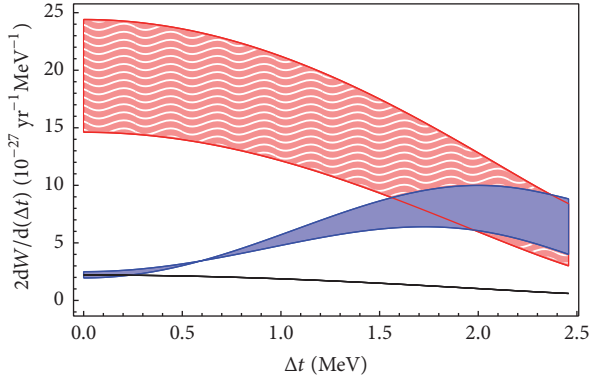
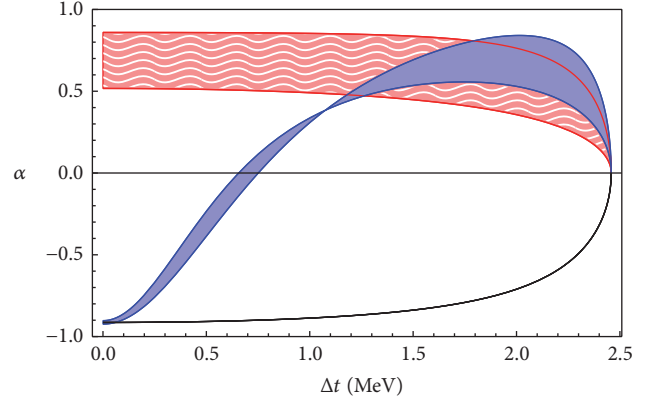
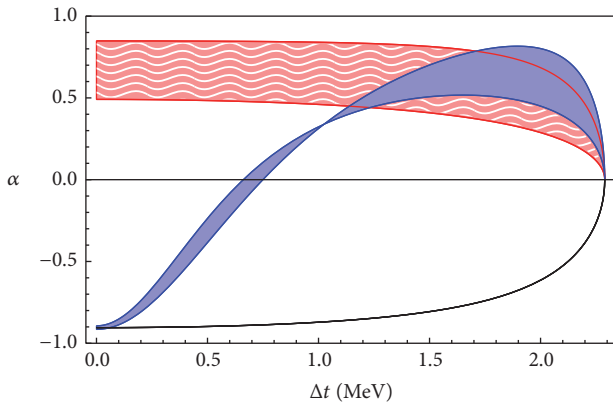
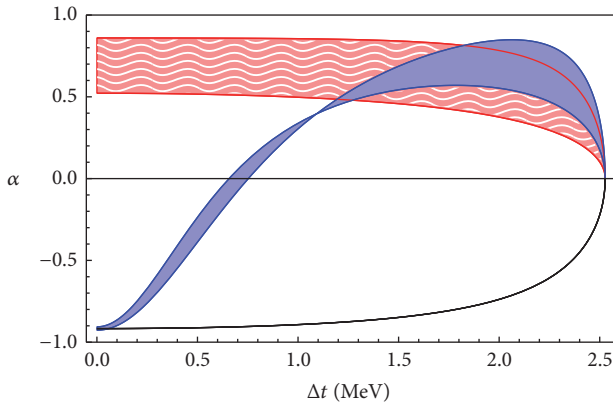


FIGURE 6: Same as Figure 5 for  $^{130}\text{Te}$ .

phases, as seen in Figure 3.  $^{136}\text{Xe}$  angular distribution is very similar to that of  $^{124}\text{Sn}$  and is presented in Figure 4.

In principle,  $\lambda$  and  $\eta$  contributions could be identified in the shapes of the two-electron energy distributions. While the tails of the distributions (when the difference between the energy of one electron and that of the other is maximal) overlap, the starting points (when both electrons have almost

FIGURE 7: Same as Figure 5 for  $^{136}\text{Xe}$ .FIGURE 10: Same as Figure 8 for  $^{136}\text{Xe}$ .FIGURE 8: The angular correlation coefficient for  $^{124}\text{Sn}$ . The red band corresponds to  $\eta$  mechanism and the blue band corresponds to  $\lambda$  mechanism. The width of the bands represents the uncertainties arising from the unknown CP phases  $\phi_1$  and  $\phi_2$ .FIGURE 9: Same as Figure 8 for  $^{130}\text{Te}$ .

equal energies) are very different for  $\lambda$  mechanism from  $\eta$  mechanism. Figure 5 shows the energy distribution for  $^{124}\text{Sn}$ .  $^{130}\text{Te}$  energy distribution is presented in Figure 6. For  $^{136}\text{Xe}$  (Figure 7), we find an energy distribution very similar to that of  $^{124}\text{Sn}$ , like in the case of the angular distributions.

To further aid with the disentanglement of  $\lambda$  and  $\eta$  mechanisms, we provide plots of the angular correlation

coefficient:  $\alpha = B(\epsilon)/A(\epsilon)$  in our (4). This may help reduce the uncertainties induced by the unknown CP phases (see, e.g., Figures 6.5–6.9 of [14] and Figure 7 of [35]). From  $\alpha(\Delta t)$ , one may also obtain clearer separation from the mass mechanism over a wide range of energies. The angular correlation coefficient for  $^{124}\text{Sn}$  is presented in Figure 8. The same behavior can be identified in Figure 9 for  $^{130}\text{Te}$  and in Figure 10 for  $^{136}\text{Xe}$ .

#### 4. Conclusions

In this paper, we report shell model calculations necessary to disentangle the mixed right-handed/left-handed currents contributions (commonly referred to as  $\eta$  and  $\lambda$  mechanisms) from the mass mechanism in the left-right symmetric model. We perform an analysis of these contributions by considering three theoretical scenarios, one for the mass mechanism, one for  $\lambda$  dominance in competition with the mass mechanism, and one where  $\eta$  mechanism dominates in competition with the mass mechanism.

The figures presented support the conclusions [14, 21] that one can distinguish  $\lambda$  or  $\eta$  dominance over the mass mechanism from the shape of the two-electron angular distribution, while one can discriminate  $\lambda$  from  $\eta$  mechanism using the shape of the energy distribution and that of the angular coefficient. The tables and the figures presented also show the uncertainties related to the effects of interference from the unknown CP-violating phases.

We show our results for phase space factors, nuclear matrix elements, and lifetimes for  $0\nu\beta\beta$  transitions of  $^{124}\text{Sn}$ ,  $^{130}\text{Te}$ , and  $^{136}\text{Xe}$  to ground states. In the case of the mass mechanism nuclear matrix elements, we obtain results which are consistent with previous calculations [21, 30], where the same SVD Hamiltonian was used. Similar to the case of  $^{82}\text{Se}$  [21], the inclusion of  $\eta$  and  $\lambda$  mechanisms contributions tends to decrease the half-lives.

The phase space factors included in the analysis of lifetimes and two-electron distributions are calculated using a recently proposed accurate effective method [9] that provides results very close to those of [35]. Reference [35] takes into account consistently the effects of the realistic finite size

proton distribution in the daughter nucleus, but it does not provide all the energy-dependent phase space contributions necessary for our analysis.

Consistent with the calculations and the conclusions we obtained for  $^{82}\text{Se}$  [21], if  $\eta$  mechanism exists, it may be favored to compete with the mass mechanisms because of the larger contribution from the phase space factors.

Finally, we conclude that, in experiments where outgoing electrons can be tracked, such as SuperNEMO [12, 13] and NEXT [49], this analysis is possible if enough data is collected, generally of the order of a few tens of events. This may be beyond the capabilities of some of the current experiments, but should a positive neutrinoless double-beta decay measurement be achieved, it is expected that more resources could be allocated to improve the design, the statistics, and the variety of the investigated isotopes of the experiments which have realistic tracking capabilities.

## Competing Interests

The authors declare that they have no competing interests.

## Acknowledgments

Support from the NUCLEI SciDAC Collaboration under US Department of Energy (Grant no. DE-SC0008529) is acknowledged. Mihai Horoi also acknowledges US NSF, Grant no. PHY-1404442, and US Department of Energy, Grant no. DE-SC0015376.

## References

- [1] J. Schechter and J. W. F. Valle, "Neutrinoless double- decay in  $SU(2)\times U(1)$  theories," *Physical Review D*, vol. 25, no. 11, pp. 2951–2954, 1982.
- [2] J. Nieves, "Dirac and pseudo-Dirac neutrinos and neutrinoless double beta decay," *Physics Letters B*, vol. 147, no. 4-5, pp. 375–379, 1984.
- [3] E. Takasugi, "Can the neutrinoless double beta decay take place in the case of Dirac neutrinos?" *Physics Letters B*, vol. 149, no. 4-5, pp. 372–376, 1984.
- [4] M. Hirsch, S. Kovalenko, and I. Schmidt, "Extended Black box theorem for lepton number and flavor violating processes," *Physics Letters B*, vol. 642, no. 1-2, pp. 106–110, 2006.
- [5] J. D. Vergados, H. Ejiri, and F. Šimković, "Theory of neutrinoless double-beta decay," *Reports on Progress in Physics*, vol. 75, no. 10, Article ID 106301, 2012.
- [6] M. Horoi, "Shell model analysis of competing contributions to the double- $\beta$  decay of  $^{48}\text{Ca}$ ," *Physical Review C*, vol. 87, no. 1, Article ID 014320, 2013.
- [7] M. Mitra, G. Senjanović, and F. Vissani, "Neutrinoless double beta decay and heavy sterile neutrinos," *Nuclear Physics B*, vol. 856, no. 1, pp. 26–73, 2012.
- [8] M. Blennow, E. Fernandez-Martinez, J. Lopez-Pavon, and J. Menendez, "Neutrinoless double beta decay in seesaw models," *Journal of High Energy Physics*, vol. 2010, no. 7, article 096, 2010.
- [9] M. Horoi and A. Neacsu, "Shell model predictions for  $^{124}\text{Sn}$  double- $\beta$  decay," *Physical Review C*, vol. 93, no. 2, Article ID 024308, 2016.
- [10] J. D. Holt and J. Engel, "Effective double- $\beta$ -decay operator for  $^{76}\text{Ge}$  and  $^{82}\text{Se}$ ," *Physical Review C*, vol. 87, no. 6, Article ID 064315, 2013.
- [11] J. Retamosa, E. Caurier, and F. Nowacki, "Neutrinoless double beta decay of Ca48," *Physical Review C*, vol. 51, no. 1, pp. 371–378, 1995.
- [12] R. Arnold, C. Augier, J. Baker et al., "Probing new physics models of neutrinoless double beta decay with SuperNEMO," *The European Physical Journal C*, vol. 70, no. 4, pp. 927–943, 2010.
- [13] M. Bongrand, "Search for  $0\nu 2\beta$  of  $^{100}\text{Mo}$  by NEMO-3 and status of SuperNEMO," in *Proceedings of the 26th International Conference on Neutrino Physics and Astrophysics: Neutrino*, vol. 1666 of *AIP Conference Proceedings*, Boston, Mass, USA, June 2014.
- [14] M. Doi, T. Kotani, and E. Takasugi, "Double beta decay and Majorana neutrino," *Progress of Theoretical Physics Supplement*, vol. 83, pp. 1–175, 1985.
- [15] J. Barry and W. Rodejohann, "Lepton number and flavour violation in TeV-scale left-right symmetric theories with large left-right mixing," *Journal of High Energy Physics*, vol. 2013, no. 9, article 153, 2013.
- [16] J. C. Pati and A. Salam, "Lepton number as the fourth 'color,'" *Physical Review D*, vol. 10, no. 1, pp. 275–289, 1974.
- [17] R. N. Mohapatra and J. C. Pati, "'Natural' left-right symmetry," *Physical Review D*, vol. 11, no. 9, pp. 2558–2561, 1975.
- [18] G. Senjanovic and R. N. Mohapatra, "Exact left-right symmetry and spontaneous violation of parity," *Physical Review D*, vol. 12, no. 5, pp. 1502–1505, 1975.
- [19] W.-Y. Keung and G. Senjanovic, "Majorana neutrinos and the production of the right-handed charged Gauge Boson," *Physical Review Letters*, vol. 50, no. 19, article 1427, 1983.
- [20] V. Khachatryan, A. M. Sirunyan, A. Tumasyan et al., "Search for heavy neutrinos and W bosons with right-handed couplings in proton-proton collisions at  $\sqrt{s} = 8$  TeV," *The European Physical Journal C*, vol. 74, no. 11, article 3149, pp. 1–23, 2014.
- [21] M. Horoi and A. Neacsu, "Analysis of mechanisms that could contribute to neutrinoless double-beta decay," *Physical Review D*, vol. 93, no. 11, Article ID 113014, 2016.
- [22] V. Nanal, "Search for neutrinoless double beta decay in  $^{124}\text{Sn}$ ," in *Proceedings of the International Nuclear Physics Conference (INPC '13)*, vol. 66 of *EPJ Web of Conferences*, p. 08005, March 2014.
- [23] K. Alfonso, D. R. Artusa, F. T. Avignone et al., "Search for neutrinoless double- $\beta$  decay of  $^{130}\text{Te}$  with CUORE-0," *Physical Review Letters*, vol. 115, no. 10, Article ID 102502, 2015.
- [24] C. Alduino, K. Alfonso, D. R. Artusa et al., "CUORE-0 detector: design, construction and operation," *Journal of Instrumentation*, vol. 11, no. 7, pp. 1–35, 2016.
- [25] S. Andringa, E. Arushanova, S. Asahi et al., "Current status and future prospects of the SNO+ experiment," *Advances in High Energy Physics*, vol. 2016, Article ID 6194250, 21 pages, 2016.
- [26] J. J. Gomez-Cadenas, V. Álvarez, F. I. G. Borges et al., "Present status and future perspectives of the NEXT experiment," *Advances in High Energy Physics*, vol. 2014, Article ID 907067, 22 pages, 2014.
- [27] J. B. Albert, D. J. Auty, P. S. Barbeau et al., "Search for Majorana neutrinos with the first two years of EXO-200 data," *Nature*, vol. 510, no. 7504, pp. 229–234, 2014.
- [28] A. Gando, Y. Gando, T. Hachiya et al., "Search for Majorana neutrinos near the inverted mass Hierarchy region with KamLAND-Zen," *Physical Review Letters*, vol. 117, no. 8, Article ID 082503, 6 pages, 2016.

- [29] C. Qi and Z. X. Xu, "Monopole-optimized effective interaction for tin isotopes," *Physical Review C*, vol. 86, no. 4, Article ID 044323, 11 pages, 2012.
- [30] A. Neacsu and M. Horoi, "Shell model studies of the  $^{130}\text{Te}$  neutrinoless double- $\beta$  decay," *Physical Review C*, vol. 91, no. 2, Article ID 024309, 9 pages, 2015.
- [31] M. Horoi and B. A. Brown, "Shell-model analysis of the  $^{136}\text{Xe}$  double beta decay nuclear matrix elements," *Physical Review Letters*, vol. 110, no. 22, Article ID 222502, 2013.
- [32] M. Doi, T. Kotani, H. Nishiura, and E. Takasugi, "Double beta decay," *Progress of Theoretical Physics*, vol. 69, no. 2, pp. 602–635, 1983.
- [33] J. Suhonen and O. Civitarese, "Weak-interaction and nuclear-structure aspects of nuclear double beta decay," *Physics Report*, vol. 300, no. 3-4, pp. 123–214, 1998.
- [34] M. Horoi and A. Neacsu, "An effective method to accurately calculate the phase space factors for  $\beta^-\beta^-$  decay," *Advances in High Energy Physics*, vol. 2016, Article ID 7486712, 8 pages, 2016.
- [35] D. Štefánik, R. Dvornický, F. Šimkovic, and P. Vogel, "Reexamining the light neutrino exchange mechanism of the  $0\nu\beta\beta$  decay with left- and right-handed leptonic and hadronic currents," *Physical Review C*, vol. 92, no. 5, Article ID 055502, 2015.
- [36] J. Kotila and F. Iachello, "Phase-space factors for double- $\beta$  decay," *Physical Review C*, vol. 85, no. 3, Article ID 034316, 2012.
- [37] S. Stoica and M. Mirea, "New calculations for phase space factors involved in double- $\beta$  decay," *Physical Review C*, vol. 88, no. 3, Article ID 037303, 2013.
- [38] G. Bhattacharyya, H. V. Klapdor-Kleingrothaus, H. Pas, and A. Pilaftsis, "Neutrinoless double beta decay from singlet neutrinos in extra dimensions," *Physical Review D*, vol. 67, no. 11, Article ID 113001, 2003.
- [39] F. Deppisch and H. Päs, "Pinning down the mechanism of neutrinoless double  $\beta$  decay with measurements in different nuclei," *Physical Review Letters*, vol. 98, no. 23, Article ID 232501, 4 pages, 2007.
- [40] C. N. Leung, "Neutrino tests of general and special relativity," *Nuclear Instruments and Methods in Physics Research A*, vol. 451, no. 1, pp. 81–85, 2000.
- [41] H. Klapdor-Kleingrothaus, H. Päs, and U. Sarkar, "Test of special relativity and equivalence principle from neutrinoless double beta decay," *The European Physical Journal A—Hadrons and Nuclei*, vol. 5, no. 1, pp. 3–6, 1999.
- [42] G. Barenboim, J. Beacom, L. Borisso, and B. Kayser, "CPT violation and the nature of neutrinos," *Physics Letters B*, vol. 537, no. 3-4, pp. 227–232, 2002.
- [43] P. S. Bhupal Dev, S. Goswami, and M. Mitra, "TeV-scale left-right symmetry and large mixing effects in neutrinoless double beta decay," *Physical Review D*, vol. 91, no. 11, Article ID 113004, 2015.
- [44] M. Horoi and S. Stoica, "Shell model analysis of the neutrinoless double- $\beta$  decay of  $^{48}\text{Ca}$ ," *Physical Review C*, vol. 81, no. 2, Article ID 024321, 7 pages, 2010.
- [45] K. A. Olive, K. Agashe, C. Amsler et al., "Review of particle physics," *Chinese Physics C*, vol. 38, no. 9, Article ID 090001, 2014.
- [46] R. A. Sen'kov, M. Horoi, and B. A. Brown, "Neutrinoless double- $\beta$  decay of  $^{82}\text{Se}$  in the shell model: beyond the closure approximation," *Physical Review C*, vol. 89, no. 5, Article ID 054304, 7 pages, 2014.
- [47] R. A. Sen'kov and M. Horoi, "Accurate shell-model nuclear matrix elements for neutrinoless double- $\beta$  decay," *Physical Review C*, vol. 90, no. 5, Article ID 051301, 2014.
- [48] R. A. Sen'kov and M. Horoi, "Neutrinoless double- $\beta$  decay of  $^{48}\text{Ca}$  in the shell model: closure versus nonclosure approximation," *Physical Review C*, vol. 88, no. 6, Article ID 064312, 2013.
- [49] S. Cebrián, J. Pérez, I. Bandac et al., "Radiopurity assessment of the tracking readout for the NEXT double beta decay experiment," *Journal of Instrumentation*, vol. 10, Article ID P05006, 2015.

## Research Article

# Analysis of the Intermediate-State Contributions to Neutrinoless Double $\beta^-$ Decays

Juhani Hyvärinen and Jouni Suhonen

Department of Physics, University of Jyväskylä, P.O. Box 35, 40014 Jyväskylä, Finland

Correspondence should be addressed to Juhani Hyvärinen; [juhani.t.hyvarinen@student.jyu.fi](mailto:juhani.t.hyvarinen@student.jyu.fi)

Received 1 April 2016; Accepted 26 May 2016

Academic Editor: Luca Stanco

Copyright © 2016 J. Hyvärinen and J. Suhonen. This is an open access article distributed under the Creative Commons Attribution License, which permits unrestricted use, distribution, and reproduction in any medium, provided the original work is properly cited. The publication of this article was funded by SCOAP<sup>3</sup>.

A comprehensive analysis of the structure of the nuclear matrix elements (NMEs) of neutrinoless double beta-minus ( $0\nu\beta^-\beta^-$ ) decays to the  $0^+$  ground and first excited states is performed in terms of the contributing multipole states in the intermediate nuclei of  $0\nu\beta^-\beta^-$  transitions. We concentrate on the transitions mediated by the light (I-NMEs) Majorana neutrinos. As nuclear model we use the proton-neutron quasiparticle random-phase approximation (pnQRPA) with a realistic two-nucleon interaction based on the Bonn one-boson-exchange  $G$  matrix. In the computations we include the appropriate short-range correlations, nucleon form factors, and higher-order nucleonic weak currents and restore the isospin symmetry by the isoscalar-isovector decomposition of the particle-particle proton-neutron interaction parameter  $g_{pp}$ .

## 1. Introduction

Thanks to neutrino-oscillation experiments much is known about the basic properties of the neutrino concerning its mixing and squared mass differences. What is not known is the absolute mass scale, the related mass hierarchy, and the fundamental nature (Dirac or Majorana) of the neutrino. This can be studied by analyzing the neutrinoless double beta ( $0\nu2\beta$ ) decays of atomic nuclei [1–4] through analyses of the participating nuclear matrix elements (NMEs). The  $0\nu2\beta$  decays proceed by virtual transitions through states of all multipoles  $J^\pi$  in the intermediate nucleus,  $J$  being the total angular momentum and  $\pi$  being the parity of the intermediate state. Most of the present interest is concentrated on the double beta-minus variant ( $0\nu\beta^-\beta^-$  decay) of the  $0\nu2\beta$  decays due to their relatively large decay energies ( $Q$  values) and natural abundancies.

In this work we concentrate on analyses of the intermediate contributions to the  $0\nu\beta^-\beta^-$  decays for the  $0^+ \rightarrow 0^+$  ground-state-to-ground-state and ground-state-to-excited-state transitions in nuclear systems of experimental interest. We focus on the light Majorana neutrino mediated transitions

by taking into account the appropriate short-range nucleon-nucleon correlations [5] and contributions arising from the induced currents and the finite nucleon size [6]. There are several nuclear models that have recently been used to compute the  $0\nu\beta^-\beta^-$  decay NMEs (see, e.g., the extensive discussions in [3, 7–11]). However, the only model that avoids the closure approximation and retains the contributions from individual intermediate states is the proton-neutron quasiparticle random-phase approximation (pnQRPA) [7, 12–14].

Some analyses of the intermediate-state contributions within the pnQRPA approach have been performed in [12, 13, 15, 16] and recently quite extensively in [17]. In [17] an intermediate multipole  $J^\pi$  decomposition was done for decays of  $^{76}\text{Ge}$ ,  $^{82}\text{Se}$ ,  $^{96}\text{Zr}$ ,  $^{100}\text{Mo}$ ,  $^{110}\text{Pd}$ ,  $^{116}\text{Cd}$ ,  $^{124}\text{Sn}$ ,  $^{128,130}\text{Te}$ , and  $^{136}\text{Xe}$  to the ground state of the respective daughter nuclei. In this paper we extend the analysis of [17] to a more detailed scrutiny of the intermediate contributions to the  $0\nu\beta^-\beta^-$  decay NMEs of the above-mentioned nuclei. We also extend the scope of [17] by considering transitions to the first  $0^+$  excited states in addition to the ground-state-to-ground-state transitions.

## 2. Theory Background

In this section a very brief introduction to the computational framework of the present calculations is given. The present analyses on ground-state-to-ground-state decays are based on the calculations done in [17]. Details considering the excited-state decays are given in a future publication. We assume here that the  $0\nu\beta^-\beta^-$  decay proceeds via the light Majorana neutrino so that the inverse half-life can be written as

$$\left[ t_{1/2}^{(0\nu)}(0_i^+ \rightarrow 0_f^+) \right]^{-1} = g_A^4 G_{0\nu} |M^{(0\nu)}|^2 |\langle m_\nu \rangle|^2, \quad (1)$$

where  $G_{0\nu}$  is a phase-space factor for the final-state leptons defined here without the axial vector coupling constant  $g_A$ . The quantity  $\langle m_\nu \rangle$  denotes the neutrino effective mass and describes the physics beyond the standard model [17]. The quantity  $M^{(0\nu)}$  is the light neutrino nuclear matrix element (1-NME). The nuclear matrix element can be decomposed into Gamow-Teller (GT), Fermi (F), and tensor (T) contributions as

$$M^{(0\nu)} = M_{\text{GT}}^{(0\nu)} - \left( \frac{g_V}{g_A} \right)^2 M_{\text{F}}^{(0\nu)} + M_{\text{T}}^{(0\nu)}, \quad (2)$$

where  $g_V$  is the vector coupling constant.

Each of the NMEs  $K = \text{GT}, \text{F}, \text{and T}$  in (2) can be decomposed in terms of the intermediate multipole contributions  $J^\pi$  as

$$M_K^{(0\nu)} = \sum_{J^\pi} M_K^{(0\nu)}(J^\pi), \quad (3)$$

where each multipole contribution is, in turn, decomposed in terms of the two-particle transition matrix elements and one-body transition densities as

$$\begin{aligned} M_K^{(0\nu)}(J^\pi) &= \sum_{k_1, k_2, J'} \sum_{pp', nn'} (-1)^{j_n + j_{p'} + J + J'} \sqrt{2J' + 1} \\ &\times \begin{Bmatrix} j_p & j_n & J \\ j_{p'} & j_{n'} & J' \end{Bmatrix} (pp' : J' \parallel \mathcal{O}_K \parallel nn' : J') \\ &\times \left( 0_f^+ \parallel \left[ c_{p'}^\dagger \bar{c}_{n'} \right]_J \parallel J_{k_1}^\pi \right) \langle J_{k_1}^\pi \mid J_{k_2}^\pi \rangle \left( J_{k_2}^\pi \parallel \left[ c_p^\dagger \bar{c}_n \right]_J \parallel 0_i^+ \right), \end{aligned} \quad (4)$$

where  $k_1$  and  $k_2$  label the different pnQRPA solutions for a given multipole  $J^\pi$  and the indices  $p, p', n, n'$  denote the proton and neutron single-particle quantum numbers. The operators  $\mathcal{O}_K$  inside the two-particle matrix element contain the neutrino potentials for the light Majorana neutrinos, the characteristic two-particle operators for the different  $K = \text{GT}, \text{F}, \text{T}$  and a function taking into account the short-range correlations (SRC) between the two decaying neutrons in the mother nucleus of  $0\nu\beta^-\beta^-$  decay [17]. The final  $0_f^+$  state,  $0_f^+$ , can be either the ground state or an excited state of the  $0\nu\beta^-\beta^-$  daughter nucleus, and the overlap factor between the two one-body transition densities helps connect the corresponding intermediate  $J^\pi$  states emerging from the pnQRPA calculations in the mother and daughter nuclei.

As mentioned before, our calculations contain the appropriate short-range correlators, nucleon form factors, and higher-order nucleonic weak currents. In addition, we decompose the particle-particle proton-neutron interaction strength parameter  $g_{\text{pp}}$  of the pnQRPA into its isoscalar ( $T = 0$ ) and isovector ( $T = 1$ ) components and adjust these components independently as described in [17]: the isovector component is fixed such that the NME of the two-neutrino double beta-decay ( $2\nu\beta^-\beta^-$ ) vanishes and the isospin symmetry is thus restored for both the  $2\nu\beta^-\beta^-$  and  $0\nu\beta^-\beta^-$  decays. The isoscalar component, in turn, is fixed such that the measured half-life of the  $2\nu\beta^-\beta^-$  decay is reproduced. The resulting values of both components of  $g_{\text{pp}}$  are shown in Table I of [17]. The details of the chosen valence spaces and the determination of the other Hamiltonian parameters are presented in [17]. We further note that in [17] two sets of NME computations, related to the value of the axial vector coupling  $g_A$ , were performed: first with the quenched value  $g_A = 1.00$  and then with the bare value  $g_A = 1.26$ . In both computations the value of  $g_A$  was fixed first. After this the Hamiltonian parameters were adjusted by using the experimental data, as briefly described above and more thoroughly in [17].

## 3. Results and Discussion

In this section we discuss and present the results of our calculations. Presentation of the results follows top to bottom approach. First we analyze the multipole decompositions and total cumulative sums of the matrix elements. From these we can extract the most important multipole components and energy regions contributing to the NMEs. After this we continue and dissect the most important multipole components into contributions coming from different individual states of the  $0\nu\beta\beta$  intermediate nucleus. Throughout these computations we have used a conservatively quenched value of the axial vector coupling  $g_A = 1.00$ ; that is, we use the pnQRPA parameters which are related to the first set of computations in [17] as was explained at the end of Section 2.

There has been a lot of discussion about the correct value of  $g_A$  in both the  $2\nu\beta\beta$  and  $0\nu\beta\beta$  decays lately. This is so due to the fact that a large portion of the theoretical half-life uncertainties are related to the present ambiguity in the value of  $g_A$ . In [9] the quenching of  $g_A$  was studied in the framework of IBM-2 and the interacting shell model (ISM). The effective  $g_A$  values were parametrized as  $g_A^{\text{eff}} = 1.269A^{-0.18}$  (IBM-2) and as  $g_A^{\text{eff}} = 1.269A^{-0.12}$  (ISM). These parametrizations were obtained by comparing the model calculations with experimental data on  $2\nu\beta\beta$  decays. Further studies were performed within the framework of the pnQRPA by using the available Gamow-Teller beta-decay and  $2\nu\beta\beta$  decay data in several publications (see [18] and the references therein). A wide systematic study of the quenching of  $g_A$  for Gamow-Teller beta decays was performed in [18]. Even the quenching related to spin-dipole  $2^-$  states was studied in [19]. While the beta decays and  $2\nu\beta\beta$  decays are low-energy processes with small momentum transfers, the  $0\nu\beta\beta$  decay involves large momentum transfers and the thus

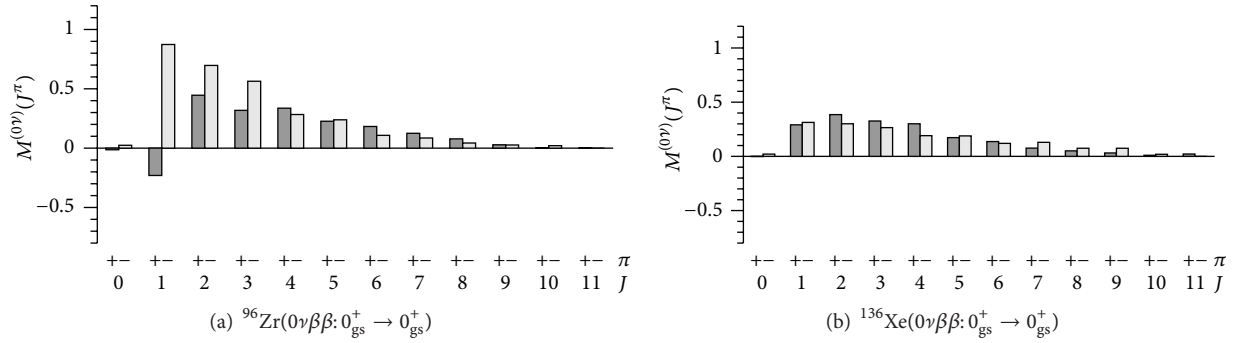


FIGURE 1: Multipole decomposition of the 1-NME for the nuclei  $^{96}\text{Zr}$  and  $^{136}\text{Xe}$  corresponding to the  $0_{\text{gs}}^+ \rightarrow 0_{\text{gs}}^+$  decay transitions.

activated high-energy and high-multipolarity intermediate states. For higher momentum transfers the effective  $g_A$  can be momentum-dependent [20] and different multipoles can be affected in different ways. At present there exists no known recipe on how to determine the value of  $g_A$  for the neutrinoless double beta decays, and that is why we have chosen in the present study to work with a moderately quenched value  $g_A = 1.00$ , assumed to be the same for all intermediate multipoles. We will study, however, the effect of changing the value of  $g_A$  to the characteristics of the intermediate-state contributions in Section 3.3.

**3.1. Ground-State-to-Ground-State Transitions.** Let us begin by considering the ground-state-to-ground-state decays mediated by light neutrino exchange. In Figures 1(a) and 1(b) we have plotted the multipole decomposition (3) of the 1-NMEs corresponding to the  $A = 96$  and  $136$  nuclear systems. For most nuclei considered in this work, the leading multipole component is  $1^-$ . This is the case also for the nucleus  $^{96}\text{Zr}$  shown in Figure 1(a). Most important contribution to the NMEs comes from the lowest multipole components  $1^\pm - 4^\pm$ . It can also be observed that the shape of the overall multipole distribution is leveled when going towards heavier nuclei. This can be seen by comparing the distribution of  $^{96}\text{Zr}$  with the distribution of  $^{136}\text{Xe}$  displayed in Figure 1(b).

Nuclei can be grouped into different types according to the shapes of their cumulative NME distributions. For  $0_{\text{gs}}^+ \rightarrow 0_{\text{gs}}^+$  transitions via light neutrino exchange, we can differentiate four types of nuclei. *Type 1:* nuclei belonging to this type are  $^{76}\text{Ge}$ ,  $^{82}\text{Se}$ ,  $^{96}\text{Zr}$ , and  $^{128}\text{Te}$ . Representative of this type,  $^{76}\text{Ge}$ , is presented in Figure 2(a). Characteristic feature of the cumulative sum distribution belonging to type 1 is the strong drop in the value of the NME occurring between 12 and 17 MeV. Soon after this drop the NME saturates as can be seen from panel (a). *Type 2:* nuclei belonging to this type are  $^{100}\text{Mo}$  and  $^{110}\text{Pd}$ . Representative of this type,  $^{110}\text{Pd}$ , is presented in Figure 2(b). Characteristic feature of this type is the large enhancement and almost immediate cancellation of this enhancement around 10 MeV. This produces a spike-like structure into the cumulative sum distribution as can be seen from panel (b). *Type 3:* nuclei belonging to type 3 are  $^{116}\text{Cd}$ ,  $^{124}\text{Sn}$ , and  $^{130}\text{Te}$ . Type 3 is represented by  $^{124}\text{Sn}$ ,

shown in Figure 2(c). Characteristic features of this type are that there occurs neither sharp cancellation of the NME around 12–17 MeV, as in type 1, nor a spike like structure around 10 MeV, as in type 2. Value of the NME rather increases more or less smoothly to its highest value and then smoothly saturates to its final value around 20 MeV. *Type 4:* type 4 is special in a sense that it includes only one nucleus,  $^{136}\text{Xe}$ . Cumulative sum of the NME for  $^{136}\text{Xe}$  is shown in Figure 2(d). Characteristic feature of type 4 is that the lowest energy region, roughly between 0 and 1.5 MeV, contributes practically nothing to the value of the NME as can be noticed from panel (d).

Using the multipole decompositions, we have extracted the most important multipole components contributing to the light neutrino mediated ground-state-to-ground-state decays. These most important components can be divided into contributions coming from different energy levels of the  $0\nu\beta\beta$  intermediate nucleus. These contributions are collected into Table 1 for  $A = 76$ – $100$  systems, into Table 2 for  $A = 110$ – $124$  systems, and into Table 3 for  $A = 128$ – $136$  systems. We see from the tables that often a very small set of states collects the largest part of a given multipole contribution to the NMEs. Also in some cases notable contributions are coming from high excitation energies, well above 10 MeV, like in the case of  $1^-$  contributions for almost all nuclei,  $1^+$  contributions for  $^{76}\text{Ge}$ ,  $^{82}\text{Se}$ ,  $^{110}\text{Pd}$ ,  $^{116}\text{Cd}$ , and  $^{124}\text{Sn}$ ,  $2^+$  contributions for  $^{130}\text{Te}$  and  $^{136}\text{Xe}$ , and a  $3^-$  contribution for  $^{124}\text{Sn}$ .

We notice a single-state dominance for the  $2^-$  mode in nuclei  $^{76}\text{Ge}$ ,  $^{82}\text{Se}$ , and  $^{96}\text{Zr}$ . In [19] an analysis of the unique first forbidden single  $\beta^\pm 2^- \rightarrow 0^+$  ground-state-to-ground-state transitions in the mass region  $A = 72$ – $132$  was performed. It was found that a strong renormalization of the axial vector  $2^-$  single  $\beta$  matrix elements is needed to be able to explain the experimental transition rates. It was then speculated that the same kind of an effect may also appear in the  $0\nu\beta\beta$  NMEs. This may have a large effect on the  $0\nu\beta\beta$  transition rates due to the important contribution of the  $2^-$  multipole to the  $0\nu\beta\beta$  NMEs.

The energies of the intermediate states listed in Tables 1, 2, and 3 (and also those in Tables 4 and 5 for the transitions to the excited states) originate from pnQRPA calculations. Usually the pnQRPA cannot reproduce the fine details of

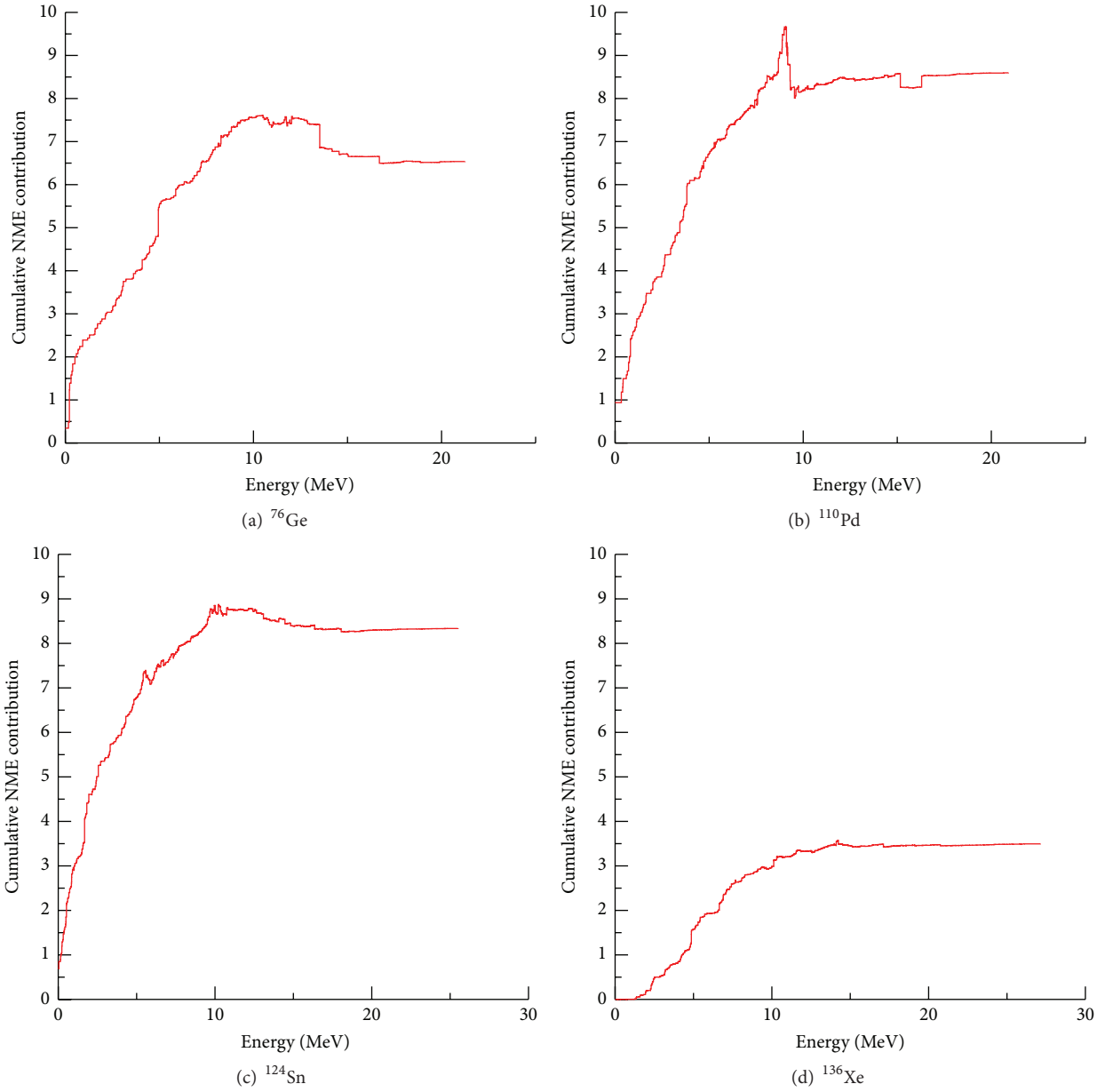


FIGURE 2: Cumulative values of the computed l-NMEs corresponding to the  $0_{\text{gs}}^+ \rightarrow 0_{\text{gs}}^+$  decay transitions for the nuclear systems  $A = 76, 110, 124$  and  $136$ . The horizontal axis gives the excitation energies of the intermediate states contributing to the  $0\nu\beta\beta$  transition.

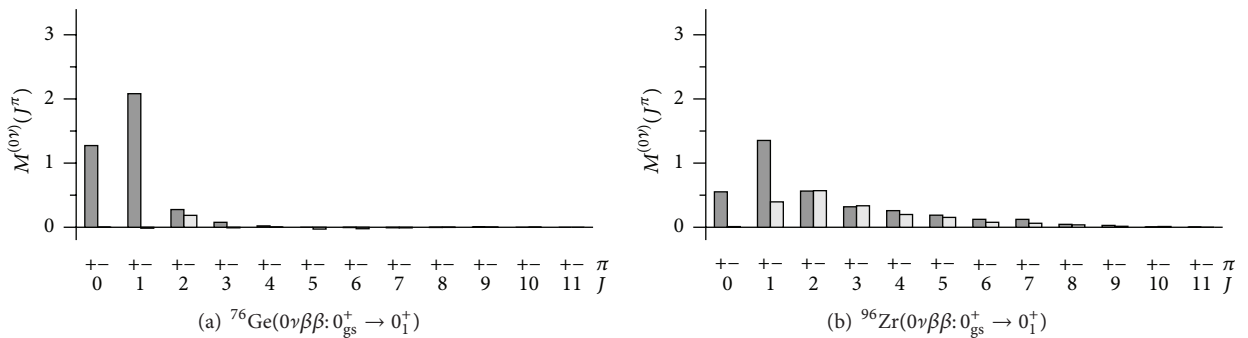


FIGURE 3: Multipole decomposition of the l-NME for the nuclei  $^{76}\text{Ge}$  and  $^{96}\text{Zr}$  corresponding to the  $0_{\text{gs}}^+ \rightarrow 0_1^+$  decay transitions.

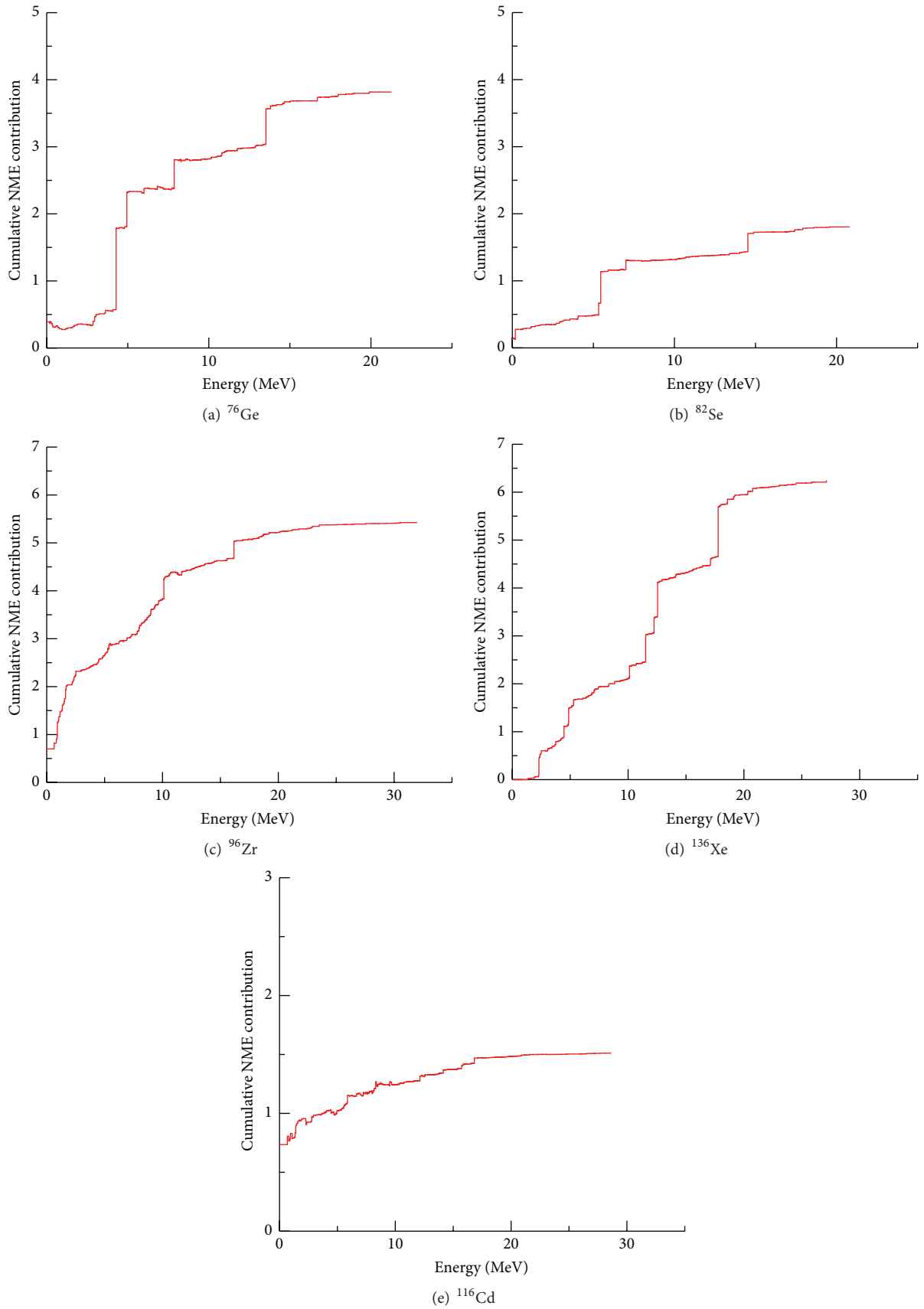


FIGURE 4: Cumulative values of the computed 1-NMEs corresponding to the  $0_{gs}^+ \rightarrow 0_1^+$  decay transitions for the nuclear systems  $A = 76, 82, 96, 116,$  and  $136$ . The horizontal axis gives the excitation energies of the intermediate states contributing to the  $0\nu\beta\beta$  transition.

TABLE 1: Most important multipoles and intermediate states contributing to the ground-state-to-ground-state  $0\nu\beta\beta$  decays mediated by the light neutrino exchange. Columns  $E$  give the energies (in MeVs) and multipoles of the intermediate states. Multipoles are organized from left to right in terms of their importance, the most important being on the left. Columns labeled  $C$  give the corresponding NME contributions. Last two numbers in each  $C$  column give the summed contribution and the percentual part which the displayed states give to the total multipole strength. The percentage inside the parenthesis gives the fraction with which the displayed states contribute to the total NME.

$^{76}\text{Ge}$	$E(2^-)$	$C$	$E(1^-)$	$C$	$E(2^+)$	$C$	$E(1^+)$	$C$	$E(3^-)$	$C$	
	0.22	0.748	5.87	0.155	0.51	0.166	0.00	0.344	0.30	0.189	
			6.32	0.058	1.87	0.056	4.09	0.199	0.92	0.148	
			7.00	0.077	3.04	0.094	4.48	0.148	6.77	0.056	
			7.16	0.064	3.62	0.108	4.94	0.578	6.85	0.053	
			8.27	0.190	4.81	0.058	10.80	-0.053	11.63	0.062	
			11.04	0.084	7.73	0.054	11.75	-0.109	12.07	-0.053	
			12.03	0.165			13.52	-0.522			
			16.70	0.158							
			0.748		0.635		0.556		0.668		0.454
		79% (11%)		83% (10%)		77% (9%)		88% (10%)		70% (7%)	
$^{82}\text{Se}$	$E(2^-)$	$C$	$E(2^+)$	$C$	$E(1^-)$	$C$	$E(3^-)$	$C$	$E(1^+)$	$C$	
	0.00	0.510	0.65	0.137	5.27	0.116	0.07	0.140	0.19	0.264	
			1.73	0.065	6.85	0.065	0.82	0.138	3.16	0.095	
			2.22	0.051	7.98	0.134			4.07	0.065	
			3.56	0.084	9.79	0.083			4.55	0.105	
			4.05	0.052	12.25	0.065			5.32	0.559	
			4.93	0.054	17.41	0.070			7.01	-0.253	
									14.53	-0.396	
			0.510		0.442		0.393		0.278		0.439
			81% (11%)		81% (9%)		76% (8%)		57% (6%)		92% (9%)
$^{96}\text{Zr}$	$E(1^-)$	$C$	$E(2^-)$	$C$	$E(3^-)$	$C$	$E(2^+)$	$C$	$E(4^+)$	$C$	
	1.75	0.056	0.92	0.498	1.35	0.151	0.64	0.150	1.05	0.099	
	2.28	0.063	2.21	0.065	2.35	0.051	1.63	0.114	1.68	0.071	
	2.52	0.150	3.75	0.050	7.77	0.064			5.69	0.064	
	4.46	0.050	4.43	0.052	11.36	-0.091					
	5.04	0.077	8.53	0.057							
	5.27	0.209	8.77	-0.056							
	8.65	0.060									
	11.33	0.061									
			0.728		0.666		0.175		0.265		0.234
		83% (16%)		96% (15%)		31% (4%)		59% (6%)		69% (5%)	
$^{100}\text{Mo}$	$E(1^-)$	$C$	$E(2^+)$	$C$	$E(4^+)$	$C$	$E(3^+)$	$C$	$E(2^-)$	$C$	
	3.12	0.307	0.90	0.192	1.32	0.158	1.33	0.202	1.76	0.205	
	4.41	0.109	2.10	0.154	2.26	0.097	1.68	0.076	2.85	0.147	
	6.68	0.091	11.68	0.082			7.43	0.152	5.52	-0.061	
	11.15	0.117	11.97	-0.070			7.76	-0.173	10.17	0.219	
	16.72	0.058							10.93	-0.194	
	20.26	-0.060									
	23.90	-0.060									
			0.562		0.359		0.255		0.257		0.316
			70% (11%)		62% (7%)		53% (5%)		54% (5%)		72% (6%)

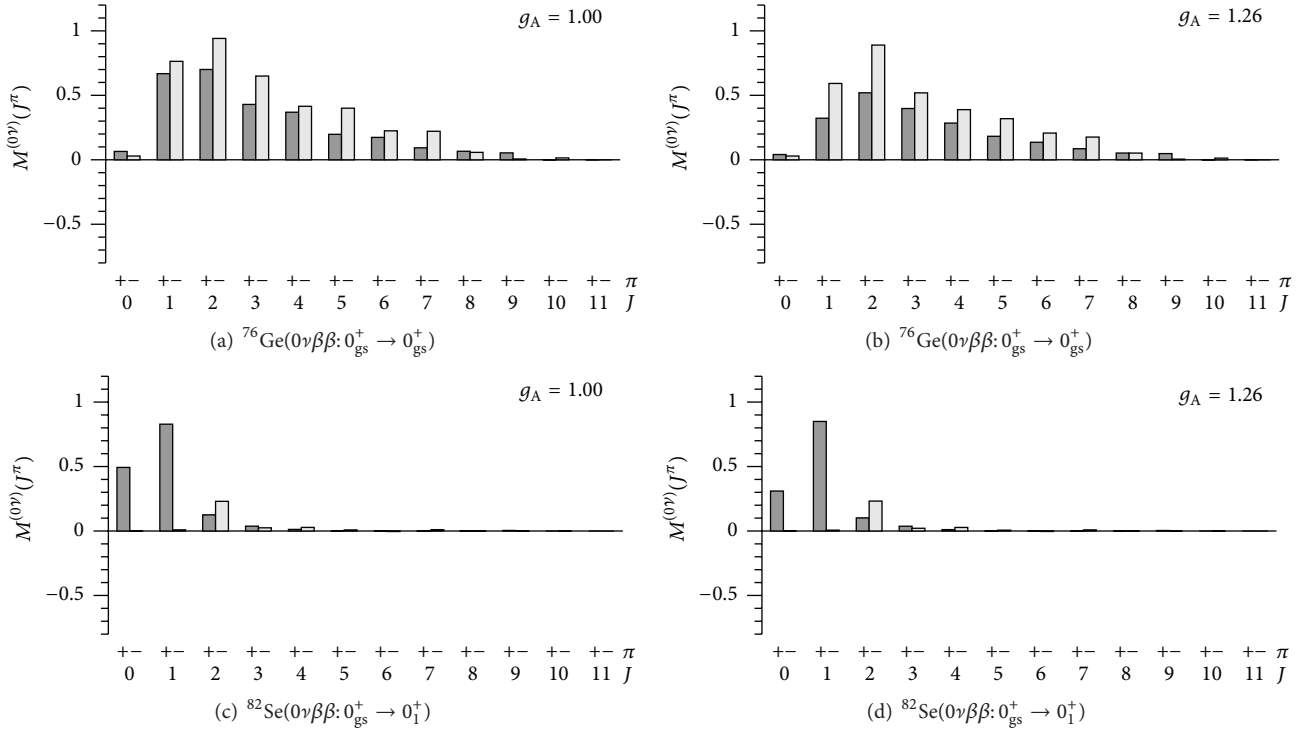


FIGURE 5: Multipole decompositions for the ground-state-to-ground-state decay of the nucleus  $^{76}\text{Ge}$  ((a) and (b) panels) and for the ground-state-to-excited-state decay of the nucleus  $^{82}\text{Se}$  ((c) and (d) panels). The value  $g_A = 1.00$  was used for (a) and (c) panels and the value  $g_A = 1.26$  for (b) and (d) panels.

the level structures found in all intermediate odd-odd nuclei considered in this work. This is due to the general feature of odd-odd nuclei: the extremely high density of states even at low energies. This high density of nuclear states becomes a problem, not only for the pnQRPA, but for any other nuclear many-body approach, including the nuclear shell model. The reason for this is that even small perturbations in the two-body interaction matrix elements tend to change the ordering of the levels at random. For this reason the spectra of the odd-odd intermediate nuclei are not a very good measure of the reliability of the calculations but, instead, a better way is to adjust the model parameters in such a way that the transition rates of some other known processes, for example, single or  $2\nu\beta\beta$  decays, can be reproduced by the theory and this is the philosophy which we have followed in this work.

**3.2. Ground-State-to-Excited-State Decays.** Let us then consider  $0_{\text{gs}}^+ \rightarrow 0_1^+$  transitions mediated by the light neutrino exchange. In Figures 3(a) and 3(b) we have plotted the multipole decomposition of the 1-NMEs corresponding to the  $A = 76$  and  $96$  nuclear systems. The multipole distributions for the excited-state transitions are greatly different from those corresponding to the ground-state transitions. Usually there is only a couple of multipoles,  $0^+$  and  $1^+$ , which give by far the largest contribution to the NMEs. In this sense the excited-state transitions are more simple than the ground-state transitions. Typical example is the nucleus  $^{76}\text{Ge}$ , displayed in Figure 3(a). One nucleus deviating from this

trend is  $^{96}\text{Zr}$  which is presented in Figure 3(b). Its multipole distribution resembles somewhat more those shown for the ground-state decays in Figures 1(a) and 1(b). Most of this differing behaviour can be traced back to the one-phonon structure of the final  $0_1^+$  excited state in the nucleus  $^{96}\text{Mo}$ . The  $0_1^+$  final states in this work are modeled as one-phonon basic QRPA excitations for the daughter nuclei  $^{96}\text{Mo}$  and  $^{116}\text{Sn}$ . Rest of the final states are modeled as two-quadrupole-phonon states. Nucleus  $^{96}\text{Zr}$  is an exceptional case since the  $0_1^+$  state in  $^{96}\text{Mo}$  has a relatively low excitation energy and thus boasts rather strong collective features. This is why the excited-state transition has a wide multipole distribution and is greatly enhanced.

Again we can divide nuclei into different groups by considering the shapes of their total cumulative sum distributions. For  $0_{\text{gs}}^+ \rightarrow 0_1^+$  transitions via light neutrino exchange, we can differentiate two types of nuclei. *Type 1:* nuclei belonging to type 1 are  $^{76}\text{Ge}$ ,  $^{82}\text{Se}$ ,  $^{124}\text{Sn}$ ,  $^{130}\text{Te}$ , and  $^{136}\text{Xe}$ . Typical examples of this type,  $^{76}\text{Ge}$ ,  $^{82}\text{Se}$ , and  $^{136}\text{Xe}$ , are shown in Figures 4(a), 4(b), and 4(d). Characteristic feature of this type is that there exist only few energy states which give most of the total matrix element producing a staircase-like structure as seen in the panels. For example, for  $^{76}\text{Ge}$  there seems to be only five such energy states. *Type 2:* nuclei belonging to this type are  $^{96}\text{Zr}$ ,  $^{100}\text{Mo}$ ,  $^{110}\text{Pd}$ , and  $^{116}\text{Cd}$ . Typical examples of this type are  $^{96}\text{Zr}$  and  $^{116}\text{Cd}$  shown in Figures 4(c) and 4(e). Characteristic feature of type 2 is that a large number of intermediate states give

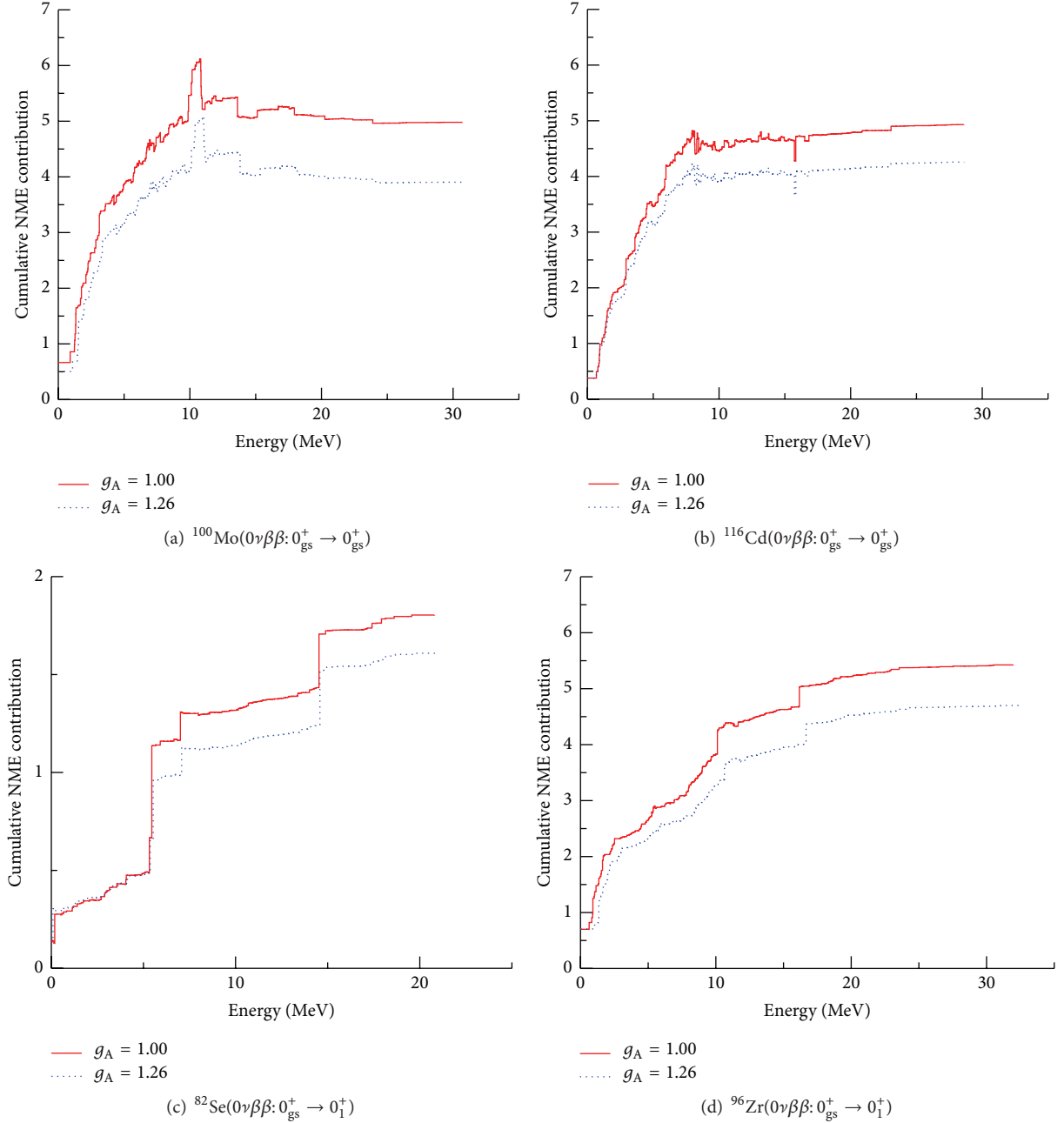


FIGURE 6: Cumulative values of the 1-NMEs for ground-state-to-ground-state decays of the nuclei  $^{100}\text{Mo}$  and  $^{116}\text{Cd}$  ((a) and (b) panels), and for the ground-state-to-excited-state decays of the nuclei  $^{82}\text{Se}$  and  $^{96}\text{Zr}$  ((c) and (d) panels). The horizontal axis gives the excitation energies of the intermediate states contributing to the  $0\nu\beta\beta$  transition. Two different values for the axial coupling were used as indicated in the panels.

important contributions to the NMEs. In case of  $^{116}\text{Cd}$ , panel (e), around 50% of the total NME comes from transitions through the ground state of the intermediate nucleus. The other 50% is distributed rather evenly on the interval 0–20 MeV.

Using the multipole decompositions, we extracted the most important multipole components contributing to the light neutrino mediated  $0_{\text{gs}}^+ \rightarrow 0_1^+$  decay transitions. These most important components were then again divided into contributions coming from different energy levels of

the  $0\nu\beta\beta$  intermediate nucleus. These contributions are collected into Table 4 for  $A = 76\text{--}116$  systems and into Table 5 for  $A = 124\text{--}136$  systems. Again we notice that often only a few intermediate states give the largest contribution to the dominant multipoles  $1^+$  and  $0^+$ . Extreme case is the nucleus  $^{116}\text{Cd}$  for which the dominant intermediate ground state gives 81% of the total  $1^+$  strength. Combining this with the fact that  $1^+$  is by far the largest multipole component, we get a rather good approximation for the total NME by considering just a single virtual transition through the  $1^+$  ground state

TABLE 2: Most important multipoles and intermediate states contributing to the ground-state-to-ground-state  $0\nu\beta\beta$  decays mediated by the light neutrino exchange. Columns  $E$  give the energies (in MeVs) and multipoles of the intermediate states. Multipoles are organized from left to right in terms of their importance, the most important being on the left. Columns labeled  $C$  give the corresponding NME contributions. Last two numbers in each  $C$  column give the summed contribution and the percentual part which the displayed states give to the total multipole strength. The percentage inside the parenthesis gives the fraction with which the displayed states contribute to the total NME.

$^{110}\text{Pd}$	$E(1^-)$	$C$	$E(2^-)$	$C$	$E(1^+)$	$C$	$E(3^-)$	$C$	$E(2^+)$	$C$
	2.95	0.130	0.82	0.387	0.00	0.938	1.14	0.118	0.33	0.244
	3.19	0.106	2.47	0.091	4.70	-0.062	1.64	0.128	0.95	0.087
	3.44	0.221	2.63	0.163	9.61	0.153	1.91	0.080	8.68	0.061
	3.81	0.426	5.94	0.107	9.75	-0.146	3.07	0.053	8.73	0.075
	4.52	0.126	8.88	0.161	10.22	0.079	3.61	0.075	9.00	0.061
	9.11	0.109	9.54	-0.256	15.16	-0.316	5.33	0.066	9.07	0.053
					16.30	0.256	8.08	0.167	9.16	0.199
							8.37	-0.051	9.30	-0.366
							8.45	0.052		
							8.68	0.275		
						9.11	-0.468			
	1.118		0.653		0.903		0.496		0.414	
	77% (13%)		68% (7%)		96% (10%)		60% (6%)		55% (5%)	
$^{116}\text{Cd}$	$E(1^-)$	$C$	$E(3^-)$	$C$	$E(2^-)$	$C$	$E(1^+)$	$C$	$E(3^+)$	$C$
	3.61	0.223	1.72	0.081	1.84	0.065	0.00	0.378	0.90	0.158
	4.47	0.099	2.30	0.053	2.93	0.287	8.37	-0.102	1.40	0.068
	5.37	0.118	2.79	0.051	7.56	0.075	9.51	0.087	3.89	0.057
	5.87	0.140	7.24	0.104	8.31	0.246	10.74	-0.083		
	8.61	0.102			8.34	0.103	11.20	0.081		
	23.07	0.071			8.45	-0.262	13.75	0.080		
					9.69	-0.051	13.79	-0.087		
							15.73	-0.363		
							15.83	0.440		
							16.51	-0.082		
						16.83	0.092			
	0.753		0.289		0.463		0.439		0.284	
	72% (15%)		65% (6%)		106% (9%)		102% (9%)		76% (6%)	
$^{124}\text{Sn}$	$E(1^-)$	$C$	$E(1^+)$	$C$	$E(2^+)$	$C$	$E(2^-)$	$C$	$E(3^-)$	$C$
	1.68	0.522	0.00	0.690	0.23	0.157	0.52	0.271	0.36	0.050
	4.82	0.089	1.00	-0.067	0.60	0.083	1.82	0.225	0.49	0.110
	6.54	0.082	2.56	0.252	1.06	0.056	4.55	0.051	1.95	0.150
	9.57	0.059	3.31	0.153	2.15	0.066	7.60	0.057	9.67	0.086
	10.74	0.159	6.72	-0.130	7.11	0.055	7.66	-0.064	9.70	0.062
	14.07	0.065	9.51	0.098			10.20	0.183	9.82	-0.087
	14.46	-0.099	13.09	-0.112			10.35	-0.094	12.64	-0.053
	14.83	-0.058								
	16.36	-0.087								
	18.05	-0.067								
	0.664		0.884		0.417		0.629		0.318	
	55% (8%)		95% (11%)		53% (5%)		89% (8%)		49% (4%)	

of the intermediate nucleus  $^{116}\text{In}$ . As for the ground-state-to-ground-state decays in some cases notable contributions are coming from high excitation energies, well above 10 MeV. There are high-energy contributions in case of  $1^+$  multipole for all nuclei, and in the cases of  $2^-$  and  $2^+$  multipoles for  $^{130}\text{Te}$  and  $^{136}\text{Xe}$ .

3.3. *Effects of  $g_A$  on the Intermediate-State Contributions.* As mentioned earlier, we have used in this work the quenched value for the axial vector coupling  $g_A = 1.00$ . Next we shall briefly examine how our results will change if we increase the value of  $g_A$  from the quenched value 1.00 to the bare value 1.26. The effect of this amplification of the axial coupling

TABLE 3: Most important multipoles and intermediate states contributing to the ground-state-to-ground-state  $0\nu\beta\beta$  decays mediated by the light neutrino exchange. Columns  $E$  give the energies (in MeVs) and multipoles of the intermediate states. Multipoles are organized from left to right in terms of their importance, the most important being on the left. Columns labeled  $C$  give the corresponding NME contributions. Last two numbers in each  $C$  column give the summed contribution and the percentual part which the displayed states give to the total multipole strength. The percentage inside the parenthesis gives the fraction with which the displayed states contribute to the total NME.

$^{128}\text{Te}$	$E(1^-)$	$C$	$E(2^+)$	$C$	$E(3^-)$	$C$	$E(2^-)$	$C$	$E(3^+)$	$C$
	4.22	0.200	0.04	0.066	0.16	0.055	0.61	0.335	0.02	0.074
	4.72	0.060	0.51	0.052	0.58	0.140	4.02	0.060	2.37	0.063
	6.21	0.078	2.93	0.084	3.97	0.052	4.55	0.101	6.22	0.078
	6.44	0.059	3.97	0.053	10.04	0.061	4.89	-0.070	6.77	-0.065
	8.07	-0.084	6.77	0.050			10.14	0.136	9.82	-0.062
	8.30	0.151					10.57	-0.056	10.27	-0.057
	8.98	0.068					11.55	0.058		
	10.69	-0.052								
	11.12	0.182								
	17.48	-0.079								
19.19	-0.100									
		0.484		0.305		0.308		0.564		0.154
		69% (8%)		52% (5%)		58% (5%)		120% (10%)		33% (3%)
$^{130}\text{Te}$	$E(1^-)$	$C$	$E(2^+)$	$C$	$E(3^-)$	$C$	$E(3^+)$	$C$	$E(2^-)$	$C$
	4.18	0.184	0.13	0.054	0.84	0.113	0.10	0.056	0.97	0.277
	5.72	0.059	3.16	0.089			0.36	0.052	10.25	0.061
	6.27	0.059	4.70	0.064			2.60	0.056	11.33	-0.100
	8.56	0.096	10.49	-0.065			6.35	0.063		
	11.26	0.115	10.57	0.145			6.83	0.054		
	17.77	-0.062	10.97	-0.088			12.31	0.059		
	19.51	-0.079	16.44	0.150			12.41	-0.065		
			16.54	-0.132						
			0.373	0.216		0.113		0.166		0.237
			61% (7%)	40% (4%)		25% (2%)		39% (3%)		56% (5%)
$^{136}\text{Xe}$	$E(2^+)$	$C$	$E(3^+)$	$C$	$E(1^-)$	$C$	$E(2^-)$	$C$	$E(4^+)$	$C$
	1.59	0.033	1.35	0.033	6.65	0.141	4.86	0.188	2.34	0.032
	2.26	0.038	2.39	0.054	7.32	0.044	7.42	0.068	2.44	0.061
	2.50	0.037	4.81	0.050	10.31	0.053			4.43	0.031
	5.29	0.067	8.27	0.035					4.76	0.049
	6.57	0.033	9.99	0.027					7.67	0.034
	7.05	0.027	10.65	-0.027					9.10	0.045
	14.11	0.087							9.65	-0.038
	14.25	-0.085								
			0.238	0.172		0.238		0.256		0.214
			62% (7%)	53% (5%)		76% (7%)		85% (7%)		71% (6%)

strength on the NMEs is demonstrated in Figure 5 where we have plotted the multipole decompositions for nuclei  $^{76}\text{Ge}$  and  $^{82}\text{Se}$  calculated with both values of the axial coupling  $g_A = 1.00$  and  $g_A = 1.26$ . In case of the ground-state-to-ground-state decays, the  $1^+$  multipole changes rather fast when the axial coupling is increased from 1.00 to 1.26. This happens mainly due to the changing of the  $g_{pp}$  parameter (for each  $g_A$  value, the parameter  $g_{pp}$  is adjusted in such a way that the measured  $2\nu\beta\beta$  rate is reproduced). The  $1^+$  multipole contribution is very sensitive to the value of  $g_{pp}$ . We can see from Figures 5(a) and 5(b) that for  $g_A = 1.00$  the

$1^+$  component is among the five most important multipoles, while for  $g_A = 1.26$  it is not. Some of the higher multipoles change also somewhat, but not so rapidly. Ground-state-to-excited-state transitions proceed mainly through the  $0^+$  and  $1^+$  multipole channels. We see from Figures 5(c) and 5(d) that increasing the value of  $g_A$  affects mostly the  $0^+$  component.

Figure 6 displays the total cumulative sum distributions for ground-state-to-ground-state decays of the nuclei  $^{100}\text{Mo}$  and  $^{116}\text{Cd}$  (panels (a) and (b)), and for ground-state-to-excited-state decays of the nuclei  $^{82}\text{Se}$  and  $^{96}\text{Zr}$  (panels (c) and (d)). Axial coupling values  $g_A = 1.00$  and  $g_A = 1.26$



TABLE 5: Most important multipoles and intermediate states contributing to the ground-state-to-excited-state  $0\nu\beta\beta$  decays mediated by the light neutrino exchange. Columns  $E$  give the energies (in MeVs) and multipoles of the intermediate states. Multipoles are organized from left to right in terms of their importance, the most important being on the left. Columns labeled  $C$  give the corresponding NME contributions. Last two numbers in each  $C$  column give the summed contribution and the percentual part which the displayed states give to the total multipole strength. The percentage inside the parenthesis gives the fraction with which the displayed states contribute to the total NME.

Nucleus	$E(1^+)$	$C$	$E(0^+)$	$C$				
$^{124}\text{Sn}$	0.00	0.101	2.70	0.667				
	0.66	0.433	4.60	0.088				
	1.00	0.146	7.35	0.567				
	2.25	0.051						
	2.56	0.227						
	3.31	0.664						
	6.72	0.289						
	7.91	0.424						
	13.09	0.473						
	13.86	0.161						
	2.968		1.322					
	94% (44%)		94% (19%)					
Nucleus	$E(1^+)$	$C$	$E(0^+)$	$C$	$E(2^-)$	$C$	$E(2^+)$	$C$
$^{130}\text{Te}$	0.25	0.390	7.40	0.719	0.97	0.340	0.41	0.019
	1.50	0.082	8.35	0.631	5.07	0.073	0.59	0.047
	2.32	0.097			17.26	0.106	1.83	0.017
	2.76	0.134			18.95	0.083	2.80	0.043
	4.53	0.064					4.70	0.024
	5.59	0.338					4.86	0.027
	7.57	0.592					5.18	0.033
	14.66	0.065					6.27	0.016
	15.01	0.259					6.75	0.051
	15.07	0.773					9.10	0.032
	15.39	0.089					10.57	0.045
							17.87	0.026
							23.14	0.024
		2.882		1.351		0.602		0.390
	95% (41%)		99.6% (19%)		79% (9%)		65% (6%)	
Nucleus	$E(1^+)$	$C$	$E(0^+)$	$C$	$E(2^-)$	$C$	$E(2^+)$	$C$
$^{136}\text{Xe}$	2.30	0.366	12.24	0.317	2.50	0.060	4.86	0.204
	3.06	0.050	12.54	0.712	4.86	0.056	18.58	0.083
	3.75	0.066			5.29	0.113	20.34	0.059
	4.46	0.226			8.34	0.053		
	10.12	0.232			14.11	0.054		
	11.52	0.565						
	17.12	0.137						
	17.78	1.031						
		2.675		1.029		0.335		0.346
	93% (43%)		101% (16%)		53% (5%)		67% (6%)	

were adopted. We notice from the figures that increasing the axial coupling strength shifts the distributions downwards. This is especially true for the higher energy parts. Despite this fact, the overall shapes of the cumulative sum distributions do not change much and the same classification of nuclei into different categories according to their cumulative distribution shapes seems to hold also for larger values of  $g_A$ .

#### 4. Conclusions

In this paper we have extended our previous work [17] on the ground-state-to-ground-state  $0\nu\beta\beta$  decay transitions. In the present work we have concentrated our studies on the intermediate contributions to the NMEs involved in the light neutrino mediated  $0\nu\beta\beta$  decay. We have calculated the intermediate state multipole decompositions of the NMEs and extracted the most important multipole components. Cumulative sums of the NMEs were calculated to investigate the important energy regions contributing to the  $0\nu\beta\beta$  transitions. Finally, the most important multipole components were divided into contributions coming from the virtual transitions through the individual states of the  $0\nu\beta\beta$  intermediate nuclei. An extensive tabulation of these important intermediate states were given for all the nuclei considered in this paper.

We have done these computations by using realistic two-body interactions and single-particle bases. All the appropriate short-range correlations, nucleon form factors, and higher-order nucleonic weak currents are included in our present results.

We found in the calculations that often there exists only a few relevant intermediate states which collect most of the strength corresponding to a given multipole. We also found that there exists a single-state dominance in the important  $2^-$  components related to the ground-state decays of nuclei  $^{76}\text{Ge}$ ,  $^{82}\text{Se}$  and perhaps also for  $^{96}\text{Zr}$ .

#### Competing Interests

The authors declare that they have no competing interests.

#### Acknowledgments

This work has been partially supported by the Academy of Finland under the Finnish Centre of Excellence Programme 2012–2017 (Nuclear and Accelerator Based Programme at JYFL).

#### References

- [1] J. Suhonen and O. Civitarese, “Weak-interaction and nuclear-structure aspects of nuclear double beta decay,” *Physics Report*, vol. 300, no. 3-4, pp. 123–214, 1998.
- [2] F. T. Avignone, S. R. Elliott, and J. Engel, “Double beta decay, Majorana neutrinos, and neutrino mass,” *Reviews of Modern Physics*, vol. 80, no. 2, pp. 481–516, 2008.
- [3] J. D. Vergados, H. Ejiri, and F. Šimkovic, “Theory of neutrinoless double-beta decay,” *Reports on Progress in Physics*, vol. 75, no. 10, p. 106301, 2012.
- [4] J. Maalampi and J. Suhonen, “Neutrinoless double  $\beta^+/\text{EC}$  decays,” *Advances in High Energy Physics*, vol. 2013, Article ID 505874, 18 pages, 2013.
- [5] M. Kortelainen, O. Civitarese, J. Suhonen, and J. Toivanen, “Short-range correlations and neutrinoless double beta decay,” *Physics Letters, Section B: Nuclear, Elementary Particle and High-Energy Physics*, vol. 647, no. 2-3, pp. 128–132, 2007.
- [6] F. Šimkovic, G. Pantis, J. D. Vergados, and A. Faessler, “Additional nucleon current contributions to neutrinoless double  $\beta$  decay,” *Physical Review C*, vol. 60, no. 5, Article ID 055502, 14 pages, 1999.
- [7] J. Suhonen and O. Civitarese, “Review of the properties of the  $0\nu\beta^-\beta^-$  nuclear matrix elements,” *Journal of Physics G: Nuclear and Particle Physics*, vol. 39, no. 12, Article ID 124005, 2012.
- [8] P. Vogel, “Nuclear structure and double beta decay,” *Journal of Physics G: Nuclear and Particle Physics*, vol. 39, no. 12, p. 124002, 2012.
- [9] J. Barea, J. Kotila, and F. Iachello, “Nuclear matrix elements for double- $\beta$  decay,” *Physical Review C*, vol. 87, no. 1, Article ID 014315, 2013.
- [10] A. Neacsu and S. Stoica, “Study of nuclear effects in the computation of the  $0\nu\beta\beta$  decay matrix elements,” *Journal of Physics G: Nuclear and Particle Physics*, vol. 41, no. 1, Article ID 015201, 2014.
- [11] J. Engel, “Uncertainties in nuclear matrix elements for neutrinoless double-beta decay,” *Journal of Physics G: Nuclear and Particle Physics*, vol. 42, no. 3, Article ID 034017, 2015.
- [12] F. Šimkovic, A. Faessler, V. Rodin, P. Vogel, and J. Engel, “Anatomy of the  $0\nu\beta\beta$  nuclear matrix elements,” *Physical Review C: Nuclear Physics*, vol. 77, no. 4, Article ID 045503, 2008.
- [13] M. T. Mustonen and J. Engel, “Large-scale calculations of the double- $\beta$  decay of  $^{76}\text{Ge}$ ,  $^{130}\text{Te}$ ,  $^{136}\text{Xe}$ , and  $^{150}\text{Nd}$  in the deformed self-consistent Skyrme quasiparticle random-phase approximation,” *Physical Review C*, vol. 87, Article ID 064302, 2013.
- [14] F. Šimkovic, V. Rodin, A. Faessler, and P. Vogel, “ $0\nu\beta\beta$  and  $2\nu\beta\beta$  nuclear matrix elements, quasiparticle random-phase approximation, and isospin symmetry restoration,” *Physical Review C*, vol. 87, no. 4, Article ID 045501, 9 pages, 2013.
- [15] V. A. Rodin, A. Faessler, F. Šimkovic, and P. Vogel, “Assessment of uncertainties in QRPA  $0\nu\beta\beta$ -decay nuclear matrix elements,” *Nuclear Physics A*, vol. 766, pp. 107–131, 2006.
- [16] D.-L. Fang, A. Faessler, V. Rodin, and F. Šimkovic, “Neutrinoless double- $\beta$  decay of deformed nuclei within quasiparticle random-phase approximation with a realistic interaction,” *Physical Review C*, vol. 83, no. 3, Article ID 034320, 8 pages, 2011.
- [17] J. Hyvärinen and J. Suhonen, “Nuclear matrix elements for  $0\nu\beta\beta$  decays with light or heavy Majorana-neutrino exchange,” *Physical Review C*, vol. 91, no. 2, Article ID 024613, 12 pages, 2015.
- [18] P. Pirinen and J. Suhonen, “Systematic approach to  $\beta$  and  $2\nu\beta\beta$  decays of mass  $A = 100 - 136$  nuclei,” *Physical Review C*, vol. 91, no. 5, Article ID 054309, 2015.
- [19] H. Ejiri, N. Soukouti, and J. Suhonen, “Spin-dipole nuclear matrix elements for double beta decays and astro-neutrinos,” *Physics Letters B*, vol. 729, pp. 27–32, 2014.
- [20] J. Menéndez, D. Gazit, and A. Schwenk, “Chiral two-body currents in nuclei: Gamow-Teller transitions and neutrinoless double-beta decay,” *Physical Review Letters*, vol. 107, no. 6, Article ID 062501, 5 pages, 2011.

## Research Article

# Lepton Pair Čerenkov Radiation Emitted by Tachyonic Neutrinos: Lorentz-Covariant Approach and IceCube Data

Ulrich D. Jentschura<sup>1</sup> and Robert Ehrlich<sup>2</sup>

<sup>1</sup>Department of Physics, Missouri University of Science and Technology, Rolla, MO 65409, USA

<sup>2</sup>Department of Physics, George Mason University, Fairfax, VA 22030, USA

Correspondence should be addressed to Ulrich D. Jentschura; ulj@mst.edu

Received 22 February 2016; Revised 28 April 2016; Accepted 17 May 2016

Academic Editor: Theocharis Kosmas

Copyright © 2016 U. D. Jentschura and R. Ehrlich. This is an open access article distributed under the Creative Commons Attribution License, which permits unrestricted use, distribution, and reproduction in any medium, provided the original work is properly cited. The publication of this article was funded by SCOAP<sup>3</sup>.

Current experiments do not exclude the possibility that one or more neutrinos are very slightly superluminal or that they have a very small tachyonic mass. Important bounds on the size of a hypothetical tachyonic neutrino mass term are set by lepton pair Čerenkov radiation (LPCR), that is, by the decay channel  $\nu \rightarrow e^+e^-\nu$ , which proceeds via a virtual  $Z^0$  boson. Here, we use a Lorentz-invariant dispersion relation which leads to very tight constraints on the tachyonic mass of neutrinos; we also calculate decay and energy loss rates. A possible cutoff seen in the IceCube neutrino spectrum for  $E_\nu > 2$  PeV, due to the potential onset of LPCR, is discussed.

## 1. Introduction

The early arrival of a neutrino burst from the 1987A supernova [1] still motivates speculations about a possible superluminal nature of neutrinos, even if it is generally assumed that the delay in the arrival of electromagnetic radiation (light) is caused by the time the shock wave from the core collapse needs in order to reach the surface of the exploding star. If neutrinos are ever so slightly superluminal, then they may emit Čerenkov radiation in the form of light lepton pairs. In this paper, we attempt to answer three questions: (i) How would the energy threshold for the decay channel  $\nu \rightarrow e^+e^-\nu$  (lepton pair Čerenkov radiation, LPCR) have to be calculated if we assume a strictly Lorentz-covariant, space-like dispersion relation for the relevant neutrino flavor eigenstate? (ii) How would the decay rate and the energy loss rate have to be calculated under this assumption? Can the tachyonic Dirac equation [2–5] and its bispinor solutions [6, 7] be used in that context? (iii) What implications could be derived for astrophysics under the assumption that a possible cutoff seen by IceCube for neutrinos with energies  $E_\nu > 2$  PeV is confirmed by future experiments?

Theoretical arguments can be useful in restricting the possible degree of superluminality of neutrinos and

maximum attainable neutrino velocities [8–10]. In [8, 9], a Lorentz-noncovariant dispersion relation  $E_\nu = |\vec{p}|v_\nu$  was used, where  $v_\nu > c$  is a constant parameter. This assumption leads to an energy-dependent effective “mass” square  $E_\nu^2 - \vec{p}^2 \approx E_\nu^2(v_\nu^2 - 1)v_\nu^{-2} \equiv m_{\text{eff}}^2$ . The effective mass  $m_{\text{eff}} = E_\nu \sqrt{v_\nu^2 - 1}v_\nu^{-1}$  then grows linearly with the neutrino energy. (Natural units with  $\hbar = c = \epsilon_0 = 1$  are used in this paper, yet we shall include explicit factors of  $c$  when indicated by the context.) Indeed, at the time, a best fit to the available experimental neutrino mass data including the initial OPERA claim [11] suggested the conceivable existence of an “energy-dependent mass” of the neutrino, as evidenced in Figure 1 of [12]. The choice of the relation  $E_\nu = |\vec{p}|v_\nu$ , made in [8] was consistent with the need to model the initial OPERA claim [11] and is perfectly compatible with the concept of perturbative Lorentz breaking terms in the neutrino sector [9]. A Dirac-type equation leading to the Lorentz-noncovariant dispersion relation used by Cohen and Glashow [8] can be obtained [9] from the current operator given in Eq. (2) of [13] upon a particular choice of  $c^{\mu\nu}$  parameters in the generalized fermionic current operator (in the notation adopted in [13]). Then, assuming a constant neutrino speed  $v_\nu > c$ , one can effectively describe the apparent absence of

energy dependence of the deviation of the neutrino speed from the speed of light  $v_\nu \approx \text{const.} \geq c$  (in the range  $5 \text{ GeV} < E_\nu < 50 \text{ GeV}$ ), according to the (falsified) initial claim made by OPERA [11], while remaining compatible with the framework of perturbative Lorentz breaking [13].

However, while there are advantages to assuming a Lorentz-noninvariant dispersion relation for superluminal neutrinos (such as the preservation of the timelike positive quantity  $E_\nu^2 - \vec{p}^2 > 0$ ), there are also a number of disadvantages. For example, if the dispersion relation  $E_\nu = |\vec{p}|v_\nu$  holds in one particular Lorentz frame, then, under a Lorentz boost, in general, one has  $E'_\nu \neq |\vec{p}'|v_\nu$  in the moving frame [8, 9]. In order to illustrate the consequences of Lorentz noncovariance, let us consider a boost along positive  $z$ -axis into a frame which moves with velocity  $u = c^2/v_\nu < c$ . A particle moving along positive  $z$ -axis of the lab frame with four-momentum  $p^\mu = (|\vec{p}|v_\nu, |\vec{p}|\hat{e}_z)$  is mapped onto  $p'^\mu = (|\vec{p}'|\sqrt{v_\nu^2 - 1}, \vec{0})$  and thus is ‘‘at rest’’ in the moving frame. However, the general dispersion relation in the moving frame,

$$E'_\nu = -\frac{p'_z}{2v_\nu} - \frac{(p'^2_x + p'^2_y + p'^2_z)v_\nu}{2p'_z} \quad (p'_z \neq 0), \quad (1)$$

is much more complicated. (Throughout this paper, we denote the spatial components of the four-vector  $p^\mu = (E_\nu, \vec{p})$  by  $\vec{p}$  and keep  $|\vec{p}|$  explicitly in order to avoid confusion between  $p^2 = p^\mu p_\mu$  and  $p^2 \neq \vec{p}^2$ .)

An alternative, commonly accepted dispersion relation for so-called tachyons (these are space-like, faster-than-light particles described by a Lorentz-invariant wave equation) reads as  $E_\nu^2 = \vec{p}^2 - m_\nu^2$ , that is, it is the ‘‘normal’’ dispersion relation with the negative sign of the mass square term (see [2–7, 14–23]). Here, we calculate the threshold energy and the decay rate under the assumption of a Lorentz-invariant dispersion relation for the neutrino. We find that the alternate dispersion relation imposes tight restrictions on superluminality and has important phenomenological implications for neutrino masses.

## 2. Dispersion Relations and Thresholds

For tachyonic particles, starting from the pioneering work of Sudarshan et al. [14–16], continuing with the works of Feinberg [17, 18], and including the tachyonic neutrino hypothesis [2–6, 19–23], the following dispersion relation has been assumed for the tachyonic (space-like) solutions:

$$E_\nu = \gamma_\nu m_\nu, \quad (2a)$$

$$|\vec{p}_\nu| = \gamma_\nu m_\nu v_\nu,$$

$$|\vec{p}_\nu| = E_\nu v_\nu, \quad (2b)$$

$$p^\mu p_\mu = E_\nu^2 - \vec{p}_\nu^2 = -m_\nu^2,$$

where we use the suggestive subscript  $\nu$  for ‘‘neutrino.’’ These relations imply that  $|\vec{p}| = E_\nu v_\nu$  instead of  $E_\nu = |\vec{p}|v_\nu$ . Here, the tachyonic Lorentz factor appears, which is  $\gamma_\nu =$

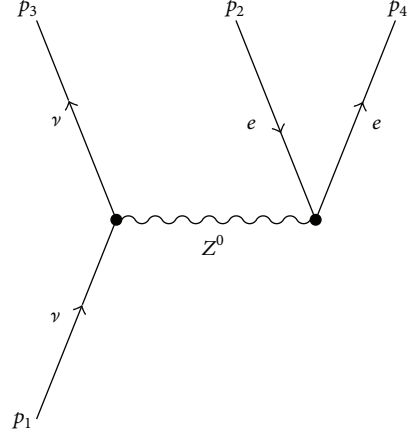


FIGURE 1: Conventions for tachyonic neutrino decay.

$1/\sqrt{v_\nu^2 - 1}$ . Tachyonic and tardyonic dispersion relations are unified upon assuming an imaginary value for  $m$  in the tachyonic case (starting from the tardyonic case, one has  $E = m/\sqrt{1 - v^2} \rightarrow im/\sqrt{1 - v^2} = m/\sqrt{v^2 - 1}$ , where the latter equation holds for tachyons). With the standard definitions of  $\vec{p}$  and  $E_\nu$ , one has  $|\vec{p}_\nu| = \gamma_\nu m_\nu v_\nu = E_\nu v_\nu$  for both tardyons and tachyons.

In order to obtain the threshold energy for the LPCR decay  $\nu \rightarrow e^+ e^- \nu$ , we use the following conventions (see Figure 1), inspired by Chap. 10 of [24], and define  $E_1 = \sqrt{\vec{p}_1^2 - m_\nu^2}$  and  $E_3 = \sqrt{\vec{p}_3^2 - m_\nu^2}$  as the oncoming and outgoing neutrino energies, with  $q = (E_1, \vec{p}_1) - (E_3, \vec{p}_3)$  being the four-momentum of  $Z^0$ . Pair production threshold is reached for  $q^2 = 4m_e^2$  and  $\cos \theta = \vec{p}_1 \cdot \vec{p}_3 / (|\vec{p}_1||\vec{p}_3|) = 1$ . For collinear geometry, with all momenta pointing along  $z$ -axis, we have

$$q^2 = \left( \sqrt{p_{1z}^2 - m_\nu^2} - \sqrt{p_{3z}^2 - m_\nu^2} \right)^2 - (p_{1z} - p_{3z})^2 \quad (3)$$

$$= 4m_e^2.$$

Furthermore, threshold obviously requires  $E_3 = 0$ . (This is possible for tachyonic particles, when  $|\vec{p}_3| = p_{3z} = m_\nu$ . In this limit, the tachyonic particle becomes infinitely fast and loses all of its energy, which implies that it is impossible to detect it [25]. The counterintuitive loss of energy for tachyons under acceleration is a consequence of standard tachyonic kinematics [2, 6, 7, 14–18, 26–28].) When the relations  $E_3 = 0$  and  $|\vec{p}_3| = p_{3z} = m_\nu$  are substituted into (3), this yields

$$p_{1z}^2 - m_\nu^2 - (p_{1z} - m_\nu)^2 = 4m_e^2. \quad (4)$$

Identifying  $p_{1z} = |\vec{p}|_{\text{th}}$  with the threshold momentum, one easily finds

$$|\vec{p}|_{\text{th}} = \frac{2m_e^2}{m_\nu} + m_\nu. \quad (5)$$

The threshold energy is then easily found as

$$E_{\text{th}} = \sqrt{\vec{p}_{\text{th}}^2 - m_\nu^2} = 2\frac{m_e}{m_\nu} \sqrt{m_e^2 + m_\nu^2} \approx 2\frac{m_e^2}{m_\nu}. \quad (6)$$

Because we are using a tachyonic dispersion relation, the threshold energy can be expressed as a function of only the mass parameters. Larger tachyonic masses  $m_\nu$  lead to lower threshold energies. In view of the tachyonic dispersion relation  $m_\nu = E_{\text{th}} \sqrt{v_{\text{th}}^2 - 1}$ , where  $v_{\text{th}}$  is the neutrino velocity *at threshold*, we may convert the threshold energy into a function of the electron mass and the neutrino threshold velocity. For given  $E_\nu$ , the limit  $m_\nu \ll m_e$  is equivalent to the limit  $v_{\text{th}}^2 - 1 = \delta_{\text{th}} \rightarrow 0$  because  $m_\nu = E_\nu \sqrt{\delta_{\text{th}}}$ . In this limit, we have

$$E_{\text{th}} \approx 2 \frac{m_e^2}{m_\nu} = 2 \frac{m_e^2}{E_{\text{th}} \sqrt{v_{\text{th}}^2 - 1}} \implies E_{\text{th}} \approx \frac{\sqrt{2} m_e}{(v_{\text{th}}^2 - 1)^{1/4}}. \quad (7)$$

Substituting the exact dispersion relation into the threshold condition  $E_{\text{th}} = 2(m_e/m_\nu) \sqrt{m_e^2 + m_\nu^2}$ , and solving for  $E_{\text{th}}$ , one obtains

$$E_{\text{th}} = \sqrt{2} m_e \left( 1 + \frac{v_{\text{th}}}{\sqrt{v_{\text{th}}^2 - 1}} \right)^{1/2} \quad (8)$$

$$= \begin{cases} \frac{\sqrt{2} m_e}{\delta_{\text{th}}^{1/4}} & \delta_{\text{th}} \ll 1 \\ 2m_e + \frac{m_e}{4\delta_{\text{th}}} & \delta_{\text{th}} \gg 1. \end{cases}$$

The exact expression (8) confirms (7) in the limit  $\delta_\nu \ll 1$ , which corresponds to the phenomenologically important limit of high-energy neutrinos. Smaller values of  $\delta_{\text{th}}$  (approaching zero) correspond to smaller tachyonic neutrino masses and therefore to larger threshold energies. For given neutrino speed  $v_{\text{th}}$ , neutrinos with energy  $E_{\text{th}}$  (or larger), under the hypothetical assumption of the tachyonic dispersion relation, have a tachyonic neutrino mass term large enough to make the decay via LPCR kinematically possible. Expressed differently, the tachyonic mass term  $m_\nu = E_{\text{th}} \sqrt{v_{\text{th}}^2 - 1}$  in this case is large enough to lead to LPCR decay at energy  $E_{\text{th}}$ , according to (6).

### 3. Decay Rate and Timelike Noncovariant Dispersion Relation

Given the complexities of calculating the decay rate due to LPCR using a tachyonic dispersion relation, it is extremely useful to first discuss the case of a Lorentz-noncovariant form  $E_\nu = |\vec{p}|v_\nu$ , using lab frame variables. For collinear incoming and outgoing neutrinos, threshold for pair production is reached at  $q^2 = (E_1 - E_3)^2 - (p_{1z} - p_{3z})^2 = (p_{1z} - p_{3z})^2 (v_\nu^2 - 1) = 4m_e^2$ , from which one derives (setting  $\vec{p}_3 = \vec{0}$ ) the following threshold values (in agreement with [8]):

$$|\vec{p}_1|_{\text{th}} = \frac{2m_e}{\sqrt{v_\nu^2 - 1}} \quad (9)$$

$$(E_1)_{\text{th}} = \frac{2m_e v_\nu}{\sqrt{v_\nu^2 - 1}}$$

Here,  $G_F$  is Fermi's coupling constant and  $u$  and  $v$  are the standard fundamental positive-energy and negative-energy bispinor solutions of the Dirac equation [29]. The invariant matrix element is

$$\mathcal{M} = \frac{G_F}{\sqrt{2}} \left[ \bar{u}(p_3) \gamma_\lambda (1 - \gamma^5) u(p_1) \right] \times \left[ \bar{u}(p_4) (c_V \gamma_\lambda - c_A \gamma_\lambda \gamma^5) v(p_2) \right]. \quad (10)$$

Here,  $c_V \approx 0$ , and  $c_A \approx -1/2$  [see Eq. (5.57) on p. 153 of [30]]. Following [9], we now make the additional assumption that the functional form of the projector sum over the spin orientations remains the same as for the ordinary Dirac equation even if the underlying dispersion relation is Lorentz-noncovariant (for a general discussion on such models, see [31, 32]). In this case, the sum over final state and the averaging over the initial spins leads to  $(1/2) \sum_{\text{spins}} |\mathcal{M}|^2 = 64G_F^2 (p_1 \cdot p_2)(p_3 \cdot p_4)$ . This enters the lab frame expression for the decay rate [33]:

$$\Gamma = \frac{1}{2E_1} \int \frac{d^3 p_3}{(2\pi)^3 2E_3} \left( \int \frac{d^3 p_2}{(2\pi)^3 2E_2} \int \frac{d^3 p_4}{(2\pi)^3 2E_4} \right) \times (2\pi)^4 \delta^{(4)}(p_1 - p_3 - p_2 - p_4) \left[ \frac{1}{2} \sum_{\text{spins}} |\mathcal{M}|^2 \right] \quad (11)$$

$$= \frac{G_F^2}{12\pi^4 (2E_1)} \int \frac{d^3 p_3}{2E_3} (p_1 \cdot p_3 q^2 + 2(p_1 \cdot q)(p_3 \cdot q)),$$

where  $q = p_1 - p_3$ . The azimuthal symmetry suggests the use of cylindrical coordinates. The domain of integration contains, for given  $p_1 = (p_{1z} v_\nu, 0, 0, p_{1z})$ , all permissible  $\vec{p}_3 = p_{3\rho} \hat{e}_\rho + p_{3z} \hat{e}_z$ , where  $p_3^\mu = (|\vec{p}_3| v_\nu, \vec{p}_3)$ . With  $E_\nu = |\vec{p}| v_\nu$ , the momentum transfer is

$$q^2 = -(p_{1z} - p_{3z})^2 - p_{3\rho}^2 + (p_{1z} - \sqrt{p_{3\rho}^2 + p_{3z}^2})^2 v_\nu^2, \quad (12)$$

where we require  $q^2 > 4m_e^2 \approx 0$ . Solving (12) for  $p_{3\rho}$ , one obtains the boundary of the region of permissible  $\vec{p}_3$  vectors. An example is given in Figure 2(a) in the form of a "sharpened ellipsoid" with "sharp" top near  $p_{3\rho} \rightarrow 0$ ,  $p_{3z} \rightarrow p_{1z}$ , and a "rounded" bottom with  $p_{3\rho} \rightarrow 0$ , and  $p_{3z} \rightarrow -[(v_\nu - 1)/(v_\nu + 1)] p_{1z}$ . After somewhat tedious integration over the allowed  $\vec{p}_3$  vectors, one obtains

$$\Gamma = \frac{G_F^2}{2688\pi^3} \frac{p_{1z}^5 \delta_\nu^3}{v_\nu} \approx \frac{1}{14} \frac{G_F^2 E_\nu^5 \delta_\nu^3}{192\pi^3}$$

$$\frac{dE_\nu}{dx} \approx -\frac{G_F^2}{96\pi^4 (2E_\nu)} \int_{q^2 > 0} \frac{d^3 p_3}{2E_3} (E_\nu - E_3) \times [(p_1 \cdot p_3) q^2 + 2(p_1 \cdot q)(p_3 \cdot q)] \quad (13)$$

$$= -\frac{G_F^2}{86016\pi^3} \frac{p_{1z}^6 \delta_\nu^3}{v_\nu} \approx -\frac{25}{448} \frac{G_F^2 E_\nu^6 \delta_\nu^3}{192\pi^3},$$

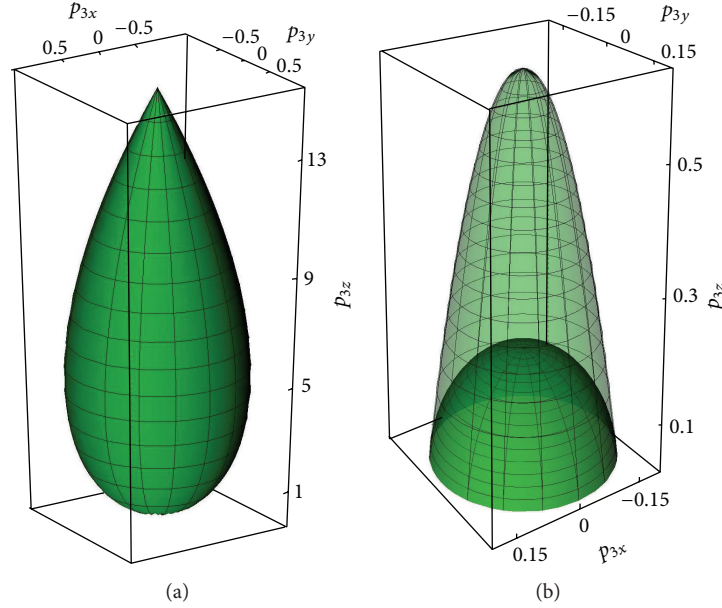


FIGURE 2: (a) Region of allowed outgoing momenta  $\vec{p}_3$  for the decay of an incoming superluminal neutrino with  $E_\nu = |\vec{p}|v_\nu$ . The neutrino is incoming along positive  $z$ -axis ( $p_{1z} = 15$ ). The boundary of allowed  $\vec{p}_3$  vectors constitutes a distorted ellipsoid with a “sharpened tip,” obtained as a solution of setting  $q^2 = 0$  in (12). (b) Region of allowed  $\vec{p}_3$  vectors for an incoming tachyonic neutrino with  $p_{1z} = 62$  and  $-m_\nu^2 = -(0.2)^2$ , producing an electron-positron pair of mass  $m_e = 1$  (dispersion relation  $E_\nu = \sqrt{p_\nu^2 - m_\nu^2}$ ). Final wave vectors  $|\vec{p}_3| < m_e$  correspond to evanescent waves and are thus to be excluded [6].

for the energy loss per unit length, confirming the results given in Eq. (2) and Eq. (3) of [8] and in [9]. This confirmation of the results given in [8] (under the assumptions made in the cited paper, namely, the dispersion relation  $E_\nu = |\vec{p}|v_\nu$ ), but using a different method, namely, phase-space integration directly in the laboratory frame, encourages us to apply the same method to the calculation of the tachyonic neutrino decay rate, where the use of the laboratory frame is indispensable. The confirmation also underlines the consistency of the theoretical formalism under a change of the assumptions made in the calculation.

#### 4. Decay Rate and Space-Like Covariant Dispersion Relation

For an incoming tachyon, the particle state (space-like neutrino) may transform into an antiparticle state upon Lorentz transformation, and its trajectory may reverse the time ordering (see Figure 3). Thus, the interpretation of a tachyonic neutrino state as a particle or antiparticle may depend on the frame of reference, and we should calculate the process directly in the lab frame. The necessity to transform certain tachyonic particle field operators into antiparticle operators under Lorentz boosts has been stressed in [6, 17, 18]. Incoming and outgoing states are required to be above-threshold positive-energy states in the lab frame (causality and tachyonic trajectories are discussed in [2, 14–18] and Appendix A.2 of [34]).

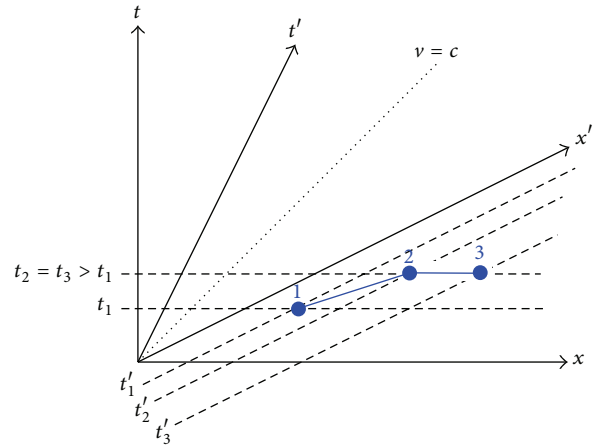


FIGURE 3: The world line  $1 \mapsto 2 \mapsto 3$  describes the tachyonic neutrino decay into a zero-energy, infinitely fast neutrino. Complete reversal of the time ordering of the decay process takes place in the primed frame; the observer interprets the process as the decay of an incoming antineutrino along the trajectory  $3 \mapsto 2 \mapsto 1$ .

We consider the matrix element

$$\begin{aligned} \mathcal{M} = & \frac{G_F}{\sqrt{2}} [\bar{u}^{\mathcal{F}}(p_3) \gamma_\lambda (1 - \gamma^5) u^{\mathcal{F}}(p_1)] \\ & \times [\bar{u}(p_4) (c_V \gamma^\lambda - c_A \gamma^\lambda \gamma^5) v(p_2)]. \end{aligned} \quad (14)$$

Here,  $u^\sigma(p_1)$  and  $u^\sigma(p_3)$  are Dirac spinor solutions of the tachyonic Dirac equation [6, 7]. The bar denotes the Dirac adjoint. In the helicity basis (see Chap. 23 of [35] and [6, 7]), these are given by

$$u_\pm^\sigma(p) = \begin{pmatrix} \sqrt{|\vec{p}| \pm ma_\pm(\vec{p})} \\ \pm \sqrt{|\vec{p}| \mp ma_\pm(\vec{p})} \end{pmatrix}, \quad (15)$$

where  $a_\pm(\vec{p})$  are the fundamental helicity spinors (see p. 87 of [29]). Following [6, 7, 19], we use the tachyonic sum rule of the fundamental tachyonic bispinor solutions [see Eq. (34a) of [6]]:

$$\sum_\sigma (-\sigma) u_\sigma^\sigma(p) \otimes \bar{u}_\sigma^\sigma(p) \gamma^5 = \not{p} - \gamma^5 m, \quad (16)$$

where  $p = (E, \vec{p})$  is the four-momentum and  $\sigma$  is a helicity quantum number. We refer to [6, 7] for a thorough discussion; roughly speaking, factor  $(-\sigma)$  in (16) restores the correct sign in the calculation of the time-ordered product of tachyonic field operators (the propagator) for the contribution of all virtual degrees of freedom of the tachyonic field [see Eqs. (46)–(57) and Eq. (73)–(75) of [7]].  $\gamma^5$  matrix in (16) is a part of the natural Dirac “adjoint” for the tachyonic spinor. Namely, the adjoint equation to the tachyonic Dirac equation,  $(i\gamma^\mu \partial_\mu - \gamma^5 m)\psi(x) = 0$ , reads as  $[\bar{\psi}(x)\gamma^5](i\gamma^\mu \overleftarrow{\partial}_\mu - \gamma^5 m)\psi(x) = 0$ . As explained in Eqs. (73)–(75) of [17], right-handed particle states and left-handed antiparticle states (those with the “wrong” helicity) are excluded from the physical spectrum of the tachyonic field by a Gupta-Bleuler condition; these cannot contribute to the oncoming and outgoing neutrino states in Figure 1 [while they do contribute to the virtual states, that is, the propagator; see Eqs. (46)–(57) of [7]]. Both the incoming and the outgoing neutrinos in Figure 1 are real rather than virtual neutrinos. Hence, in order to calculate the LPCR decay rate, we use the modified sum over tachyonic spinors:

$$\widetilde{\sum}_\sigma u_\sigma^\sigma(p) \otimes \bar{u}_\sigma^\sigma(p) = (1 + \gamma^5 \not{\tau} \hat{p}) (\not{p} - \gamma^5 m_\nu) \gamma^5, \quad (17)$$

where  $\tau = (1, 0, 0, 0)$  is a timelike unit vector,  $\hat{p} = \vec{p}/|\vec{p}|$  is the unit vector in  $\vec{p}$  direction, and upon promotion to a four-vector, we have  $\hat{p}^\mu = (0, \hat{p})$ , so that  $1 + \gamma^5 \not{\tau} \hat{p} = 1 - \vec{\Sigma} \cdot \hat{p}/|\vec{p}|$  becomes a left-handed helicity projector.

We thus calculate with an incoming, positive-energy, left-helicity tachyonic neutrino. One obtains the modified sum over spins  $\widetilde{\sum}_{\text{spins}}$  in the matrix element:

$$\begin{aligned} \widetilde{\sum}_{\text{spins}} |\mathcal{M}|^2 &= \frac{G_F^2}{2} \text{Tr} \left[ \frac{1}{2} (1 + \gamma^5 \not{\tau} \hat{p}_3) (\not{p}_3 - \gamma^5 m_\nu) \right. \\ &\cdot \gamma^5 \gamma_\lambda (1 - \gamma^5) \frac{1}{2} (1 + \gamma^5 \not{\tau} \hat{p}_1) (\not{p}_1 - \gamma^5 m_\nu) \\ &\cdot \gamma^5 \gamma_\nu (1 - \gamma^5) \left. \right] K^{\lambda\rho}. \end{aligned} \quad (18)$$

Here,  $K^{\lambda\rho} = \text{Tr}[(\not{p}_4 + m_e)(c_V \gamma^\lambda - c_A \gamma^\lambda \gamma^5)(\not{p}_2 + m_e)(c_V \gamma^\rho - c_A \gamma^\rho \gamma^5)]$  is the familiar trace from the outgoing fermion

pair. The decay rate is given by (11) under the replacement  $(1/2) \sum_{\text{spins}} |\mathcal{M}|^2 \rightarrow \widetilde{\sum}_{\text{spins}} |\mathcal{M}|^2$ . The integrals over the momenta of the outgoing fermion pair ( $d^3 p_2$  and  $d^3 p_4$ ) are done using ( $p_2^2 = p_4^2 = m_e^2$ ). Consider

$$\begin{aligned} J_{\lambda\rho}(q) &= \int \frac{d^3 p_2}{2E_2} \int \frac{d^3 p_4}{2E_4} \delta^{(4)}(q - p_2 - p_4) (p_{2\lambda} p_{4\rho}) \\ &= \frac{\pi}{24} \sqrt{1 - \frac{4m_e^2}{q^2}} \left[ g_{\lambda\rho} (q^2 - 4m_e^2) \right. \\ &\quad \left. + 2q_\lambda q_\rho \left( 1 + \frac{2m_e^2}{q^2} \right) \right]. \end{aligned} \quad (19)$$

It remains to analyze the domain of allowed  $\vec{p}_3$  vectors [see the “cupola structure” in Figure 2(b)], which is defined by the requirement  $q^2 > 4m_e^2$ , for  $p_1^\mu = (\sqrt{p_{1z}^2 - m_\nu^2}, 0, 0, p_{1z})$ . The dispersion relation  $E_\nu = \sqrt{\vec{p}_\nu^2 - m_\nu^2}$  implies that

$$q^2 = 2 \left( \sqrt{E_1^2 + m_\nu^2} \sqrt{E_3^2 + m_\nu^2} \cos \theta - E_1 E_3 - m_\nu^2 \right). \quad (20)$$

Here,  $\theta$  is the polar angle in spherical coordinates:

$$p_3^\mu = (E_3, |\vec{p}_3| \sin \theta \cos \varphi, |\vec{p}_3| \sin \theta \sin \varphi, |\vec{p}_3| \cos \theta). \quad (21)$$

Pair production threshold is reached, for given  $E_1$  and  $E_3$ , by solving (20) for  $u = \cos \theta$ , setting  $q^2 = 4m_e^2$ . After somewhat tedious integration over the allowed  $\vec{p}_3$  vectors (no masses can be neglected), one obtains

$$\Gamma = \begin{cases} \frac{G_F^2 m_\nu^6}{128\pi^3 m_e^2} \frac{(E_\nu - E_{\text{th}})^2}{E_{\text{th}}} & E_\nu \gtrsim E_{\text{th}} \\ \frac{G_F^2 m_\nu^4}{288\pi^3} E_\nu & E_\nu \gg E_{\text{th}}, \end{cases} \quad (22a)$$

for the decay rate, and

$$\frac{dE_\nu}{dx} = \begin{cases} \frac{G_F^2 m_\nu^5}{64\pi^3} \frac{(E_\nu - E_{\text{th}})^2}{E_{\text{th}}} & E_\nu \gtrsim E_{\text{th}} \\ \frac{G_F^2 m_\nu^4}{144\pi^3} E_1^2 & E_\nu \gg E_{\text{th}}, \end{cases} \quad (22b)$$

for the energy loss rate. In the high-energy limit, one may (somewhat trivially) rewrite the expressions as follows ( $m_\nu = E_1 \sqrt{\delta_\nu}$ ):

$$\begin{aligned} \Gamma &= \frac{G_F^2 E_\nu^5 \delta_\nu^2}{288\pi^3}, \\ \frac{dE_\nu}{dx} &= \frac{G_F^2 E_\nu^6 \delta_\nu^2}{144\pi^3}, \end{aligned} \quad (23)$$

$$E_\nu \gg E_{\text{th}}.$$

These results confirm that it is possible to use the tachyonic bispinor formalism [2–7] for the calculation of decay rates of tachyonic particles.

## 5. Constraints on the Mass of a Tachyonic Neutrino

Our threshold relation (8) is based on a Lorentz-covariant dispersion relation. Only neutrinos with  $E_\nu < E_{\text{th}} = \sqrt{2}m_e/\delta_{\text{th}}^{1/4}$  survive the possibility of generalized leptonic Čerenkov radiation over a sufficiently long path length. The hypothetical observation of an absence of neutrinos above some energy  $E_{\text{th}}$  could thus be interpreted as a constraint on the neutrino mass. Let us assume a neutrino mass of  $m_\nu = X$  eV, where  $X$  is generally assumed to be of order unity or less. Then, threshold is reached for  $m_\nu = X$  eV,  $\delta_{\text{th}} = 3.67 \times 10^{-24} X^4$ , and  $E_{\text{th}} = (522/X)$  GeV.

The IceCube experiment [36, 37] has observed 37 neutrinos having energies  $E_\nu > 10$  TeV during 3 years of data taking. Three of these events had energies  $E_\nu > 1$  PeV, and one (often referred to as “Big Bird”) had  $E_\nu = (2.004 \pm 0.236)$  PeV. According to the IceCube collaboration [37], the spectrum of the 37 neutrinos is well fitted by a slope  $\sim E_\nu^{-2}$ , which includes astrophysical as well as background atmospheric neutrinos, the latter being exclusively below 0.4 PeV. However, their best fit to the spectrum predicts 3.1 additional events for  $E_\nu > 2$  PeV, and yet none were seen. Preliminary data for the fourth year includes 17 additional events, with none seen for  $E_\nu > 1$  PeV [38]. These facts suggest to the IceCube authors [36, 37] the possibility that there may be a cutoff for the spectrum for neutrinos above  $E \approx 2$  PeV. The hypothesis is given further support by models which show that the Glashow resonance [39] (resonant  $\bar{\nu}_e e^- \rightarrow W^- \rightarrow \text{anything}$ ) should add between zero and three times the number of events that appear in the interval  $1 \text{ PeV} < E_\nu < 2 \text{ PeV}$  as part of a broad peak centered around 6.3 PeV [40]. While evidence for the cutoff is disputed and alternative explanations have been proposed [41], the significance of such a cutoff has been analyzed in the light of superluminal neutrinos [42, 43].

Let us add a few clarifying remarks here. First, we note that the plots in the paper [37] refer to the neutrino flux as a function of neutrino energy; the events were apparently sufficiently well reconstructed so that no excess neutrino energy in addition to the energy deposited inside the detector is expected. Our Figure 4 is based on Figure 4 of [37]. Meanwhile, members of the IceCube collaboration have presented preliminary evidence for a throughgoing muon of energy  $\geq (2.6 \pm 0.3)$  PeV which could be interpreted as a decay product of a neutrino of even higher energy [44, 45]. If the throughgoing muon could indeed be assigned to an ultra-high-energy neutrino of nonatmospheric origin, then it would push the conceivable cutoff seen by IceCube to even higher energies, further constraining the tachyonic mass term of the relevant neutrino flavor. So far, the authors of [37] (see the right column on page 4 of [37]) observe that “this [the lack of high-energy events] may indicate, along with the slight excess in lower energy bins, either a softer spectrum or a cutoff at high energies.”

Assuming  $E_{\text{th}} \approx 2$  PeV we would find using (8) that  $\delta_{\text{th}} = (\sqrt{2}m_e/E_{\text{th}})^4 \approx 1.7 \times 10^{-38}$ , and we would, furthermore, find that  $m_\nu = \sqrt{\delta_{\text{th}}} E_{\text{th}} \approx 0.00026$  eV (i.e.,  $-m_\nu^2 \approx -6.8 \times 10^{-8}$  eV<sup>2</sup>) for one or more of the three neutrino flavors (conceivably,

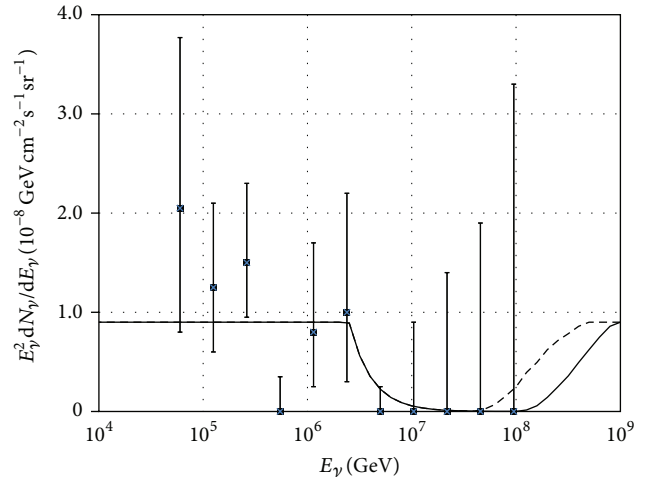


FIGURE 4: Three years of data from the IceCube experiment showing flux  $dN_\nu/dE_\nu$ , multiplied by  $E_\nu^2$  plotted against the neutrino energy  $E_\nu$ . The solid and dashed curves show what would be expected for  $E_\nu^{-2}$  power law for the flux, with  $E_{\text{th}} = 2.5$  PeV threshold, and two arbitrarily assumed values for the source distance,  $L$  (dashed curve) and  $L/2$  (solid curve). The drop to zero above  $E_{\text{th}}$  only occurs for those neutrino flavors having a tachyonic mass consistent with a 2.5 PeV threshold.

the one with the smallest absolute value of  $m_\nu^2$ ). A shifted cutoff [44, 45] of  $E_{\text{th}} \approx 3$  PeV would be consistent with a tachyonic neutrino mass of  $m_\nu = 0.00017$  eV. One might object that it is not possible to have one (or more) tachyonic flavor masses ( $m^2 < 0$ ) and satisfy both neutrino oscillation data and the recent findings from cosmology for the sum of the flavor masses; that is,  $\Sigma m \approx 0.32$  eV [46, 47]. However, such consistency can be achieved using 3 active-sterile  $\pm m^2$  (tardyon-tachyon) neutrino pairs [48]. The curves in Figure 4 were generated using an assumed pure  $E_\nu^{-2}$  power law for flux  $N$  beyond the assumed threshold,  $E_{\text{th}}$ . We then use our  $dE_\nu/dx$  formula (22b) for  $E_\nu > E_{\text{th}}$  to find the modified  $NE_\nu^2$  spectrum. Good agreement is found with the IceCube data at a threshold  $E_{\text{th}} = 2.5$  PeV, although much more statistics will be needed to determine if the cutoff is real.

## 6. Conclusions

Three main conclusions of the current investigation can be drawn. (i) As described in Section 2, the assumption of a Lorentz-covariant, tachyonic dispersion relation leads to tight bounds on conceivable tachyonic neutrino mass terms, for whatever neutrino flavor is causing the possible 2 PeV cutoff. The tachyonic decay rate due to LPCR is most conveniently calculated in the laboratory frame because of the space-like kinematics involved in the process, which leads to a nonunique time ordering of the trajectories, as discussed in Section 4. (ii) We may apply the formalism of the tachyonic bispinor solutions of the tachyonic Dirac equation [2–5] recently developed in [6, 7, 19] to the calculation of the tachyonic neutrino decay, as outlined in Section 4. (iii) A comparison of recent IceCube data with the results for the

calculated tachyonic decay rates reveals that a tachyonic neutrino could possibly explain a possible sharp cutoff in IceCube data but only if the neutrino flavor involved has a very specific tachyonic mass. In a more general context, the calculation of tachyonic thresholds and decay rates based on Lorentz-covariant dispersion relations could be of phenomenological significance for string theories, some of which predict the existence of tachyons [49, 50]. The same is true for the precise calculation of the tail of the beta decay spectrum, which is influenced by a conceivably tachyonic neutrino mass term [51].

## Competing Interests

The authors declare that there are no competing interests regarding the publication of this paper.

## Acknowledgments

This research has been supported by the National Science Foundation (Grant no. PHY-1403973).

## References

- [1] V. L. Dadykin, G. T. Zatsepin, V. B. Karchagin et al., "Detection of a rare event on 23 February 1987 by the neutrino radiation detector under Mont Blanc," *JETP Letters*, vol. 45, pp. 593–595, 1987, *Pis'ma ZhETF*, vol. 45, pp. 464, 1987.
- [2] A. Chodos, A. I. Hauser, and V. A. Kostelecký, "The neutrino as a tachyon," *Physics Letters B*, vol. 150, no. 6, pp. 431–435, 1985.
- [3] T. Chang, "A new Dirac-type equation for tachyonic neutrinos," <https://arxiv.org/abs/hep-th/0011087>.
- [4] T. Chang, "Parity violation and neutrino mass," *Nuclear Science and Techniques/Hewuli*, vol. 13, no. 3, pp. 129–133, 2002.
- [5] T. Chang, "Parity violation and a preferred frame," <http://arxiv.org/abs/quant-ph/0204002v1>.
- [6] U. D. Jentschura and B. J. Wundt, "Localizability of tachyonic particles and neutrinoless double beta decay," *European Physical Journal C*, vol. 72, no. 2, pp. 1–13, 2012.
- [7] U. D. Jentschura and B. J. Wundt, "From generalized dirac equations to a candidate for dark energy," *ISRN High Energy Physics*, vol. 2013, Article ID 374612, 21 pages, 2013.
- [8] A. G. Cohen and S. L. Glashow, "Pair creation constrains superluminal neutrino propagation," *Physical Review Letters*, vol. 107, no. 18, Article ID 181803, 2011.
- [9] F. Bezrukov and H. M. Lee, "Model dependence of the bremsstrahlung effects from the superluminal neutrino at OPERA," *Physical Review D*, vol. 85, no. 3, Article ID 031901, 2012.
- [10] P. C. W. Davies and I. G. Moss, "Cosmological bounds on tachyonic neutrinos," *Astroparticle Physics*, vol. 35, no. 10, pp. 679–680, 2012.
- [11] T. Adam, N. Agafonova, A. Aleksandrov et al., "The influence of Earth rotation in neutrino speed measurements between CERN and the OPERA detector," 2011, <http://arxiv.org/abs/1109.4897>.
- [12] F. Tamburini and M. Laveder, "Apparent Lorentz violation with superluminal Majorana-tachyonic neutrinos at OPERA?" *Physica Scripta*, vol. 85, no. 3, Article ID 035101, 2012.
- [13] V. A. Kostelecky and R. Lehnert, "Stability, causality, and Lorentz and CPT violation," *Physical Review D*, vol. 63, Article ID 065008, 2001.
- [14] O. M. P. Bilaniuk, V. K. Deshpande, and E. C. G. Sudarshan, "'Meta' relativity," *American Journal of Physics*, vol. 30, pp. 718–723, 1962.
- [15] J. Dhar and E. C. G. Sudarshan, "Quantum field theory of interacting tachyons," *Physical Review*, vol. 174, no. 5, pp. 1808–1815, 1968.
- [16] O.-M. Bilaniuk and E. C. G. Sudarshan, "Causality and space-like signals," *Nature*, vol. 223, no. 5204, pp. 386–387, 1969.
- [17] G. Feinberg, "Possibility of faster-than-light particles," *Physical Review*, vol. 159, no. 5, pp. 1089–1105, 1967.
- [18] G. Feinberg, "Lorentz invariance of tachyon theories," *Physical Review D*, vol. 17, no. 6, pp. 1651–1660, 1978.
- [19] U. D. Jentschura and B. J. Wundt, "Neutrino helicity reversal and fundamental symmetries," *Journal of Physics G: Nuclear and Particle Physics*, vol. 41, no. 7, Article ID 075201, 2014.
- [20] R. Ehrlich, "Implications for the cosmic ray spectrum of a negative electron neutrino ( $mass$ )<sup>2</sup>," *Physical Review D*, vol. 60, no. 1, Article ID 017302, 4 pages, 1999.
- [21] R. Ehrlich, "Is there a 4.5 PeV neutron line in the cosmic ray spectrum?" *Physical Review D—Particles, Fields, Gravitation and Cosmology*, vol. 60, Article ID 073005, 1999.
- [22] R. Ehrlich, "Evidence for two neutrino mass eigenstates from SN 1987A and the possibility of superluminal neutrinos," *Astroparticle Physics*, vol. 35, no. 10, pp. 625–628, 2012.
- [23] R. Ehrlich, "Tachyonic neutrinos and the neutrino masses," *Astroparticle Physics*, vol. 41, pp. 1–6, 2013.
- [24] D. Griffiths, *Introduction to Elementary Particles*, John Wiley & Sons, New York, NY, USA, 1987.
- [25] See the neutrino cross sections tabulated at <http://cupp oulu fi/neutrino/nd-cross.html>.
- [26] E. Recami, "Superluminal waves and objects: an overview of the relevant experiments," *Journal of Physics: Conference Series*, vol. 196, Article ID 012020, 2009.
- [27] O. M. Bilaniuk, "Tachyons," *Journal of Physics: Conference Series*, vol. 196, no. 1, Article ID 012021, 2009.
- [28] S. K. Bose, "Aspects of Tachyon theory," *Journal of Physics: Conference Series*, vol. 196, Article ID 012022, 2009.
- [29] C. Itzykson and J. B. Zuber, *Quantum Field Theory*, McGraw-Hill, New York, NY, USA, 1980.
- [30] J. Horejsi, *Fundamentals of Electroweak Theory*, Karolinum Press, Prague, Czech Republic, 2002.
- [31] G. Rubtsov, P. Satunin, and S. Sibiryakov, "Calculation of cross sections in Lorentz-violating theories," *Physical Review D*, vol. 86, no. 8, Article ID 085012, 2012.
- [32] V. A. Kostelecky and M. Mewes, "Neutrinos with Lorentz-violating operators of arbitrary dimension," *Physical Review D*, vol. 85, no. 9, Article ID 096005, 2012.
- [33] M. John, "Phase space and decay rates," in *Particle Basics*, pp. 1–8, 2011.
- [34] U. D. Jentschura, D. Horváth, S. Nagy, I. Nándori, Z. Trócsányi, and B. Ujvári, "Weighing the neutrino," *International Journal of Modern Physics E*, vol. 23, no. 1, Article ID 1450004, 2014.
- [35] V. B. Berestetskii, E. M. Lifshitz, and L. P. Pitaevskii, "Quantum electrodynamics," in *The Course on Theoretical Physics*, vol. 4, Pergamon Press, Oxford, UK, 2nd edition, 1982.
- [36] M. G. Aartsen, R. Abbasi, Y. Abdou et al., "First observation of PeV-energy neutrinos with icecube," *Physical Review Letters*, vol. 111, Article ID 021103, 2013.

- [37] M. G. Aartsen, M. Ackermann, J. Adams et al., “Observation of high-energy astrophysical neutrinos in three years of icecube data,” *Physical Review Letters*, vol. 113, no. 10, Article ID 101101, 2014.
- [38] O. Botner, “IceCube Neutrino Observatory: present and future,” in *Proceedings of the IceCube Particle Astrophysics Symposium*, Madison, Wis, USA, May 2015.
- [39] S. L. Glashow, “Resonant scattering of antineutrinos,” *Physical Review*, vol. 118, no. 1, pp. 316–317, 1960.
- [40] V. Barger, L. Fu, J. G. Learned, D. Marfatia, S. Pakvasa, and T. J. Weiler, “Glashow resonance as a window into cosmic neutrino sources,” *Physical Review D*, vol. 90, Article ID 121301, 2014.
- [41] O. Kalashev and S. Troitsky, “IceCube astrophysical neutrinos without a spectral cutoff and 1015–1017 eV cosmic gamma radiation,” *JETP Letters*, vol. 100, no. 12, pp. 761–765, 2015.
- [42] F. W. Stecker and S. T. Scully, “Propagation of superluminal PeV IceCube neutrinos: a high energy spectral cutoff or new constraints on Lorentz invariance violation,” *Physical Review D*, vol. 90, no. 4, Article ID 043012, 2014.
- [43] F. W. Stecker, “Limiting superluminal electron and neutrino velocities using the 2010 Crab Nebula flare and the IceCube PeV neutrino events,” *Astroparticle Physics*, vol. 56, pp. 16–18, 2014.
- [44] S. Schoenen and L. Raedel, “Detection of a multi-PeV neutrino-induced muon event from the Northern sky with IceCube,” 2015, <http://www.astronomerstelegam.org/?read=7856>.
- [45] S. S. Schoenen and L. Raedel, 2015, <https://www.icrr.u-tokyo.ac.jp/indico/getFile.py/access?contribId=43&sessionId=6/&resId=0&materialId=slides&confId=23>.
- [46] R. A. Battye and A. Moss, “Evidence for massive neutrinos from cosmic microwave background and lensing observations,” *Physical Review Letters*, vol. 112, Article ID 051303, 2014.
- [47] J. Hamann and J. Hasenkamp, “A new life for sterile neutrinos: resolving inconsistencies using hot dark matter,” *Journal of Cosmology and Astroparticle Physics*, vol. 2013, no. 10, article 044, 2013.
- [48] R. Ehrlich, “Six observations consistent with the electron neutrino being a  $m^2 = -0.11 \pm 0.02 \text{ eV}^2$  tachyon,” *Astroparticle Physics*, vol. 66, pp. 11–17, 2015.
- [49] J. Polchinski, *String Theory (Volume 1): An Introduction to the Bosonic String*, Cambridge University Press, Cambridge, UK, 1998.
- [50] J. Polchinski, *String Theory (Volume 2): Superstring Theory and Beyond*, Cambridge University Press, Cambridge, UK, 1998.
- [51] J. Ciborowski, “Hypothesis of tachyonic neutrinos,” *Acta Physica Polonica B*, vol. 29, pp. 113–121, 1998.

## Research Article

# Do Small-Mass Neutrinos Participate in Gauge Transformations?

Y. S. Kim,<sup>1</sup> G. Q. Maguire Jr.,<sup>2</sup> and M. E. Noz<sup>3</sup>

<sup>1</sup>Center for Fundamental Physics, University of Maryland, College Park, MD 20742, USA

<sup>2</sup>School of Information Technology, KTH Royal Institute of Technology, 16440 Stockholm, Sweden

<sup>3</sup>Department of Radiology, New York University, New York, NY 10016, USA

Correspondence should be addressed to M. E. Noz; [marilyne.noz@gmail.com](mailto:marilyne.noz@gmail.com)

Received 31 March 2016; Revised 25 May 2016; Accepted 12 June 2016

Academic Editor: Theocharis Kosmas

Copyright © 2016 Y. S. Kim et al. This is an open access article distributed under the Creative Commons Attribution License, which permits unrestricted use, distribution, and reproduction in any medium, provided the original work is properly cited. The publication of this article was funded by SCOAP<sup>3</sup>.

Neutrino oscillation experiments presently suggest that neutrinos have a small but finite mass. If neutrinos have mass, there should be a Lorentz frame in which they can be brought to rest. This paper discusses how Wigner's little groups can be used to distinguish between massive and massless particles. We derive a representation of the  $SL(2, c)$  group which separates out the two sets of spinors: one set is gauge dependent and the other set is gauge invariant and represents polarized neutrinos. We show that a similar calculation can be done for the Dirac equation. In the large-momentum/zero-mass limit, the Dirac spinors can be separated into large and small components. The large components are gauge invariant, while the small components are not. These small components represent spin-1/2 non-zero-mass particles. If we renormalize the large components, these gauge invariant spinors represent the polarization of neutrinos. Massive neutrinos cannot be invariant under gauge transformations.

## 1. Introduction

Whether or not neutrinos have mass and the consequences of this relative to the Standard Model and lepton number are the subject of much theoretical speculation [1, 2], as well as cosmological [3–5], nuclear reactor [6, 7], and high energy experimentation [8–11]. Neutrinos are fast becoming an important component of the search for dark matter and dark radiation [12, 13]. Their importance within the Standard Model is reflected in the fact that they are the only particles which seem to exist with only one direction of chirality; that is, only left-handed neutrinos have been confirmed to exist thus far. It was speculated some time ago that neutrinos in constant electric and magnetic fields would acquire a small mass and that right-handed neutrinos would be trapped within the interaction field [14]. Additionally there are several physical problems which right-handed neutrinos might help solve [15–17]. Solving generalized electroweak models using left- and right-handed neutrinos has also been discussed [18]. Today right-handed neutrinos which do not participate in

weak interactions are called “sterile” neutrinos [19]. A comprehensive discussion of the place of neutrinos in the present scheme of particle physics has been given by Drewes [12].

In this paper, we use representations of the Lorentz group to understand the physical implications of neutrinos having mass. In Section 2, two-by-two representations of the Lorentz group are presented. In Section 3, the internal symmetries of massive and massless particles are derived. A representation of the  $SL(2, c)$  group, which separates out the two sets of spinors contained therein, is presented in Section 4. One set of spinors is gauge dependent and represents massive particles. The other is gauge invariant and represents polarized neutrinos. In Section 5, we show how, in the large-momentum/zero-mass limit, the Dirac spinors can be separated into two components, one of which can represent a spin-1/2 non-zero-mass particle. The question of gauge invariance is then discussed. In Section 6, we discuss the zero-mass limit and gauge invariance in the Lorentz transformation framework. Some concluding remarks are made in Section 7.

## 2. Representations of the Lorentz Group

The Lorentz group starts with a group of four-by-four matrices performing Lorentz transformations on the four-dimensional Minkowski space of  $(t, z, x, y)$  which leaves the quantity  $(t^2 - z^2 - x^2 - y^2)$  invariant. Since there are three generators of rotations and three boost generators, the Lorentz group is a six-parameter group.

Einstein observed that the Lorentz group is also applicable to the four-dimensional energy and momentum space of  $(E, p_z, p_x, p_y)$ . He derived the Lorentz-covariant energy-momentum relation commonly known as  $E = mc^2$ . As this transformation leaves  $(E^2 - p_z^2 - p_x^2 - p_y^2)$  invariant, the particle mass is a Lorentz invariant quantity.

In his 1939 paper [20], Wigner studied the symmetry properties of free particles by using operators which commute with the specified four-momentum of the particle. His "little groups" were defined to be those transformations that do not change this four-momentum. For massive particles, the little group is isomorphic to  $O(3)$ ; indeed the  $O(3)$ -like little group's kinematics is well understood. Massless particles are isomorphic to the Euclidean group commonly known as  $E(2)$ . Wigner noted that the  $E(2)$ -like subgroup of  $SL(2, c)$  is isomorphic to the Lorentz group of transformations [21], but the kinematics of this group is not as well established as that of the  $O(3)$ -like little group as there is no Lorentz frame in which a massless particle is at rest.

It is possible to construct the Lie algebra of the Lorentz group from the three Pauli spin matrices [22–25] as

$$\begin{aligned} J_i &= \frac{1}{2}\sigma_i, \\ K_i &= \frac{i}{2}\sigma_i. \end{aligned} \quad (1)$$

These two-by-two matrices satisfy the following set of commutation relations:

$$\begin{aligned} [J_i, J_j] &= i\epsilon_{ijk}J_k, \\ [J_i, K_j] &= i\epsilon_{ijk}K_k, \\ [K_i, K_j] &= -i\epsilon_{ijk}J_k, \end{aligned} \quad (2)$$

where the generators  $J_i$  represent rotations and the generators  $K_i$  represent boosts. There are six generators of the Lorentz group which satisfy the three sets of commutation relations given in (2). The Lie algebra of the Lorentz group consists of these sets of commutation relations.

These commutation relations are invariant under Hermitian conjugation; however, while the rotation generators are Hermitian, the boost generators are anti-Hermitian:

$$\begin{aligned} J_i^\dagger &= J_i, \\ \text{while } K_i^\dagger &= -K_i. \end{aligned} \quad (3)$$

Thus, it is possible to construct two representations of the Lorentz group, one with  $K_i$  and the other with  $-K_i$ . For this purpose, we will use the notation [24, 26, 27]

$$\tilde{K}_i = -K_i. \quad (4)$$

To demonstrate that this set of generators do perform Lorentz transformations, let us consider a point  $X$  in four-dimensional space such as the Minkowskian four-vector  $(t, z, x, y)$ . A Hermitian matrix of the form

$$X = \begin{pmatrix} t + z & x - iy \\ x + iy & t - z \end{pmatrix}, \quad (5)$$

with determinant

$$t^2 - z^2 - x^2 - y^2, \quad (6)$$

can be written where all the components of  $X$  are real. Indeed, every Hermitian matrix can be written this way with real components. Consider next a matrix of the form

$$G = \begin{pmatrix} \alpha & \beta \\ \gamma & \delta \end{pmatrix}, \quad (7)$$

with four complex matrix elements, thus eight real parameters, and require that the determinant be equal to one. If

$$G^\dagger = \begin{pmatrix} \alpha^* & \gamma^* \\ \beta^* & \delta^* \end{pmatrix} \quad (8)$$

is the Hermitian conjugate of  $G$ , then

$$X' = GXG^\dagger \quad (9)$$

defines a linear transformation with real coefficients such that the determinant of  $X'$  is equal to the determinant of  $X$ . This constitutes a real Lorentz transformation. The transformation of (9) can be explicitly written as

$$\begin{pmatrix} t' + z' & x' - iy' \\ x' + iy' & t' - z' \end{pmatrix} \quad (10)$$

$$= \begin{pmatrix} \alpha & \beta \\ \gamma & \delta \end{pmatrix} \begin{pmatrix} t + z & x - iy \\ x + iy & t - z \end{pmatrix} \begin{pmatrix} \alpha^* & \gamma^* \\ \beta^* & \delta^* \end{pmatrix}.$$

It is important to note that the transformation of (9) is not a similarity transformation. In the  $SL(2, c)$  regime, not all the matrices are Hermitian [25]. Moreover, since the determinants of  $G$  and  $G^\dagger$  are one, the determinant of  $GG^\dagger$  is also one. As

$$\text{Tr}(GG^\dagger) = (\alpha\alpha^* + \beta\beta^* + \gamma\gamma^* + \delta\delta^*) \geq 1, \quad (11)$$

(9) is a proper Lorentz transformation [25, 28, 29].

Since the determinant of  $G$  is fixed and is equal to one, there are six independent parameters. This six-parameter group is commonly called  $SL(2, c)$ . As the Lorentz group has six generators, this two-by-two matrix can serve as a representation of the Lorentz group.

Likewise, the two-by-two matrix for the four-momentum of the particle takes the form

$$P = \begin{pmatrix} p_0 + p_z & p_x - ip_y \\ p_x + ip_y & p_0 - p_z \end{pmatrix} \quad (12)$$

with  $p_0 = \sqrt{m^2 + p_z^2 + p_x^2 + p_y^2}$ . The transformation of this matrix takes the same form as that for space-time given in (9) and (10). The determinant of this matrix is  $m^2$  and remains invariant under Lorentz transformations. The explicit form of the transformation is

$$P' = GPG^\dagger = \begin{pmatrix} p'_0 + p'_z & p'_x - ip'_y \\ p'_x + ip'_y & p'_0 - p'_z \end{pmatrix} \quad (13)$$

$$= \begin{pmatrix} \alpha & \beta \\ \gamma & \delta \end{pmatrix} \begin{pmatrix} p_0 + p_z & p_x - ip_y \\ p_x + ip_y & p_0 - p_z \end{pmatrix} \begin{pmatrix} \alpha^* & \gamma^* \\ \beta^* & \delta^* \end{pmatrix}.$$

It is this Lorentz invariant mass that is important for discussing neutrino oscillation. In the next section, the internal symmetry of particles will be discussed using Wigner's little groups.

### 3. Internal Symmetries of Massive and Massless Particles

When special relativity was formulated, the main focus was point particles, without internal space-time structures. How these particles look to moving observers can be studied using Wigner's little groups [20] where the subgroup of the Lorentz group whose transformations leave the particle momentum invariant are considered. However, the little groups can transform the internal space-time structure of the particles. Since the particle momentum is fixed and remains invariant, it is possible to consider that the particle momentum is along the  $z$  direction.

This momentum is thus invariant under rotations around the  $z$ -axis. In addition, these rotations commute with the Lorentz boost along the  $z$ -axis because, according to the Lie algebra of (2),

$$[J_3, K_3] = 0. \quad (14)$$

In Section 2, it was shown that the Lorentz transformation of the four-momentum can be represented by two-by-two matrices and an explicit form for this transformation was given. If the particle moves along the  $z$  direction, the four-momentum matrix becomes

$$P = \begin{pmatrix} E + p & 0 \\ 0 & E - p \end{pmatrix}, \quad (15)$$

where  $E$  and  $p$  are the energy and the magnitude of momentum, respectively.

Let  $W$  be a subset of matrices which leaves the four-momentum invariant; then we can write

$$P = WPW^\dagger. \quad (16)$$

These matrices constitute Wigner's little groups dictating the internal space-time symmetry of the particle.

If the particle is massive, it can be brought to the system where it is at rest with  $p = 0$ . The four-momentum matrix is then proportional to

$$P = \begin{pmatrix} 1 & 0 \\ 0 & 1 \end{pmatrix}. \quad (17)$$

Since the momentum matrix is proportional to the unit matrix, the  $W$  matrix forms a unitary subset of the  $G$  matrices and is Hermitian. The corresponding little group is the  $SU(2)$  subgroup of the Lorentz group. It is sufficient to consider rotations around the  $y$ -axis, as rotations around the  $z$ -axis do not change the momentum. Thus the rotation matrix

$$R(\theta) = \begin{pmatrix} \cos\left(\frac{\theta}{2}\right) & -\sin\left(\frac{\theta}{2}\right) \\ \sin\left(\frac{\theta}{2}\right) & \cos\left(\frac{\theta}{2}\right) \end{pmatrix} \quad (18)$$

can be used. This forms a representation of Wigner's  $O(3)$ -like little group for massive particles which describes the spin orientation of the particle in the rest frame.

For the massless particle,  $E = p$ . Thus the four-momentum matrix is proportional to

$$P = \begin{pmatrix} 1 & 0 \\ 0 & 0 \end{pmatrix}, \quad (19)$$

and the Wigner matrix is necessarily triangular and should take the form

$$T(\gamma) = \begin{pmatrix} 1 & -\gamma \\ 0 & 1 \end{pmatrix}. \quad (20)$$

This matrix cannot be diagonalized. Its inverse and Hermitian conjugate are

$$T^-(\gamma) = \begin{pmatrix} 1 & \gamma \\ 0 & 1 \end{pmatrix}, \quad (21)$$

$$T^\dagger(\gamma) = \begin{pmatrix} 1 & 0 \\ -\gamma & 1 \end{pmatrix},$$

respectively. Since the inverse is not the same as the Hermitian conjugate,  $T$  is not a Hermitian matrix. In order to preserve the Lorentz properties of the boosted four-momentum,  $\gamma$  must be real.

To understand this better, consider that as the  $O(3)$  group is contracted into the Euclidean group ( $E(2)$ ) group, one can think of  $E(2)$  as a plane tangent to the North Pole. Since  $E(2)$  consists of two translation operators and a rotation operator, the rotation around the  $z$ -axis remains unchanged as the radius becomes large and rotations around the  $x$ - and  $y$ -axes become translations in the  $x$  and  $-y$  directions, respectively, within the tangent plane. For a massless particle, the  $E(2)$ -like little group bears the same relation to the  $E(2)$  group as the  $O(3)$ -like little group does to  $O(3)$  for a massive particle. Thus (20) is the representation of Wigner's  $E(2)$ -like little group [21, 27, 30] for massless particles. It is now possible to apply this formalism to spin-1/2 particles by considering the  $SL(2, c)$  representation of the Lorentz group.

### 4. $SL(2, c)$ and Spinors

In the case of  $SL(2, c)$ , or spin-1/2 particles, it is necessary to consider both signs of the boost generators  $K_i$ . In Section 2,

we considered that  $SL(2, c)$  consists of nonsingular two-by-two matrices which have the form defined in (7). This matrix is applicable to spinors that have the following form:

$$\begin{aligned} U &= \begin{pmatrix} 1 \\ 0 \end{pmatrix}, \\ V &= \begin{pmatrix} 0 \\ 1 \end{pmatrix}, \end{aligned} \quad (22)$$

for spin-up and spin-down states, respectively.

Among the subgroups of  $SL(2, c)$ , there are  $E(2)$ -like little groups which correspond to massless particles. If we consider a massless particle moving along the  $z$  direction, then the little group is generated by  $J_3$ ,  $N_1$ , and  $N_2$ , where

$$\begin{aligned} N_1 &= K_1 - J_2, \\ N_2 &= K_2 + J_1, \\ J_3 &= \left(\frac{1}{2}\right)\sigma_3. \end{aligned} \quad (23)$$

As usual,  $J_3$  is the generator of rotations and  $N_i$  generate translation-like transformations where

$$D(u, v) = D(u, 0) D(0, v) = D(0, v) D(u, 0). \quad (24)$$

As these  $N$  operators have been shown to be the generators of gauge transformations in the case of the photon [21], they will be referred to as the gauge transformation in the  $SL(2, c)$  regime [20, 31–33]. Their role with respect to massless particles of spin-1/2 will now be discussed [25].

For massless spin-1/2 particles,  $J_i$  are still the generators of rotations. However, because of the sign change allowed for  $K_i$ , it is necessary to have two sets of  $N_i$  operators designated as  $N_i^{(+)}$  and  $N_i^{(-)}$ , where, as defined in (23),  $N_i^{(+)}$  have the explicit form

$$\begin{aligned} N_1^{(+)} &= \begin{pmatrix} 0 & i \\ 0 & 0 \end{pmatrix}, \\ N_2^{(+)} &= \begin{pmatrix} 0 & 1 \\ 0 & 0 \end{pmatrix}. \end{aligned} \quad (25)$$

The Hermitian conjugates of the above  $N_i^{(+)}$  provide  $N_1^{(-)}$  and  $N_2^{(-)}$ . Thus, there are two sets of boost generators involved.

The transformation matrices defined in (24) can then be written as [34]

$$\begin{aligned} D^{(+)}(u, v) &= \exp\left(-i\left[uN_1^{(+)} + vN_2^{(+)}\right]\right) \\ &= \begin{pmatrix} 1 & u - iv \\ 0 & 1 \end{pmatrix}, \\ D^{(-)}(u, v) &= \exp\left(-i\left[uN_1^{(-)} + vN_2^{(-)}\right]\right) \\ &= \begin{pmatrix} 1 & 0 \\ -u - iv & 1 \end{pmatrix}. \end{aligned} \quad (26)$$

Since there are two sets of spinors in  $SL(2, c)$ , the spinors whose boosts are generated by  $K_i = i/2\sigma$  will be written as  $\alpha$  for spin in the positive direction and  $\beta$  for spin in the negative direction. For the boosts generated by  $K_i = -i/2\sigma$ , we will use  $\dot{\alpha}$  and  $\dot{\beta}$ . These spinors are gauge invariant in the sense that

$$\begin{aligned} D^{(+)}(u, v) \alpha &= \alpha, \\ D^{(-)}(u, v) \dot{\beta} &= \dot{\beta}. \end{aligned} \quad (27)$$

However, if we carry out the explicit multiplication, these spinors are gauge dependent in the sense that

$$\begin{aligned} D^{(+)}(u, v) \beta &= \beta + (u - iv) \alpha, \\ D^{(-)}(u, v) \dot{\alpha} &= \dot{\alpha} - (u + iv) \dot{\beta}. \end{aligned} \quad (28)$$

The gauge invariant spinors of (27) appear as polarized neutrinos [21, 30, 35].

Let us examine further the gauge dependent spinors of (28). To accomplish this, we construct unit vectors in Minkowskian space by taking the direct product of two  $SL(2, c)$  spinors:

$$\begin{aligned} -\alpha\dot{\alpha} &= (1, i, 0, 0), \\ \beta\dot{\beta} &= (1, -i, 0, 0), \\ \alpha\dot{\beta} &= (0, 0, 1, 1), \\ \beta\dot{\alpha} &= (0, 0, 1, -1). \end{aligned} \quad (29)$$

This combines two half integer spins into integer spins. To make  $D(u, v)$  consistent with (29), it is necessary to choose

$$D(u, v) = D^{(+)}(u, v) D^{(-)}(u, v), \quad (30)$$

where  $D^{(+)}$  and  $D^{(-)}$  apply to the first and second spinors of (29), respectively. Since the plane wave photon four-potential does not depend on  $\beta\dot{\alpha}$  because of the Lorentz condition [21, 30, 31, 34, 35], we have

$$\begin{aligned} D(u, v) (-\alpha\dot{\alpha}) &= -\alpha\dot{\alpha} + (u + iv) \alpha\dot{\beta}, \\ D(u, v) (\beta\dot{\beta}) &= \beta\dot{\beta} + (u - iv) \alpha\dot{\beta}, \\ D(u, v) \alpha\dot{\beta} &= \alpha\dot{\beta}. \end{aligned} \quad (31)$$

The first two equations in (31) correspond to gauge transformations of the photon polarization vectors. The third equation corresponds to the effect of the  $D$  transformation of the four-momentum. This shows that  $D(u, v)$  is an element of the little group. We look next at how we can apply this analysis to Dirac spinors.

## 5. Dirac Spinors and Massless Particles

The Dirac equation is applicable to massive particles. Here we will consider the massless particle as the limiting case of the massive particle by considering the large-momentum/zero-mass limit of the Dirac spinors.

Starting with the spin operators defined in (1), a boost along the  $z$  direction will take the form

$$J'_i = B(P) J_i B^{-1}(P). \quad (32)$$

This is a similarity transformation. Here the boost matrix is given by

$$B(P) = \begin{pmatrix} e^{\eta/2} & 0 \\ 0 & e^{-\eta/2} \end{pmatrix}, \quad (33)$$

where

$$e^{\eta/2} = \left( \frac{E+P}{E-P} \right). \quad (34)$$

In the large-momentum or large-mass limit for a massive particle we obtain

$$e^{\eta} \rightarrow \frac{2E}{M}. \quad (35)$$

Using the similarity transformation of (32),  $J_3$  is invariant, but  $J_1$  and  $J_2$  take the form

$$J'_1 = \begin{pmatrix} 0 & \frac{1}{2}e^{\eta} \\ \frac{1}{2}e^{-\eta} & 0 \end{pmatrix}, \quad (36)$$

$$J'_2 = \begin{pmatrix} 0 & -\frac{i}{2}e^{\eta} \\ \frac{i}{2}e^{-\eta} & 0 \end{pmatrix}.$$

In the large-momentum or large-mass limit for a massive particle, we can obtain the  $N_i$  matrices of (23) as

$$N_1 = -\frac{M}{E} J'_2, \quad (37)$$

$$N_2 = \frac{E}{M} J'_1.$$

Remembering that we have to consider both signs of the boost generators, the generators of  $SL(2, c)$  can take the form

$$J_i = \begin{pmatrix} \left(\frac{1}{2}\right)\sigma_i & 0 \\ 0 & \left(\frac{1}{2}\right)\sigma_i \end{pmatrix}, \quad (38)$$

$$K_i = \begin{pmatrix} \left(\frac{i}{2}\right)\sigma_i & 0 \\ 0 & \left(-\frac{i}{2}\right)\sigma_i \end{pmatrix}$$

which is applicable to Dirac wave functions in the Weyl representation [14, 24]. Using the gauge transformation matrices from (26), we can write

$$D(u, v) = \begin{pmatrix} D^{(+)}(u, v) & 0 \\ 0 & D^{(-)}(u, v) \end{pmatrix}. \quad (39)$$

This matrix is applicable to the Dirac spinors. To evaluate the result of applying the  $D$  matrix from (39), we first look at the eigenspinors given in (22) applied to a massive Dirac particle that is at rest. Thus we have

$$U(0) = \begin{pmatrix} \alpha \\ \pm\dot{\alpha} \end{pmatrix}, \quad (40)$$

$$V(0) = \begin{pmatrix} \pm\beta \\ \dot{\beta} \end{pmatrix},$$

where the positive and negative energy states are denoted by the  $+$  and  $-$  signs, respectively. If these spinors are boosted along the  $z$ -axis using the operator generated by  $K_3$ , then

$$U(P) = \begin{pmatrix} e^{(+\eta/2)}\alpha \\ \pm e^{(-\eta/2)}\dot{\alpha} \end{pmatrix}, \quad (41)$$

$$V(P) = \begin{pmatrix} \pm e^{(-\eta/2)}\beta \\ e^{(+\eta/2)}\dot{\beta} \end{pmatrix}.$$

In the large-momentum/zero-mass limit, the large components,  $e^{(+\eta/2)}$ , are, according to (27), gauge invariant, while the small components, according to (28), are gauge dependent. This again shows that non-zero-mass, spin-1/2 particles are not invariant under gauge transformations. Furthermore, in this limit, the spinors of (41) can be renormalized as

$$U(P) = \begin{pmatrix} \alpha \\ 0 \end{pmatrix}, \quad (42)$$

$$V(P) = \begin{pmatrix} 0 \\ \beta \end{pmatrix}.$$

It is clear that the  $D$  transformation leaves these spinors invariant. It is this invariance, as shown before, that is responsible for the polarization of neutrinos [30, 35].

Additionally, one could interpret the results of (41) in terms of  $E(2)$  translations on free Weyl neutrino states. In this case, the gauge invariant transformations leave the left-handed neutrino invariant but translate the right-handed neutrino into a linear combination of left-handed and right-handed neutrinos [14, 30]. These coupled states could have implications requiring that in a constant electric and magnetic field neutrinos should acquire a small effective mass [14].

## 6. Neutrino Mass and Lorentz Transformations

In Section 3, we introduced the fact that Wigner [20] proposed that his “little groups” be defined as those Lorentz transformations that do not change the four-momentum of the free particle. Because there is no Lorentz frame in which a massless particle is at rest, we had to consider a momentum four-vector of the form given in (19). From this we were able to write down the transformation matrix given in (20) which

left the four-momentum invariant. In this section, we begin with a massive particle with fixed energy  $E$ . Then we can write the Lorentz boost along the  $z$  direction as

$$\begin{aligned} z &\longrightarrow (\cosh \xi) z + (\sinh \xi) t, \\ t &\longrightarrow (\sinh \xi) z + (\cosh \xi) t. \end{aligned} \quad (43)$$

As we saw in Section 5, the limiting case of  $e^\xi$  is given in (35) for the large-momentum limit. Within the framework of Lorentz transformations,  $E$  can become large and thus  $\xi$  can also become large. This has been discussed in the literature [24].

In addition,  $\xi$  can become large when the mass becomes very small. This cannot be achieved by Lorentz boosts, because the mass is a Lorentz-invariant quantity. With this point in mind, we can consider what happens when the mass is varied but the energy is held fixed. We can write the energy-momentum four-vector as

$$E(0, 0, \cos \chi, 1). \quad (44)$$

Then the mass becomes

$$M = E\sqrt{1 - \cos^2 \chi} = E \sin \chi. \quad (45)$$

Hence, the mass can be increased by increasing  $\chi$  from zero [36].

While the four-by-four matrix which makes the transformation of (43) is

$$\begin{pmatrix} 1 & 0 & 0 & 0 \\ 0 & 1 & 0 & 0 \\ 0 & 0 & \cosh \xi & \sinh \xi \\ 0 & 0 & \sinh \xi & \cosh \xi \end{pmatrix}, \quad (46)$$

its two-by-two equivalent to the spinor is

$$\begin{pmatrix} e^{\xi/2} & 0 \\ 0 & e^{-\xi/2} \end{pmatrix} \quad (47)$$

as seen in (33) [36]. The two-by-two matrix corresponding to a rotation around the  $y$ -axis is

$$\begin{pmatrix} \cos\left(\frac{\theta}{2}\right) & -\sin\left(\frac{\theta}{2}\right) \\ \sin\left(\frac{\theta}{2}\right) & \cos\left(\frac{\theta}{2}\right) \end{pmatrix}. \quad (48)$$

Thus we can now perform the Lorentz boost by making a similarity transformation:

$$\begin{pmatrix} e^{\xi/2} & 0 \\ 0 & e^{-\xi/2} \end{pmatrix} \begin{pmatrix} \cos\left(\frac{\theta}{2}\right) & -\sin\left(\frac{\theta}{2}\right) \\ \sin\left(\frac{\theta}{2}\right) & \cos\left(\frac{\theta}{2}\right) \end{pmatrix} \begin{pmatrix} e^{-\xi/2} & 0 \\ 0 & e^{\xi/2} \end{pmatrix}, \quad (49)$$

which becomes

$$\begin{pmatrix} \cos\left(\frac{\theta}{2}\right) & -e^\xi \sin\left(\frac{\theta}{2}\right) \\ e^{-\xi} \sin\left(\frac{\theta}{2}\right) & \cos\left(\frac{\theta}{2}\right) \end{pmatrix}. \quad (50)$$

For this matrix to remain finite in the large  $\xi$  limit, we can let  $e^\xi \sin \theta = \gamma$ . For  $\gamma$  to remain finite as  $\xi$  increases,  $\theta$  must approach zero. Then, in the limiting case, the matrix given in (50) becomes

$$\begin{pmatrix} 1 & -\gamma \\ 0 & 1 \end{pmatrix}. \quad (51)$$

It has been shown that the  $\gamma$  parameter performs gauge transformations on the photon case and its equivalent transformation on massless neutrinos [24, 30, 35]. If the neutrino indeed has mass, then we should observe neutrinos participating in gauge transformations.

## 7. Concluding Remarks

As there is currently much interest in massive neutrinos, it would be interesting to see if there was indeed a Lorentz frame in which neutrinos could be brought to rest. Additionally, it would be useful to understand if neutrinos participate in gauge transformations. The issue of whether or not the neutrino is a Dirac particle as opposed to a Majorana particle will be settled only if lepton number violation is observed. Furthermore, if right-handed neutrinos could be found separated from left-handed neutrinos, and if these right-handed neutrinos did not participate in weak interactions, this would have implications for physics beyond the Standard Model.

## Competing Interests

The authors declare that they have no competing interests.

## References

- [1] D. K. Papoulias and T. S. Kosmas, "Exotic lepton flavour violating processes in the presence of nuclei," *Journal of Physics: Conference Series*, vol. 410, no. 1, Article ID 012123, 2013.
- [2] D. N. Dinh, S. T. Petcov, N. Sasao, M. Tanaka, and M. Yoshimura, "Observables in neutrino mass spectroscopy using atoms," *Physics Letters, Section B: Nuclear, Elementary Particle and High-Energy Physics*, vol. 719, no. 1-3, pp. 154-163, 2013.
- [3] L. Miramonti and V. Antonelli, "Advancements in solar neutrino physics," *International Journal of Modern Physics E*, vol. 22, no. 5, Article ID 1330009, 2013.
- [4] A. Higuera, A. Mislivec, L. Aliaga et al., "The MINERvA Collaboration. Measurement of coherent production of  $\pi^\pm$  in neutrino and antineutrino beams on carbon from  $E_\nu$  of 1.5 to 20 GeV," *Physical Review Letters*, vol. 113, no. 26, Article ID 261802, 2014.
- [5] M. Ahlers and F. Halzen, "High-energy cosmic neutrino puzzle: a review," *Reports on Progress in Physics*, vol. 78, no. 12, Article ID 126901, 2015.
- [6] Y. Abe, J. C. dos Anjos, J. C. Barriere et al., "Improved measurements of the neutrino mixing angle  $\theta_{13}$  with the Double Chooz detector," *Journal of High Energy Physics*, vol. 2014, no. 10, article 86, pp. 1-40, 2014.
- [7] Y.-F. Li, J. Cao, Y. Wang, and L. Zhan, "Unambiguous determination of the neutrino mass hierarchy using reactor neutrinos," *Physical Review D*, vol. 88, no. 1, Article ID 013008, 9 pages, 2013.

- [8] J. Bergström, “Combining and comparing neutrinoless double beta decay experiments using different nuclei,” *Journal of High Energy Physics*, vol. 2013, no. 2, pp. 1–26, 2013.
- [9] P. Adamson, I. Anghel, C. Backhouse et al., “Measurement of neutrino and antineutrino oscillations using beam and atmospheric data in MINOS,” *Physical Review Letters*, vol. 110, no. 25, Article ID 251801, 2013.
- [10] T. Han, I. Lewis, R. Ruiz, and Z.-G. Si, “Lepton number violation and  $W'$  chiral couplings at the LHC,” *Physical Review D-Particles, Fields, Gravitation and Cosmology*, vol. 87, no. 3, Article ID 035011, 2013.
- [11] T. Asaka and T. Tsuyuki, “Seesaw mechanism at electron-electron colliders,” *Physical Review D*, vol. 92, no. 9, Article ID 094012, 2015.
- [12] M. Drewes, “The phenomenology of right handed neutrinos,” *International Journal of Modern Physics E*, vol. 22, no. 9, Article ID 1392003, 2013.
- [13] P. Ko and Y. Tang, “IceCube events from heavy DM decays through the right-handed neutrino portal,” *Physics Letters B*, vol. 751, pp. 81–88, 2015.
- [14] A. O. Barut and J. McEwan, “The four states of the massless neutrino with Pauli coupling by spin-gauge invariance,” *Letters in Mathematical Physics*, vol. 11, no. 1, pp. 67–72, 1986.
- [15] M. Drewes and B. Garbrecht, “Leptogenesis from a GeV seesaw without mass degeneracy,” *Journal of High Energy Physics*, vol. 2013, article 96, 2013.
- [16] M. Drewes, “Heavy neutrinos in particle physics and cosmology,” in *Proceedings of Science The European Physical Society Conference on High Energy Physics*, vol. 2229 of PoS(EPS-HEP 2015)075, Vienna, Austria, July 2015.
- [17] L. Canetti, M. Drewes, and B. Garbrecht, “Probing leptogenesis with GeV-scale sterile neutrinos at LHCb and Belle II,” *Physical Review D*, vol. 90, no. 12, Article ID 125005, 9 pages, 2014.
- [18] A. Palcu, “Neutrino mass as a consequence of the exact solution of 3-3-1 gauge models without exotic electric charges,” *Modern Physics Letters A*, vol. 21, no. 15, pp. 1203–1217, 2006.
- [19] S. M. Bilenky, “Neutrino,” *Physics of Particles and Nuclei*, vol. 44, no. 1, pp. 1–46, 2013.
- [20] E. Wigner, “On unitary representations of the inhomogeneous Lorentz group,” *Annals of Mathematics*, vol. 40, no. 1, pp. 149–204, 1939.
- [21] Y. S. Kim and E. P. Wigner, “Cylindrical group and massless particles,” *Journal of Mathematical Physics*, vol. 28, no. 5, pp. 1175–1179, 1987.
- [22] P. A. Dirac, “Application of quaternions to Lorentz transformations,” *Proceedings of the Royal Irish Academy*, vol. 50, pp. 261–270, 1945.
- [23] M. A. Naimark, “Linear representation of the Lorentz group,” *Uspekhi Matematicheskikh Nauk*, vol. 9, no. 62, pp. 19–93, 1954, Translated by F. V. Atkinson, *American Mathematical Society Translations Series 2*, vol. 6, pp. 379–458, 1957.
- [24] Y. S. Kim and M. E. Noz, *Theory and Applications of the Poincaré Group*, Fundamental Theories of Physics, Kluwer Academic, Dordrecht, The Netherlands, 1986.
- [25] S. Başkal, Y. S. Kim, and M. E. Noz, “Wigner’s space-time symmetries based on the two-by-two matrices of the damped harmonic oscillators and the Poincaré sphere,” *Symmetry*, vol. 6, no. 3, pp. 473–515, 2014.
- [26] V. B. Berestetskii, E. M. Lifshitz, and L. P. Pitaevskii, *Quantum Electrodynamics*, vol. 4 of *The Course of Theoretical Physics*, Pergamon Press, Oxford, UK, 2nd edition, 1982.
- [27] S. Bakal, Y. S. Kim, and M. E. Noz, *Physics of the Lorentz Group*, Morgan & Claypool Publishers IOPScience, Bristol, UK, 2015.
- [28] V. Bargmann, “Irreducible unitary representations of the Lorentz group,” *Annals of Mathematics*, vol. 48, pp. 568–640, 1947.
- [29] S. Başkal and Y. S. Kim, “de Sitter group as a symmetry for optical decoherence,” *Journal of Physics A: Mathematical and General*, vol. 39, no. 24, 2006.
- [30] D. Han, Y. S. Kim, and D. Son, “E(2)-like little group for massless particles and neutrino polarization as a consequence of gauge invariance,” *Physical Review D*, vol. 26, no. 12, pp. 3717–3725, 1982.
- [31] D. Han, Y. S. Kim, and D. Son, “Photon spin as a rotation in gauge space,” *Physical Review D*, vol. 25, no. 2, pp. 461–463, 1982.
- [32] D. Han, M. E. Noz, Y. S. Kim, and D. Son, “Space-time symmetries of confined quarks,” *Physical Review D*, vol. 25, no. 6, pp. 1740–1743, 1982.
- [33] D. Han, Y. S. Kim, and D. Son, “Photons, neutrinos, and gauge transformations,” *American Journal of Physics*, vol. 54, pp. 818–821, 1986.
- [34] D. Han, Y. S. Kim, and D. Son, “Eulerian parametrization of Wigner’s little groups and gauge transformations in terms of rotations in two-component spinors,” *Journal of Mathematical Physics*, vol. 27, no. 9, pp. 2228–2235, 1986.
- [35] Y. S. Kim, “Neutrino polarization as a consequence of gauge invariance,” *Czechoslovak Journal of Physics*, vol. 52, no. S3, pp. C353–C360, 2002.
- [36] Y. S. Kim and M. E. Noz, “Symmetries shared by the Poincaré Group and the Poincaré Sphere,” *Symmetry*, vol. 5, no. 3, pp. 233–252, 2013.

## Research Article

# On a Search for Hidden Photon CDM by a Multicathode Counter

**A. V. Kopylov, I. V. Orekhov, and V. V. Petukhov**

*Institute for Nuclear Research of Russian Academy of Sciences, Prospect of 60th Anniversary of October Revolution 7A,  
Moscow 117312, Russia*

Correspondence should be addressed to A. V. Kopylov; beril@inr.ru

Received 23 March 2016; Accepted 23 May 2016

Academic Editor: Hiroyasu Ejiri

Copyright © 2016 A. V. Kopylov et al. This is an open access article distributed under the Creative Commons Attribution License, which permits unrestricted use, distribution, and reproduction in any medium, provided the original work is properly cited. The publication of this article was funded by SCOAP<sup>3</sup>.

We report a new technique of a multicathode counter (MCC) developed to search for hidden photon (HP) cold dark matter (CDM) with a mass from 5 to 500 eV. The method is suggested in the assumption that HP-photon mixing causes emission of single electrons from a metal cathode if the mass of hidden photon  $m_{\gamma'}$  is greater than a work function of the metal  $\varphi_W$ . The measured effect from HP should be dependent on  $\varphi_W$  and on the structure of electronic shells of the metal used as a cathode. Potentially this can be used for a verification of the results obtained. Some preliminary results for the upper limit for mixing parameter  $\chi$  have been obtained for HP with a mass from 5 eV to 10 keV as a pure illustration of the potential of this technique. The efforts are continued to refine the procedure of data treatment and to improve the work of MCC. A new detector with a more developed design is under construction.

## 1. Introduction

The present data on the structure formation in the Universe indicate that most dark matter (DM) is “cold”; that is, it should be nonrelativistic. Neutrino in a hot dark matter concept can be envisaged only in combination with cold dark matter (CDM). Now the most attractive DM candidates appear to be Weakly Interactive Massive Particles (WIMP). Great progress in this field of research is outlined in [1]. However, there are other alternatives, among them axion and axion-like particles (ALP) which is probably a next most promising field. The efforts towards discovering axion are described in detail in [2]. Another interesting opportunity is a hidden photon which is a light extra  $U(1)$  gauge boson. As it was suggested in [3, 4] hidden photons (HP) may be observed in experiment through a kinetic mixing term  $(\chi/2)F_{\mu\nu}X^{\mu\nu}$  with the ordinary photons, where  $\chi$  is a parameter quantifying the kinetic mixing. Here  $F_{\mu\nu}$  is the field stress of the ordinary electromagnetic field  $A^\mu$  and  $X^{\mu\nu}$  is the field stress of the HP field  $X^\mu$ .

Recently the eV mass range of HP was investigated with a dish antenna [5], a novel method proposed in [6]. The idea is to detect electromagnetic wave which is emitted by the oscillation of electrons of the antenna's surface under tiny

ordinary electromagnetic field  $A^\mu$  induced by HP. A dark matter solution for HP with a mass  $m_{\gamma'}$  reads [6]

$$\left. \begin{pmatrix} \mathbf{A} \\ \mathbf{X} \end{pmatrix} \right|_{\text{DM}} = \mathbf{X}_{\text{DM}} \begin{pmatrix} -\chi \\ 1 \end{pmatrix} \exp(-i\omega t); \quad (1)$$

that is, it has a spatially constant mode  $k = 0$ , oscillating with frequency  $\omega = m_{\gamma'}$ . This method works well only if the reflectance of antenna is high which is observed for  $\omega < 5$  eV. In the work [5] using an optical mirror and a photon-counting PMT at the point of convergence of the photons emitted from mirror, the upper limit of  $6 \times 10^{-12}$  was obtained for a mixing parameter  $\chi$  for the hidden photon mass  $m_{\gamma'} = 3.1 \pm 1.2$  eV. This work was a first measurement of  $\chi$  within this range of  $m_{\gamma'}$  using a dish antenna. Our work was the search for hidden photons for the upper range of  $m_{\gamma'}$  using a gaseous proportional counter as a detector of electrons emitted from a metal cathode by hidden photons. This constitutes the novelty of our method.

## 2. A Method and Experimental Apparatus

The principal difference of our approach from [6] is that here we focus on shorter wavelengths, that is, higher masses of

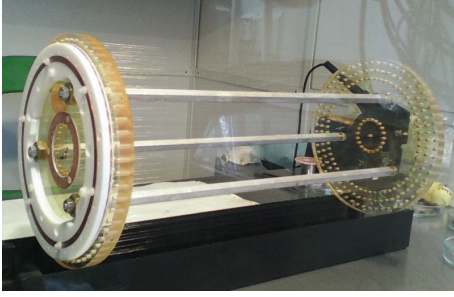


FIGURE 1: The central part of the counter.

HPs for which the reflectance of antenna is low. We make an assumption that in this case a HP-photon conversion will cause emission of single electrons from the surface of antenna similar to what one observes when metal is exposed to UV radiation. To register this conversion the detector should be highly sensitive to single electrons emitted from metal. Here we would like to draw attention to the fact that the detector in this case is sensitive exclusively to HP-photon conversion, not to photon-HP conversion. For the latter this method does not work. We assume here that probability for the electron to be emitted after a hidden photon gets converted into ordinary electric field in a metal cathode would be equal to quantum efficiency  $\eta$  for a given metal to emit electron after absorption of a real UV photon of energy  $\omega = m_{\gamma'}$ . The details of how electrons are created after photons get absorbed by a metal photocathode are described in many papers; see, for example, [7]. The obvious difference between these two processes is that UV photons are strongly absorbed by the metal, while HPs move freely through the metal, but this leads only to some underestimation of the effect from HP-photon conversion. We did not take this into account. Neither did we take into account the effects of surface roughness of the cathode. We consider this to be small corrections and leave it for our further study. To make a practical implementation of this idea a special technique of a multicathode counter (MCC) has been developed and some very preliminary data as a pure illustration of the potential of this technique in the search for hidden photons has been obtained.

To count electrons emitted from a metal cathode we used a gaseous proportional counter filled by argon-methane (10%) mixture at 0.2 MPa. To detect single electrons the counter should have high ( $\geq 10^5$ ) coefficient of gas amplification. The general view of the counter is presented in Figure 1 and the electronic scheme in Figure 2. Present design of MCC first described in [8] is a further development of the work with the aim of making an apparatus to register neutrino-nucleus coherent scattering [9, 10]. The cathode of the counter is 194 mm in diameter and 400 mm in length. It has relatively large ( $\approx 0.2 \text{ m}^2$ ) surface which acts in this experiment as “antenna” for HP but instead of reflecting electromagnetic waves it emits single electrons. The counter has a central anode wire of  $20 \mu\text{m}$  and 4 cathodes; 3 of them are composed of an array of  $50 \mu\text{m}$  nichrome wires tensed with a pitch of a few mm around anode one after another, and a fourth one, more distant from anode, is a cathode made of copper.

The apparatus is counting electrons emitted from the walls of a cathode at short wavelengths  $\omega = m_{\gamma'} \approx 5\text{--}500 \text{ eV}$ . The diameter of the first cathode  $D_1$  is 40 mm to ensure high ( $\geq 10^5$ ) coefficient of gas amplification in the central section of the counter. Three different configurations of the same counter are used to measure the count rate of single electrons. In the first configuration electrons, emitted from copper, drift freely to the central section with high gas amplification. The highest negative potential is applied in this configuration to the copper cathode. The rate  $R_1$  measured in this configuration is as follows:

$$R_1 = R_{\text{Cu}} + R_{\text{sp}}. \quad (2)$$

Here  $R_{\text{Cu}}$  is the count rate from single electrons emitted from copper and  $R_{\text{sp}}$  is the rate from spurious pulses generated in the volume limited by a diameter 194 mm. What is the origin of spurious pulses? This question will be the subject of our further study. Here we assume that they are produced by “hot” spots on the surface of metal and are the effect of microstructure of a metal. The microprotrusions (spearheads) on the surface of wires may generate single electrons in strong electric fields. The spots with impurities of other metals, especially alkaline, may generate emission of single electrons and so forth. Only the future work can show how successful can this approach be.

In the second configuration the highest negative potential is applied to the third cathode  $D_3 = 180 \text{ mm}$ . In this configuration the count rate is as follows:

$$R_2 = 0.11 \cdot R_{\text{Cu}} + R_{\text{sp}}. \quad (3)$$

The factor 0.11 was obtained by calibration of the counter in 1st and 2nd configurations by UV source of the same intensity. Here the key point is that in 1st and 2nd configurations the counter has approximately the same geometry and the same wires. So if “hot” spots are on the surface of wires, the difference of the count rates in 1st and 2nd configurations will contain only 89% of the count rate of single electrons emitted from copper cathode. Because the geometry of the counter in 1st configuration is very similar to its geometry in 2nd configuration the same reasoning is valid for spurious pulses generated by a leakage current through dielectric used in the construction of the counter.

In the third configuration the highest negative potential is applied to a second cathode  $D_2 = 140 \text{ mm}$ . The rate  $R_3$  measured in this configuration is determined by spurious pulses generated within a volume limited by smaller diameter 140 mm with different number of wires and different isolators, so

$$R_3 = r_{\text{sp}}. \quad (4)$$

In experiment the rate  $R_3$  turned out to be approximately 3 times smaller than the rates  $R_1$  and  $R_2$  (which are very close) not in contradiction with our explanation of the origin of the spurious pulses. All this explains why as a measure of the effect from HPs we use the count rate

$$R_{\text{MCC}} = \frac{(R_1 - R_2)}{0.89} = R_{\text{Cu}}. \quad (5)$$

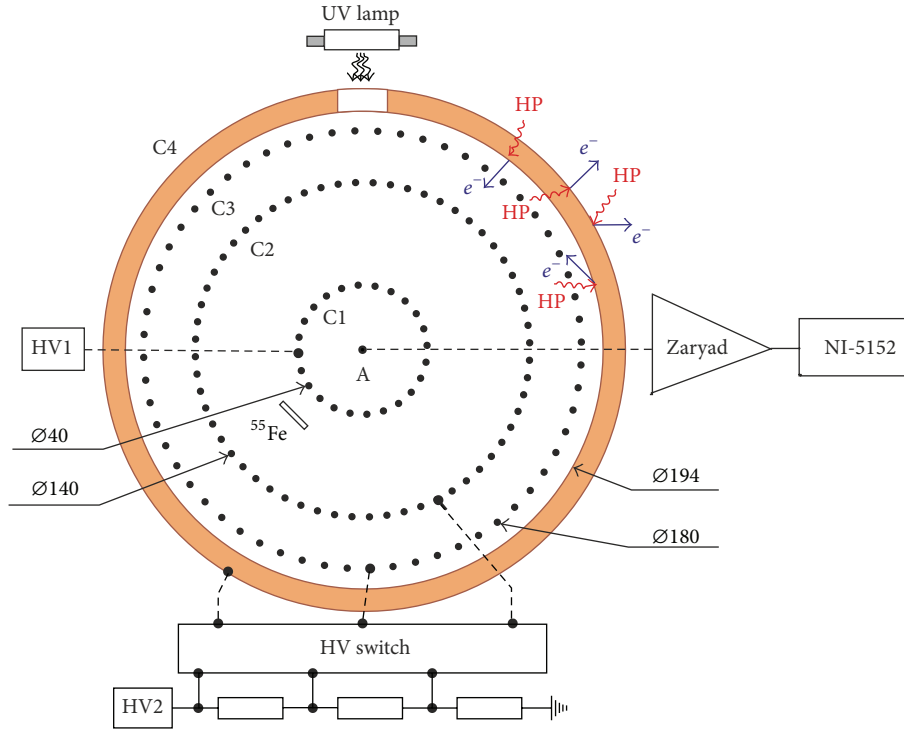


FIGURE 2: A simplified electronic scheme of a multicathode counter (MCC). A: anode, C1-C4: cathodes, and “Zaryad”: charge sensitive preamplifier.

The measurements were performed in each configuration by switching the counter consecutively in three different configurations, by calibration of the counter, and by measuring the rates  $R_1$ ,  $R_2$ , and  $R_3$ . Then from a number of measured points the average rates  $\bar{R}_1$ ,  $\bar{R}_2$  were found and from here the average rate  $\bar{R}_{MCC}$  is found. Then from the scattering of the experimental points the uncertainties were calculated for each rate and, finally, for  $R_{MCC}$ . The count rate  $R_3$  has been used to monitor the counting process to exclude some possible interference by external sources of electromagnetic disturbances.

### 3. Energy Calibration and Analysis

The calibration of the counter has been conducted by  $^{55}\text{Fe}$  source and by UV light of the mercury lamp. The calibration by  $^{55}\text{Fe}$  source was used to determine at what high voltages, HV1 and HV2, the counter was working in a mode of limited proportionality with high ( $>10^5$ ) gas amplification. Here we followed the standard technique described in many papers, for example, in [11]. It was also described in our earlier papers [9, 10]. High voltage at first cathode was 2060 V and the ones from the voltage divider have been used for all three configurations such as to ensure the amplitude of the pulse corresponding to peak 5.9 keV from K-line of  $^{55}\text{Mn}$ , which is eradiated as a result of K-electron capture by  $^{55}\text{Fe}$ , on the output of charge sensitive preamplifier to be at the level 1400 mV which corresponds to a gas amplification  $A \approx 10^5$ . Figure 3 shows the calibration spectrum.

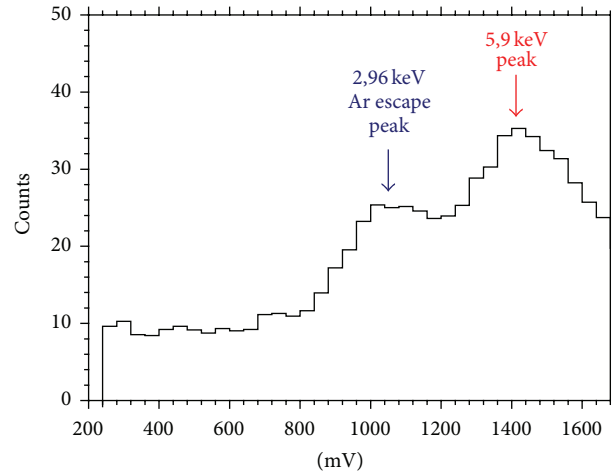


FIGURE 3: The calibration spectrum from  $^{55}\text{Fe}$  source introduced directly in a working volume of the counter facing first cathode.

The amplitude of the escape peak of argon at the energy 2.96 keV (5.9 keV minus 2.94 keV of K X-ray of argon escaping the detection region) was shifted from the due position in case of a linear response at about 700 mV to the one at approximately 1000 mV. This nonlinearity in the spectrum indicates that the counter was working in the regime of limited proportionality. From the approximation done through three points, zero and two peaks, 5.9 keV at 1400 mV and 2.96 keV at 1000 mV, one can find that at

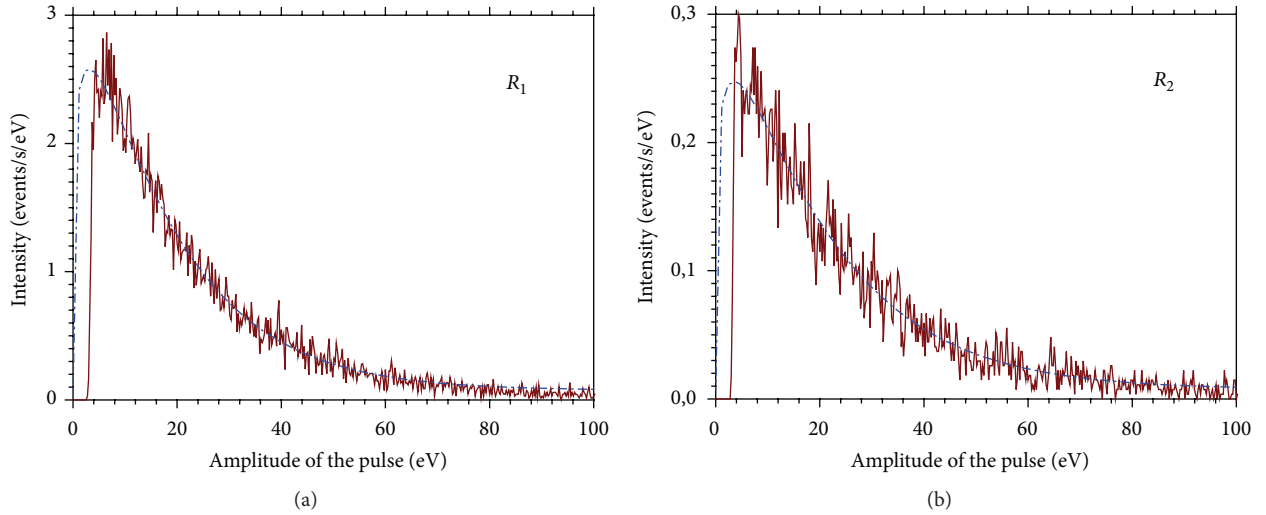


FIGURE 4: The single electron spectra obtained in measurements in 1st ( $R_1$ ) and 2nd ( $R_2$ ) configurations at the same flux of UV photons. The dashed curves indicate the Polya distribution.

energies less than 100 eV a gas amplification  $A \approx 1.8 \cdot 10^5$  and the conversion factor is  $\approx 2.3$  eV/mV. It takes approximately 27 eV to create one electron-ion pair in argon. This means that single electron pulses should be observed in the region below 50 mV. The calibration by UV photons demonstrates that this is really so. The  $^{55}\text{Fe}$  source has been removed and the internal walls of the counter were irradiated by UV light from a mercury lamp placed outside through a window made of melted silica. The physics and techniques of single electron counting were described in detail in many devoted articles; see, for example, [12–14]. Figure 4 shows the single electron spectra obtained in measurements in 1st and 2nd configurations.

Comparing the count rates  $R_1$  and  $R_2$  presented in Figure 4 one can see that in the 2nd configuration the count rate of single electrons was about 0.11 of the rate measured in the first one. It proves that in the 2nd configuration the electrons emitted from the walls of the counter were really rejected back by the 3rd cathode. This means that the counter in the 2nd configuration can be used for measurement of the background count rate. To compare the gains in different configurations we used the same procedure as the one described in [15]; the inverse indexes of exponents were used as a measure of the gain of the counter. For the pulses above a threshold 7 eV the deviation from exponential distribution was small and could be neglected. The inverse indexes of exponent for all three configurations were in the range  $19.3 \pm 1.2$  eV. The counting efficiency for the interval from 7 eV till 70 eV was found to be  $76 \pm 5\%$ . This number has been obtained by using Polya distribution [16]:

$$P(A) = \left( \frac{A(1+\theta)}{A} \right)^\theta \exp\left( \frac{-A(1+\theta)}{A} \right), \quad (6)$$

where  $A$  is gas amplification and  $\theta$  is parameter which depends on a working gas and electric field configuration. From the approximation of the measured spectrum by Polya

curve it was found that  $\theta \approx 0.16$  which is in a reasonable agreement with the expected one for our working gas and electric field configuration. The counting efficiency has been corrected upon the results of calibrations performed in each of three configurations. The possibility to increase the counting efficiency is a subject of our further study. To have a further progress we need to decrease the threshold or to increase the gas amplification.

In the measurements the shapes of the pulses on the output of a charge sensitive preamplifier are recorded by 8-bit digitizer. In our previous paper [9] the shapes of “true” and “wrong” pulses are presented. The “true” pulses have typically a relatively short front edge (a few microseconds) corresponding to the drift of positive ions to cathode and long (hundreds of microseconds) tail corresponding to the time of the baseline restoration of the charge sensitive preamplifier. The “wrong” pulses usually have a wrong (too fast or too slow or irregular) front edge or nonexponential tail. In the analyses of the data only pulses with a baseline within  $\pm 2$  mV were taken with a proper evaluation of the resulted live time. Figures 6 and 7 show the distribution of the events on the diagram “duration of front edge-parameter  $\beta$ ” for the UV lamp and for real measurements. The parameter  $\beta$  is proportional to first derivative of the baseline approximated by a straight line in the interval  $50 \mu\text{s}$  before the front edge. We used it as a measure of the quality of baseline in the prehistory of the event which has been used in a procedure of automatic screening of all data. The events with  $\beta$  beyond the allowed range of  $0 \pm 0.1$  were considered as “not having a reliable determined amplitude” events and were discarded from analyses. The statistic collected during a day or even a few days for each configuration was rather high so we could afford to do this discrimination without substantial loss of information. The region of interest (ROI) box contains “true” pulses with amplitude in the interval [7–70] eV with a front edge in the interval [2–25  $\mu\text{s}$ ] and a parameter  $\beta$  in the interval  $0.0 \pm 0.1$ . The pulses beyond this region were

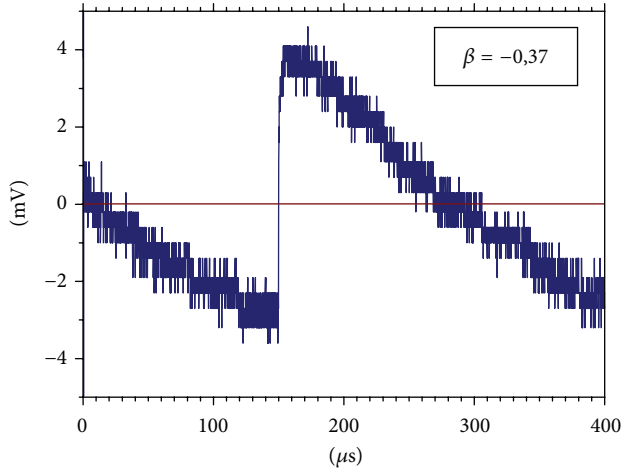


FIGURE 5: One example of the pulse with “bad” prehistory.

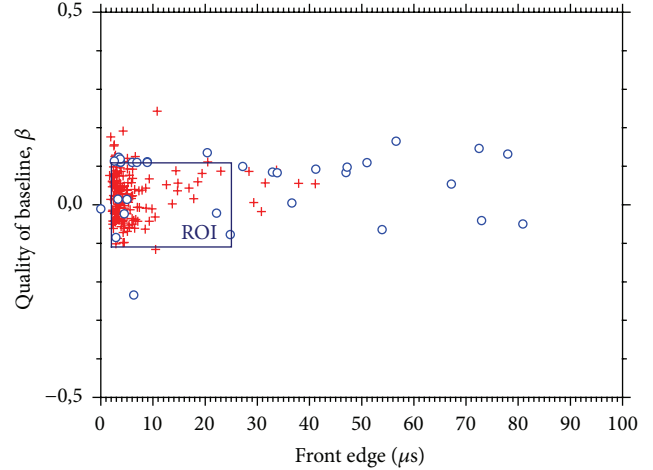


FIGURE 7: The distribution of the real events.

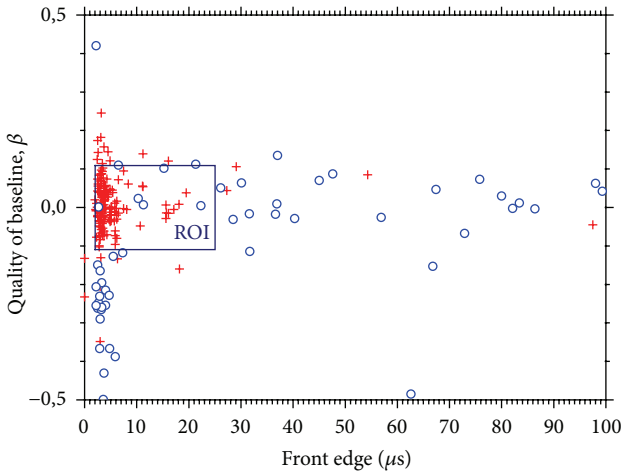


FIGURE 6: The distribution of the events for UV lamp.

rejected as “noisy” pulses. One of the typical “noise” pulses is presented in Figure 5.

One can see that a ROI region contains  $95 \pm 5\%$  of all pulses (crosses) from UV lamp. By inspecting directly a small sample of the real pulses we found that inside of ROI region one can see only about 10% of the pulses with the “wrong” shape (circles).

To reduce the background from external  $\gamma$ -radiation the counter has been placed in a cabinet with 30 cm iron shield. It resulted in decrease of the count rates of single electron events by a factor of 2 (detector on a porch of a cabinet versus detector inside a cabinet) while the flux of gamma rays in the region around 200 keV has been attenuated in these layouts by a factor of 50. From here one gets a simple estimate of the background: inside a cabinet the  $\gamma$ -radiation cannot be a major source of the single electron events; its contribution is not more than a few percent. The main source is spurious pulses similar to what one observes with PMT; this was also a limiting factor in experiment with a dish antenna [5]. To reduce this dark current we should make further

improvements in the construction of the detector. This is our task for future.

The data were collected frame by frame. Each frame contained 2 M points, each point 100 ns. After collection of the data they were stored on a disk and then the collection resumed. The analysis of the collected data was performed offline. The frames with the signs of excessive noisiness were removed from analysis.

#### 4. Sensitivity of the Method

Here we follow the same ideology as developed in [6] for a dish antenna with one principal difference: instead of detecting electromagnetic waves we look for single electrons emitted from the surface of antenna. That is, why we use in our experiment not antenna but gaseous proportional counter (see Figure 1). We assume that similar to the emission of single electrons from metal by UV light or by X-rays the probability for the electron to be emitted when HP of the mass  $m_{\gamma'}$  gets converted into an ordinary electric field in metal is equal to the quantum efficiency  $\eta$  for the photon's energy  $\omega = m_{\gamma'}$ . According to [6] if DM is totally made up of hidden photons, the power collected by antenna is

$$P = 2\alpha^2 \chi^2 \rho_{\text{CDM}} A_{\text{dish}}, \quad (7)$$

where  $\alpha^2 = \cos^2 \theta$ ,  $\theta$  is the angle between the HP field, when it points in the same direction everywhere, and the plane of antenna,  $\alpha^2 = 2/3$  if HPs have random orientation,  $\chi$  is the dimensionless parameter quantifying the kinetic mixing,  $\rho_{\text{CDM}} \approx 0.3 \text{ GeV/cm}^3$  is the energy density of CDM which is taken here to be equal to the energy density of HPs, and  $A_{\text{dish}}$  is the antenna's surface. In our case of gaseous proportional counter  $P = R_{\text{MCC}} m_{\gamma'} / \eta$  and this expression will be as follows:

$$R_{\text{MCC}} m_{\gamma'} = 2\eta \alpha^2 \chi^2 \rho_{\text{CDM}} A_{\text{MCC}}. \quad (8)$$

Here  $A_{\text{MCC}}$  is the surface of the metal cathode of our counter. From here one can easily obtain

$$\chi_{\text{sens}} = 2.9 \times 10^{-12} \left( \frac{R_{\text{MCC}}}{\eta \text{ 1 Hz}} \right)^{1/2} \left( \frac{m_{\gamma'}}{\text{1 eV}} \right)^{1/2} \cdot \left( \frac{0.3 \text{ GeV/cm}^3}{\rho_{\text{CDM}}} \right)^{1/2} \left( \frac{1 \text{ m}^2}{A_{\text{MCC}}} \right)^{1/2} \cdot \left( \frac{\sqrt{2/3}}{\alpha} \right). \quad (9)$$

## 5. First Data Obtained

The detector was placed at the ground floor of a building in Troitsk, Moscow region, in a specially constructed cabinet with 30 cm iron shield. All count rates were in a few Hz range. The average value of  $R_{\text{MCC}}$  calculated for “quiet” interval during 28 days of measurements was found to be  $\bar{R}_{\text{MCC}} = -0.06 \pm 0.36 \text{ Hz}$ . The uncertainty has been found from the real scattering of the experimental points. So if we take the normal distribution for uncertainties, then we obtain that, at 95% confidence level,  $\bar{R}_{\text{MCC}} < 0.66 \text{ Hz}$ . The quantum efficiency  $\eta$  was taken from [17] for masses of HPs  $m_{\gamma'} < 11.6 \text{ eV}$  (magenta), from [18] for  $10 \text{ eV} < m_{\gamma'} < 60 \text{ eV}$  (red), from [19] for  $20 \text{ eV} < m_{\gamma'} < 10 \text{ keV}$  (green), and from [20] for  $50 \text{ eV} < m_{\gamma'} < 10 \text{ keV}$  (blue). From expression (9) we obtain an upper limit for a mixing constant  $\chi$ . The values of a mixing constant  $\chi$  allowed by this experiment are below the curve presented in Figure 8. The systematic uncertainty is mainly determined by the uncertainty in quantum efficiency which is taken to be about 30% following the estimates done in [17]. To decrease this limit one should construct a detector with lower count rate of spurious pulses. The difference in the curves presented in Figure 8 is explained by different purity of copper used in measurements. The data from [17, 20] were obtained for atomically clean copper samples prepared by evaporation of copper in high vacuum while routinely cleaned (by solvents) copper samples were used in [18, 19]. For example, in the paper [21], it was shown that cleaning of the surface of the copper cathode by ionized controlled etching (ICE) can increase the quantum efficiency by an order of magnitude. For atomically clean copper one can see the effect of electronic shells while for routinely cleaned copper the spectra are rather smudged. In our detector for cathode we used routinely cleaned (by solvents) copper. It would be expedient to use a quantum efficiency measured for the specific sample used for a cathode in our detector and we are planning this work for the future. There is a strong dependence of the effect not only on the work function but also on the structure of the electronic shells of the metal used for a cathode. Potentially this can be used for verification that the obtained result is really from HPs. For this we should make measurements using cathodes made of different metals.

The numbers presented in Figure 8 are first very preliminary results for hidden photons with a mass from 5 to 500 eV. One can see that the region of highest sensitivity for our method is from 10 to 30 eV, that is, approximately

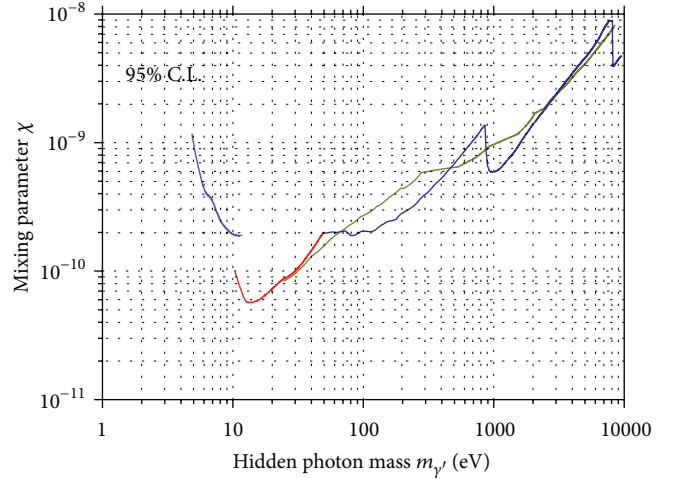


FIGURE 8: The limit for a mixing constant  $\chi$ .

equal to the energy needed to produce one ion pair in argon. This result has been obtained in direct measurements in a laboratory experiment by observing single electrons emitted from the surface of a copper cathode. At present time this is the only experiment using this technique which is based on measurement of the rate of single electron emission from a metal cathode of the counter sensitive only to HP-photon conversion and not sensitive to photon-HP conversion. Stellar astrophysics provides stringent constraints for this value. The limits obtained by using some astrophysical models (see, e.g., [22, 23] and references therein) are lower by several orders of magnitude. The limits obtained from stellar astrophysics are based on the models when both conversions are alike. The most impressive results have been obtained by observing electron emission from liquid xenon [23]. The threshold energy for the production of a single electron in liquid xenon is only 12 eV and in a xenon detector the total fiducial volume is a target for CDM. To reach the comparable sensitivity we need to decrease the spurious count rate of single electron events of our detector by several orders of magnitude. We are not aware of any reasons why it cannot be realized in view that this is the first multicathode counter ever constructed. This question needs further study. We plan to make further improvements in the construction of MCC mainly with the aim of reducing the count rate of spurious pulses.

We consider that a key element in reducing the rate of spurious counts would be to use good isolating materials and very clean metals with meticulously polished surfaces and to assemble the counter in very clean dust-free environments. Approaching this strategy we hope to decrease the rate of spurious counts by about an order of magnitude. At this level, as our measurements with and without active and passive shields have shown, the background rate will be determined by ionized particles (muons and electrons) and by gammas from the material of passive shield. To decrease further the background rate we will go to underground laboratory, where the flux of muons is negligible in comparison with the one at a surface laboratory, and there we will also use a passive



- antenna,” *Journal of Cosmology and Astroparticle Physics*, vol. 4, article 16, 2013.
- [7] D. H. Dowell and J. F. Schmerge, “The quantum efficiency and thermal emittance of metal photocathodes,” Tech. Rep. SLAC-PUB-13535, 2009.
- [8] A. V. Kopylov, I. V. Orekhov, and V. V. Petukhov, “Using a Multi-Cathode Counter (MCC) in the Search for Hidden Photon CDM,” <http://arxiv.org/abs/1509.03033>.
- [9] A. V. Kopylov, I. V. Orekhov, V. V. Petukhov, and A. E. Solomatin, “Gaseous detector with Sub-keV threshold to study neutrino scattering at low recoil energies,” *Advances in High Energy Physics*, vol. 2014, Article ID 147046, 8 pages, 2014.
- [10] A. V. Kopylov, I. V. Orekhov, V. V. Petukhov, and A. E. Solomatin, “Gaseous detector of ionizing radiation for registration of coherent neutrino scattering on nuclei,” *Technical Physics Letters*, vol. 40, no. 3, pp. 185–187, 2014.
- [11] M. Campbell, M. Chefdeville, P. Colas et al., “Detection of single electrons by means of a Micromegas-covered MediPix2 pixel CMOS readout circuit,” *Nuclear Instruments and Methods in Physics Research Section A: Accelerators, Spectrometers, Detectors and Associated Equipment*, vol. 540, no. 2-3, pp. 295–304, 2005.
- [12] H. S. Snyder, “Fluctuations for proportional counters,” *Physical Review*, vol. 72, p. 181, 1947.
- [13] G. D. Alkhazov, “Statistics of electron avalanches and ultimate resolution of proportional counters,” *Nuclear Instruments and Methods*, vol. 89, pp. 155–165, 1970.
- [14] A. F. Buzulutskov, “Gaseous photodetectors with solid photocathodes,” *Physics of Particles and Nuclei*, vol. 39, no. 3, pp. 424–453, 2008.
- [15] Z. Ahmed, M. A. Bowles, R. Bunker et al., “A prototype low-background multiwire proportional chamber,” *Journal of Instrumentation*, vol. 9, no. 1, Article ID P01009, 2014.
- [16] G. F. Knoll, *Radiation Detection and Measurement*, John Wiley & Sons, New York, NY, USA, 3rd edition, 2000.
- [17] W. F. Krolikowski and W. E. Spicer, “Photoemission studies of the noble metals. I. Copper,” *Physical Review*, vol. 185, no. 3, pp. 882–900, 1969.
- [18] R. B. Cairns and J. A. Samson, “Metal photocathodes as secondary standards for absolute intensity measurements in the vacuum ultraviolet,” *Journal of the Optical Society of America*, vol. 56, no. 11, pp. 1568–1573, 1966.
- [19] R. H. Day, P. Lee, E. B. Saloman, and D. J. Nagel, “Photoelectric quantum efficiencies and filter window absorption coefficients from 20 eV to 10 KeV,” *Journal of Applied Physics*, vol. 52, no. 11, pp. 6965–6973, 1981.
- [20] H. Henneken, F. Scholze, M. Krumrey, and G. Ulm, “Quantum efficiencies of gold and copper photocathodes in the VUV and X-ray range,” *Metrologia*, vol. 37, no. 5, pp. 485–488, 2000.
- [21] E. Chevallay, J. Durand, S. Hutchins, G. Suberlucq, and M. Wurgel, “Photocathodes tested in the dc gun of the CERN photoemission laboratory,” *Nuclear Instruments and Methods in Physics Research Section A: Accelerators, Spectrometers, Detectors and Associated Equipment*, vol. 340, no. 1, pp. 146–156, 1994.
- [22] H. An, M. Pospelov, and J. Pradler, “Dark matter detectors as dark photon helioscopes,” *Physical Review Letters*, vol. 111, no. 4, Article ID 041302, 2013.
- [23] H. An, M. Pospelov, J. Pradler, and A. Ritz, “Direct detection constraints on dark photon dark matter,” *Physics Letters B*, vol. 747, pp. 331–338, 2015.
- [24] M. Klasen, M. Pohl, and G. Sigl, “Indirect and direct search for dark matter,” *Progress in Particle and Nuclear Physics*, vol. 85, pp. 1–32, 2015.

## Research Article

# Combined Effect of NSI and SFP on Solar Electron Neutrino Oscillation

**Deniz Yilmaz**

*Department of Physics Engineering, Faculty of Engineering, Ankara University, Tandogan, 06100 Ankara, Turkey*

Correspondence should be addressed to Deniz Yilmaz; [dyilmaz@eng.ankara.edu.tr](mailto:dyilmaz@eng.ankara.edu.tr)

Received 12 January 2016; Revised 22 April 2016; Accepted 15 May 2016

Academic Editor: Theocharis Kosmas

Copyright © 2016 Deniz Yilmaz. This is an open access article distributed under the Creative Commons Attribution License, which permits unrestricted use, distribution, and reproduction in any medium, provided the original work is properly cited. The publication of this article was funded by SCOAP<sup>3</sup>.

The combined effect of spin-flavor precession (SFP) and the nonstandard neutrino interaction (NSI) on the survival probability of solar electron neutrinos (assumed to be Dirac particles) is examined for various values of  $\epsilon_{11}$ ,  $\epsilon_{12}$ , and  $\mu B$ . It is found that the neutrino survival probability curves affected by SFP and NSI effects individually for some values of the parameters ( $\epsilon_{11}$ ,  $\epsilon_{12}$ , and  $\mu B$ ) get close to the standard MSW curve when both effects are combined. Therefore, the combined effect of SFP and NSI needs to be taken into account when the solar electron neutrino data obtained by low energy solar neutrino experiments is investigated.

## 1. Introduction

After first observation of the solar neutrino oscillation in Homestake neutrino experiment, serious solar, atmospheric, and reactor neutrino experiments were established to confirm it during the last decades. Both KamLAND experiment detecting reactor neutrinos [1, 2] and the combined analysis of the solar neutrino experiments (high precision water Cherenkov experiments SNO [3, 4] and SK [5, 6] and the radiochemical experiments Homestake [7], SAGE [8], GALLEX [9], and GNO [10]) strongly pointed out the so-called large mixing angle (LMA) region of the neutrino parameter space [11–16]. One of the implications of the physics beyond the Standard Model (SM) is the neutrino oscillation. Since neutrinos have a mass in a minimal extension of the SM, they have also magnetic moment [17]:

$$\mu_\nu = \frac{3eG_f m_\nu}{8\pi^2 \sqrt{2}} = \frac{3eG_f m_e m_\nu}{4\pi^2 \sqrt{2}} \mu_B, \quad (1)$$

where  $G_f$  is Fermi constant;  $m_e$  and  $m_\nu$  are the masses of electron and neutrino, respectively; and  $\mu_B$  is Bohr magneton. While Majorana type neutrinos can only have off-diagonal (transition) magnetic moments, Dirac type neutrinos can have diagonal and off-diagonal magnetic moments [18, 19]. If the neutrinos have magnetic moments, they can be effected

by the large magnetic fields when they are passing through the magnetic region. Their spin can flip and the left-handed neutrino becomes a right-handed neutrino [20–24]. Thus the combined effect of the matter and the magnetic field called as spin-flavor precession (SFP) can change left-handed electron neutrino to another right-handed neutrino. This yields two other transitions ( $\nu_{e_L} \rightarrow \nu_{\mu_R}$  or  $\nu_{\tau_R}$ ) in addition to the left-handed ones (i.e., in this scenario, the conversion probability is mainly affected) [24]. In the Dirac case, since the right-handed neutrinos are considered as sterile, they are not detectable by the detectors. On the other hand, if the neutrinos are of Majorana type, this conversion yields a solar antineutrino flux which is detectable by the detectors. These conversions for both Dirac and Majorana cases can also be responsible for the solar electron neutrino deficit. So far several studies related with the SFP have been studied in different aspects [25–31]. Astrophysical and cosmological arguments [32], Supernova 1987A [33, 34], solar neutrino experiments looking neutrino-electron scattering [35], and the reactor neutrino experiments [36, 37] provide some bounds on the neutrino magnetic moment. The new limit recently was obtained by GEMMA experiment:  $\mu_\nu < 2.9 \times 10^{-11} \mu_B$  at 90% CL [38]. However, another strong bound on neutrino transition magnetic moment was obtained in the presence of nonstandard neutrino-nucleus interactions by Papoulias

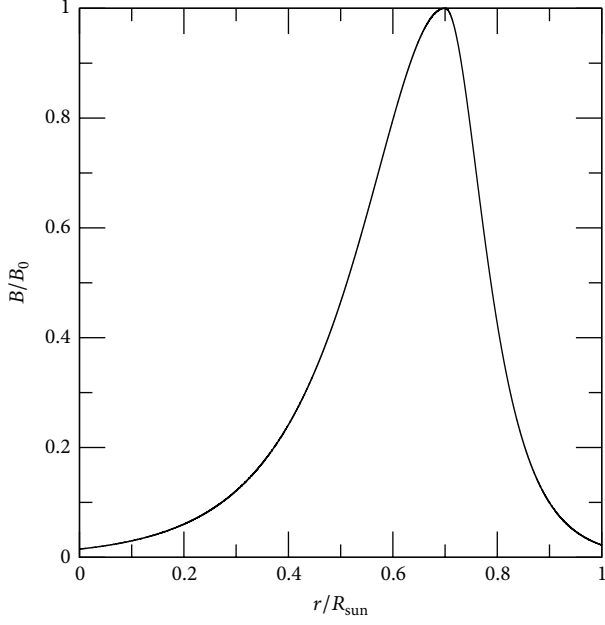


FIGURE 1: Magnetic field profile.

and Kosmas [39]. Detailed discussion on neutrino magnetic moment is also given elsewhere [40–45]. In addition to the knowledge about neutrino magnetic moment, the thorough information of solar magnetic fields is needed for the SFP analysis in the Sun. Despite the limited knowledge about it, some plausible profiles can be found in the literature [46, 47]. Standard solar model [47, 48] limits the solar magnetic field:  $\sim 20$  G near the solar surface [49], 20 kG–300 kG at the convective zone [47], and  $<10^7$  G at the solar center [47]. In this study the magnetic field profile is chosen as given in [46]. It has a peak at the bottom of the convective zone as shown in Figure 1.

Solar neutrinos can also be used for analyzing the physics beyond the Standard Model of the particle physics such as nonstandard forward scattering [50], mass varying neutrinos [51, 52], and long-range leptonic forces [53]. The probe of nonstandard neutrino interaction models is expected to observe in the transition region between 1 MeV and 4 MeV where the low energy solar neutrino experiments such as SNO+ will examine. Even though the data is poor in this region, the studies comparing the effects of nonstandard models on the neutrino oscillation to the standard MSW-LMA oscillation show that these effects modify the survival probability of neutrinos [50–56].

In this paper, the combined effect of nonstandard neutrino interactions (NSI) and SFP is examined in the case of two neutrino generations by assuming that the neutrinos are of Dirac type. The best fit LMA values are used for  $\delta m_{12}^2$  and  $\theta_{12}$  [57]. It is shown that the neutrino survival probability curves affected by SFP and NSI effects individually for some values of the parameters ( $\epsilon_{11}$ ,  $\epsilon_{12}$ , and  $\mu B$ ) get close to the standard MSW curve when both effects are combined. Therefore, one can say that the combined effect of them needs

to be taken into account when the solar electron neutrino data obtained by low energy solar neutrino experiments is investigated. Another analysis on the SFP effect in the presence of the NSI is examined for Majorana type solar neutrinos in [58].

## 2. Spin-Flavor Precession (SFP) including Nonstandard Neutrino Interaction (NSI)

The evolution equation including NSI matter effects in the SFP scenario for Dirac neutrinos can be written as

$$i \frac{d}{dt} \begin{pmatrix} \nu_{eL} \\ \nu_{\mu L} \\ \nu_{eR} \\ \nu_{\mu R} \end{pmatrix} = \begin{pmatrix} H_L + H_{\text{NSI}} & BM^\dagger \\ BM & H_R \end{pmatrix} \begin{pmatrix} \nu_{eL} \\ \nu_{\mu L} \\ \nu_{eR} \\ \nu_{\mu R} \end{pmatrix}, \quad (2)$$

where  $H_L$ ,  $H_R$ ,  $H_{\text{NSI}}$ , and  $M$  are the  $2 \times 2$  submatrices and  $B$  is the transverse magnetic field [24, 50]. For the Dirac neutrinos one writes down

$$H_L = \begin{pmatrix} V_c + V_n + \frac{\delta m_{12}^2}{2E} \sin^2 \theta_{12} & \frac{\delta m_{12}^2}{4E} \sin 2\theta_{12} \\ \frac{\delta m_{12}^2}{4E} \sin 2\theta_{12} & V_n + \frac{\delta m_{12}^2}{2E} \cos^2 \theta_{12} \end{pmatrix}, \quad (3)$$

and  $H_R = H_L$  ( $V_c = 0 = V_n$ ). The matter potentials here are given as

$$\begin{aligned} V_c &= \sqrt{2} G_F N_e, \\ V_n &= -\frac{G_F}{\sqrt{2}} N_n, \end{aligned} \quad (4)$$

where  $N_e$  and  $N_n$  are electron and neutron density, respectively [59–61]. The magnetic moment matrix for the Dirac neutrinos in (2) is written as [24]

$$M = \begin{pmatrix} \mu_{ee} & \mu_{e\mu} \\ \mu_{\mu e} & \mu_{\mu\mu} \end{pmatrix}. \quad (5)$$

The NSI contributions in (2) can be parametrized by four-fermion operator as given in [50]:

$$\begin{aligned} \mathcal{L} &= -2\sqrt{2} G_F (\nu_\alpha \gamma_\rho \nu_\beta) \left( \epsilon_{\alpha\beta}^{f\bar{f}L} \bar{f}_L \gamma^\rho \bar{f}_L + \epsilon_{\alpha\beta}^{f\bar{f}R} \bar{f}_R \gamma^\rho \bar{f}_R \right), \quad (6) \end{aligned}$$

where  $\epsilon^{f\bar{f}P}$  denotes the strength of the nonstandard interaction between  $\alpha$  and  $\beta$  types of neutrinos and the  $P$  (left- or right-handed) components of the fermions  $f$  and  $\bar{f}$ . Since the neutrino propagation can only be effected by the vector components where  $f = \bar{f}$  of the nonstandard interaction ( $\epsilon_{\alpha\beta}^f = \epsilon_{\alpha\beta}^{fL} + \epsilon_{\alpha\beta}^{fR}$ ), one can define  $\epsilon_{\alpha\beta}$  as the sum of the contributions from electrons, up quarks and down quarks in

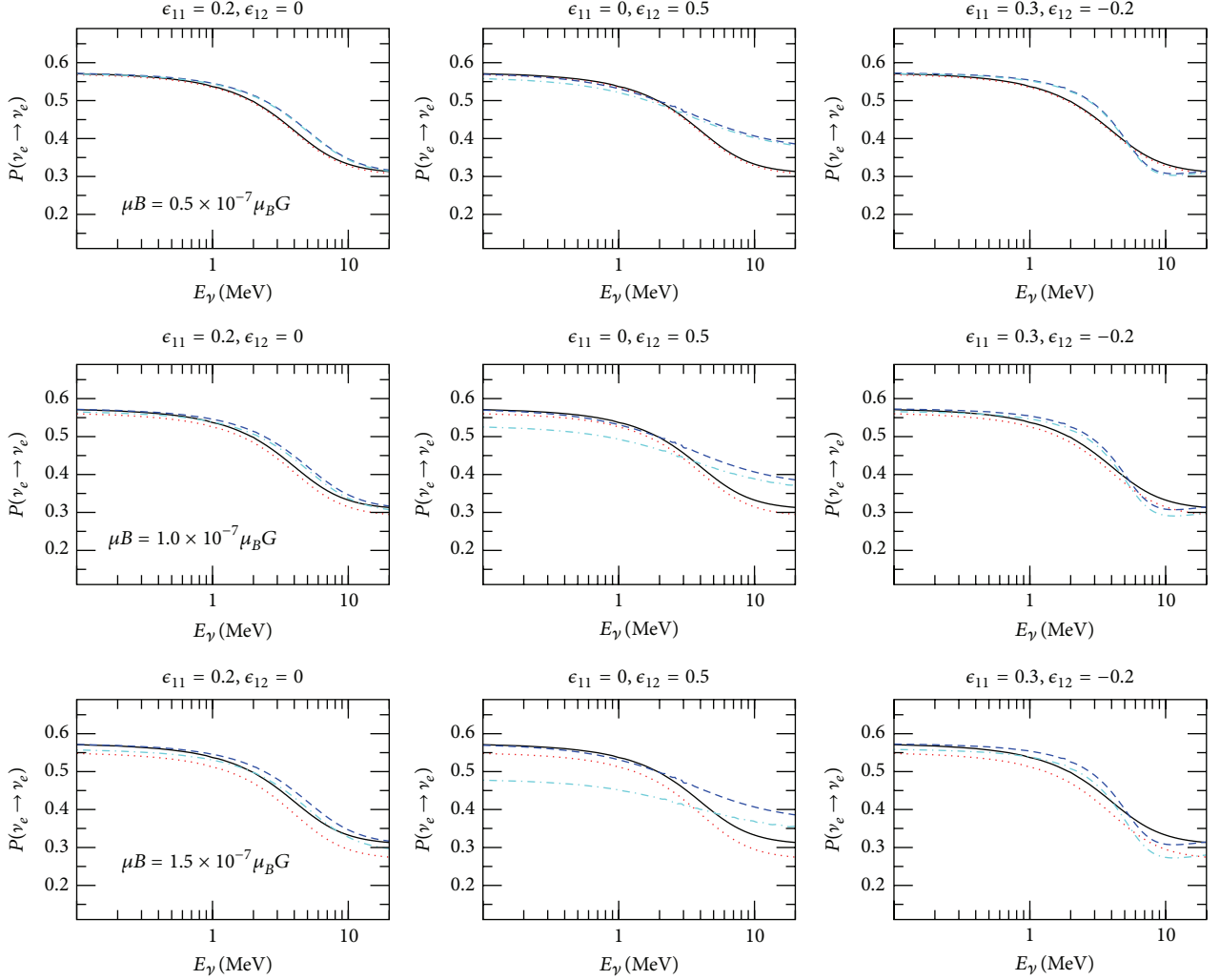


FIGURE 2: Survival probabilities for MSW-LMA prediction alone (solid lines), SFP effect at different  $\mu B$  values (dotted lines), NSI effect alone (dashed lines), and the combined effect of the NSI and SFP (dotted-dashed lines). Each column uses the same  $\epsilon_{11}$  and  $\epsilon_{12}$  values, and each row uses the same  $\mu B$  values.

matter:  $\epsilon_{\alpha\beta} = \sum_{f=e,u,d} \epsilon_{\alpha\beta}^f N_f / N_e$ . Then, the three-flavor NSI Hamiltonian can be written as

$$H_{\text{NSI}}^{3 \times 3} = V_c \begin{pmatrix} \epsilon_{ee} & \epsilon_{e\mu}^* & \epsilon_{e\tau}^* \\ \epsilon_{e\mu} & \epsilon_{\mu\mu} & \epsilon_{\mu\tau}^* \\ \epsilon_{e\tau} & \epsilon_{\mu\tau} & \epsilon_{\tau\tau} \end{pmatrix}. \quad (7)$$

After performing a rotation to  $H_{\text{NSI}}^{3 \times 3}$  by using the two factors of the neutrino mixing matrix,  $T_{13}^\dagger T_{23}$ ,

$$T_{13}^\dagger T_{23}^\dagger H_{\text{NSI}}^{3 \times 3} T_{13} T_{23}, \quad (8)$$

and decoupling the third flavor as in the standard three-flavor neutrino oscillation calculations, one can find the  $2 \times 2$  neutrino nonstandard interaction (NSI) part in (2) as

$$H_{\text{NSI}} = V_c \begin{pmatrix} 0 & \epsilon_{12}^* \\ \epsilon_{12} & \epsilon_{11} \end{pmatrix}, \quad (9)$$

where  $\epsilon_{11}$  and  $\epsilon_{12}$  are the contributions from the new physics related to the original vectorial couplings,  $\epsilon_{\alpha\beta}$ , given as

$$\begin{aligned} \epsilon_{11} &= \epsilon_{\mu\mu} c_{23}^2 - (\epsilon_{\mu\tau} + \epsilon_{\mu\tau}^*) s_{23} c_{23} + \epsilon_{\tau\tau} s_{23}^2 - \epsilon_{ee} c_{13}^2 \\ &+ s_{13} [(e^{-i\delta} \epsilon_{e\mu} + e^{i\delta} \epsilon_{e\mu}^*) c_{13} s_{23} \\ &+ (e^{-i\delta} \epsilon_{e\tau} + e^{i\delta} \epsilon_{e\tau}^*) c_{13} c_{23}] - s_{13}^2 [(\epsilon_{\mu\tau} + \epsilon_{\mu\tau}^*) s_{23} c_{23} \\ &+ \epsilon_{\mu\mu} s_{23}^2 + \epsilon_{\tau\tau} c_{23}^2], \\ \epsilon_{12} &= c_{13} (\epsilon_{e\mu} c_{23} - \epsilon_{e\tau} s_{23}) + s_{13} e^{i\delta} [\epsilon_{\mu\tau} s_{23}^2 - \epsilon_{\mu\tau}^* c_{23}^2 \\ &- (\epsilon_{\mu\mu} - \epsilon_{\tau\tau}) s_{23} c_{23}]. \end{aligned} \quad (10)$$

Here  $c_{ij} = \cos \theta_{ij}$  and  $s_{ij} = \sin \theta_{ij}$  and  $\delta$  is the CP-violating phase that we will ignore in our discussion [54].

The direct bounds on the NSI parameters come from atmospheric neutrino experiments (Super-Kamiokande,

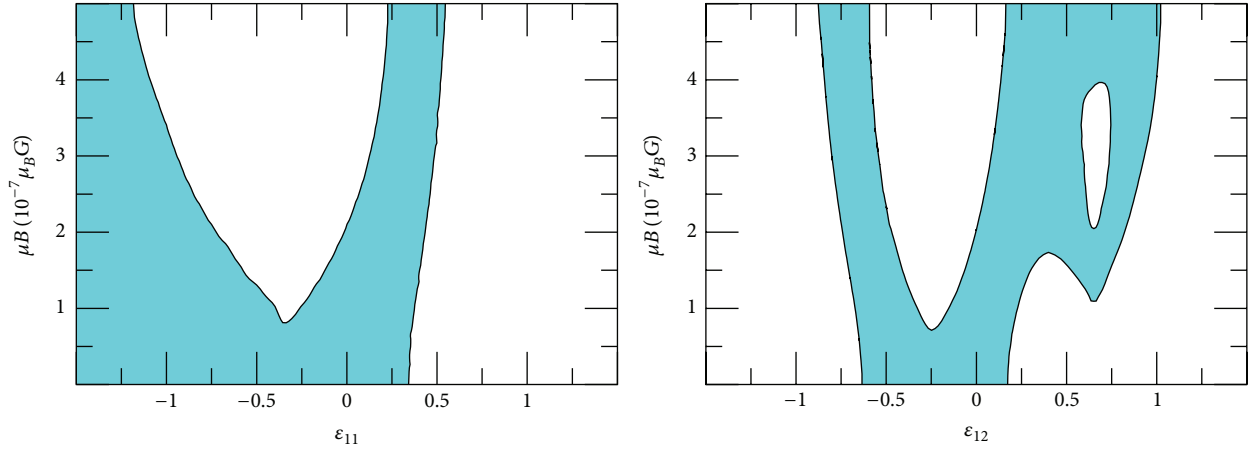


FIGURE 3: Allowed regions in the  $(\epsilon_{11}, \mu B)$  and  $(\epsilon_{12}, \mu B)$  planes at 90% CL for 10 MeV neutrino energy.

Ice-Cube-79) [62, 63], accelerator neutrino experiments (MINOS) [64], and some phenomenological studies [65–68]:  $|\epsilon_{ee}| \leq 0.5$  [62],  $|\epsilon_{e\tau}| \leq 0.5$  [62],  $|\epsilon_{\mu\tau}| \leq 6 \times 10^{-3}$  [63],  $|\epsilon_{\tau\tau} - \epsilon_{\mu\mu}| \leq 3 \times 10^{-2}$  [63],  $-0.067 \leq \epsilon_{\mu\tau} \leq 0.023$  [64]. The effects of NSI were also studied by using data of reactor neutrino experiment, Daya Bay, [69] and solar neutrino experiments [70]. Detailed analysis on the nonstandard interactions and their limits is given in [71, 72].

### 3. Results and Conclusions

In this analysis the combined effect of the nonstandard neutrino interaction and SFP on the survival probability of solar electron neutrinos (assumed to be Dirac particles) is examined for various values of  $\epsilon_{11}$ ,  $\epsilon_{12}$ , and  $\mu B$ . Results presented here are obtained numerically by diagonalizing the Hamiltonian in (2). In the calculations, the magnetic field profile given in Figure 1 is chosen as a Gaussian shape extending over the entire Sun [46] and the MSW-LMA best fit values are used:  $\delta m_{12}^2 = 7.54 \times 10^{-5} \text{ eV}^2$  and  $\sin^2 \theta_{12} = 0.308$  [57].

Electron neutrino survival probabilities plotted as a function of neutrino energy are shown in Figure 2 for all situations: MSW-LMA prediction alone (solid lines), SFP alone (dotted lines), MSW-LMA + NSI (dashed lines), and SFP + NSI (dotted-dashed lines). In this figure, different from the SFP effect seen for all neutrino energies, the new physics effects change the standard MSW-LMA curve especially at the energies of  $E \gtrsim 1 \text{ MeV}$  in which the region of  $E \gtrsim 3.5 \text{ MeV}$  is well examined by the solar neutrino experiments SNO and SK. When the combined effect of them (SFP + NSI) is considered, the curves get closer to the standard curve than the curves affected by them individually for some values of the parameters ( $\epsilon_{11}$ ,  $\epsilon_{12}$ , and  $\mu B$ ). A similar result was found in another analysis examined for Majorana neutrinos for only one NSI parameter,  $\epsilon_{12}$  [58]. However, compared to the Dirac case presented here, SFP effect is seen at almost ten times larger  $\mu B$  values in the Majorana case.

The allowed regions obtained by using the SNO results [73] are shown in Figure 3 in the  $(\epsilon_{11}, \mu B)$  and  $(\epsilon_{12}, \mu B)$  planes at 90% CL for 10 MeV neutrino energy. Even though

the values of NSI parameters are expected to be very small ( $\leq 10^{-2}$ ), the large values of them are in the allowed regions when considering the SFP and NSI effects together. It is seen that the current solar neutrino data constrain the  $\mu B$  and  $(\epsilon_{11}, \epsilon_{12})$  values poorly. A practical limit on them can be expected from the data obtained by the new low energy ( $1 \text{ MeV} \leq E \leq 4 \text{ MeV}$ ) solar neutrino experiments such as SNO+ [74] probing the evidence of new physics effect. However, as it can be seen from the analysis presented here, the combined effect of SFP and NSI needs to be taken into account when the solar electron neutrino data obtained by new solar neutrino experiments is analyzed.

### Competing Interests

The author declares that there is no conflict of interests regarding the publication of this paper.

### References

- [1] K. Eguchi, S. Enomoto, K. Furuno et al., “First results from KamLAND: evidence for reactor antineutrino disappearance,” *Physical Review Letters*, vol. 90, Article ID 021802, 2003.
- [2] T. Araki, K. Eguchi, S. Enomoto et al., “Measurement of neutrino oscillation with KamLAND: evidence of spectral distortion,” *Physical Review Letters*, vol. 94, no. 8, Article ID 081801, 2005.
- [3] Q. R. Ahmad, R. C. Allen, T. C. Andersen et al., “Measurement of the rate of  $\nu_e + d \rightarrow p + p + e^-$  interactions produced by  $^8\text{B}$  solar neutrinos at the sudbury neutrino observatory,” *Physical Review Letters*, vol. 87, no. 7, Article ID 071301, 2001.
- [4] B. Aharmim, Q. R. Ahmad, S. N. Ahmed et al., “Determination of the  $\nu_e$  and total  $^8\text{B}$  solar neutrino fluxes using the Sudbury Neutrino Observatory Phase I data set,” *Physical Review C*, vol. 75, Article ID 045502, 2007.
- [5] S. Fukuda, Y. Fukuda, M. Ishitsuka et al., “Solar  $^8\text{B}$  and hep neutrino measurements from 1258 days of super-kamiokande data,” *Physical Review Letters*, vol. 86, no. 25, p. 5651, 2001.

- [6] S. Fukuda, Y. Fukuda, M. Ishitsuka et al., "Determination of solar neutrino oscillation parameters using 1496 days of Super-Kamiokande-I data," *Physics Letters B*, vol. 539, no. 3-4, pp. 179–187, 2002.
- [7] B. T. Cleveland, T. Daily, R. Davis Jr. et al., "Measurement of the solar electron neutrino flux with the homestake chlorine detector," *The Astrophysical Journal*, vol. 496, no. 1, p. 505, 1998.
- [8] J. N. Abdurashitov, T. J. Bowles, M. L. Cherry et al., "Measurement of the solar neutrino capture rate by sage and implications for neutrino oscillations in vacuum," *Physical Review Letters*, vol. 83, no. 23, p. 4686, 1999.
- [9] W. Hampel, J. Handt, G. Heusser et al., "GALLEX solar neutrino observations: results for GALLEX IV," *Physics Letters B*, vol. 447, no. 1-2, pp. 127–133, 1999.
- [10] M. Altmann, M. Balata, P. Belli et al., "GNO solar neutrino observations: results for GNO I," *Physics Letters B*, vol. 490, no. 1-2, pp. 16–26, 2000.
- [11] A. B. Balantekin and H. Yuksel, "Global analysis of solar neutrino and KamLAND data," *Journal of Physics G: Nuclear and Particle Physics*, vol. 29, no. 4, p. 665, 2003.
- [12] J. N. Bahcall and C. Pena-Garay, "A road map to solar neutrino fluxes, neutrino oscillation parameters, and tests for new physics," *Journal of High Energy Physics*, vol. 2003, no. 11, p. 4, 2003.
- [13] M. C. Gonzalez-Garcia and C. Peña-Garay, "Three-neutrino mixing after the first results from K2K and KamLAND," *Physical Review D*, vol. 68, no. 9, Article ID 093003, 2003.
- [14] P. C. de Holanda and A. Y. Smirnov, "Homestake result, sterile neutrinos, and low energy solar neutrino experiments," *Physical Review D*, vol. 69, no. 11, Article ID 113002, 2004.
- [15] G. L. Fogli, E. Lisi, A. Marrone, and A. Palazzo, "Evidence for Mikheyev-Smirnov-Wolfenstein effects in solar neutrino flavor transitions," *Physics Letters B*, vol. 583, no. 1-2, pp. 149–156, 2004.
- [16] J. N. Bahcall, M. C. Gonzalez-Garcia, and C. Pena-Garay, "Solar neutrinos before and after neutrino 2004," *Journal of High Energy Physics*, vol. 2004, no. 8, article 016, 2004.
- [17] W. J. Marciano and A. I. Sanda, "Exotic decays of the muon and heavy leptons in gauge theories," *Physics Letters B*, vol. 67, no. 3, pp. 303–305, 1977.
- [18] J. Schechter and J. W. F. Valle, "Majorana neutrinos and magnetic fields," *Physical Review D*, vol. 24, no. 7, p. 1883, 1981, Erratum: *Physical Review D*, vol. 25, pp. 283, 1982.
- [19] R. E. Shrock, "Electromagnetic properties and decays of Dirac and Majorana neutrinos in a general class of gauge theories," *Nuclear Physics B*, vol. 206, no. 3, pp. 359–379, 1982.
- [20] L. B. Okun, M. B. Voloshin, and M. I. Vysotsky, "Electromagnetic properties of neutrino and possible semiannual variation cycle of the solar neutrino flux," *Soviet Journal of Nuclear Physics*, vol. 44, p. 440, 1986, *Yadernaya Fizika*, vol. 44, pp. 677–680, 1986.
- [21] E. K. Akhmedov, "Resonant amplification of neutrino spin rotation in matter and the solar-neutrino problem," *Physics Letters B*, vol. 213, no. 1, pp. 64–68, 1988.
- [22] E. K. Akhmedov and M. Y. Khlopov, "Resonant amplification of neutrino oscillations in longitudinal magnetic field," *Modern Physics Letters A*, vol. 3, no. 5, pp. 451–457, 1988.
- [23] R. Barbieri and G. Fiorentini, "The solar neutrino puzzle and the  $\nu_L \rightarrow \nu_R$  conversion hypothesis," *Nuclear Physics B*, vol. 304, pp. 909–920, 1988.
- [24] C.-S. Lim and W. J. Marciano, "Resonant spin-flavor precession of solar and supernova neutrinos," *Physical Review D*, vol. 37, no. 6, pp. 1368–1373, 1988.
- [25] A. B. Balantekin, P. J. Hatchell, and F. Loreti, "Matter-enhanced spin-flavor precession of solar neutrinos with transition magnetic moments," *Physical Review D*, vol. 41, no. 12, pp. 3583–3593, 1990.
- [26] A. A. Bykov, V. Y. Popov, T. I. Rashba, and V. B. Semikoz, "Resonant spin-flavor precession solution to the solar neutrino problem and electron antineutrinos from the sun," <http://arxiv.org/abs/hep-ph/0002174>.
- [27] E. K. Akhmedov and J. Pulido, "Solar neutrino oscillations and bounds on neutrino magnetic moment and solar magnetic field," *Physics Letters B*, vol. 553, no. 1-2, pp. 7–17, 2003.
- [28] B. C. Chauhan, J. Pulido, and E. Torrente-Lujan, "KamLAND, solar antineutrinos, and the solar magnetic field," *Physical Review D*, vol. 68, no. 3, Article ID 033015, 2003.
- [29] A. B. Balantekin and C. Volpe, "Does the neutrino magnetic moment have an impact on solar neutrino physics?" *Physical Review D*, vol. 72, no. 3, Article ID 033008, 2005.
- [30] D. Yilmaz and A. U. Yilmazer, "Global analysis of the data from solar neutrinos having transition magnetic moments together with KamLAND," *Journal of Physics G: Nuclear and Particle Physics*, vol. 31, no. 1, p. 57, 2005.
- [31] D. Yilmaz and A. U. Yilmazer, "Global analysis of solar neutrinos (assumed to be Majorana particles) together with the new KamLAND data," *Journal of Physics G*, vol. 31, pp. 1123–1131, 2005.
- [32] G. G. Raffelt, "New bound on neutrino dipole moments from globular-cluster stars," *Physical Review Letters*, vol. 64, no. 24, pp. 2856–2858, 1990.
- [33] J. M. Lattimer and J. Cooperstein, "Limits on the neutrino magnetic moment from SN1987A," *Physical Review Letters*, vol. 61, no. 1, pp. 23–26, 1988.
- [34] R. Barbieri and R. N. Mohapatra, "Limit on the magnetic moment of the neutrino from supernova 1987a observations," *Physical Review Letters*, vol. 61, no. 1, pp. 27–30, 1988.
- [35] D. W. Liu, Y. Ashie, S. Fukuda et al., "Limits on the neutrino magnetic moment using 1496 days of super-kamiokande-i solar neutrino data," *Physical Review Letters*, vol. 93, no. 2, Article ID 021802, 2004.
- [36] H. T. Wong, H. B. Li, S. T. Lin et al., "Search of neutrino magnetic moments with a high-purity germanium detector at the Kuo-Sheng nuclear power station," *Physical Review D*, vol. 75, no. 1, Article ID 012001, 2007.
- [37] Z. Daraktchieva, C. Amsler, M. Avenier et al., "Final results on the neutrino magnetic moment from the MUNU experiment," *Physics Letters B*, vol. 615, no. 3-4, pp. 153–159, 2005.
- [38] A. G. Beda, V. B. Brudanin, V. G. Egorov et al., "Gemma experiment: the results of neutrino magnetic moment search," *Physics of Particles and Nuclei Letters*, vol. 10, no. 2, pp. 139–143, 2013.
- [39] D. K. Papoulias and T. S. Kosmas, "Neutrino transition magnetic moments within the non-standard neutrino-nucleus interactions," *Physics Letters B*, vol. 747, pp. 454–459, 2015.
- [40] J. F. Beacom and P. Vogel, "Neutrino magnetic moments, flavor mixing, and the Super-Kamiokande solar data," *Physical Review Letters*, vol. 83, no. 25, pp. 5222–5225, 1999.
- [41] N. F. Bell, V. Cirigliano, M. J. Ramsey-Musolf, P. Vogel, and M. B. Wise, "Magnetic moments of Dirac neutrinos," *AIP Conference Proceedings*, vol. 842, no. 1, pp. 874–876, 2006.
- [42] M. Gorchtein, N. F. Bell, M. J. Ramsey-Musolf, P. Vogel, and P. Wang, "Model independent naturalness bounds on magnetic moments of Majorana neutrinos," *AIP Conference Proceedings*, vol. 903, no. 1, pp. 287–290, 2007.

- [43] A. B. Balantekin, "Neutrino magnetic moment," in *Proceedings of the Origin of Matter and Evolution of Galaxies: International Symposium on Origin of Matter and Evolution of Galaxies 2005: New Horizon of Nuclear Astrophysics and Cosmology*, vol. 847 of *AIP Conference Proceedings*, p. 128, Tokyo, Japan, November 2005.
- [44] A. Studenikin, "Neutrino magnetic moment: a window to new physics," *Nuclear Physics B—Proceedings Supplements*, vol. 188, pp. 220–222, 2009.
- [45] C. Broggin, C. Giunti, and A. Studenikin, "Electromagnetic properties of neutrinos," *Advances in High Energy Physics*, vol. 2012, Article ID 459526, 47 pages, 2012.
- [46] C. R. Das, J. Pulido, and M. Picariello, "Light sterile neutrinos, spin flavor precession, and the solar neutrino experiments," *Physical Review D*, vol. 79, no. 7, Article ID 073010, 9 pages, 2009.
- [47] S. Couvidat, S. Turck-Chièze, and A. G. Kosovichev, "Solar seismic models and the neutrino predictions," *Astrophysical Journal*, vol. 599, no. 2, pp. 1434–1448, 2003.
- [48] J. N. Bahcall and M. H. Pinsonneault, "What do we (not) know theoretically about solar neutrino fluxes?" *Physical Review Letters*, vol. 92, no. 12, Article ID 121301, 4 pages, 2004.
- [49] H. M. Antia, S. M. Chitre, and M. J. Thompson, "The Sun's acoustic asphericity and magnetic fields in the solar convection zone," *Astronomy and Astrophysics*, vol. 360, pp. 335–344, 2000.
- [50] A. Friedland, C. Lunardini, and C. Peña-Garay, "Solar neutrinos as probes of neutrino-matter interactions," *Physics Letters B*, vol. 594, no. 3–4, pp. 347–354, 2004.
- [51] M. Cirelli, M. C. Gonzalez-Garcia, and C. Peña-Garay, "Mass varying neutrinos in the Sun," *Nuclear Physics B*, vol. 719, no. 1–2, pp. 219–233, 2005.
- [52] V. Barger, P. Huber, and D. Marfatia, "Solar mass-varying neutrino oscillations," *Physical Review Letters*, vol. 95, no. 21, Article ID 211802, 4 pages, 2005.
- [53] M. C. Gonzalez-Garcia, P. C. de Holanda, E. Massó, and R. Zukanovich Funchal, "Probing long-range leptonic forces with solar and reactor neutrinos," *Journal of Cosmology and Astroparticle Physics*, vol. 2007, no. 1, article 005, 2007.
- [54] R. Bonventre, A. Latorre, J. R. Klein, G. D. Orebi Gann, S. Seibert, and O. Wasalski, "Nonstandard models, solar neutrinos, and large  $\theta_{13}$ ," *Physical Review D*, vol. 88, no. 5, Article ID 053010, 2013.
- [55] A. Palazzo and D. Phys. Rev., *Phys. Rev. D*, vol. 83, Article ID 101701, 2011, arXiv:1101.3875.
- [56] A. B. Balantekin and A. Malkus, "Solar neutrino matter effects redux," *Physical Review D*, vol. 85, no. 1, Article ID 013010, 9 pages, 2012.
- [57] K. A. Olive, K. Agashe, C. Amsler et al., "Review of particle physics," *Chinese Physics C*, vol. 38, no. 9, Article ID 090001, 2014.
- [58] D. Yilmaz, "SFP effect on Majorana type solar neutrinos in the presence of nonstandard neutrino interactions," *Turkish Journal of Physics*, vol. 39, pp. 309–313, 2015.
- [59] L. Wolfenstein, "Neutrino oscillations in matter," *Physical Review D*, vol. 17, no. 9, pp. 2369–2374, 1978.
- [60] S. P. Mikheev and A. Yu. Smirnov, "Resonance amplification of oscillations in matter and spectroscopy of solar neutrinos," *Soviet Journal of Nuclear Physics*, vol. 42, pp. 913–917, 1985, Translated from *Yadernaya Fizika*, vol. 42, pp. 1441–1448, 1985.
- [61] S. P. Mikheyev and A. Yu. Smirnov, "Resonant amplification of  $\nu$  oscillations in matter and solar-neutrino spectroscopy," *Il Nuovo Cimento C*, vol. 9, no. 1, pp. 17–26, 1986.
- [62] G. Mitsuka, K. Abe, Y. Hayato et al., "Study of nonstandard neutrino interactions with atmospheric neutrino data in Super-Kamiokande I and II," *Physical Review D*, vol. 84, no. 11, Article ID 113008, 2011.
- [63] A. Groß and IceCube Collaboration, "Atmospheric neutrino oscillations in IceCube," *Nuclear Physics B—Proceedings Supplements*, vol. 237–238, pp. 272–274, 2013.
- [64] P. Adamson, G. Barr, M. Bishai et al., "Search for flavor-changing non-standard neutrino interactions by MINOS," *Physical Review D*, vol. 88, no. 7, Article ID 072011, 6 pages, 2013.
- [65] S. Davidson, C. Pena-Garay, N. Rius, and A. Santamaria, "Present and future bounds on non-standard neutrino interactions," *Journal of High Energy Physics*, vol. 2003, no. 3, p. 11, 2003.
- [66] C. Biggio, M. Blennow, and E. Fernandez-Martinez, "Loop bounds on non-standard neutrino interactions," *Journal of High Energy Physics*, vol. 2009, no. 3, p. 139, 2009.
- [67] D. K. Papoulias and T. S. Kosmas, "Nuclear aspects of neutral current non-standard  $\nu$ -nucleus reactions and the role of the exotic  $\mu^- \rightarrow e^-$  transitions experimental limits," *Physics Letters B*, vol. 728, pp. 482–488, 2014.
- [68] R. Leitner, M. Malinsky, B. Roskovec, and H. Zhang, "Non-standard antineutrino interactions at Daya Bay," *Journal of High Energy Physics*, vol. 2011, article 1, 2011.
- [69] I. Girardi, D. Meloni, and S. T. Petcov, "The Daya Bay and T2K results on  $\sin^2 2\theta_{13}$  and non-standard neutrino interactions," *Nuclear Physics B*, vol. 886, pp. 31–42, 2014.
- [70] M. C. Gonzalez-Garcia and M. Maltoni, "Determination of matter potential from global analysis of neutrino oscillation data," *Journal of High Energy Physics*, vol. 2013, article 152, 2013.
- [71] O. G. Miranda and H. Nunokawa, "Non standard neutrino interactions: current status and future prospects," *New Journal of Physics*, vol. 17, no. 9, Article ID 095002, 2015.
- [72] T. Ohlsson, "Status of non-standard neutrino interactions," *Reports on Progress in Physics*, vol. 76, no. 4, Article ID 044201, 2013.
- [73] B. Aharmim, S. N. Ahmed, A. E. Anthony et al., "Combined analysis of all three phases of solar neutrino data from the Sudbury Neutrino Observatory," *Physical Review C*, vol. 88, no. 2, Article ID 025501, 27 pages, 2013.
- [74] C. Kraus and S. J. M. Peetersa, "The rich neutrino programme of the SNO+ experiment," *Progress in Particle and Nuclear Physics*, vol. 64, no. 2, pp. 273–277, 2010.

## Research Article

# Magnetic Hexadecapole $\gamma$ Transitions and Neutrino-Nuclear Responses in Medium-Heavy Nuclei

Lotta Jokiniemi,<sup>1</sup> Jouni Suhonen,<sup>1</sup> and Hiroyasu Ejiri<sup>2</sup>

<sup>1</sup>Department of Physics, University of Jyväskylä, P.O. Box 35, 40014 Jyväskylä, Finland

<sup>2</sup>Research Center for Nuclear Physics, Osaka University, Osaka 567-0047, Japan

Correspondence should be addressed to Jouni Suhonen; [jouni.suhonen@phys.jyu.fi](mailto:jouni.suhonen@phys.jyu.fi)

Received 17 March 2016; Accepted 14 April 2016

Academic Editor: Enrico Lunghi

Copyright © 2016 Lotta Jokiniemi et al. This is an open access article distributed under the Creative Commons Attribution License, which permits unrestricted use, distribution, and reproduction in any medium, provided the original work is properly cited. The publication of this article was funded by SCOAP<sup>3</sup>.

Neutrino-nuclear responses in the form of squares of nuclear matrix elements, NMEs, are crucial for studies of neutrino-induced processes in nuclei. In this work we investigate magnetic hexadecapole (M4) NMEs in medium-heavy nuclei. The experimentally derived NMEs,  $M_{\text{EXP}}(\text{M4})$ , deduced from observed M4  $\gamma$  transition half-lives are compared with the single-quasiparticle (QP) NMEs,  $M_{\text{QP}}(\text{M4})$ , and the microscopic quasiparticle-phonon model (MQPM) NMEs  $M_{\text{MQPM}}(\text{M4})$ . The experimentally derived M4 NMEs are found to be reduced by a coefficient  $k \approx 0.29$  with respect to  $M_{\text{QP}}(\text{M4})$  and by  $k \approx 0.33$  with respect to  $M_{\text{MQPM}}(\text{M4})$ . The M4 NMEs are reduced a little by the quasiparticle-phonon correlations of the MQPM wave functions but mainly by other nucleonic and nonnucleonic correlations which are not explicitly included in the MQPM. The found reduction rates are of the same order of magnitude as those for magnetic quadrupole  $\gamma$  transitions and Gamow-Teller (GT) and spin-dipole (SD)  $\beta$  transitions. The impacts of the found reduction coefficients on the magnitudes of the NMEs involved in astroneutrino interactions and neutrinoless double beta decays are discussed.

## 1. Introduction

Neutrino interactions in nuclei are studied, for example, by investigating scatterings of astroneutrinos on nuclei and by the attempts to record the neutrinoless double beta ( $0\nu\beta\beta$ ) decays. Here the neutrino-nuclear responses can be condensed in the squares of nuclear matrix elements (NMEs) and it is necessary to study through them the neutrino properties and astroneutrino reactions that are of interest to particle physics and astrophysics, as discussed in review articles [1–4] and references therein.

The present work aims at investigating the magnetic hexadecapole (M4)  $\gamma$  NMEs,  $M_\gamma(\text{M4})$ , in medium-heavy nuclei to study higher-multipole axial-vector NMEs associated with higher-energy components of astroneutrino reactions and  $0\nu\beta\beta$  decays. Such components are shown to be important for, for example, the  $0\nu\beta\beta$  decays [5].

Neutrino-nuclear responses associated with neutral-current (NC) and charged-current (CC) interactions are studied by investigating the relevant  $\gamma$  and  $\beta$  decay transitions or

NC and CC scatterings on nuclei. The momenta involved in astroneutrino scatterings and  $0\nu\beta\beta$  decays are of the order of 50–100 MeV/c. Accordingly, depending on the involved momentum exchanges, the multipoles  $J^\pi$  with angular momenta  $J$  up to around 4–5 are involved (e.g.,  $0\nu\beta\beta$  decays mediated by light Majorana neutrinos; see [5]), or even higher multipoles can be engaged ( $0\nu\beta\beta$  decays mediated by heavy Majorana neutrinos; see [5]).

In some previous works, axial-vector CC resonances of GT( $1^+$ ) and SD( $2^-$ ) NMEs for allowed and first-forbidden  $\beta$  transitions are shown to be reduced much in comparison with the quasiparticle (QP) and pnQRPA (proton-neutron quasiparticle random-phase approximation) NMEs [6–10] due to spin-isospin ( $\sigma\tau$ ) nucleonic and nonnucleonic correlations and nuclear-medium effects. These studies show that exact theoretical evaluations for the astroneutrino and  $0\nu\beta\beta$  NMEs, including possible renormalization of the axial-vector coupling constant  $g_A$ , are hard. The corresponding NC nuclear responses of magnetic dipole (M1) and quadrupole

(M2)  $\gamma$  transitions are also known to be much reduced with respect to the QP NMEs [11]. Similar studies have been conducted in the case of the two-neutrino double beta decays in [12, 13] in the framework of the IBA-2 model. Also the derivation of effective operators has been proposed [14]. All these studies bear relevance to the previously mentioned Majorana-neutrino mediated  $0\nu\beta\beta$  decays, to high-energy astroneutrino reactions, but also to the lower-energy (up to 30 MeV) supernova-neutrino scatterings off nuclei, as shown, for example, in [15–18].

In the light of the above discussions it is of great interest to investigate the spin-hexadecapole ( $4^-$ ) NMEs to see how the higher-multipole NMEs are reduced by the nucleonic and nonnucleonic spin-isospin correlations. Actually, there are almost no experimental CC hexadecapole  $\beta$  NMEs in medium-heavy nuclei since the  $\beta$  decays are very rare third-forbidden unique transitions. However, it turns out that there are few measurements of the half-lives and electron spectra of the more complex fourth-forbidden nonunique  $\beta$  transitions and they can serve as potential testing grounds concerning the quenching effects of the weak vector ( $g_V$ ) and axial-vector ( $g_A$ ) coupling constants [19]. On the other hand, there are many experimental data on NC M4  $\gamma$  NMEs, where the isovector component of the  $\gamma$  NME is related to the analogous  $\beta$  NME on the basis of the isospin symmetry. Thus we discuss mainly the M4  $\gamma$  transitions in the present report with the aim of helping evaluate/confirm, for example, the  $0\nu\beta\beta$  NMEs concerning their higher-multipole aspects.

## 2. Experimental M4 NMEs

Here we discuss stretched M4  $\gamma$  transitions with  $J_i = J_f \pm J$ , where  $J_i$  and  $J_f$  are the initial and final state spins and  $J = 4$ . The M4  $\gamma$  transition rate (per sec) is given in terms of the reduced M4  $\gamma$  strength  $B_\gamma(M4)$  as [20]

$$T(M4) = 1.87 \times 10^{-6} E^9 B_\gamma(M4) (1 + \alpha)^{-1}, \quad (1)$$

where  $E$  is the  $\gamma$  ray energy in units of MeV and  $\alpha$  is the conversion-electron coefficient. The reduced strength is expressed in terms of the M4  $\gamma$  NME in units of  $e\hbar/(2Mc) \text{ fm}^3$  as

$$B_\gamma(M4) = (2J_i + 1)^{-1} [M_\gamma(M4)]^2. \quad (2)$$

The M4  $\gamma$  NME is expressed in terms of the M4  $\gamma$  coupling constants  $g(M4)$  and the M4 matrix element  $M(M4)$  as

$$M_\gamma(M4) = g_p(M4) \tau_p M(M4) + g_n(M4) \tau_n M(M4), \quad (3)$$

where the first and the second terms are for the odd-proton ( $\tau_p = (1 - \tau_3)/2$ ) and odd-neutron ( $\tau_n = (1 + \tau_3)/2$ ) transition NMEs with  $\tau_3$  being the isospin  $z$  component ( $\tau_3 = 1$  for neutron and  $\tau_3 = -1$  for proton). The  $\gamma$  coupling constant is written as

$$g_i(M4) = \frac{e\hbar}{2Mc} 6 \left( \mu_i - \frac{1}{5} g_i \right), \quad (4)$$

where  $i = p$  for proton and  $i = n$  for neutron,  $\mu_p = 2.79$  and  $\mu_n = -1.91$  are the proton and neutron magnetic moments,

TABLE 1:  $M(M4)$  NMEs for M4  $\gamma$  transitions in the mass region of  $A = 70$ – $120$ , where the major single-QP transition is  $1g_{9/2}$ - $2p_{1/2}$ . Here p/n stands for the odd-proton/odd-neutron transition.  $M_{\text{EXP}}$ ,  $M_{\text{QP}}$ , and  $M_{\text{MQPM}}$  are the experimental, single-QP, and MQPM NMEs in units of  $10^3 \text{ fm}^3$ .

Nucleus	Transition	p/n	$M_{\text{EXP}}$	$M_{\text{QP}}$	$M_{\text{MQPM}}$
<sup>85</sup> Kr	$2p_{1/2} \rightarrow 1g_{9/2}$	n	0.528	1.57	1.44
<sup>89</sup> Y	$2p_{1/2} \rightarrow 1g_{9/2}$	p	0.739	2.12	2.02
<sup>89</sup> Zr	$2p_{1/2} \rightarrow 1g_{9/2}$	n	0.559	1.60	1.47
<sup>91</sup> Y	$1g_{9/2} \rightarrow 2p_{1/2}$	p	0.480	2.13	1.83
<sup>105</sup> In	$2p_{1/2} \rightarrow 1g_{9/2}$	p	0.706	2.38	2.09
<sup>107</sup> In	$2p_{1/2} \rightarrow 1g_{9/2}$	p	0.670	2.40	2.13
<sup>109</sup> In	$2p_{1/2} \rightarrow 1g_{9/2}$	p	0.640	2.33	2.10
<sup>111</sup> In	$2p_{1/2} \rightarrow 1g_{9/2}$	p	0.609	2.45	2.03
<sup>113</sup> In	$2p_{1/2} \rightarrow 1g_{9/2}$	p	0.603	2.46	2.05
<sup>115</sup> In	$2p_{1/2} \rightarrow 1g_{9/2}$	p	0.614	2.48	2.03

TABLE 2: The same as Table 1 for  $A = 130$ – $150$ , where the major single-quasiparticle transition is  $1h_{11/2}$ - $2d_{3/2}$ .

Nucleus	Transition	p/n	$M_{\text{EXP}}$	$M_{\text{QP}}$	$M_{\text{MQPM}}$
<sup>135</sup> Xe	$1h_{11/2} \rightarrow 2d_{3/2}$	n	1.11	3.12	2.87
<sup>137</sup> Ba	$1h_{11/2} \rightarrow 2d_{3/2}$	n	1.03	3.13	2.77
<sup>139</sup> Ba	$1h_{11/2} \rightarrow 2d_{3/2}$	n	0.968	3.12	2.82
<sup>141</sup> Nd	$1h_{11/2} \rightarrow 2d_{3/2}$	n	0.893	3.17	2.79
<sup>143</sup> Sm	$1h_{11/2} \rightarrow 2d_{3/2}$	n	0.878	3.19	2.81

and  $g_{lp} = 1$  and  $g_{ln} = 0$  are the proton and neutron orbital  $g$  coefficients. The M4  $\gamma$  matrix element is expressed as

$$M(M4) = \langle f || i^3 r^3 [\sigma \times Y_3]_4 || i \rangle, \quad (5)$$

where  $r$  is the nuclear radius and  $Y_3$  is the spherical harmonic for multipole  $l = 3$ .

The isotopes used for ongoing and/or future  $\beta\beta$  experiments are <sup>76</sup>Ge, <sup>82</sup>Se, <sup>96</sup>Zr, <sup>100</sup>Mo, <sup>116</sup>Cd, <sup>130</sup>Te, and <sup>136</sup>Xe [2]. They are in the mass regions of  $A = 70$ – $120$  and  $A = 130$ – $150$ . The single-quasiparticle (single-QP) M4 transitions in these mass regions are uniquely tagged by the pairs  $1g_{9/2}$ - $2p_{1/2}$  and  $1h_{11/2}$ - $2d_{3/2}$ , respectively. Here the higher spin state is the intruder one from the higher major shell with opposite parity. The single-particle M4 NMEs corresponding to these tagging transitions are quite large because of the large radial and angular overlap integrals.

The single-quasiparticle M4  $\gamma$  transitions in the mentioned two mass regions are analyzed in Tables 1 and 2. The M4 NMEs derived from the experimental half-lives are given in the third column of these tables.

The values of  $M_{\text{EXP}}(M4)$  are plotted against the mass number in Figure 1. They are around  $(0.6 \pm 0.1) \times 10^3 \text{ fm}^3$  and  $(1.0 \pm 0.1) \times 10^3 \text{ fm}^3$  for the two mass regions, respectively. They are well expressed as

$$M_{\text{EXP}}(M4) \approx 6 \times A \text{ fm}^3, \quad (6)$$

where the mass number  $A$  reflects the  $r^3$  dependence of the M4 NME.

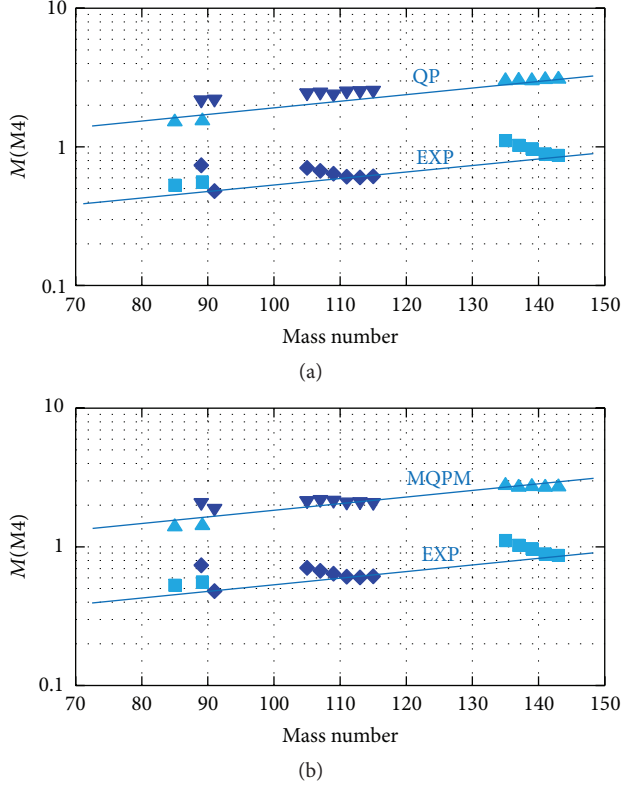


FIGURE 1: (a) EXP: experimental NMEs  $M_{\text{EXP}}(\text{M4})$  for odd-neutron transitions (light-blue squares) and odd-proton transitions (dark-blue diamonds). QP: quasiparticle NMEs  $M_{\text{QP}}(\text{M4})$  for odd-neutron transitions (light-blue tip-up triangles) and odd-proton transitions (dark-blue tip-down triangles). (b) EXP: experimental NMEs  $M_{\text{EXP}}(\text{M4})$  for odd-neutron transitions (light-blue squares) and odd-proton transitions (dark-blue diamonds). MQPM: NMEs  $M_{\text{MQPM}}(\text{M4})$  for odd-neutron transitions (light-blue tip-up triangles) and odd-proton transitions (dark-blue tip-down triangles).

### 3. Quasiparticle M4 NMEs

The M4  $\gamma$  transitions given in Tables 1 and 2 are all, in their simplest description, transitions between single-quasiparticle states. The NMEs for the single-quasiparticle transitions are written by using the single-particle matrix element  $M_{\text{SP}}(\text{M4})$  and the pairing coefficient  $P$  as

$$M_{\text{QP}}(\text{M4}) = M_{\text{SP}}(\text{M4}) P_{ij}, \quad (7)$$

where the pairing coefficient is given by

$$P_{ij} = U_i U_f + V_i V_f, \quad (8)$$

and  $U_i$  ( $U_f$ ) and  $V_i$  ( $V_f$ ) are the vacancy and occupation amplitudes for the initial (final) state. The single-quasiparticle states discussed here are low-lying states located at the diffused Fermi surface, as shown in Figure 2. Thus the occupation and vacancy probabilities are in the region of  $U^2 = 1 - V^2 = 0.5 \pm 0.3$ , and the pairing coefficient is given roughly as  $P \approx 1$ . In this work the single-quasiparticle NMEs  $M_{\text{QP}}(\text{M4})$  are calculated by using the BCS wave functions with HO

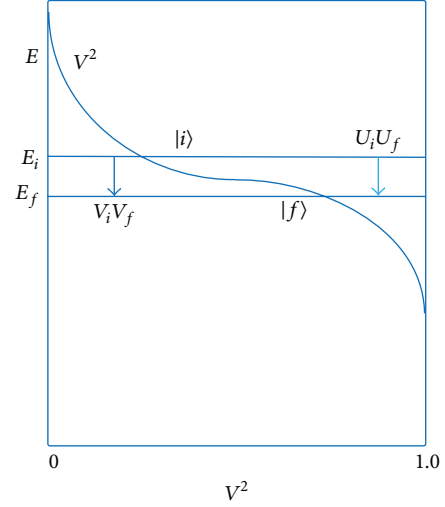


FIGURE 2: Schematic diagram of the energy ( $E$ ) and the occupation probabilities,  $V_i^2$  and  $V_f^2$ , for the initial and final states (see body of text). The energy levels are shown by the horizontal lines. Vacancy probabilities are given as  $U_i^2 = V_i^2 - 1$  and  $U_f^2 = V_f^2 - 1$ . The pairing coefficient  $P_{ij}$  for the  $\gamma$  transition is given by  $U_i U_f + V_i V_f$ .

single-particle states. They are given in the fifth column of Tables 1 and 2 and are plotted in Figure 1(a).

The experimental M4 matrix elements  $M_{\text{EXP}}(\text{M4})$  are uniformly smaller by a coefficient of around  $0.29 \pm 0.05$  than the single-quasiparticle ones,  $M_{\text{QP}}(\text{M4})$ . We introduce a reduction coefficient  $k_i$  as in the case of  $\text{GT}(1^+)$  and  $\text{SD}(2^-)$  [8, 10] transitions. It is defined as

$$M_{\text{EXP}}(\text{M4}) = k_i(\text{M4}) M_{\text{QP}}(\text{M4}), \quad (9)$$

where  $k_i$ , with  $i = p, n$ , are the reduction coefficients for single quasi-proton and quasi-neutron M4  $\gamma$  transitions, respectively. The ratios  $k_i(\text{M4})$  are  $k_p \approx 0.3$  and  $k_n \approx 0.3$ , as shown in Figure 3(a). The found reductions are consistent with the reductions discussed in [11].

The quasiparticle NMEs  $M_{\text{QP}}(\text{M4})$  are calculated by assuming a stretched M4 transition between the initial and final nuclear states (see column 2 of Tables 1 and 2) that are assumed to have a one-quasiparticle structure. These states are thus described as

$$|\alpha\rangle = a_\alpha^\dagger |\text{BCS}\rangle, \quad (10)$$

where  $a_\alpha^\dagger$  creates a quasiparticle on a nuclear mean-field orbital with quantum numbers  $\alpha = a, m_\alpha$ , where  $a$  contains the principal quantum number  $n$ , the orbital angular momentum ( $l$ ), and total angular momentum ( $j$ ) quantum numbers in the form  $nl_j$  as displayed in column 2 of Tables 1 and 2. Here  $m_\alpha$  is the  $z$  projection of the total angular momentum and  $|\text{BCS}\rangle$  is the BCS vacuum. The quasiparticles are defined by the Bogoliubov-Valatin transformation as

$$\begin{aligned} a_\alpha^\dagger &= U_a c_\alpha^\dagger + V_a \bar{c}_\alpha, \\ \bar{a}_\alpha &= U_a \bar{c}_\alpha - V_a c_\alpha^\dagger, \end{aligned} \quad (11)$$

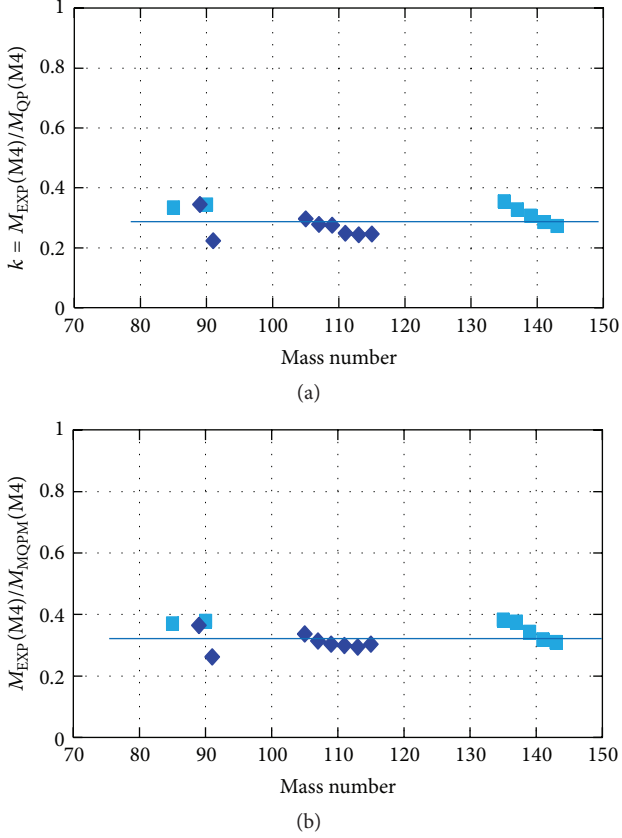


FIGURE 3: Reduction coefficients  $k$  for the M4 NMEs. (a)  $k$ : ratios of experimental NMEs  $M_{\text{EXP}}(\text{M4})$  to the quasiparticle NMEs  $M_{\text{QP}}(\text{M4})$  for odd-neutron transitions (light-blue squares) and odd-proton transitions (dark-blue diamonds). (b)  $k$ : ratios of experimental NMEs  $M_{\text{EXP}}(\text{M4})$  to the MQPM NMEs  $M_{\text{MQPM}}(\text{M4})$  for odd-neutron transitions (light-blue squares) and for odd-proton transitions (dark-blue diamonds).

where  $c_{\alpha}^{\dagger}$  is the particle creation operator and the time-reversed particle annihilation operator  $\tilde{c}_{\alpha}$  is defined by  $\tilde{c}_{\alpha} = (-1)^{j_{\alpha}+m_{\alpha}} c_{-\alpha}$  with  $-\alpha = (a, -m_{\alpha})$ . The  $U$  and  $V$  coefficients are the vacancy and occupation amplitudes present also in the quasiparticle matrix elements of (7) and (8). The values of these amplitudes are obtained in BCS calculations (for details see, e.g., [21]) and they are used also in the subsequent nuclear-structure calculations of the odd-mass nuclei and their neighboring even-even-mass reference nuclei.

#### 4. Microscopic Quasiparticle-Phonon Model for M4 NMEs

The microscopic quasiparticle-phonon model (MQPM) takes the structure of the nuclear states beyond the approximation (10). In the MQPM this extension is done in the traditional way of starting from an even-even reference nucleus where the states are described as QRPA (quasiparticle random-phase approximation) states called here phonons since the lowest ones are usually collective vibrational states. These states can be formally written as

$$|\omega\rangle = Q_{\omega}^{\dagger} |\text{QRPA}\rangle, \quad (12)$$

where the phonon operator  $Q_{\omega}^{\dagger}$  creates a nuclear state with quantum numbers  $\omega$ , containing the angular momentum  $J_{\omega}$ , parity  $\pi_{\omega}$ , and the quantum number  $k_{\omega}$  which enumerates states with the same angular momentum and parity. The state (12) is a linear combination of two-quasiparticle states as explicitly written in [22] where the MQPM was first introduced. To arrive at a state in the neighboring odd-mass nucleus one has to couple a proton (proton-odd nucleus) or a neutron (neutron-odd nucleus) quasiparticle to the phonon operator  $Q_{\omega}^{\dagger}$  which is a two-quasiparticle operator. In this way one creates three-quasiparticle states in the traditional quasiparticle-phonon coupling scheme and these states are then mixed with the one-quasiparticle states by the residual nuclear Hamiltonian (for details see [22]). Hence we obtain the MQPM states

$$|kjm\rangle = \Gamma_k^{\dagger}(jm) |\text{QRPA}\rangle, \quad (13)$$

where a  $k$ th state of angular momentum  $j$  and its  $z$  projection  $m$  is created in an odd-mass nucleus by a creation operator which mixes one-quasiparticle and three-quasiparticle components in the form

$$\Gamma_k^{\dagger}(jm) = \sum_n X_n^k a_{njm}^{\dagger} + \sum_{a\omega} X_{a\omega}^k [a_a^{\dagger} Q_{\omega}^{\dagger}]_{jm}, \quad (14)$$

where the first term is the one-quasiparticle contribution and the second term is the quasiparticle-phonon contribution. The amplitudes  $X_n^k$  and  $X_{a\omega}^k$  are computed from the MQPM equations of motion [22]. In solving these equations special care is to be taken to handle the overcompleteness and the nonorthogonality of the quasiparticle-phonon basis, as described in detail in [22].

In the actual calculations we used slightly modified Woods-Saxon single-particle energies to improve the quality of the computed energy spectra of the odd-mass nuclei involved in the present work. This resulted in a good correspondence between the computed and experimental low-energy spectra of these nuclei. We adopted a residual Hamiltonian with realistic effective two-nucleon interactions derived from the Bonn-A one-boson-exchange potential [23]. The free parameters of the interaction were fixed in the BCS and QRPA phases of the calculations as explained in [24, 25]. The two-body monopole matrix elements were multiplied by one parameter for protons and one for neutrons to scale phenomenologically the proton and neutron pairing strengths separately. This was done by fitting the computed pairing gaps to the phenomenological ones, derived from the measured proton and neutron separation energies [26]. The QRPA step contained two parameters for each multipole  $J^{\pi}$  to control the energies of the even-even excited states. These were the strengths of the particle-hole and particle-particle parts of the two-nucleon interaction. The particle-hole interaction controls the energies of collective states and thus it was fitted to reproduce the experimental excitation energy of the lowest state of a given multipolarity  $J^{\pi}$ , whenever data existed. When no data was available the bare  $G$ -matrix was used in the calculations. Also the particle-particle part of the multipole interaction was kept as bare  $G$ -matrix interaction.

After performing the BCS and QRPA calculations in the reference even-even nuclei, the initial and final nuclear states

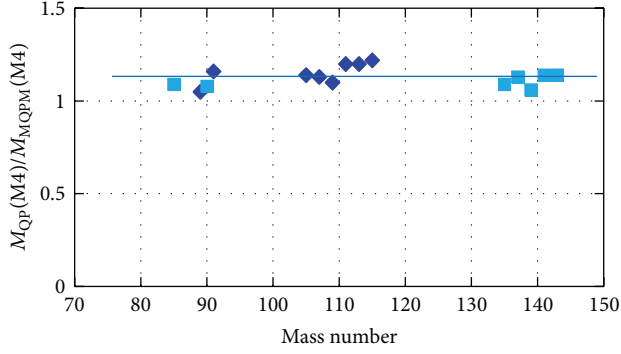


FIGURE 4: Ratios of the quasiparticle NMEs  $M_{QP}(M4)$  to the MQPM NMEs  $M_{MQPM}(M4)$  for odd-neutron transitions (light-blue squares) and odd-proton transitions (dark-blue diamonds).

in the neighboring odd-mass nuclei, of interest in the present work, were formed by first creating the quasiparticle-phonon components of the operator (14). The convergence of the MQPM results for the energies of the involved states and the M4 transition amplitudes between them were monitored by adding more and more QRPA phonons of different multipolarities  $\omega$  in the diagonalization of the residual Hamiltonian. In terms of the cut-off energy of the added phonons the convergence was achieved at around 14 MeV.

The converged M4 results are given in the sixth column of Tables 1 and 2 and are plotted in Figures 1(b) and 3(b). It is seen that the experimental M4 matrix elements,  $M_{QP}(M4)$ , are uniformly smaller, by a coefficient around 0.33, than the MQPM NMEs  $M_{MQPM}(M4)$ . Actually, the MQPM NMEs  $M_{MQPM}(M4)$  are 10–20% smaller than the QP NMEs  $M_{QP}(M4)$ , as shown in Figure 4. The admixtures of the quasiparticle-phonon components in the wave functions (14) of the M4 initial and final states reduce the M4 NMEs a little, but not nearly enough to bring the MQPM NMEs close to the corresponding experimental ones, at least by using the bare  $g$  coefficients (4) adopted in the present work. Hence, the major part of reduction from the MQPM NME to the experimental one (a reduction coefficient of 0.3) is considered to be due to such nucleonic and nonnucleonic  $\tau\sigma$  correlations and nuclear-medium effects that are not explicitly included in the (traditional) quasiparticle-phonon coupling scheme that MQPM uses, that is, the even-even nucleus serving as a reference for the odd-mass one.

## 5. Reduction of the Axial-Vector NMEs

The  $\gamma$  NME is decomposed into the isovector and isoscalar ones as [11]

$$M_\gamma(M4) = g_-(M4) \frac{\tau_3}{2} M(M4) + g_+(M4) \frac{\tau_0}{2} M(M4), \quad (15)$$

where  $M_\gamma(M4)$  is  $g_p M(M4)$  and  $g_n M(M4)$  for an odd-proton and odd-neutron transition, respectively, and  $g_-$  and  $g_+$  are

the isovector and isoscalar  $\gamma$  coupling constants. They are written as

$$g_\pm(M4) = \frac{e\hbar}{2Mc} 6 \left( \mu_\pm - \frac{1}{5} g_{l\pm} \right), \quad (16)$$

with  $\mu_\pm = \mu_n \pm \mu_p$  and  $g_{l\pm} = g_{ln} \pm g_{lp} \approx \mp 1$ .

The proton, neutron, isovector, and isoscalar M4  $\gamma$  coupling constants are given as

$$\begin{aligned} g_p &= 2.59G, \\ g_n &= -1.91G, \\ g_- &= -4.50G, \\ g_+ &= 0.68G, \end{aligned} \quad (17)$$

where  $G = 6e\hbar(2Mc)^{-1}$  is the M4  $\gamma$  coupling coefficient.

The M4 NMEs in (15) are rewritten as  $k_i g_i M_{QP}(M4)$  with  $i = p, n, -, +$ , the symbols standing for the proton, neutron, isovector, and isoscalar components, respectively. Then the reduction coefficients and the weak couplings for proton and neutron transitions are expressed in terms of those for the isovector and isoscalar components as [11]

$$\begin{aligned} k_p g_p &= -\frac{g_-}{2} k_- + \frac{g_+}{2} k_+, \\ k_n g_n &= \frac{g_-}{2} k_- + \frac{g_+}{2} k_+. \end{aligned} \quad (18)$$

After this the isovector and isoscalar reduction coefficients can be derived as

$$k_- = k_n - 0.567(k_n - k_p), \quad (19)$$

$$k_+ = k_n - 3.89(k_n - k_p). \quad (20)$$

Since the experimentally derived NMEs for the proton and neutron transitions are approximately the same, that is,  $k_n \approx k_p$ , we get from (19)  $k_- \approx k_n \approx k_p \approx 0.3$ . The isovector M4 NMEs are reduced by the coefficient  $k_- \approx 0.3$ , in the same way as the M4  $\gamma$  transition NMEs. It is notable that the amount of reduction for the isovector  $4^-$   $\gamma$  NMEs is the same as that found for the  $GT(1^+)$  and  $SD(2^-)$   $\beta$  decay NMEs [8, 10].

Axial-vector  $\beta$  and  $\gamma$  NMEs for low-lying states are much reduced with respect to the QP NMEs due to the strong repulsive  $\tau\sigma$  interactions since the axial-vector  $\tau\sigma$  strengths are pushed up into the  $\tau\sigma$  giant-resonance (GR) and the  $\Delta$ -isobar regions. The M4 reduction coefficient of  $k(M4) \approx 0.29$  is nearly the same as the coefficient  $k(M2) \approx 0.24$  for M2  $\gamma$  transitions and  $k(GT) \approx 0.235$  and  $k(SD) \approx 0.18$  in the  $GT(1^+)$  and  $SD(2^-)$   $\beta$  decay NMEs, respectively [8, 10]. These reduction coefficients are plotted in Figure 5 with  $\lambda$  denoting the angular momentum content of the transition operator.

It seems that the reduction coefficients of the axial-vector NMEs are universal for NC and CC NMEs and for the angular momenta of  $\lambda = 1-4$ . The reduction is considered to be due to such  $\sigma\tau$  polarization interactions and nuclear-medium effects that are not explicitly included in the models. Then the

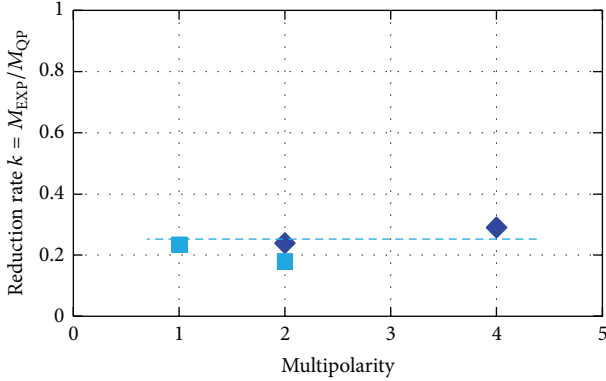


FIGURE 5: Reduction coefficients  $k(M) = M_{\text{EXP}}(M)/M_{\text{QP}}(M)$  for the multipolarity  $M = M2$  ( $\lambda = 2$ )  $\gamma$  and  $M = M4$  ( $\lambda = 4$ )  $\gamma$  transitions (dark-blue diamonds) and those for  $M = \text{GT}$  ( $\lambda = 1$ )  $\beta$  and  $M = \text{SD}$  ( $\lambda = 2$ )  $\beta$  transitions (light-blue squares) in medium-heavy nuclei. Here  $\lambda$  denotes the transition angular momentum. The dotted line shows  $k(M) = 0.27$ .

reduction rate  $k(M) \approx 0.2\text{--}0.3$ , with respect to the QP NME, is expressed as [8, 10]

$$k(M) = k_{\sigma\tau}(M) \times k_{\text{NM}}(M), \quad (21)$$

where  $k_{\sigma\tau}(M) \approx 0.5$  and  $k_{\text{NM}}(M) \approx 0.5$  stand for the reductions due to the nucleonic  $\sigma\tau$  polarization effects and nonnucleonic  $\Delta$ -isobar and nuclear-medium effects, respectively.

These universal effects may be represented by the effective weak coupling  $g_A^{\text{eff}}$ , depending on the model NME, to incorporate the effects that are not explicitly included in the nuclear-structure model. In case of the pnQRPA with explicit nucleonic  $\sigma\tau$  correlations, one may use  $g_A \approx 0.6$ , while in the case of the QP model, without any  $\sigma\tau$  correlations,  $g_A \approx 0.3$ , both in units of the bare value of  $g_A = 1.26g_V$ .

Here we note that the  $\tau\sigma$  repulsive interaction concentrates the  $\tau\sigma$  strength to the highly excited  $\tau\sigma$  GR, resulting in the reduction of the  $\tau\sigma$  NMEs for low-lying states. Such reduction effect is incorporated in the pnQRPA with the strong  $\tau\sigma$  interaction, so that the reduction factor is improved from  $k_{\text{QP}} \approx 0.3$  to  $k_{\text{QRPA}} \approx 0.6$ . On the other hand, such strong  $\tau\sigma$  interaction to give rise to the possible M4 GR is not explicitly incorporated in the MQPM, and thus the reduction factor is only a little improved from  $k_{\text{QP}} \approx 0.29$  to  $k_{\text{MQPM}} \approx 0.33$ .

## 6. Discussion and Conclusions

Among other models, the QRPA-based models are used to compute the NMEs of double beta decays [4, 27]. In these calculations the importance of the quenching of  $g_A$  magnifies since the  $0\nu\beta\beta$  NME includes the axial-vector NME proportional to the square of  $g_A$ . The M4 NC  $\gamma$  results of the present investigation, together with the earlier M2 NC and GT and SD CC results, suggest that many of the leading multipoles in the decomposition of the neutrinoless  $\beta\beta$  NMEs are quenched roughly by the same amount by

the  $\sigma\tau$  correlations of the  $\Delta$  region as well as other nuclear-medium effects. Since the corresponding investigations have been done using data on low-lying nuclear states it is safe to say that the quenching applies at least to the low-lying states in nuclei. These observations are very relevant for the two-neutrino  $\beta\beta$  decays since they are low-energy phenomena and usually involve only one or few lowest states in the intermediate nucleus [1, 28, 29]. A consistent description of these decays can be achieved by using the quenched  $g_A$  derived from the GT  $\beta$  decays [30].

Actually, the observed single  $\beta$  GT NMEs are reduced by the effective coupling constant  $k^{\text{eff}}$  with respect to the model NME, and thus the observed  $2\nu\beta\beta$  NMEs are well reproduced by using the experimental  $k^{\text{eff}}$ , that is, the experimental single  $\beta$  NMEs for low-lying states [1, 2, 31]. However, it should be kept in mind that these results, important as such, cannot be directly applied to the  $0\nu\beta\beta$  processes since there large momentum exchanges are involved and also vector-type of NMEs and higher excited states contribute. In this case it is a big challenge to develop such nuclear models for the axial-vector weak processes that include explicitly appropriate nucleonic and nonnucleonic correlations. If successful, then in such models one could use the axial weak coupling of  $g_A = 1.26g_V$  and be free from the uncertainties introduced by the effective (quenched)  $g_A^{\text{eff}}$ .

Neutrino-nucleus scatterings are important to probe many astrophysical phenomena, like the solar and supernova neutrinos [1, 32, 33]. The GT NMEs bring in most of the contributions for solar neutrinos and low-energy supernova neutrinos for neutrino energies below 15 MeV (see, e.g., [16, 17]). The SD NMEs play a role for medium-energy neutrinos above 15 MeV. For the low-energy solar neutrinos reliable calculations of the GT NMEs are needed to evaluate the SNU values for the pp,  ${}^7\text{Be}$ , CNO, and other neutrinos. Experimental GT strengths can also be used, if available [1]. The SD contributions can be important for the CC supernova antineutrino scatterings off nuclei even at low energies, as shown in [15–18].

The supernova-neutrino nucleosyntheses are sensitive to the neutrino CC and NC interactions, as discussed in a review article [33]. Here SD and higher-multipole NMEs are involved in the high-energy components of the supernova neutrinos. It is important for accurate evaluations of the isotope distributions to use appropriate NMEs and effective weak couplings of  $g_A^{\text{eff}}$  and  $g_V^{\text{eff}}$ . QRPA calculations were made for  ${}^{92}\text{Nb}$  nuclei in [34].

The involved GT and SD NMEs can be studied via beta decays in nuclei where beta decay data is available. In some of these studies a strong quenching of both  $g_A$  and  $g_V$  has been conjectured [35–38]. Such quenching for the higher multipoles is extremely hard to study, the present study being a rather unique one in this respect. Quenching of the higher multipoles can also be studied via high-forbidden beta decays [19] but the available data is extremely scarce at the moment. Perspectives for the studies of the quenching of both  $g_A$  and  $g_V$  are given by the spectrum-shape method introduced in [19]. There the shape of the beta spectrum of the high-forbidden nonunique beta decays has been studied for the determination of the possible quenching of the weak

constants. Use of this method can be boosted by future high-sensitive measurements of electron spectra in underground laboratories.

Finally, it is worth pointing out that the universal reduction/quenching of the  $\tau\sigma$  NME, including  $g_A$ , is related to the shift of the strength to the higher GR and  $\Delta$  isobar regions. Charge-exchange reactions report about a 50–60% of the GT sum rule (the Ikeda sum rule) up to GT GR, while the (p, n) reactions claim that around 90% of the GT sum-rule strength is seen by including the strength beyond the GT GR up to 50 MeV [39]. Very careful investigations of the GT, SD, and higher-multipole strength distributions, by using charge-exchange reactions, are called for to see if the reduction/quenching of the  $\tau\sigma$  strengths is partly due to the nonnucleonic ( $\Delta N^-$ )  $\tau\sigma$  correlations [8, 20]. These investigations not only are interesting from the point of view of the double beta decay but also touch the projected double charge-exchange reactions [40] where the high-momentum response of nuclei is also probed.

## Competing Interests

The authors declare that they have no competing interests.

## Acknowledgments

This work was supported by the Academy of Finland under the Finnish Center of Excellence Program 2012–2017 (Nuclear and Accelerator Based Program at JYFL).

## References

- [1] H. Ejiri, “Nuclear spin isospin responses for low-energy neutrinos,” *Physics Reports*, vol. 338, no. 3, pp. 265–351, 2000.
- [2] J. D. Vergados, H. Ejiri, and F. Šimkovic, “Theory of neutrinoless double-beta decay,” *Reports on Progress in Physics*, vol. 75, no. 10, Article ID 106301, 2012.
- [3] F. T. Avignone, S. R. Elliott, and J. Engel, “Double beta decay, Majorana neutrinos, and neutrino mass,” *Reviews of Modern Physics*, vol. 80, no. 2, pp. 481–516, 2008.
- [4] J. Suhonen and O. Civitarese, “Weak-interaction and nuclear-structure aspects of nuclear double beta decay,” *Physics Report*, vol. 300, no. 3–4, pp. 123–214, 1998.
- [5] J. Hyvärinen and J. Suhonen, “Nuclear matrix elements for  $0\nu\beta\beta$  decays with light or heavy Majorana-neutrino exchange,” *Physical Review C*, vol. 91, no. 2, Article ID 024613, 2015.
- [6] A. Faessler, G. L. Fogli, E. Lisi, V. Rodin, A. M. Rotunno, and F. Šimkovic, “Overconstrained estimates of neutrinoless double beta decay within the QRPA,” *Journal of Physics G: Nuclear and Particle Physics*, vol. 35, no. 7, Article ID 075104, 2008.
- [7] J. Suhonen and O. Civitarese, “Probing the quenching of  $g_A$  by single and double beta decays,” *Physics Letters B*, vol. 725, no. 1–3, pp. 153–157, 2013.
- [8] H. Ejiri, N. Soukouti, and J. Suhonen, “Spin-dipole nuclear matrix elements for double beta decays and astro-neutrinos,” *Physics Letters B*, vol. 729, pp. 27–32, 2014.
- [9] J. Suhonen and O. Civitarese, “Single and double beta decays in the  $A = 100$ ,  $A = 116$  and  $A = 128$  triplets of isobars,” *Nuclear Physics A*, vol. 924, pp. 1–23, 2014.
- [10] H. Ejiri and J. Suhonen, “GT neutrino-nuclear responses for double beta decays and astro neutrinos,” *Journal of Physics G: Nuclear and Particle Physics*, vol. 42, no. 5, Article ID 055201, 2015.
- [11] H. Ejiri and J. I. Fujita, “Effective coupling constants for beta and gamma transitions in medium and heavy nuclei,” *Physics Reports*, vol. 38, no. 2, pp. 85–131, 1978.
- [12] J. Barea, J. Kotila, and F. Iachello, “Nuclear matrix elements for double- $\beta$  decay,” *Physical Review C*, vol. 87, no. 1, Article ID 014315, 2013.
- [13] J. Barea, J. Kotila, and F. Iachello, “ $0\nu\beta\beta$  and  $2\nu\beta\beta$  nuclear matrix elements in the interacting boson model with isospin restoration,” *Physical Review C*, vol. 91, no. 3, Article ID 034304, 2015.
- [14] J. D. Holt and J. Engel, “Effective double- $\beta$ -decay operator for  $^{76}\text{Ge}$  and  $^{82}\text{Se}$ ,” *Physical Review C*, vol. 87, no. 6, Article ID 064315, 7 pages, 2013.
- [15] C. Volpe, N. Auerbach, G. Colò, and N. Van Giai, “Charged-current neutrino- $^{208}\text{Pb}$  reactions,” *Physical Review C*, vol. 65, no. 4, Article ID 044603, 2002.
- [16] W. Almosly, E. Ydrefors, and J. Suhonen, “Neutral- and charged-current supernova-neutrino scattering off  $^{116}\text{Cd}$ ,” *Journal of Physics G: Nuclear and Particle Physics*, vol. 40, no. 9, Article ID 095201, 2013.
- [17] W. Almosly, E. Ydrefors, and J. Suhonen, “Neutrino scattering off the stable cadmium isotopes: II. Charged-current processes,” *Journal of Physics G: Nuclear and Particle Physics*, vol. 42, no. 9, Article ID 095106, 2015.
- [18] R. Lazauskas and C. Volpe, “Neutrino beams as a probe of the nuclear isospin and spin-isospin excitations,” *Nuclear Physics A*, vol. 792, no. 3–4, pp. 219–228, 2007.
- [19] M. Haaranen, P. C. Srivastava, and J. Suhonen, “Forbidden non-unique  $\beta$  decays and effective values of weak coupling constants,” *Physical Review C*, vol. 93, no. 3, Article ID 034308, 2016.
- [20] A. Bohr and B. R. Mottelson, *Nuclear Structure Volume I, II*, Benjamin, New York, NY, USA, 1969, 1975.
- [21] J. Suhonen, *From Nucleons to Nucleus: Concepts of Microscopic Nuclear Theory*, Theoretical and Mathematical Physics, Springer, Berlin, Germany, 2007.
- [22] J. Toivanen and J. Suhonen, “Microscopic quasiparticle-phonon description of odd-mass  $\text{Xe}^{127-133}$  isotopes and their  $\beta$  decay,” *Physical Review C*, vol. 57, no. 3, pp. 1237–1245, 1998.
- [23] K. Holinde, “Two-nucleon forces and nuclear matter,” *Physics Reports*, vol. 68, no. 3, pp. 121–188, 1981.
- [24] J. Suhonen, A. Faessler, T. Taigel, and T. Tomoda, “Suppression of the  $\beta^+$ -decays of  $^{148}\text{Dy}$ ,  $^{150}\text{Er}$  and  $^{152}\text{Yb}$ ,” *Physics Letters B*, vol. 202, no. 2, pp. 174–178, 1988.
- [25] J. Suhonen, T. Taigel, and A. Faessler, “pnQRPA calculation of the  $\beta^+$ /EC quenching for several neutron-deficient nuclei in mass regions  $A = 94$ –110 and  $A = 146$ –156,” *Nuclear Physics A*, vol. 486, no. 1, pp. 91–117, 1988.
- [26] G. Audi, F. G. Kondev, M. Wang et al., “The Nubase2012 evaluation of nuclear properties,” *Chinese Physics C*, vol. 36, no. 12, p. 1157, 2012.
- [27] J. Suhonen and O. Civitarese, “Double-beta-decay nuclear matrix elements in the QRPA framework,” *Journal of Physics G: Nuclear and Particle Physics*, vol. 39, no. 8, Article ID 085105, 2012.
- [28] M. Bhattacharya, A. García, M. M. Hindi et al., “Electron capture decay of  $^{116}\text{In}$  and nuclear structure of double  $\beta$  decays,” *Physical Review C*, vol. 58, no. 2, p. 1247, 1998.

- [29] O. Civitarese and J. Suhonen, "Systematic study of the single-state dominance in  $2\nu\beta\beta$  decay transitions," *Nuclear Physics A*, vol. 653, no. 3, pp. 321–337, 1999.
- [30] P. Pirinen and J. Suhonen, "Systematic approach to  $\beta$  and  $2\nu\beta\beta$  decays of mass  $A = 100 - 136$  nuclei," *Physical Review C*, vol. 91, no. 5, Article ID 054309, 2015.
- [31] H. Ejiri, "Experimental nuclear matrix elements for two neutrino double beta decays and single beta decays," *Journal of the Physical Society of Japan*, vol. 78, no. 7, Article ID 074201, 2009.
- [32] S. E. Woosley, D. H. Hartman, R. D. Hoffman, and W. C. Haxton, "The neutrino-process," *The Astrophysical Journal*, vol. 356, pp. 272–301, 1990.
- [33] K. Langanke and G. Martínez-Pinedo, "Nuclear weak-interaction processes in stars," *Reviews of Modern Physics*, vol. 75, no. 3, pp. 819–862, 2003.
- [34] M.-K. Cheoun, E. Ha, T. Hayakawa et al., "Neutrino induced reactions for  $\nu$ -process nucleosynthesis of  $^{92}\text{Nb}$  and  $^{98}\text{Tc}$ ," *Physical Review C*, vol. 85, no. 6, Article ID 065807, 12 pages, 2012.
- [35] E. K. Warburton, "Core polarization effects on spin-dipole and first-forbidden  $\beta$ -decay operators in the lead region," *Physical Review C*, vol. 42, no. 6, pp. 2479–2486, 1990.
- [36] E. K. Warburton, "First-forbidden  $\beta$  decay in the lead region and mesonic enhancement of the weak axial current," *Physical Review C*, vol. 44, no. 1, pp. 233–260, 1991.
- [37] T. Suzuki, T. Yoshida, T. Kajino, and T. Otsuka, " $\beta$  decays of isotones with neutron magic number of  $N = 126$  and  $r$ -process nucleosynthesis," *Physical Review C*, vol. 85, no. 1, Article ID 015802, 2012.
- [38] Q. Zhi, E. Caurier, J. J. Cuenca-García, K. Langanke, G. Martínez-Pinedo, and K. Sieja, "Shell-model half-lives including first-forbidden contributions for  $r$ -process waiting-point nuclei," *Physical Review C*, vol. 87, no. 2, Article ID 025803, 2013.
- [39] T. Wakasa, H. Sakai, H. Okamura et al., "Gamow-Teller strength of  $^{90}\text{Nb}$  in the continuum studied via multipole decomposition analysis of the  $^{90}\text{Zr}(p,n)$  reaction at 295 MeV," *Physical Review C*, vol. 55, no. 6, p. 2909, 1997.
- [40] F. Cappuzzello, M. Cavallaro, C. Agodi et al., "Heavy-ion double charge exchange reactions: a tool toward  $0\nu\beta\beta$  nuclear matrix elements," *The European Physical Journal A*, vol. 51, article 145, 2015.